Thèse

présentée pour obtenir le titre de DOCTEUR
ECOLE DOCTORALE DE SCIENCES PHYSIQUES ET DE L'INGENIEUR
Spécialité: Astrophysique, Plasmas, Nucléaire

Sections efficaces neutroniques via la méthode de substitution

Neutron-induced cross-sections via the surrogate method

Guillaume Boutoux
boutoux@cenbg.in2p3.fr

Soutenue publiquement le 25/11/2011 devant un jury composé de :

Président	M. Phillipe Moretto	Professeur Univ. Bordeaux 1
Rapporteurs	M. Laurent Tassan-Got	Directeur de Recherche CNRS
	M. Frank Gunsing	Physicien CEA Saclay
Examinateurs	M. Olivier Sérot	Physicien CEA Cadarache
	M. Pascal Romain	Physicien CEA DAM-DIF
Directeur de thèse	M. Gérard Barreau	Directeur de Recherche CNRS
Co-encadrante de thèse	Mme Béatriz Jurado	Chargée de Recherche CNRS

n° d'ordre: 4375

Thèse réalisée au	Centre d'Etudes Nucléaires de Bordeaux Gradignan
	Chemin du Solarium
	Le Haut Vigneau
	BP120
	33175 GRADIGNAN Cedex
	Tél : +33 5 57 12 08 04
	Fax : +33 5 57 12 08 01
	Web : http://www.cenbg.in2p3.fr

| *Sous la direction de* | Dr. Gérard Barreau | barreau@cenbg.in2p3.fr |

| *Co-encadrement* | Dr. Béatriz Jurado | jurado@cenbg.in2p3.fr |
| | Dr. Olivier Sérot | olivier.serot@cea.fr |

| *Financement* | Bourse Docteur-Ingénieur |
| | cofinancée par le CNRS et le CEA Cadarache |

Synthèse (en français)

Les sections efficaces neutroniques des noyaux de courte durée de vie sont des données cruciales pour la physique fondamentale et appliquée dans des domaines tels que la physique des réacteurs ou l'astrophysique nucléaire. En général, l'extrême radioactivité de ces noyaux ne nous permet pas de procéder à des mesures induites par neutrons. Cependant, il existe une méthode de substitution (« surrogate » dans la littérature) qui permet de déterminer ces sections efficaces neutroniques par l'intermédiaire de réactions de transfert ou de réactions de diffusion inélastique. Son intérêt principal est de pouvoir utiliser des cibles moins radioactives et ainsi d'accéder à des sections efficaces neutroniques qui ne pourraient pas être mesurées directement. La méthode est basée sur l'hypothèse de formation d'un noyau composé et sur le fait que sa désexcitation dépend essentiellement de l'énergie d'excitation et du spin et parité de l'état composé peuplé. Toutefois, les distributions de moments angulaires et parités peuplés dans des réactions de transfert et celles induites par neutrons sont susceptibles d'être différentes. Ce travail fait l'état de l'art sur la méthode de substitution et sa validité. En général, la méthode de substitution fonctionne très bien pour extraire des sections efficaces de fission. Par contre, la méthode de substitution dédiée à la capture radiative est mise à mal par la comparaison aux réactions induites par neutrons. Nous avons réalisé une expérience afin de déterminer les probabilités de desexcitation gamma du ^{176}Lu et du ^{173}Yb à partir des réactions de substitution $^{174}Yb(^{3}He, p\gamma)^{176}Lu^{*}$ et $^{174}Yb(^{3}He, \alpha\gamma)^{173}Yb^{*}$, respectivement, et nous les avons comparées avec les probabilités de capture correspondantes aux réactions $^{175}Lu(n, \gamma)$ et $^{172}Yb(n, \gamma)$ qui sont bien connues. Cette expérience a permis de comprendre pourquoi, dans le cas de la desexcitation gamma, la méthode de substitution donne des écarts importants par rapport à la réaction neutronique correspondante. Ce travail apporte donc un éclairage nouveau sur la méthode de substitution.

Le chapitre 1 est un panorama théorique des réactions nucléaires induites par noyaux légers et de la désexcitation statistique. En particulier, on montre que les réactions de substitution induisent majoritairement la formation d'un noyau composé tant que l'énergie d'excitation ne dépasse pas la dizaine de MeV et que donc la méthode de substitution est à priori applicable dans ce domaine. On détaille ensuite comment l'approximation Weisskopf-Ewing dérive du formalisme Hauser-Feshbach. La validité de la méthode est ensuite investiguée à l'aide de calculs basés sur le modèle statistique. Ces calculs illustrent bien la sensibilité au spin et à la parité du noyau composé de la désexcitation, en particulier pour ce qui concerne l'émission gamma.

Au travers d'une bibliographie riche, le chapitre 2 est une revue des expériences de substitution dédiées à la fission et à la capture radiative effectuées à ce jour (fin 2011). La revue montre aussi, là où c'est possible, le degré d'accord avec les données des réactions induites par neutrons. En général, la méthode de substitution fonctionne très bien pour extraire des sections efficaces de fission. Par contre, la méthode de substitution dédiée à la capture radiative est mise à mal par la comparaison aux réactions induites par neutrons. De récentes expériences montrent que les sections efficaces obtenues peuvent être surestimées par un facteur supérieur à 2. La revue pose la problématique du travail de la thèse sur la validité des réactions de substitution. Le bilan de la revue justifie l'expérience $^{174}Yb(^{3}He, x\gamma)$ comme test de la méthode de substitution. La réalisation et l'analyse de cette expérience constituent le cœur de la thèse.

Le système expérimental, décrit au chapitre 3, est complexe : il comprend deux détecteurs de particules chargées, 4 scintillateurs liquides C_6D_6 et 6 détecteurs Ge. De façon indépendante, les germaniums sont utilisés pour faire la spectroscopie des noyaux excités à basse énergie et les scintillateurs C_6D_6 permettent de faire du comptage des photons jusqu'à des énergies de l'ordre d'une dizaine de MeV.

La procédure d'analyse est ensuite décrite dans le chapitre 4. L'étalonnage et la détermination de la résolution des détecteurs sont expliquées, ainsi que la soustraction du bruit de fond provenant des réactions contaminantes avec le support en carbone. Une discrimination entre neutrons et photons détectés est réalisée par analyse de la forme du signal. De plus, la contribution des gammas provenant des noyaux résiduels après émissions de neutrons est supprimée en fixant artificiellement un seuil de détection gamma élevé. La partie cruciale de l'analyse est la détermination de l'efficacité de détection pour un événement de capture. Le principe de détection totale de l'énergie combiné à des fonctions de pondération permet de déterminer cette quantité indépendamment des chemins empruntés par les cascades-gamma. Cette technique fréquemment utilisée dans des expériences neutroniques à n_ToF (CERN) et à GELINA (IRMM) est détaillée ici de façon pédagogique. En parallèle, nous avons développé une technique originale basée sur l'hypothèse que l'efficacité de détection des cascades-gamma est constante au voisinage du seuil de séparation neutron S_n. La détermination de l'efficacité via cette

méthode alternative a été validée par comparaison avec l'efficacité déterminée à l'aide des fonctions de poids. Cette méthode a l'avantage d'être beaucoup plus simple que la méthode des fonctions de poids. Les probabilités de capture radiative ont été extraites pour chaque voie de transfert. Enfin, il est important de noter qu'à notre connaissance, c'est la première fois qu'une expérience de substitution associe la détection des gammas avec des détecteurs de type C_6D_6 et germanium. Les deux méthodes donnent des résultats concordants.

Dans le cas des voies $(^3He, p\gamma)$ et $(^3He, \alpha\gamma)$ où il existe des mesures pour les noyaux équivalents formés par les réactions (n, γ), les probabilités de desexcitation gamma sont surestimées d'un facteur 3 à 10, confirmant ainsi les écarts déjà révélés dans des expériences antérieures. Dans la mesure où les spins transférés sont très difficiles à calculer de manière fiable, le chapitre 5 présente une méthode permettant d'avoir des informations sur les distributions de spins des noyaux formés dans les réactions de transfert. La méthode est basée sur la très forte sensibilité en spin de la désexcitation par émission gamma. En combinant un modèle pour la distribution de spin et des calculs TALYS pour les rapports d'embranchement, un fit de la probabilité d'émission gamma expérimentale permet de déduire la distributions de spin du noyau composé.

La conclusion fondamentale de cette étude est donnée dans la discussion du chapitre 6. La différence en spin des noyaux formés par réactions de substitution, par rapport à la réaction induite par neutrons, défavorise l'émission de neutrons. Par conséquent, la compétition renforce l'émission gamma, ce qui explique pourquoi les probabilités expérimentales de capture radiative sont surestimées dans la méthode de substitution. Ce travail dans la région de terres rares est extrêmement utile pour évaluer dans quelle mesure la méthode de substitution peut s'appliquer pour extraire des probabilités de capture dans la région des actinides. Des expériences précédentes sur la fission et la capture ont aussi pu être réinterprétées.

Pour conclure, le chapitre 7 décrit les perspectives (à court, moyen et long terme) en relation avec la méthode de substitution.

Contents

Interpretation & Consequences   173

5   Interpretation of results   175

Introduction

Data needs

The interaction of neutrons with nuclei is a topic of great importance in many areas: fundamental nuclear physics, nuclear astrophysics and many nuclear applications, such as nuclear reactors. For all these applications, cross sections for particular reactions must be known, often accurately. Measured data are afterwards used to provide reliable evaluations.

Nuclear reactors

Current nuclear reactors produce two kinds of waste which are extremely problematic: some fission products whose half-lives often reach million of years and heavy nuclei, i.e minor actinides. The latter are mainly Np, Am and Cm isotopes. Some of the minor actinides are highly radiotoxic like ^{242}Cm and others have long half-lifes like ^{237}Np. In France, it is envisaged to glaze these wastes and stock them in deep geological site. Nevertheless, the possibility of incinerating (i.e. transmuting by fission into less radiotoxic species) is also explored. Incineration was defined as an important research topic by the so-called «Bataille» law of December $30th$ 1991 (law relative to the research on radioactive waste management). This research topic was reinforced by the law of June $28th$ 2006.

More precisely, incineration consists of using a fast neutron flux produced in a reactor to destroy the minor actinides by making them fission. The advantage of fission is that it leads mainly to short-lived fission products whose radioactivity is easier to manage than the one of the original actinide. In addition, the fission reaction produces additional neutrons that can be use to incinerate other waste or feed the chain reaction. When a heavy nucleus is bombarded with neutrons of less than few MeV energy, radiative capture and neutron emission compete with fission. For the incineration to be effective, neutron capture needs to be minimized since it leads to heavier and heavier actinides which are potentially more radioactive.

For this reason, in reactor physics one defines the α ratio:

$$\alpha = \frac{\sigma_{capture}}{\sigma_{fission}} \tag{0.1}$$

This ratio reflects the incineration power. This parameter is essential in the demonstration of the transmutation capacities of fast reactors or, presumably, of future Accelerator-Driven Systems ([Salvatores 06]). Table 0.1 shows why the fast-neutron spectrum is best-suited for minor-actinide incineration.

Isotopes	«Thermal» reactor PWR			«Fast» reactor SFR		
	$\sigma_{fission}$/b	$\sigma_{capture}$/b	α	$\sigma_{fission}$/b	$\sigma_{capture}$/b	α
^{237}Np	0.52	33	63	0.32	1.7	5.3
^{241}Am	1.1	110	100	0.27	2	7.4
^{243}Am	0.44	49	111	0.21	1.8	8.6
^{242}Cm	1.14	4.5	3.9	0.58	1.0	1.7
^{243}Cm	88	14	0.16	7.2	1.0	0.14
^{244}Cm	1.0	16	16	0.42	0.6	1.4

Table 0.1: Mean evaluated fission $\sigma_{fission}$ and radiative capture $\sigma_{capture}$ cross sections, and the ratio α for several isotopes ([Varaine 06]).

Defining the feasibility of incineration requires high-quality fission and capture cross sections (5% is the required uncertainty) of minor actinides. Figure 0.1 illustrates the case of the three more important minor actinides. Fission cross sections are known with an error of 8% for $^{237}Np(n,f)$ and 10% for $^{241}Am(n,f)$ and evaluations are in good agreement for these two nuclei. However, the data for $^{244}Cm(n,f)$ suffer from big uncertainties ($\sim$45%) that lead to large differences between the evaluations. Concerning radiative capture, except for ^{237}Np, no data are available for ^{241}Am and ^{244}Cm. As a consequence, the available evaluations may disagree by an order of magnitude.

The development of innovative systems and concepts, like the ADS MYRRHA and the GEN-IV reactor ASTRID, relies on accurate and consistent neutron cross-sections. In the context of the NEA Nuclear Data High Priority Request List (HPRL), a demand has been developed for improving neutron cross-section data of minor actinides in the fast energy range.
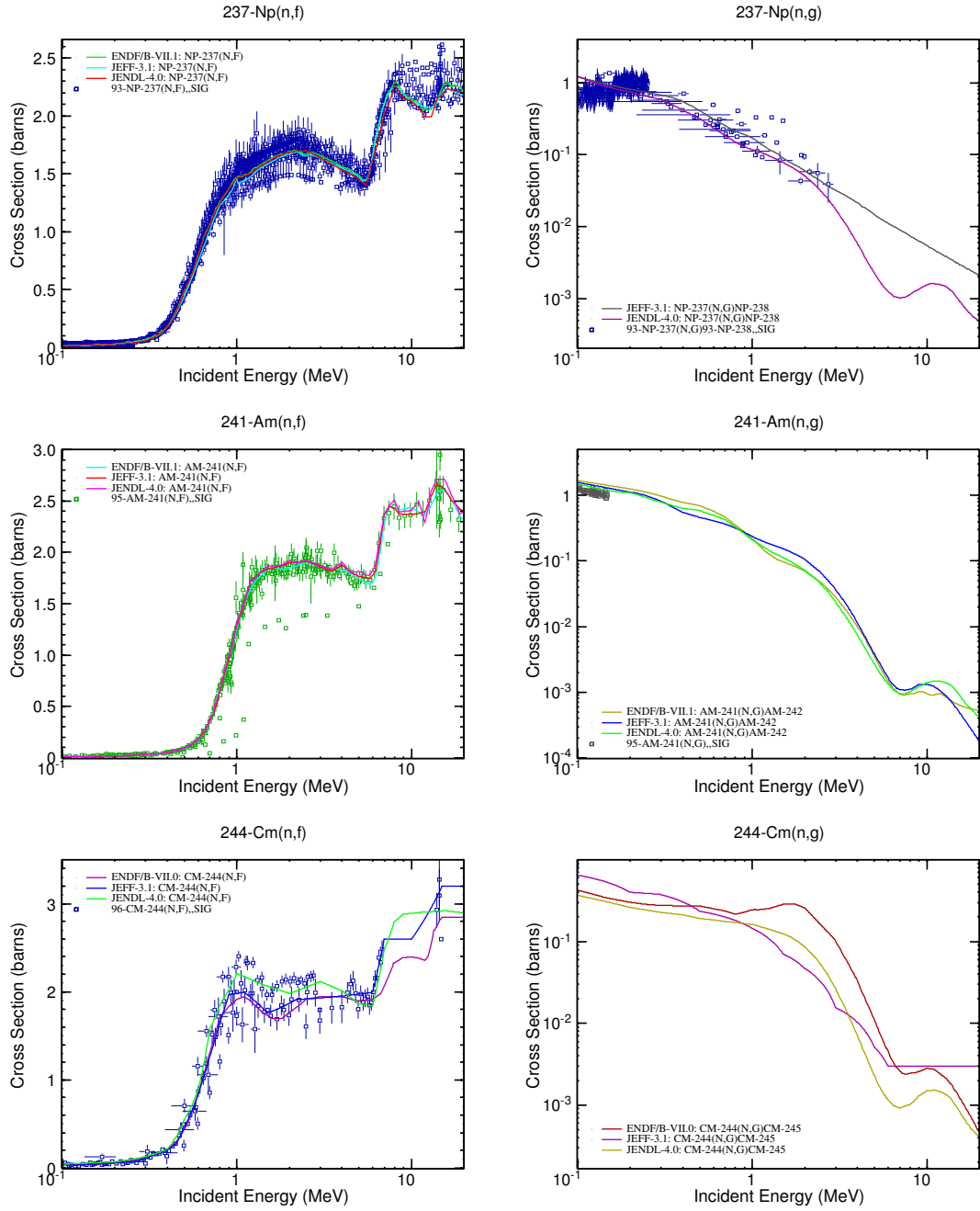
Figure 0.1: Neutron-induced fission and capture cross sections of key minor actinides. Experimental data (NNDC-EXFOR) are compared with available international libraries in the energy range $[0.1; 20]$ MeV. The half-lives for ^{237}Np, ^{241}Am and ^{244}Cm are 2144000 years , 432.2 years, 18.10 years, respectively.

Astrophysics

Neutron-induced reactions on short-lived nuclei are also important for understanding astrophysical phenomena and the origin of the elements. Among all the modes of stellar synthesis, the s and r processes produce almost all heavy elements and are directly linked to stellar evolution. In fact, the nuclei beyond iron are produced by a sequence of neutron capture reactions and subsequent β-decays.

- The **s-process** is the process of neutron capture with the emission of gamma radiation (n, γ) which takes place on a long time-scale, ranging from 100 years to 10^5 years for each neutron capture. If the neutron flux is weak, unstable nuclei can decay before they have the possibility to capture another neutron, and the neutron capture chain proceeds rather close to the valley of β-stability. This slow (s) mode of synthesis is responsible for the production of the majority of the isotopes in the range $23 < A < 46$, and for a considerable proportion of the isotopes in the range $63 < A < 209$.

- The **r-process** is the process of neutron capture on a very short time-scale, $\sim 0.01 - 10$ sec for the β decay processes interspersed between the neutron captures. The neutron captures occur at a rapid (r) rate compared to the β decays. That is why the r-process path approaches the neutron drip-line. This mode of synthesis is responsible for production of a large number of isotopes in the range $70 < A < 209$, and also for the synthesis of uranium and thorium.

Figure 0.2 shows the different stellar mode paths with a special emphasis in the rare-earth region. Abundance patterns are predicted by models, which require neutron-induced cross sections as inputs ([Burbidge 57]). The cross sections of the key isotopes for the s-process should be determined with uncertainties of $\approx 1\%$. This goal has been reached for several stable nuclei but enhanced efforts should be directed to measurements on unstable nuclei, as the important branching points ^{79}Se, ^{85}Kr, ^{147}Pm, ^{151}Sm, ^{163}Ho, $^{170,171}Tm$, ^{179}Ta, ^{204}Tl and ^{205}Pb ([Kappeler 06]). These nuclei have the particularity to have a long enough life time to allow the reaction path to proceed by either neutron capture or β decay.
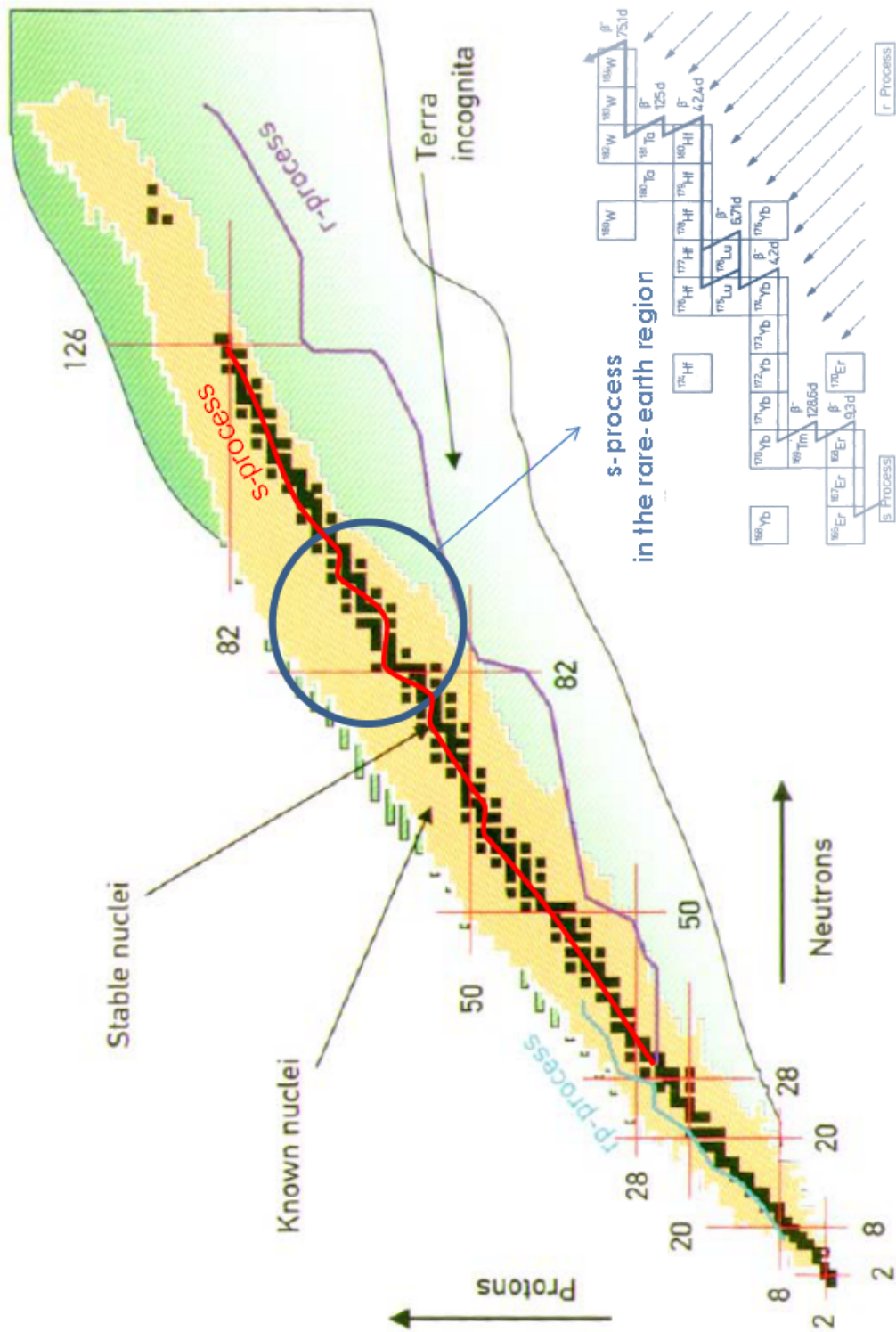
Figure 0.2: Nuclear chart with stellar modes paths. The s-process synthesis path in the vicinity of lutetium is detailed in the inset with possible r-process contributions indicated by dashed arrows. ([Beer 80]) Note that the rp-process is relative to (p, γ) reactions.

Neutron-induced cross section measurements

Experimentally, the usual method to determine neutron-induced cross sections involves putting a target under a neutron flux and measuring the quantities which compose the following equation:

$$\sigma(E_n, reac) = \frac{N_{reac}}{\Phi_n(E_n).N_{target}.\triangle t.\epsilon_{det}} \tag{0.2}$$

where:

- $\frac{N_{reac}}{\triangle t.\epsilon_{det}}$ is the total number of detected reactions N_{reac} within a time $\triangle t$ corrected for the detection efficiency ϵ_{det}.

- N_{target} is the number of nuclei in the target.

- $\Phi_n(E_n)$ is the neutron flux ($s^{-1}cm^{-2}$) at an energy E_n which impinges on the target.

The neutron flux is probably the most difficult quantity to determine in neutron-induced experiments. Since the neutron does not ionize matter, it is detected via secondary reactions that emit a charged particle or photons, which are easier to detect. A well-known reference cross section is usually used to infer the neutron flux. At the CENBG, the elastic scattering (n, p) cross section is used as reference. Note that this reaction presents the particularity to be very well known with a precision of 0.5% over a large energy range of energy. More details can be found in [Kessedjian 08].

For short-lived nuclei, measurements are very complicated because of the high radioactivity of the target. The following problems are encountered:

- Radioactive targets are very difficult to manipulate. Radioactivity obstructs the fabrication of targets and the purity of the target is difficult to obtain. Only few specialized laboratories are able to prepare such targets.

- The radioactivity of the target must be lower than the upper activity limit authorized in the experimental area. For very short-lived nuclei, the quantity of matter that can be used is extremely small. For instance, the specific activity of a ^{233}Pa sample is about $0, 8.10^9 \ Bq.\mu g^{-1}$. Consequently measurements may need a very long time since usually neutron fluxes are very small.

- Neutron-rich short-lived nuclei may have a high α activity and sometimes decay by spontaneous fission. This activity is responsible for an important background that mixes up with the signals of interest. Also for very radioactive targets one needs to correct for the variation of N_{target} with time and the reactions on the daughter nuclei.

An alternative way to deduce neutron-induced cross sections: the surrogate method

To overcome these difficulties, an alternative method was proposed by J.D.Cramer and H.C.Britt ([Cramer 70b]) in the seventies.
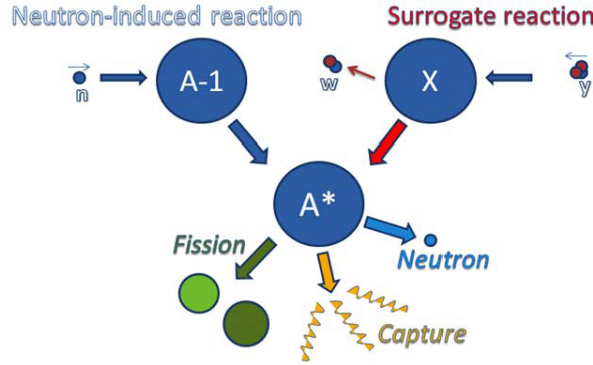
Figure 0.3: Schematic representation of the surrogate reaction method. The surrogate reaction is here a transfer reaction $X(y,w)A*$. Three possible exit channels (fission, capture and neutron emission) are also represented.

The left part of figure 0.3 illustrates a neutron-induced reaction on target $A-1$, which leads to the compound-nucleus A at an excitation energy E^*. The nucleus A^* can decay through different exit channels: fission, gamma-decay, neutron emission, etc... On the right part of figure 0.3, in the surrogate reaction method, the same compound-nucleus A^* is produced by a transfer reaction between a projectile y (a light charged particle) and a target X. The transfer reaction $(y + X \longrightarrow A + w)$ leads to a heavy recoil nucleus $A*$ and an ejectile w. The identification of the ejectile permits to determine the mass A and charge Z of the decaying nucleus. In addition, we can deduce the excitation energy E^* of the compound-nucleus A by measuring the kinetic energy and the emission angle of the ejectile w. The measurement of the number of coincidences between the ejectiles and the decay products normalised to the total number of detected ejectiles allows one to extract the decay probability $P_{decay}^{A,exp}$ for the corresponding decay channel. According to the surrogate reaction method in its standard form, the neutron-induced cross section for the nucleus $A-1$ can be deduced from the product of the calculated compound-nucleus cross section formation after neutron absorption σ_{CN}^A and the experimental decay probability $P_{decay}^{A,exp}$:

$$\sigma_{decay}^{A-1}(E_n) = \sigma_{CN}^A(E_n).P_{decay}^{A,exp}(E^*) \tag{0.3}$$

Usually, $\sigma_{CN}^A(E_n)$ is obtained from optical model calculations. The relation between incident neutron energy E_n and excitation energy E^* of the compound-nucleus A can be written as:

$$E^* = S_n + \frac{A-1}{A}.E_n \tag{0.4}$$

where S_n is the one-neutron separation energy in the nucleus A. The interest of this

method is that in some cases the target X is stable or less radioactive than the target $A - 1$. Therefore, the surrogate reaction method enables cross sections to be extracted for nuclear reactions on short-lived nuclei that otherwise can not be measured.

Equation 0.3 is based on the hypothesis that the excited nucleus is a compound-nucleus whose decay is independent of the formation. In the following sections, we will discuss whether this hypothesis is fulfilled in our measurements. In addition, a significant uncertainty in the use of the surrogate reaction method lies in the spin J and parity Π population differences between the compound-nuclei produced in the neutron- and transfer-induced reactions. Since the decay probability strongly depends on $J\Pi$, the spin-parity mismatch can lead to important deviations between the neutron-induced results and the ones obtained with the surrogate method. Previous experiments have tested the surrogate reaction method to infer fission cross sections in the actinide region and have shown a good agreement between neutron-induced and surrogate cross sections, even at low neutron energies. However, it is not yet clear to what extent the surrogate method can be applied to infer radiative capture cross sections (n, γ). To help answer this question, in this work we study the transfer reactions $^{174}Yb(^{3}He, p\gamma)^{176}Lu$ and $^{174}Yb(^{3}He,^{4}He\gamma)^{173}Yb$ as surrogates for the well-known $^{175}Lu(n, \gamma)$ and $^{172}Yb(n, \gamma)$ reactions, respectively. We will show that, even though this work concerns rare-earth nuclei, it has important consequences for the application of the surrogate method in the actinide region.

Outline of this work

This work is organised in the following way: in chapter **1**, the theoretical aspects related to the surrogate method will be introduced. The validity of the surrogate method will be investigated by means of statistical model calculations. In chapter **2,** a review on experiments based on the surrogate method will be presented. Our experimental set-up will be described in chapter **3**. In chapter **4**, the data analysis will be detailed with special emphasis on the determination of the γ-cascade detection efficiency. In chapter **5**, we will compare our results with existing neutron-induced data and TALYS calculations and infer the angular momentum distribution populated in the transfer reactions used. In chapter **6**, the consequences of our study for the application of the surrogate method will be discussed and finally, in chapter **7**, we will present briefly our perspectives for the surrogate technique.

The surrogate method: theory & experimental review

Chapter 1

Theoretical aspects

1.1 Reaction mechanisms

1.1.1 Overview

Nuclear reactions can occur via different mechanisms. E. Weisskopf presented a simple conceptual model ([Weisskopf 57]), as illustrated in figure 1.1:

DIRECT STAGE   PRE-COMPOUND STAGE   COMPOUND STAGE

Shape elastic

INCIDENT PARTICLE

Direct reactions

Pre-equilibrium emissions

CN

Compound elastic

Evaporation

ELASTIC SCATTERING

INELASTIC SCATTERING

CHARGE EXCHANGE

RADIATIVE CAPTURE

FISSION

time

$10^{-22}s$

$10^{-17}s$
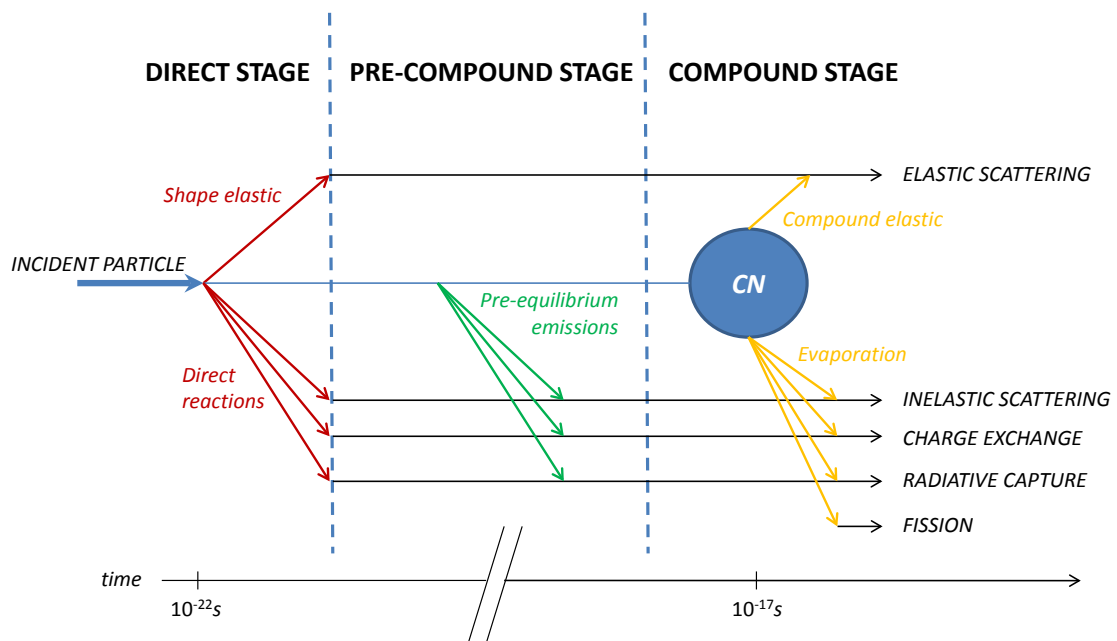
Figure 1.1: Conceptual view of the stages of a nuclear reaction.

When a nucleus is bombarded with a particle, different processes may occur. The particle may be elastic scattered and the sum of the kinetic energies of the reaction partners stays constant. However, the particle can also transfer a part of its energy

to the nucleus leading to a single particle excitation or to the excitation of a collective motion in the nucleus, where a vibrational or rotational state is excited. The projectile may also be captured in the potential well of the nucleus and excite a single particle state with a unbound nucleon that leaves the nucleus. These three «direct» processes occur in a time that corresponds to the time that a nucleon needs to traverse the nucleus, i.e. 10^{-22} s ([Austern 70]). However, the excitation energy may be distributed among all the nucleons through a complicated mechanism and a particular equilibrium state can be reached where all the possible states of the nucleus (single particle and collective) at a given E^* are equally probable. This type of reaction is called compound-nucleus (CN) reaction ([Bohr 36]). This reaction mechanism is much longer (10^{-14} - 10^{-18} s) than a direct reaction. The equilibration process that leads to a compound-nucleus can be imagined to proceed as shown in Fig. 1.2 ([Griffin 66]).
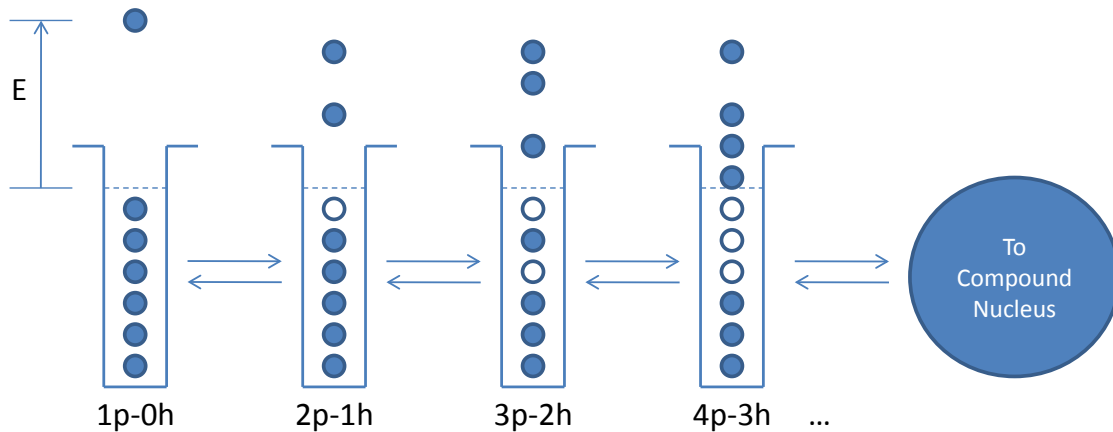
Figure 1.2: Intermediate stages on the way to the formation of a compound-nucleus.

After entering the target nucleus, the incident particle interacts with one of the constituent nucleons leading to successive two-body single-particle interactions, starting from the entrance channel $1p$-$0h$ state (one-particle-zero-hole), we distinguish three different stages:

- The **direct** reaction occurs if a particle is emitted directly after the first stage of Fig. 1.2. In the case where the projectile interacts with the nuclear mean field of the nucleus and then suffers a change in direction but no loss in energy, this direct reaction mechanism is called potential or shape elastic scattering.

- The nuclear reaction proceeds with the formation of intermediate states ($2p$-$1h$, $3p$-$2h$, $5p$-$4h$,...). At each stage, particle emission may be possible: it is called **pre-equilibrium** (or pre-compound) emission. The pre-equilibrium is not described in this work. For a detailed presentation, we refer to Refs. [Feshbach 74] and [Adhikari 86].

- The succession of more complex $p-h$ interactions leads ultimately to the formation of a compound-nucleus, which can then decay by particle emission.

Unfortunately, it is not possible to measure the time of emission of particles after a nuclear reaction with sufficient precision to identify whether the reaction proceeds through a compound-nucleus or not. In the following, we will discuss several possibilities to distinguish experimentally between CN and direct reactions.

1.1.2 Angular distribution

The angular distribution of an emitted particle can help extracting information on the reaction mechanism. For instance, figure 1.3 shows the angular distribution of the neutrons emitted in the reaction $^{89}Y(n,n)$ ([Towle 69]). For direct reactions (shape elastic), the particle emission is preferentially forward-peaked, whereas it is symmetrical about 90° for compound reactions, which characterize an evaporation process.
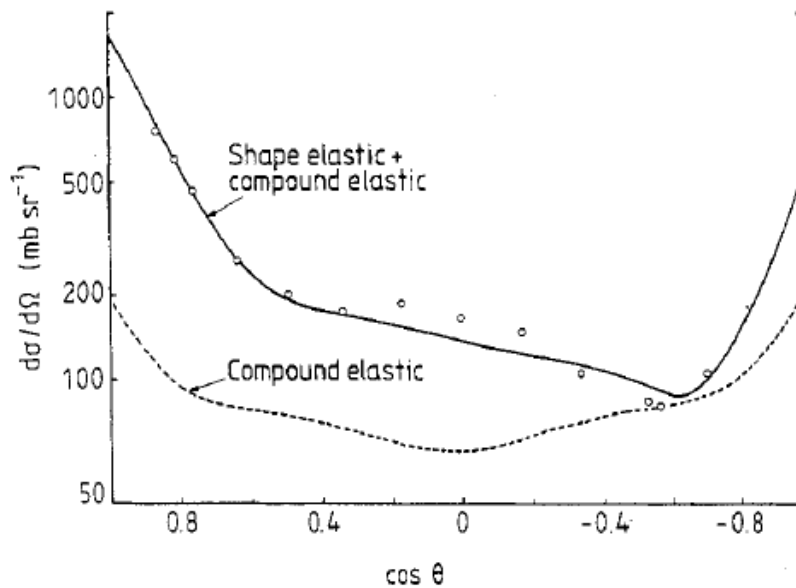
Figure 1.3: Calculated differential cross section and experimental data for the elastic scattering of 2.35 MeV neutrons by ^{89}Y ([Towle 69]).

1.1.3 Particle emission spectrum

The neutron emission spectrum of figure 1.4 shows nicely the contributions from the different reaction mechanisms. The discrete peaks at high energies correspond to the excitation of low-energy states of the residual nucleus, mainly populated by the direct reaction mechanism. The low-energy part of the spectrum is dominated by a smooth Maxwellian distribution corresponding to an evaporation process. When the excitation energy of the residual nucleus rises, the energy of scattered neutrons becomes weaker and the level density is so high that the observed distribution is continuous. The part between these two extreme regions corresponds to pre-equilibrium reactions.
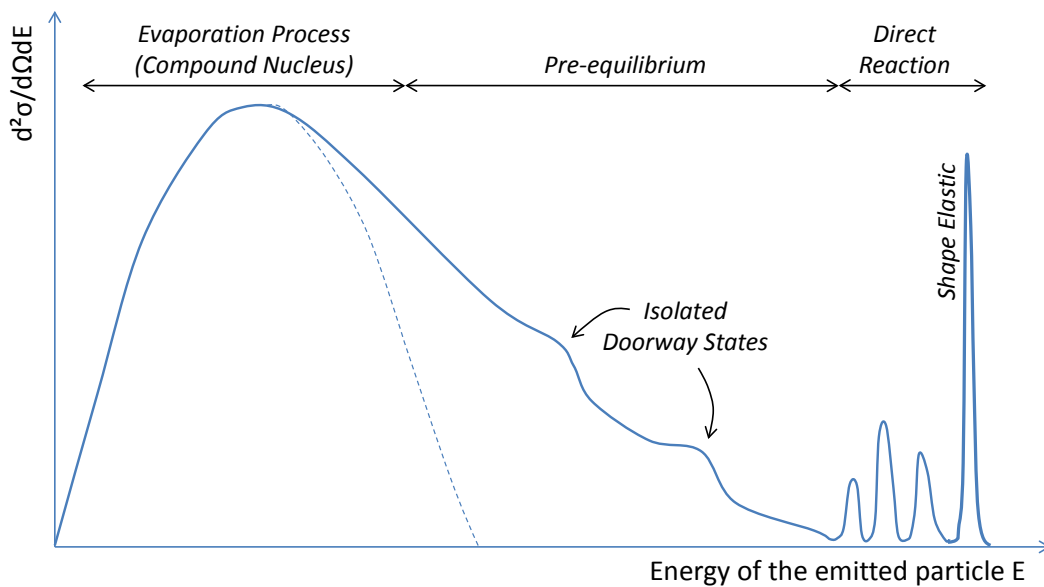
Figure 1.4: Schematic energy spectrum of particles emitted in a (n, n') reaction.

1.1.4 Beam energy

The importance of a particular nuclear reaction mechanism depends on the incident energy. In the following, we are interested in the direct and compound contributions to the (n, n') and (n, γ) reactions. Direct inelastic contributions are known to become predominant at high neutron energies while direct radiative capture (also called valence capture) reactions may occur in the thermal and resonance regions (at low neutron energies $En < 10$ keV) where an incident neutron may be captured directly in an unoccupied bound state ([Raman 88],[Borella 05]). For intermediate to heavy nuclei far from closed shells, neutrons are generally captured into a region of high density with overlapping states and for this reason, valence capture is expected to be improbable. Figure 1.5 shows the direct and compound contributions in the $^{175}Lu(n, n')$ and $^{175}Lu(n, \gamma)$ reactions as calculated with TALYS ([Koning 00]). Valence capture is found to be negligible.

The direct inelastic contribution increases with incident energy but it never represents more than 10% of the compound inelastic contribution in the energy range considered. This is reinforced by a study performed by Wilenzick et al. ([Wilenzick 65]) where the elastic and inelastic scattering of 6 MeV neutrons for seven heavy nuclei were measured. The observed angular distributions and cross sections were consistent with a 10±5 % direct contribution to the inelastic scattering. This clearly indicates that the compound-nucleus mechanism prevails up to incident neutron energies of several MeV.
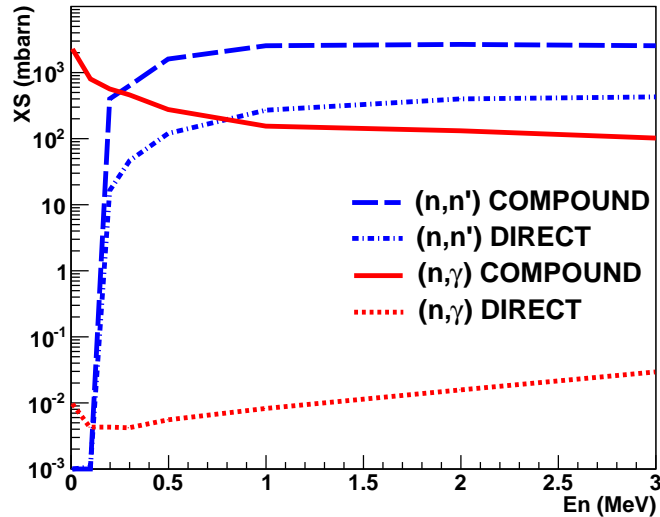
Figure 1.5: Direct and compound contributions in the $^{175}Lu(n, n')$ and $^{175}Lu(n, \gamma)$ reactions as calculated by TALYS.

Above a limit that depends on the nucleus considered, direct and pre-equilibrium reactions will become predominant compared to compound reactions. At high excitation energies, a particularity of the radiative capture is the predominance of the Giant Dipole Resonance (GDR). The GDR corresponds to the collective oscillation of protons against neutrons. The concept of collective excitations in nuclei is fully detailed in [Chomaz 97] and [Santonocito 06]. The importance of the GDR can be intuitively seen in the following way: the oscillation of a proton within a nucleus can be assimilated to an antenna. The electric field created by the antenna is proportional to the current. Therefore, the electromagnetic field is much larger when all the protons oscillate, as is the case of the GDR. At low excitation energies, the GDR preferentially dumps to a compound-nucleus. At higher energies, the incident neutron can excite the GDR and then be captured into a bound state. In this case, the decay occurs before the formation of a compound-nucleus. This pre-equilibrium-like mechanism is called «semi-direct» in the literature. Therefore, the Direct-Semi-Direct (DSD) calculations account for both valence capture and semi-direct radiative capture. By comparing DSD calculations with experimental radiative capture cross sections for several nuclei, one can see that the compound-nucleus model accounts reasonably well for the observed cross sections for neutron energies below ∼4

MeV, whereas for incident neutron energies above ~ 7 MeV, the capture process is well described by the direct-semi-direct (DSD) mechanism. For example, in [Lindholm 80], S. Joly et al. measured γ-ray spectra at neutron energies between 0.5 and 11 MeV from the radiative capture of neutrons in calcium, nickel, yttrium and lead. Figure 1.6 shows the comparison between measured cross sections for $^{206}Pb(n,\gamma)$ with predictions of the DSD and statistical models. A similar work was recently done by L. Bonneau et al. ([Bonneau 07]) to study the $^{208}Pb(n,\gamma)$ and $^{238}U(n,\gamma)$ reactions.
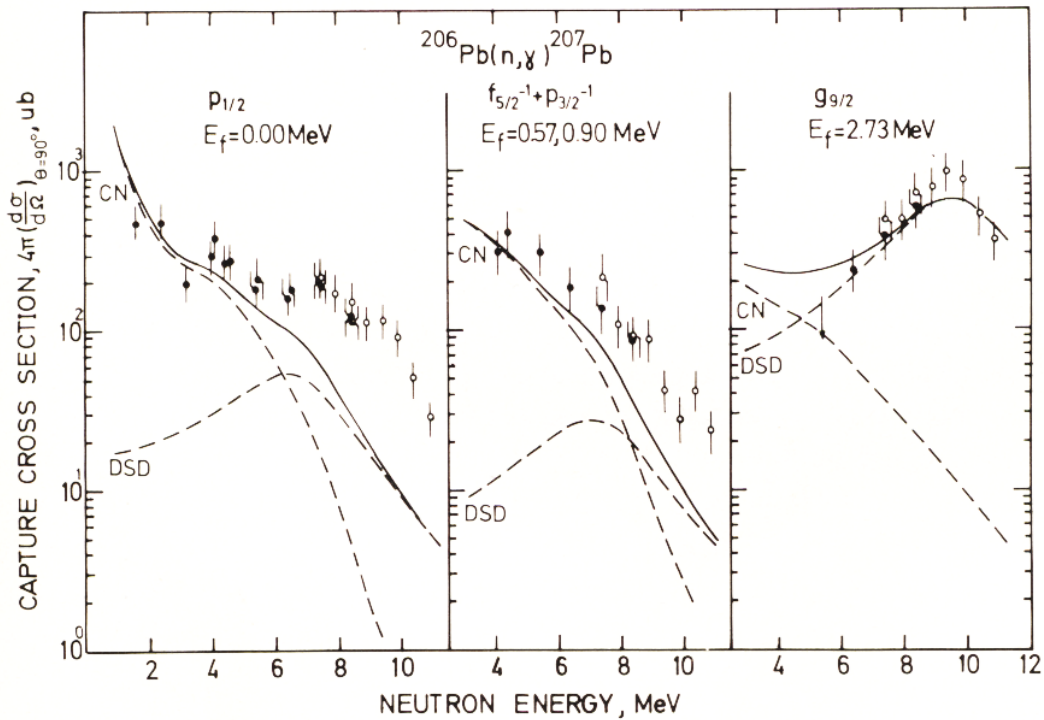
Figure 1.6: Cross sections for capture to the $p_{1/2}$ ground state (left), the $f_{5/2}$ and $p_{3/2}$ (middle) and $g_{9/2}$ (right) excited states in $^{206}Pb(n,\gamma)^{207}Pb$. The CN and direct/semi-direct contributions are compared with experimental data. [Lindholm 80]

1.2 The compound-nucleus

In this work, we will consider neutron-induced reactions for energies below 4 MeV. It is therefore reasonable to assume the formation of a compound-nucleus (see figure 1.7). As has been said before, in a compound-nucleus, all the possible configurations (quasi-particle or collective states) of the excited nucleus at given excitation energy E^*, spin J and parity Π are equiprobable. This involves:

- that the compound-nucleus has fully forgotten the memory of the entrance channel. This leads to an uncoupling between the formation and the decay of the compound-nucleus (this is the Bohr hypothesis, described in Ref. [Bohr 36]).

- that the compound-nucleus decay can be described statistically (see Ref. [Weisskopf 37]).
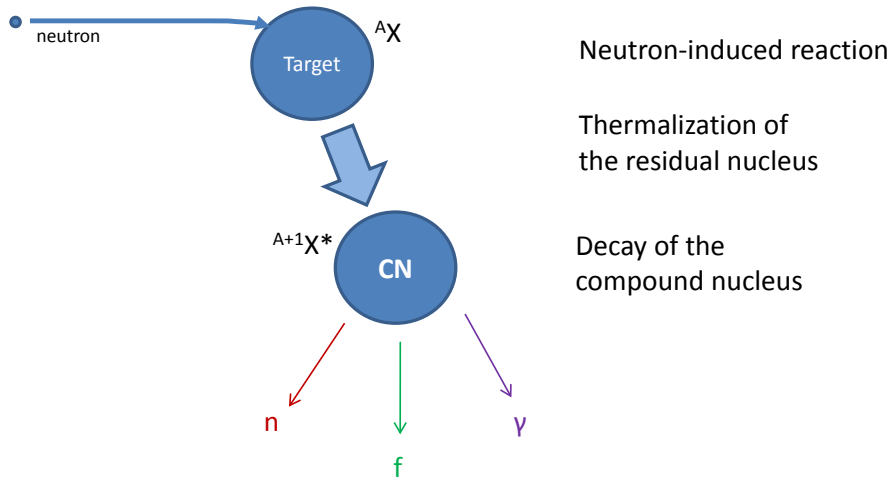
Figure 1.7: Desired neutron-induced reaction $n +^A X \to^{A+1} X^*$ that leads to the compound-nucleus $^{A+1}X^*$

As a consequence, the compound-nucleus reaction can be described in two independent steps: the formation of the compound-nucleus and its decay. By conserving rigorously the total angular momentum and the parity, the neutron-induced cross section for a given decay channel χ can be written in the Hauser-Feshbach formalism ([Hauser 52]) as:

$$\sigma_{n,\chi}(E_n) = \sum_{J\Pi} \sigma_n^{CN}(E^*, J, \Pi) . G_\chi^{CN}(E^*, J, \Pi) \tag{1.1}$$

where:

- $\sigma_{n,\chi}(E_n)$ is the neutron-induced cross section for the reaction $^A X(n, \chi)$.

- $J\Pi$ is the spin and parity of the compound-nucleus.

- σ_n^{CN} is the compound-nucleus $^{A+1}X^*$ formation cross section in the $\{E^*, J, \Pi\}$ state.

- $G_\chi^{CN}(E^*, J, \Pi)$ is the branching ratio of the compound state $\{E^*, J, \Pi\}$ associated to the desired exit channel χ. Note that, at the neutron energies considered here, three exit channels χ can be observed: fission, radiative capture and neutron emission.

- E^* is the excitation energy of the compound-nucleus, that is related to the incident neutron energy E_n via the neutron separation energy S_n of the compound-nucleus:

$$E^* = S_n + \frac{A}{A+1}.E_n \tag{1.2}$$

Nomenclature used to described a compound-nucleus reaction

One considers here the compound nuclear reaction $^AX(n,b)Y$, defined as follows:

$$
\begin{array}{ccccccccc}
n & + & ^AX & \longrightarrow & ^{A+1}X^* & \longrightarrow & Y & + & b \\
\vec{i} & & \vec{I} & & J & & \vec{J'} & & \vec{i'} \\
& \Downarrow & & & & & & \Downarrow & \\
& \vec{j} = \vec{i} + \vec{l} & & & (CN) & & & \vec{j'} = \vec{i'} + \vec{l'} &
\end{array}
\tag{1.3}
$$
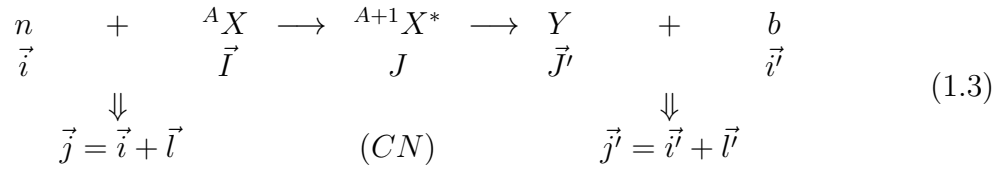
where the projectile (a neutron n) and the target nucleus ^AX form a compound-nucleus $^{A+1}X^*$ with a spin J and a parity Π at an excitation energy E^*. One considers a target nucleus ^AX with spin I and parity π_I. The incident neutron has an intrinsic spin $i = \frac{1}{2}\hbar$ and parity π_i. The total angular momentum transferred by the neutron is $\vec{j} = \vec{i} + \vec{l}$ where l is the orbital angular momentum of the neutron. Consequently, this leads to:

$$J = \vec{I} + \vec{i} + \vec{l} \tag{1.4}$$

The angular momentum conservation in the entrance channel implies:

$$\mid J - I \mid \leq j \leq J + I \tag{1.5}$$

and

$$\mid j - i \mid \leq l \leq j + i \tag{1.6}$$

The parity of the compound-nucleus is governed by the following equation:

$$\Pi = (-1)^l \pi_I \pi_i \tag{1.7}$$

The outgoing channel is represented with primed symbols, where the residual nucleus after decay has a spin J' and a parity Π'. The angular momentum conservation in the outgoing channel is given by eqs. 1.5 and 1.6 but with primed symbols.

In the following two sections, we are interested in the modelling neutron-induced reactions. We have used the nuclear reaction program TALYS ([Koning 00]). Chapters 1.3 and 1.4 are dedicated to the general description of the quantities appearing in eq. 1.1 with special emphasis on the methodology used in TALYS.

1.3 Optical model and compound-nucleus formation cross section

1.3.1 Optical model calculations

The compound-nucleus formation cross section σ_n^{CN} is usually deduced from optical model calculations. The framework of the optical model is detailed in appendix A. The elastic scattering matrix elements S_l are obtained from the solution of the Schrödinger equation (appendix A.1) using a complex optical potential (appendix A.3). A S_l-value gives the probability for the scattering of an incoming neutron with a given orbital angular momentum l. Note that S_l is the identity matrix if the particles do not interact between each other. Once the S-matrix is known, the total, shape elastic (appendix A.2) and reaction cross sections are:

$$\sigma_{total} = \frac{2\pi}{k^2} \sum_{l=0}^{\infty} (2l+1)(1 - Re\,[S_l]) \qquad (1.8)$$

$$\sigma_{SE} = \frac{\pi}{k^2} \sum_{l=0}^{\infty} (2l+1)\mid S_l - 1 \mid^2 \qquad (1.9)$$

$$\sigma_{reaction} = \frac{\pi}{k^2} \sum_{l=0}^{\infty} (2l+1)(1- \mid S_l \mid^2) \qquad (1.10)$$

where $k = \frac{\sqrt{2\mu E}}{\hbar}$ is the wave number, μ is the reduced mass ($\mu = \frac{1}{\frac{1}{m_1}+\frac{1}{m_2}} = \frac{m_1 m_2}{m_1+m_2}$) of the projectile-target system and E is the system energy in the center of mass. The total cross section σ_{total} is the sum of σ_{SE} (optical model scattering) and $\sigma_{reaction}$ (optical model absorption). The transmission coefficients T_l are determined from the elastic scattering matrix elements S_l as:

$$T_l = 1- \mid S_l \mid^2 \qquad (1.11)$$

A T_l-value gives the probability for the absorption (non-scattering) of an incoming neutron with a given orbital angular momentum l. In general, the reaction cross section $\sigma_{reaction}$, which corresponds to the loss of flux from the elastic channel, is calculated from the transmission coefficients T_l as:

$$\sigma_{reaction} = \frac{\pi}{k^2} \sum_{l=0}^{\infty} (2l+1)T_l \tag{1.12}$$

The term «reaction» corresponds to the absorption of the flux by the long-lived compound-nucleus states. The compound-nucleus reaction cross section σ_{CN} is obtained by subtracting the pre-equilibrium component σ_{PE} (via the exciton-model [Obloinsky 87] or the Feshbach-Koonin-Kermin-model [Feshbach 80]) and the direct inelastic contributions σ_{DWBA} (see appendix A.4) from the reaction cross section:

$$\sigma_{CN} = \sigma_{reaction} - \sigma_{DWBA} - \sigma_{PE} \tag{1.13}$$

As mentioned before, we assume that direct and pre-equilibrium contributions are negligible. Consequently, the compound-nucleus formation cross section is equal to the reaction cross section. Note that it is usual to distinguish between the compound elastic σ_{CE} and the compound inelastic σ_{CI} components. To summarize, figure 1.8 gives all components of the total cross section.
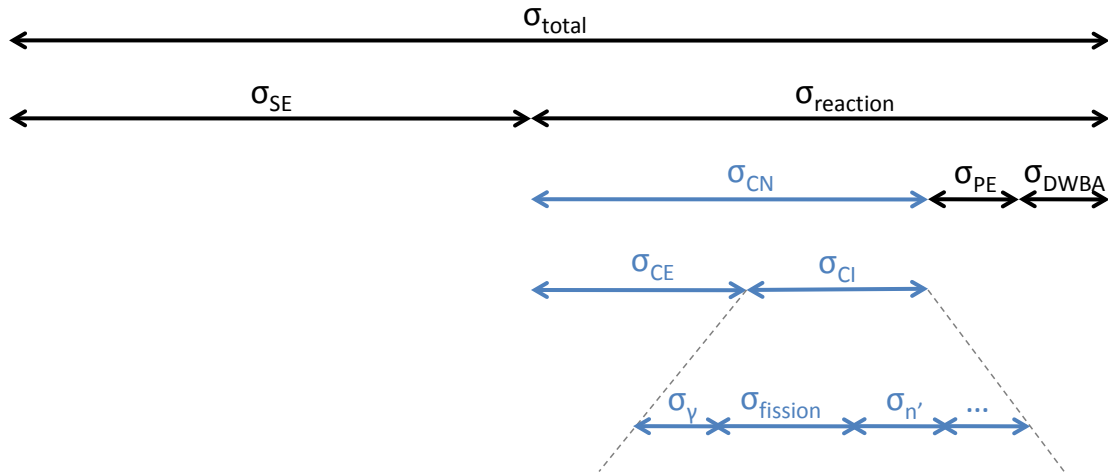
Figure 1.8: Components of the total cross section.
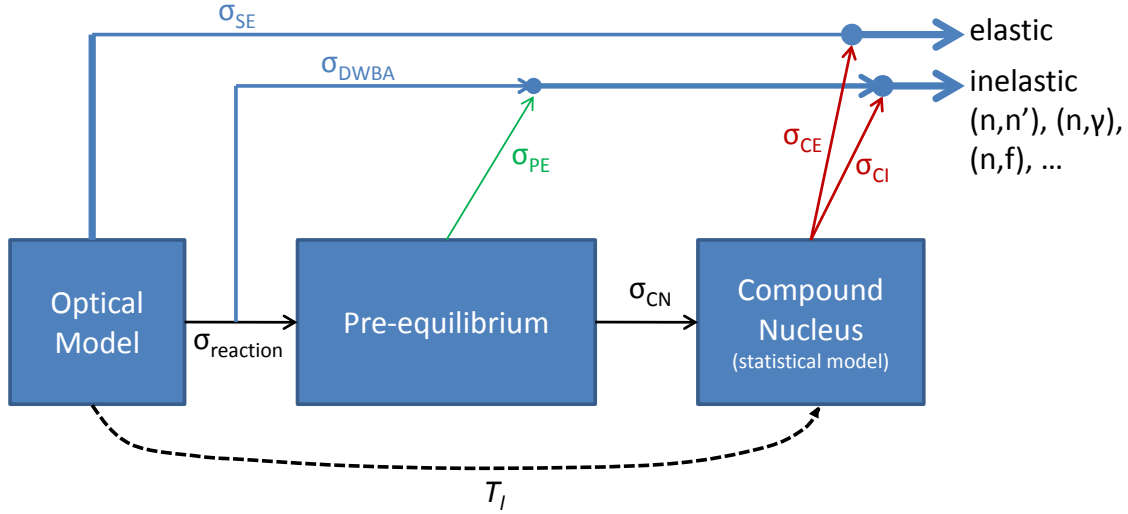
Figure 1.9: Coupling of nuclear models for the complete description of a neutron-induced reaction.

The optical model provides the transmission coefficients, DWBA cross sections (direct inelastic contributions), total and elastic cross sections that lead to the compound-nucleus reaction cross section and predict the angular momentum distribution populated in the reaction. This defines the initial conditions (A,Z,E^*,J^π) of the statistical model which governs the decay of the compound-nucleus (fission $\sigma_{fission}$, radiative capture σ_γ, inelastic neutron emission $\sigma_{n'}$ and compound elastic σ_{CE} , etc...). Figure 1.9 shows how the statistical model is linked to the optical model.

1.3.2 Compound-nucleus formation cross section

In the following, we explain our derivation of the quantity $\sigma_n^{CN}(E^*, J, \Pi)$. In practice, the optical model calculates the transmission coefficients T_l^j which are related to a given channel spin j. For completeness, we recall that $\vec{j} = \vec{i} + \vec{l}$, where i and l are the spin and the orbital angular momentum of the incoming neutron. Therefore the possible values for j are $j = l \pm \frac{1}{2}$. Using the formalism of equation 1.3, one proceeds in two steps :

- coupling of $\vec{i}$ and $\vec{l}$ to form the channel spin $\overrightarrow{j}$.

- coupling of $\overrightarrow{j}$ and $\vec{I}$ to get the compound-nucleus spin J.

The z axis has been taken as quantification axis along the direction of the incident beam and the z component of i is m_i. The z component of l is zero. Consequently $m_j = m_i$. Note that each spin-value i generates $(2i + 1)$ different values of m. Since the incident beam is unpolarized, the two neutron sub-states $(m_i = \pm\frac{1}{2})$ are equally probable. Then

the coupling between the states $|im_i\rangle$ and $|lm_l\rangle$ to form the projectile in the states $|jm_j\rangle$ can be expanded with the use of the completeness relation:

$$|jm_j\rangle = \sum_{m_i} \sum_{m_l} |im_i lm_l\rangle\langle lm_l m_i i|jm_j\rangle \tag{1.14}$$

where the projectile sub-states are explicitly defined. Note that the expansion coefficients $C_{lm_l,m_i i}^{jm_j} = \langle lm_l m_i i|jm_j\rangle$ are the Clebsch–Gordan coefficients. The probability to find the neutron in the $|jm_j\rangle$ states by coupling the states $|lm_l\rangle$ and $|im_i\rangle$ is given by the square of the Clebsch–Gordan coefficients $\langle lm_l m_i i|jm_j\rangle^2$. By using eq. **??**, the compound-nucleus formation cross section for neutrons in the state $|jm_j\rangle$ is given by:

$$\sigma_{CN}(im_i\pi_i j) = \sum_l \frac{\pi}{k^2} \quad (2l+1) \qquad T_l^j(E_n) \qquad |\,C_{lm_l,m_i i}^{jm_j}\,|^2$$
$$\qquad\qquad \Updownarrow \qquad\qquad \Updownarrow \qquad\qquad\qquad \Updownarrow \tag{1.15}$$
$$\qquad degeneracy \quad transmission \qquad coupling$$
$$\qquad term \qquad coefficient \quad Clebsch-Gordan$$

Let us consider now the production of the compound-nucleus in the state $|JM\Pi\rangle$ by coupling the latter neutron states $|jm_i\pi_i\rangle$ with the target nucleus states $|Im_I\pi_I\rangle$. Similarly, the probability that the incident particle and target nucleus will combine to form compound-nucleus of spin J is given via the square of the Clebsch-Gordan coefficients $\langle jm_i m_I I|JM\rangle^2$ with $M = m_i + m_I$ and $|\,j - I\,| < J < |\,j + I\,|$. The cross section for the compound-nucleus formation $\sigma_{CN}(E^*, J, M, \Pi)$ in a single compound state described by $|JM\Pi\rangle$ can be written as :

$$\sigma_{CN}(E^*, J, M, \Pi) = \frac{\pi}{k^2} \frac{1}{(2i+1)(2I+1)}.$$

$$\sum_l \left[(2l+1)\, \delta\left(\pi_i, \pi_I, (-1)^l, \Pi\right) \sum_j T_l^j(E_n) \sum_{m_i} |\,C_{lm_l,m_i i}^{jm_i}\,|^2 \sum_{m_I} |\,C_{jm_i,m_I I}^{JM}\,|^2 \right] \tag{1.16}$$

where $\delta\left(\pi_i, \pi_I, (-1)^l, \Pi\right) = 1$ if $\pi_i\pi_I(-1)^l = \Pi$ and 0 otherwise. This term is required in order to take into account the conservation of spin and parity. Finally, the compound-nucleus $^{A+1}X^*$ formation cross section in the $\{E^*, J, \Pi\}$ state is given by:

$$\sigma_{CN}(E^*, J, \Pi) = \sum_{M=-J}^{+J} \sigma_{CN}(E^*, J, M, \Pi) \tag{1.17}$$

1.4 Decay of the compound-nucleus

1.4.1 Resonance and continuum energy ranges

The compound-nucleus $^{A+1}X^*$ is produced in different excited states. For low excitation energies, the states are discretized and neutron-induced reaction cross sections are characterized by resonance structures. As illustrated in figure 1.10, the resonances are well separated and the average distance between them (the level distance D) is large compared to their natural decay width Γ and the instrumental resolution Δ_r. In this range of energy, the dependence of the resonance cross-section on the beam energy is given by the Breit-Wigner formula:

$$\sigma(E) \simeq \frac{\pi}{k^2} \frac{\Gamma^2/4}{(E - E_r)^2 + \Gamma^2/4} \tag{1.18}$$

where E is the incident energy and E_r is the excitation energy of the resonant state. As the energy increases, the level distance decreases and the total natural line width increases. Although at intermediate energies the resonance structure still exists ($\Gamma < D$), the resonance structure can no longer be resolved due to the limited instrumental resolution Δ_r. Therefore, one distinguishes between the resolved resonance region (RRR), for which $D > \Delta_r$, and the unresolved resonance region (URR), for which $D < \Delta_r$. At higher energies the level distance is smaller than the line width ($D < \Gamma$) and the resonance structure disappears. Therefore, the states are represented by a continuous energy distribution that corresponds to the continuum region.

1.4.2 Level-density and spin distribution

The continuum is described by the nuclear level density $\Omega(E, J, \Pi)$ that corresponds to the number of nuclear levels per MeV at an excitation energy E, for a certain spin J and parity Π. The total level density $\Omega_0(E)$ corresponds to the total number of levels per MeV at E, and is obtained by summing the level density over spin and parity:

$$\Omega_0(E) = \sum_J \sum_\Pi \Omega(E, J, \Pi) \tag{1.19}$$

We obtain the total state density $w_0(E)$ by including the $(2J + 1)$ magnetic substates for each level:

$$w_0(E) = \sum_J \sum_\Pi (2J + 1)\Omega(E, J, \Pi) \tag{1.20}$$

Actually, the nuclear level density $\Omega(E, J, \Pi)$ is usually factorized as:

$$\Omega(E, J, \Pi) = P(E, J, \Pi).R(E, J).\Omega_0(E) \tag{1.21}$$
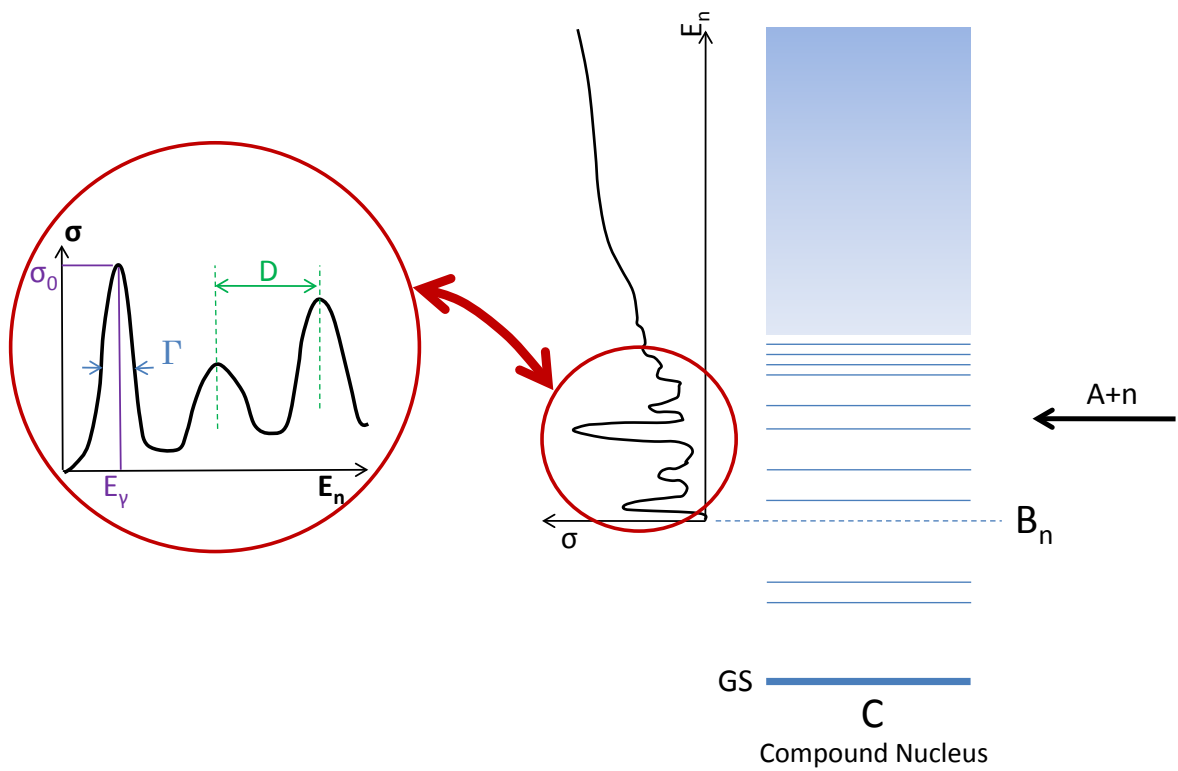
Figure 1.10: Resonance and continuum energy ranges in a neutron induced reaction. Resonance parameters are given for $\Gamma \ll D$.

where $P(E, J, \Pi)$ is the parity distribution and $R(E, J)$ is the spin distribution. In TALYS, parity equipartition is assumed, i.e.

$$P(E, J, \Pi) = \frac{1}{2} \tag{1.22}$$

The spin distribution is given by:

$$R(E, J) = \frac{2J + 1}{2\sqrt{2\pi}\sigma_{cutoff}^3} . exp\left[-\frac{(J + \frac{1}{2})^2}{2\sigma_{cutoff}^2}\right] \tag{1.23}$$

where σ_{cutoff} is the spin cut-off parameter for the considered nucleus at energy E. The spin cut-off parameter characterises the spin dependence of the level density. Typical values for σ_{cutoff} are 5-6 $\hbar$ in the rare-earth and actinide regions. The choice of a realistic total level density $\Omega_0(E)$ is of crucial importance. In TALYS, the Gilbert-Cameron model ([Gilbert 65]) is used where a constant nuclear temperature function models the low-energy part:

$$\Omega_0^{CT}(E) = \frac{1}{T} . exp\frac{(E - E_0)}{T} \tag{1.24}$$

where E_0 and T are free parameters determined by fitting experimental data. The high-energy dependence is predicted by the back-shifted Fermi-gas model:

$$\Omega_0^{FG}(E) = \frac{\sqrt{\pi}}{12a^{1/4}(E - E_0)^{5/4}}exp(2\sqrt{a(E - E_0)}) \tag{1.25}$$

where a is the level-density parameter ([Ignatyuk 75]). Note that the link between the parameters of both models is made by imposing the continuity of level density as illustrated schematically in figure 1.11.
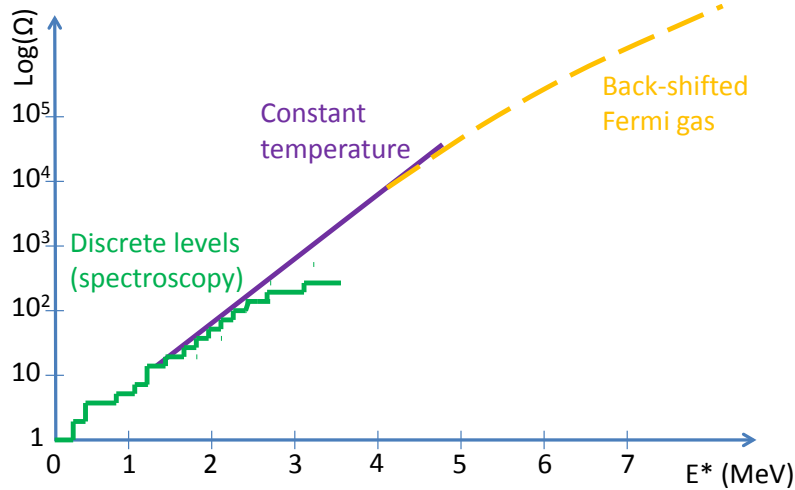
Figure 1.11: Description of the level density as function of excitation energy.

1.4.3 Decay probability

The total decay width Γ_{tot} describes the decay of the compound-nucleus and is related to the mean lifetime $\tau(E^*)$:

$$\Gamma_{tot}(E^*) = \frac{\hbar}{\tau(E^*)} \tag{1.26}$$

Γ_{tot} is $\hbar$ times the rate of disintegration per unit time. Since the compound-nucleus can decay into several channels, one can define the partial decay width Γ_χ as:

$$\Gamma_{tot}(E^*) = \sum_\chi \Gamma_\chi(E^*) \tag{1.27}$$

where Γ_χ is referred to a specific decay channel χ. The decay probability can be expressed in terms of the partial decay widths as:

$$P_\chi(E^*) = \frac{\Gamma_\chi(E^*)}{\Gamma_{tot}(E^*)} \tag{1.28}$$

It exists an important connection between the partial widths and the transmission coefficients. For the decay χ of the compound-nucleus in a given state $\{E^*, J, \Pi\}$:

$$2\pi \frac{<\Gamma_\chi(E^*, J, \Pi)>}{<D_0(E^*, J, \Pi)>} = \sum_{j'=|J-I'|}^{J+I'} \sum_{l'=|j'-i'|}^{j'+i'} \sum_{E'} T_{l',\chi}^{j'}(E^*-E').\delta(\Pi, \Pi', (-1)^{l'}) = T_\chi^{J\Pi}(E^*) \tag{1.29}$$

where $<D_0(E^*, J, \Pi)>$ is the average spacing of the compound-nucleus levels $\{J, \Pi\}$ at energy E^* and the $\delta(\Pi, \Pi', (-1)^{l'})$ function conserves the parity. In this case, the transmission coefficients $T_{l'}^{j'}$ denote transition probabilities to final states $\{E', J', \Pi'\}$ of the residual nucleus Y. That is why the transmission coefficients are evaluated at an energy $(E^* - E')$ for the outgoing particle. According to eqs. 1.5 and 1.6, the double summation takes into account all possible ways to compose $\vec{j'}$ from $\vec{J} + \vec{J'}$ and all possible ways to compose $\vec{l'}$ from $\vec{j'} + \vec{i'}$. For practical reasons, we have introduced in eq. 1.29 a transmission coefficient $T_\chi^{J\Pi}(E^*)$ which corresponds to the probability for the compound-nucleus in the state $\{E^*, J, \Pi\}$ to decay through the channel χ. This allows us to use the transmission coefficients T_l^j obtained in optical model calculations to determine the branching ratios $G_\chi(E^*, J, \Pi)$ of the compound-nucleus. Then, equations 1.28 and 1.29 yield:

$$G_\chi(E^*, J, \Pi) = \frac{T_\chi^{J\Pi}(E^*)}{T_\gamma^{J\Pi}(E^*) + T_n^{J\Pi}(E^*) + T_f^{J\Pi}(E^*)} \tag{1.30}$$

However, the transmission coefficients $T_\chi^{J\Pi}(E^*)$ correspond to all energetically possible

quantum states, namely thousands of final states! Because it is not possible to deal with every state, the idea is to take separately into account the discrete final levels of the residual nucleus with excitation energies E'_d and to introduce an effective transmission coefficient for continuum final levels by using known level densities Ω:

$$
\begin{array}{ccccc}
< T_\chi^{J\Pi}(E^*) > & = & \sum_i T_\chi^{J\Pi} & + & \int_{E'>E_d} \Omega(E', J, \Pi) T_\chi^{J\Pi} dE' \\
& & \Downarrow & & \Downarrow \\
& & discrete & & continuum \\
& & levels & & levels
\end{array}
\tag{1.31}
$$

The first summation runs over all discrete states and E_d marks the beginning of the continuum. Equation 1.30 becomes:

$$
G_\chi(E^*, J, \Pi) = \frac{< T_\chi^{J\Pi}(E^*) >}{< T_\gamma^{J\Pi}(E^*) > + < T_n^{J\Pi}(E^*) > + < T_f^{J\Pi}(E^*) >}
\tag{1.32}
$$

The probability for a decay channel χ is deduced by summing over all the spin-parity states of the compound-nucleus:

$$
P_\chi(E^*) = \sum_{J,\Pi} \frac{< T_\chi^{J\Pi}(E^*) >}{< T_\gamma^{J\Pi}(E^*) > + < T_n^{J\Pi}(E^*) > + < T_f^{J\Pi}(E^*) >}
\tag{1.33}
$$

The latter equation is the basement of the statistical model that describes the decay of the compound-nucleus. For completeness, we recall that the optical potential predicts the initial conditions (A,Z,E^*,J^π) of the statistical model which governs the competition between all the possible decay channels (fission, radiative capture, neutron emission, etc...) via eq. 1.32. Multi-step decays can be considered in the same way. For the neutron energies of interest in this work, the outgoing channels in competition are principally neutron emission and radiative capture (or gamma emission). Figure 1.12 illustrates the deexcitation process as treated by the statistical model. In the case of heavy nuclei, the fission channel may compete with the latter outgoing channels.

In the following, we explain the derivation of the branching ratios $G_\chi(E^*, J, \Pi)$. As mentioned before, the present study implies rare-earth nuclei for which fission does not occur. However, we would like to discuss the surrogate results obtained for several actinides in this thesis. That is why we will also describe how the branching ratios can be inferred for fission.

1.4.4 Neutron emission

An excited state at E^* can decay to a state at E' by neutron emission, as illustrated in figure 1.13. In the following, we define the transmission coefficient $< T_{n,l'j'}^{J\Pi} >$ for the
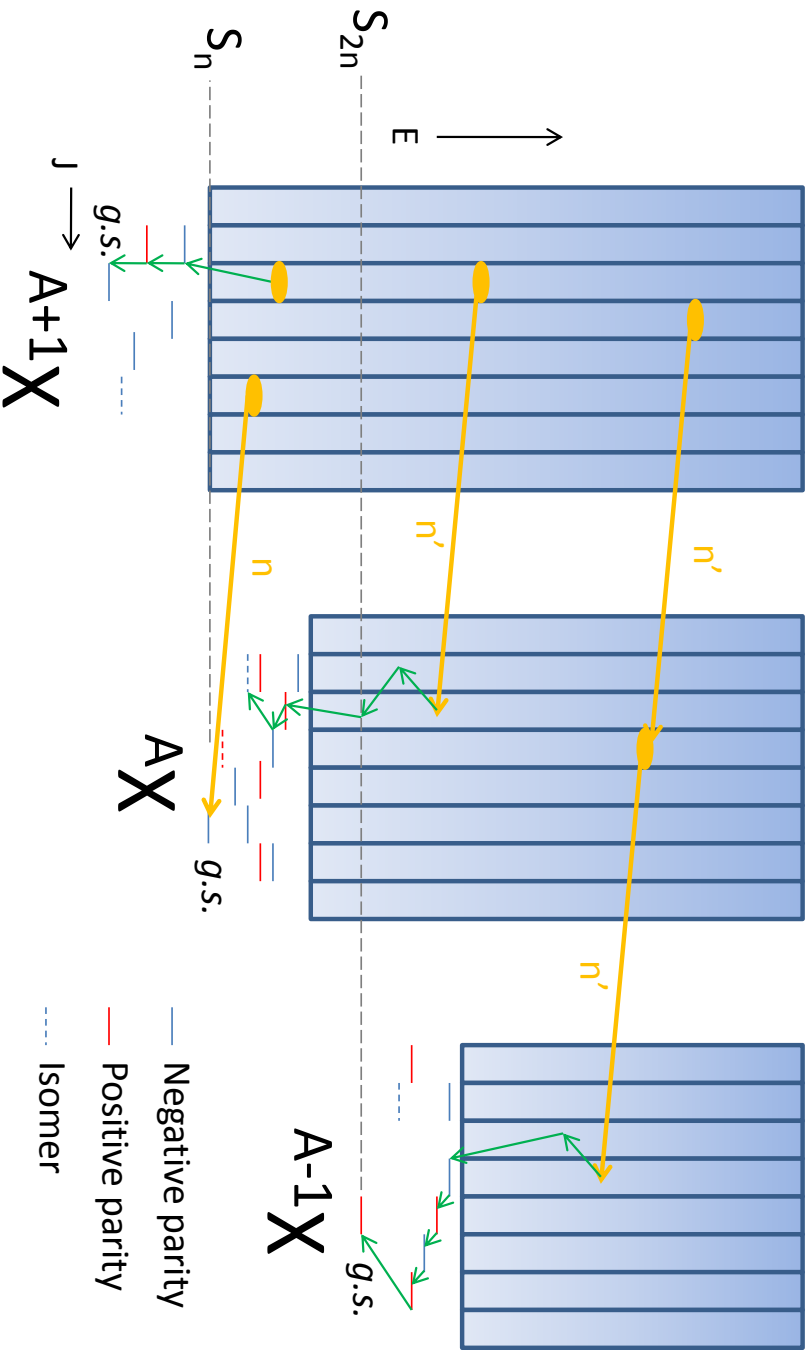
Figure 1.12: Decay process after the excitation of an intermediate compound-nucleus $^{A+1}X^*$ state. Green arrows correspond to γ-decay and orange arrows to one-neutron or two-neutron emission. For simplicity, the fission channel is not shown.

deexcitation of the compound-nucleus $^{A+1}X(E^*, J, \Pi)$ by neutron emission, leading to a residual nucleus $^{A}X(E', J', \Pi')$.
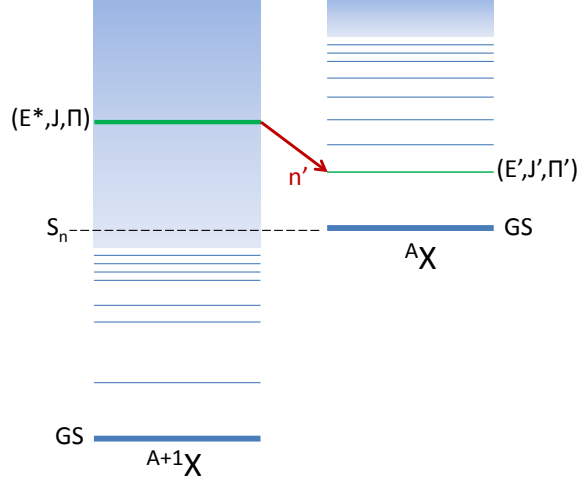
Figure 1.13: Decay scheme for a compound-nucleus $^{A+1}X(E^*, J, \Pi)$ via neutron emission to a (E', J', Π') state of the residual nucleus ^{A}X.

By combining eqs. 1.29 and 1.31:

$$< T_n^{J\Pi} > (E^*) = \sum_{E'_d} \sum_{J'\Pi'} \sum_{j'=|J-J'|}^{|J+J'|} \sum_{l'=|j'-1/2|}^{|j'+1/2|} T_{n,l'j'}^{J\Pi}(E^* - Ed')\delta(\Pi, \Pi', (-1)^{l'})$$

$$+ \int_{E_d}^{E^*-S_n} \sum_{j'=|J-J'|}^{|J+J'|} \sum_{l'=|j'-1/2|}^{|j'+1/2|} T_{n,l'j'}^{J\Pi}(E_n)\delta(\Pi, \Pi', (-1)^{l'})\Omega(E', J', \Pi')dE' \qquad (1.34)$$

The first term is the summation over the discrete levels at low excitation energies E_d. Right above the last discrete energy, the discrete levels are so numerous that their density can be treated as a continuous density $\Omega(E', J', \Pi')$. The second term is an integration of the continuum levels of higher energies up to $(E^* - S_n)$.

One should stress that for low incident neutron energies the entrance and outgoing channels are not totally independent: the compound elastic channel (n, n) is preferred over other decay channels. A width fluctuation correction (WFC) is introduced that breaks-down the independence of formation and decay of the compound-nucleus. Methods for determining such WFC can be found in [Hilaire 03]. Therefore the major effect is to enhance the elastic channel and accordingly decrease the other open channels. The correction is most important at low neutron energies and for reactions with few open channels ([Tucker 65]). At sufficiently high energies, when many competing channels are open, WFC's can be neglected.

1.4.5 Gamma emission

1.4.5.1 Electromagnetic transitions and multipolarity

An excited state at E^* can also decay to a state at E' by photon emission, as illustrated in figure 1.14. The final and the initial levels are directly linked by the knowledge of the γ transition via the conservation laws. The energy conservation gives:

$$E_\gamma = E^* - E' \tag{1.35}$$

The angular momentum composition imposes:

$$\mid J - J' \mid \leq L_\gamma \leq J + J' \tag{1.36}$$

Consequently, for a given J and J', the multipolarity of the transition is limited since the photon parity π_γ is:

- $(-1)^{L_\gamma}$ for an electric transition (EL).

- $(-1)^{L_\gamma+1}$ for a magnetic transition (ML).

For instance, in the decay from a $3^+$to a 2^+, the possible multipolar transitions are M1, E2, M3, E4, M5. Contrariwise, for a decay from a $3^-$to a 2^+, the possible multipolar transitions are E1, M2, E3, M4, E5.
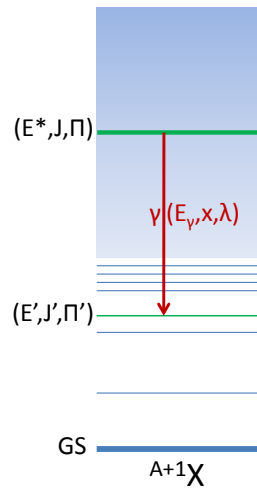
Figure 1.14: Decay scheme for a compound-nucleus $^{A+1}X(E^*, J, \Pi)$ via gamma-decay to a $^{A+1}X(E', J', \Pi')$ state.

1.4.5.2 Gamma-ray strength functions

Contrary to particle transmission, gamma transmission coefficients are determined from an energy-dependent gamma-ray strength function $f(x, \lambda)$, and read

$$T_{x,\lambda}(E_\gamma) = 2\pi f_{x,\lambda}(E_\gamma)E_\gamma^{2\lambda+1} \tag{1.37}$$

where E_γ is the energy of the γ-ray emitted, x denotes the nature of the transition ($x = E$ for electric and $x = M$ for magnetic transitions) and λ is the transition multipolarity. There are several models for the gamma-ray strength function. The strength function is a function of the gamma-ray energy E_γ only, i.e. independent of the excitation energy of the compound-nucleus. This is a consequence of the Brink hypothesis ([Brink 57]). The giant dipole resonance collective state has the highest probability to emit a γ-ray. The probability that any other state decays by gamma emission is negligible. That is why the gamma-ray strength function can be modelled with a standard Lorentzian form that describes the GDR shape:

$$f_{x,\lambda}(E_\gamma) = K_{x,\lambda}\frac{\sigma_{x,\lambda}E_\gamma\Gamma_{x,\lambda}}{(E_\gamma^2 - E_{x,\lambda}^2)^2 + (E_\gamma\Gamma_{x,\lambda})^2}(MeV^{-3}) \tag{1.38}$$

where $\sigma_{x,\lambda}$, $E_{x,\lambda}$ and $\Gamma_{x,\lambda}$ are the cross section, energy and width of the giant resonance, respectively, and:

$$K_{x,\lambda} = \frac{1}{(2l + 1)\pi^2\hbar^2c^2} \tag{1.39}$$

Parameters are based on experimental data if available or they are given by a systematics ([Belgya 06]). In the TALYS reaction code ([Koning 00]), eq. 1.38 is used for all transition types other than E1. For E1 radiation, the generalized Lorentzian form of Kopecky and Uhl ([Kopecky 90]) is preferred. Note that microscopic calculations are used to determine gamma-ray strength function for E1 radiation for exotic nuclei. In this approach, the parity is explicitly taken into account in the gamma-ray strength function, whereas the Lorentzian approach assumes that the parities are equally probable.

1.4.5.3 Transmission coefficient for E1 transitions

In the following, we choose to deal only with electric dipolar transition of the lower order, namely $E1$ transitions. According to eq. 1.37, the transmission coefficients is given by:

$$T_{E1}(E_\gamma) = 2\pi f_{E1}(E_\gamma)E_\gamma^3 \tag{1.40}$$

By analogy with particle transmission coefficients, the number of final states is so numerous that an individual description of each gamma channel can be replaced by a summation over all accessible levels described by a continuous level density. It is

understood that the integral over dE' also includes a summation over discrete states. Practically, one writes:

$$\frac{2\pi\Gamma_\gamma}{D_0} = < T_\gamma^{J\Pi} > (E^*) \approx C. \int_0^{E*} \sum_{J'=|J-1|}^{|J+1|} T_{E1}(E^* - E')\Omega(E', J', \Pi')dE' \qquad (1.41)$$

where C is a renormalization factor. The normalization factor C is chosen to ensure that the theoretical average gamma width $< \Gamma_\gamma >$ is equal to the experimental value in the resonance neutron energy range (see for example Ref. [Noguere 09]). For nuclei for which no experimental data are available, one uses the systematics for $40 < A < 250$ given by Kopecky ([Koning 00]) :

$$\Gamma_\gamma = \frac{1593}{A^2} eV \qquad (1.42)$$

Note that this equation gives $< \Gamma_\gamma > \approx 60$ meV in the rare-earth region and $< \Gamma_\gamma > \approx 30$ meV in the actinide region.

1.4.6 Fission

Heavy compound nuclei may also undergo quadrupole deformations of greater and greater amplitude that eventually lead to fission. Therefore, the fission process may compete with the two previously described decay channels. In the frame of the liquid drop model, the potential energy is given by the interplay between the Coulomb repulsion and the surface energy (whose origin is the short-range nuclear force). The result for the potential energy as a function of deformation is a fission barrier as illustrated in Fig. 1.15. Shell effects modify the shape of the potential energy leading to double or triple-humped fission barriers. As stated by N. Bohr and J.A. Wheeler ([Bohr 39]), the fission probability is defined by the number of states at the top of the fission barrier, the so-called «transition» states and not by the states of the fission fragments. If the E^* is lower than the barrier height, tunneling occurs. The Hill-Wheeler expression ([Hill 53]) gives the probability of tunneling through a barrier (described by an inverted parabola) with height B_f and width $\hbar\omega$ for a compound-nucleus with excitation energy E^*. It reads:

$$T_f(E^*) = \left[1 + exp(-2\pi\frac{(E^* - B_f)}{\hbar\omega})\right]^{-1} \qquad (1.43)$$

For a transition state with excitation energy ϵ_i above the top of the same barrier, one has:

$$T_f(E^*, \varepsilon_i) = \left[1 + exp(-2\pi\frac{(E^* - B_f - \varepsilon_i)}{\hbar\omega})\right]^{-1} \qquad (1.44)$$
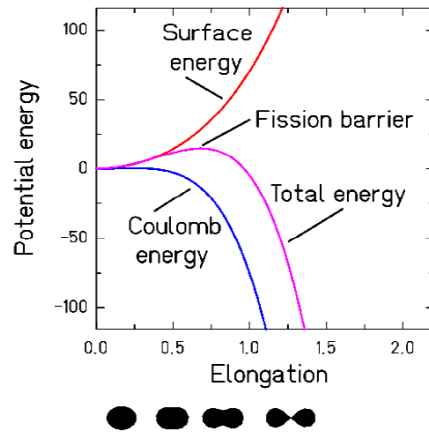
Figure 1.15: Potential energy as a function of elongation resulting from the interplay between the surface and the Coulomb energies (schematic nuclear shapes are indicated below) ([Schmidt 09])
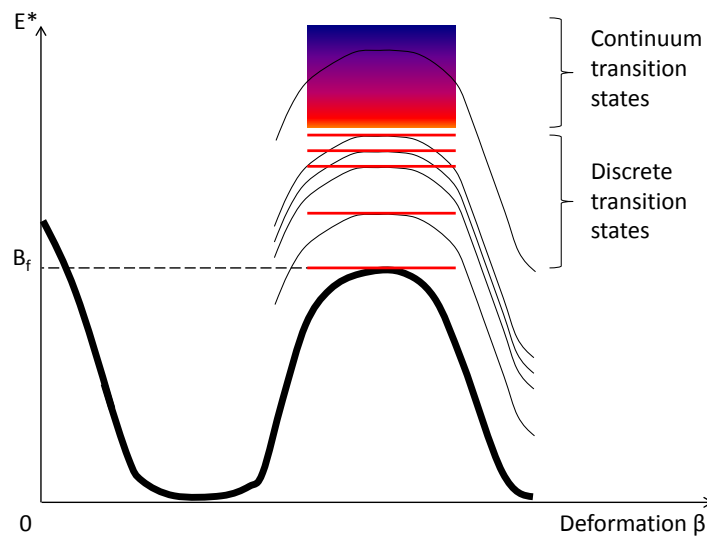
Figure 1.16: Potential energy as function of deformation for a fissile nucleus. Each transition state is associated with a barrier, which is simply obtained by translation in the modeling of the ground state barrier.

33

which means that the barrier simply shifted up by ϵ_i (see Fig. 1.16). For a compound-nucleus with excitation energy E^*, spin J and parity Π, all the transition states with spin and parity $J\Pi$ will contribute to the fission process. The total fission transmission coefficient is the sum of the individual transmission coefficients for each barrier through which the nucleus may tunnel, and thus reads in terms of the previously introduced $T_f(E^*, \varepsilon)$:

$$T_f^{J\Pi}(E^*) = \sum_i T_f(E^*, \varepsilon) f(i, J, \Pi) + \int_{E_d}^{E^*} \Omega(\varepsilon, J, \Pi) T_f(E^*, \varepsilon) d\varepsilon \qquad (1.45)$$

where the summation runs over all discrete transition states on top of the barrier and E_d marks the beginning of the continuum. In this equation, $f(i, J, \Pi) = 1$ if the spin and parity of the transition state is equal to that of the compound-nucleus and 0 otherwise. $\Omega(\varepsilon, J, \Pi)$ is the density of levels with spin J and parity Π for an excitation energy ε. The latter formula is only valid for one barrier. Nevertheless, in the actinide region, a second barrier must be crossed before undergoing fission. The double-humped
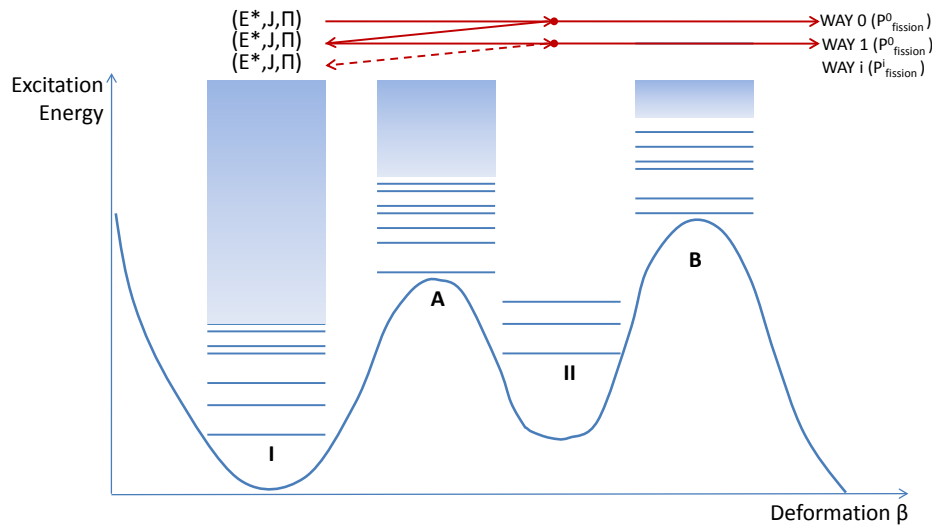
Figure 1.17: Illustration of the double humped barrier problem. In particular, paths 0 and 1 are both detailed. Note that class II states enhance locally the transmission. Nevertheless we neglect possible resonances of the class II states in the following interpretation.

barrier transmission can be decomposed in two separate steps: the first barrier (barrier A) transmission and the second (barrier B) transmission via two independent fission transmission coefficients $T_A^{J\Pi}$ and $T_B^{J\Pi}$. By analogy with the independence of the formation and decay of the compound-nucleus (see equations 1.1), the fission probability can be interpreted as the product of the probability $P_{I \to II}$ to cross the barrier A and the probability to cross the second barrier $P_{II \to fission}$ when the first barrier has been crossed.

At the second well, there are two possibilities: crossing back barrier A with probability T_A or fissioning through barrier B with probability T_B. The fission probability relative to the first possibility (way 0) is:

$$P^0_{fission} = P_{I \to II}.P_{II \to fission} = \left[\frac{T_A}{\sum T_i}\right]\left[\frac{T_B}{T_A + T_B}\right] \tag{1.46}$$

where $\sum T_i = T_A + T_n + T_\gamma$. After crossing back barrier A, it is still possible to cross again barrier A and fission through barrier B (way 1). The fission probability can thus be written as:

$$P^1_{fission} = [P_{I \to II}.P_{II \to I}][P_{I \to II}.P_{II \to fission}] \tag{1.47}$$

with $P_{I \to II}.P_{II \to I} = \left[\frac{T_A}{\sum T_i}\right]\left[\frac{T_A}{T_A + T_B}\right]$. After n «coming-backs», we have:

$$P_{fission} = \sum_i P^i_{fission} = [P_{I \to II}.P_{II \to fission}]\left[1 + [P_{I \to II}.P_{II \to I}]^1 + ... + [P_{I \to II}.P_{II \to I}]^n\right] \tag{1.48}$$

Since $P_{I \to II}.P_{II \to I} < 1$, one can write:

$$P_{fission} = \sum_i P^i_{fission} = [P_{I \to II}.P_{II \to fission}]\left[\frac{1}{1 - [P_{I \to II}.P_{II \to I}]}\right] \tag{1.49}$$

which implies:

$$P_{fission} = \left[\frac{T_A}{T_A + T_n + T_\gamma}\right]\left[\frac{T_B}{T_A + T_B}\right]\left[1 - \frac{T_A}{T_A + T_n + T_\gamma}.\frac{T_A}{T_A + T_B}\right]^{-1} \tag{1.50}$$

and leads to the well-known fission probability expression:

$$P_{fission} = \frac{\left[\frac{T_A T_B}{T_A + T_B}\right]}{T_n + T_\gamma + \left[\frac{T_A T_B}{T_A + T_B}\right]} = \frac{T_f}{T_n + T_\gamma + T_f} \tag{1.51}$$

where the fission transmission coefficient for a double-humped barrier of a compound-nucleus state (E^*, J, Π) reads:

$$T^{J\Pi}_{fission}(E^*) = \frac{T^{J\Pi}_A(E^*)T^{J\Pi}_B(E^*)}{T^{J\Pi}_A(E^*) + T^{J\Pi}_B(E^*)} \tag{1.52}$$

1.5 The surrogate method

Let us start with the Hauser-Feshbach formula of the (n, χ) cross section (already given in equation 1.1):

$$\sigma_{n,\chi}(E_n) = \sum_{J\Pi} \sigma_n^{CN}(E^*, J, \Pi).G_\chi^{CN}(E^*, J, \Pi) \qquad (1.53)$$

This expression can be factorized as:

$$\sigma_{n,\chi}(E_n) = \sigma_n^{CN}(E^*).\sum_{J\Pi} \frac{\sigma_n^{CN}(E^*, J, \Pi)}{\sigma_n^{CN}(E^*)}.G_\chi^{CN}(E^*, J, \Pi) \qquad (1.54)$$

We define the probability $P_\chi(E^*)$ that the compound-nucleus decays through channel χ as:

$$P_\chi^{CN}(E^*) = \sum_{J\Pi} F_s^{CN}(E^*, J, \Pi).G_\chi^{CN}(E^*, J, \Pi) \qquad (1.55)$$

where $F_s^{CN}(E^*, J, \Pi) = \frac{\sigma_n^{CN}(E^*, J, \Pi)}{\sigma_n^{CN}(E^*)}$ is the probability for forming $^{A+1}X^*$ with given values for (E^*, J, Π). This is nothing but the spin-parity distribution of the compound-nucleus at E^*. By definition, $\sum_{J\Pi} F_s^{CN}(E^*, J, \Pi) = 1$. Finally, equation 1.53 can be written as:

$$\sigma_{n,\chi}(E_n) = \sigma^{CN}(E^*).\sum_{J\Pi} F_s^{CN}(E^*, J, \Pi).G_\chi^{CN}(E^*, J, \Pi) \qquad (1.56)$$

In the following we explain the derivation of the Weisskopf-Ewing theory from the Hauser-Feshbach theory. The Hauser-Feshbach- theory rigorously conserves total angular momentum J and parity Π. To achieve the independence of the decay probability on $J\Pi$, the energy of the compound-nucleus must be sufficiently high for all the decay channels to be dominated by integrals over the level density. If the latter assumption is satisfied, width fluctuations are negligible. In the continuum of states, we have seen that the transmission coefficients can be expressed as the sum over the transmission coefficients and the level densities for the exit channels:

$$< T_{cl'j'}^{J\Pi} >= \sum_{J'=0}^{\infty} \sum_{l=J-J'}^{J+J'} T_l^c(\epsilon_c).\Omega_c(E', J') \qquad (1.57)$$

where ϵ_c is the kinetic energy of the outgoing particle, E' is the excitation energy in the residual nucleus and I' is the final-state spin. In equation 1.23, if the states that are populated by the compound-nucleus have angular momenta lower than the spin cut-off parameter $I' \leq \sigma_{cutoff}$, the level density can be factorized as $(2J' + 1)\Omega_0(E')$ and equation 1.57 becomes:

$$< T_{cl'j'}^{J\Pi} >= \Omega_0(E').\sum_{l,J'} T_l^c(\epsilon_c)(2J'+1)\triangle(J,l,J') \tag{1.58}$$

with a function $\triangle(J,l,I')$ which is defined as 1 if the three angular momenta satisfy the vectorial relationship $I' = J + l$ or 0 otherwise. This restriction on the magnetic sub-states permits to carry out the sum over J' :

$$\sum_{i'}(2i'+1)\triangle(J,l,i') = (2J+1)(2l+1) \tag{1.59}$$

and $< T_{cl'j'}^{J\Pi} >$ becomes:

$$< T_{cl'j'}^{J\Pi} >= (2J+1).\Omega_0^c(E').\sum_l(2l+1).T_l^c(\epsilon_c) \tag{1.60}$$

We define the inverse cross section $\sigma_c^{reac}(\epsilon_c)$, namely the cross section for absorption of the ejected particle as if it were incident on the excited nucleus in channel c. It is assumed that this cross section is the same for the absorption on any state of the compound-nucleus and is given by:

$$\sigma_c^{reac}(\epsilon_c) = \pi\bar{\lambda}_c^2 \sum_{l=0}^{\infty}(2l+1)T_l^c(E_c) \tag{1.61}$$

Consequently, the transmission coefficients read:

$$< T_{cl'j'}^{J\Pi} >= (2J+1).\Omega_0^c(E')\frac{1}{\pi\bar{\lambda}_c^2}\sigma_c^{reac}(\epsilon_c) \tag{1.62}$$

As a consequence, in the Weisskopf-Ewing limit the branching ratios are independent of $J\Pi$ and given by:

$$G_\chi(E^*) = \frac{< T_{\chi l}^J >}{\sum_c < T_{cl}^J >} = \frac{k_\chi^2.\sigma_\chi^{reac}(\epsilon_\chi).\Omega_\chi'(E_\chi)}{\sum_c \int_0^{E_c^{max}} dE_c k_c^2 \sigma_c^{reac}(\epsilon_c).\Omega_c'(E_c)} \tag{1.63}$$

where the summation over c represents all possible decay channels and k_c is the wave number.

Then the branching ratios can be extracted from the summation over $J\Pi$ in eq. 1.55 leading to:

$$P_\chi^{CN}(E^*) = G_\chi^{CN}(E^*) \tag{1.64}$$

and the expression for the neutron-induced cross section becomes:

$$\sigma_{n,\chi}(E_n) = \sigma^{CN}(E_n).P_\chi^{CN}(E^*) \tag{1.65}$$

This is the equation on which rely most applications of the surrogate method.
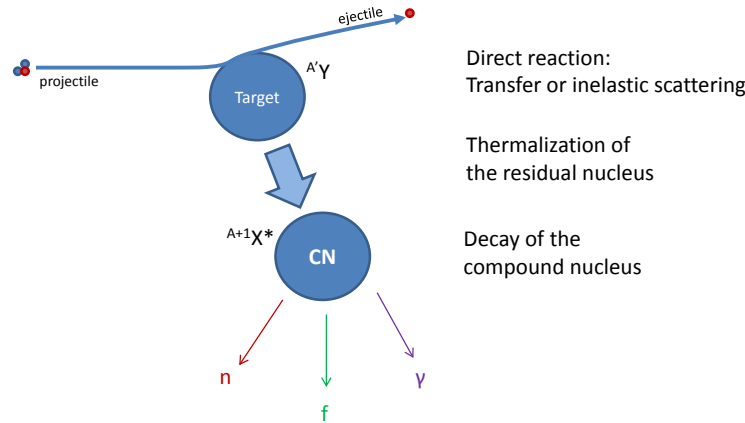
Figure 1.18: Surrogate reaction ($projectile +^{A'} Y \rightarrow ejectile +^{A+1} X^*$) that produces the compound-nucleus $^{A+1}X^*$ associated to the neutron-induced reaction ($n +^A X \rightarrow^{A+1} X^*$).

In a surrogate experiment (see figure 1.18), the compound-nucleus $^{A+1}X^*$ is produced via a transfer reaction or inelastic scattering reaction involving a light-charged projectile. These reactions are not compound reactions, but direct reactions involving only a few nucleons in the nucleus. However, in the region of excitation energy above S_n ($\approx$6 MeV in the rare-earth and actinide regions), the residual nucleus has a high probability to become a compound nucleus before deexcitation. This is due to the large degree of configuration mixing that appears at high level density. In a surrogate experiment, the decay of $^{A+1}X^*$ is observed in coincidence with the outgoing ejectile w, which is stopped in a detector that provides particle identification, as well as the kinetic energy and the emission angle of w. The desired exit channel χ is identified by detecting for example the fission fragments (fission channel) or the γ-rays (radiative capture channel). To determine the corresponding decay probability P_χ^{CN}, the number of ejectiles detected in coincidence with the desired exit channel χ ($N_{coinc-\chi}$) is divided by the total number of ejectiles ($N_{singles}$), the latter being labelled as «singles» events. When normalised to the detection efficiency ϵ_χ, the decay probability as a function of the excitation energy of the CN can be written as:

$$P_\chi^{CN}(E^*) = \frac{N_{coinc-\chi}(E^*)}{N_{singles}(E^*).\epsilon_\chi(E^*)} \tag{1.66}$$

The idea behind the surrogate method is to determine a neutron-induced cross section via a combination of theory and experiment according to the following steps:

- calculate the compound-nucleus formation cross section $\sigma^{CN}(E^*)$ for the desired neutron-induced reaction using eq. 1.16.

- measure the probability $P_\chi^{CN}(E^*)$ that the CN is formed in a surrogate reaction with energy E^* and decays into channel χ.

A crucial point is that the probability distributions $F_s^{CN}(E^*, J, \Pi)$ depend on the reaction used to form the compound-nucleus. Ideally, one would need to correct for this by calculating them theoretically[1]. Then the branching ratios $G_\chi^{CN}(E_n, J, \Pi)$ would be obtained thanks to eq. 1.55 by adjusting the parameters of the statistical model to reproduce the measured decay probabilities $P_\chi^{CN}(E^*)$. The objective of the surrogate method is to determine or constrain the branching ratios experimentally. Finally one uses eq. 1.53 to infer the desired neutron-induced reaction cross section. Unfortunately, the distributions $F_s^{CN}(E^*, J, \Pi)$ are very difficult to obtain theoretically. Actually, as mentioned before, most applications do not proceed in this way but use the Weisskopf-Ewing approximation that avoids the necessity to know $F_s^{CN}(E^*, J, \Pi)$.

1.6 The validity of the surrogate method

For neutron-induced and surrogate reactions the decay probabilities are given by:

$$P_\chi^n(E^*) = \sum_{J\Pi} F_n^{CN}(E^*, J, \Pi).G_\chi^{CN}(E^*, J, \Pi) \tag{1.67}$$

$$P_\chi^s(E^*) = \sum_{J\Pi} F_s^{CN}(E^*, J, \Pi).G_\chi^{CN}(E^*, J, \Pi) \tag{1.68}$$

where $F_n^{CN}(E^*, J, \Pi)$ and $F_s^{CN}(E^*, J, \Pi)$ correspond to the probability that the compound-nucleus at energy E^* is formed in the state $J\Pi$ by the neutron-induced (index n) and the surrogate (index s) reaction, respectively. Note that the branching ratios $G_\chi(E^*, J, \Pi)$ in the neutron-induced reaction and the surrogate reaction are the same.

The two upper decay probabilities are equal in two cases:

- hyp.1: the $J\Pi$ distributions populated in both reactions are similar:

$$F_n^{CN}(E^*, J, \Pi) \simeq F_s^{CN}(E^*, J, \Pi) \tag{1.69}$$

or

- hyp.2: the branching ratios are independent of $J\Pi$ (Weisskopf-Ewing hypothesis):

$$G_\chi(E^*, J, \Pi) = G_\chi(E^*) \tag{1.70}$$

---

[1]Note that these distributions depend on the emission angle of the ejectile.

1.6.1 Spin-parity distributions in surrogate reactions

Actually, we expect different angular momentum distributions to arise from the neutron-induced and the surrogate reactions. That is why, as we mentioned before, the ideal procedure of a surrogate measurement would be to calculate $F_s^{CN}(E^*, J, \Pi)$, then extract $G_\chi(E^*, J, \Pi)$, and insert them into the Hauser-Feshbach formula (equation 1.53). In the seventies, B.B. Back and H.C. Britt ([Back 74b]) performed DWBA calculations in order to extract the angular momentum distributions populated in (t, p), (d, p) and $(^3He, d)$ reactions (see left part of figure 1.19). For the (d, p) reaction, the mean l transferred is about $2 - 3\hbar$. The calculated mean l transferred in (t, p) and $(^3He, d)$ is about $4\hbar$. These distributions were compared by H.C. Britt and W. Younes ([Younes 03b]) with neutron-induced angular-momentum distributions. The right part of figure 1.19 shows that a low-energy neutron (E_n=0.5MeV) induces less angular momentum than the previous transfer reactions. On the other hand, for higher neutron energies (E_n=2MeV), the mean l transferred is rather close to the one populated in the (d, p) reaction.

Theoretical work carried out at Livermore suggests an important spin mismatch in the entrance channel at the lowest neutron energies. In [Thompson 06], DWBA pickup calculations were performed with FRESCO ([Thompson 00]) to infer the angular-momentum distributions generated using a $(^3He, \alpha)$ stripping reaction on ^{238}U and ^{235}U for an incident ^3He beam at 42 MeV. Figure 1.20 illustrates that the mean l transferred in $(^3He, \alpha)$ varies between $4\hbar$ and $6\hbar$, depending strongly on the spin and the parity of the ground state of the target nucleus. Nevertheless, all these calculated distributions have not yet been validated since there are no experimental spin-parity distributions available for these reactions. One could test them by using them to calculate the decay probabilities of interest and compare the latter with what is experimentally observed. Nowadays, theoreticians are focusing on pickup and stripping reactions.

S. Chiba et al. developed a dynamical model of surrogate reactions ([Aritomo 11]). In this very recent work, the transfer of several nucleons at an initial stage, thermal equilibration and the decay of the compound nuclei are treated in a unified framework. For example, the authors calculated the spin distribution of the compound nuclei $^{240}U^*$ and $^{238}U^*$ in the reactions $^{238}U(^{18}O, ^{16}O)^{240}U$ and $^{236}U(^{18}O, ^{16}O)^{238}U$, respectively, at the center-of-mass energy of $E_{c.m.} = 133.5MeV$. The results showed that the spin of the compound-nucleus was less than $10\hbar$ in both cases. This work needs to be compared to experimental results.

To conclude, an important effort from theoreticians and experimentalists should be done in order to determine these distributions. We will show later how the present work can provide very valuable information on this issue.

(a)   (b)
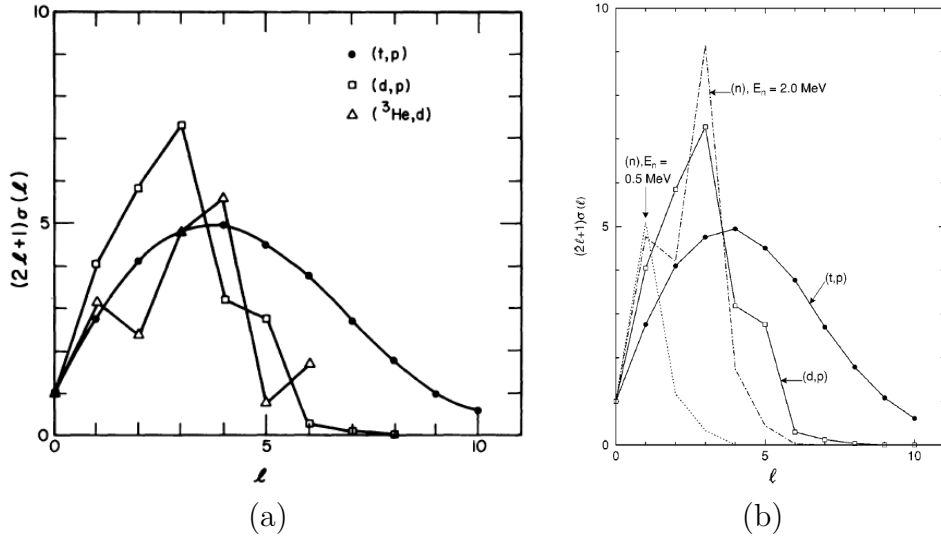
Figure 1.19: (a) Angular momentum l distributions transferred in (t, p), (d, p) et $(^3He, d)$
reactions (normalized to 1 for $l = 0$). These DWBA calculations were
done for a ^{240}Pu target at E^*=5.5 MeV and $\theta = 90°$ ([Back 74b]). (b)
Comparison of the two of the previous distributions with the transferred
orbital angular momentum l in neutron-induced reactions at E_n=0.5 and
2.0 MeV. ([Younes 03b])
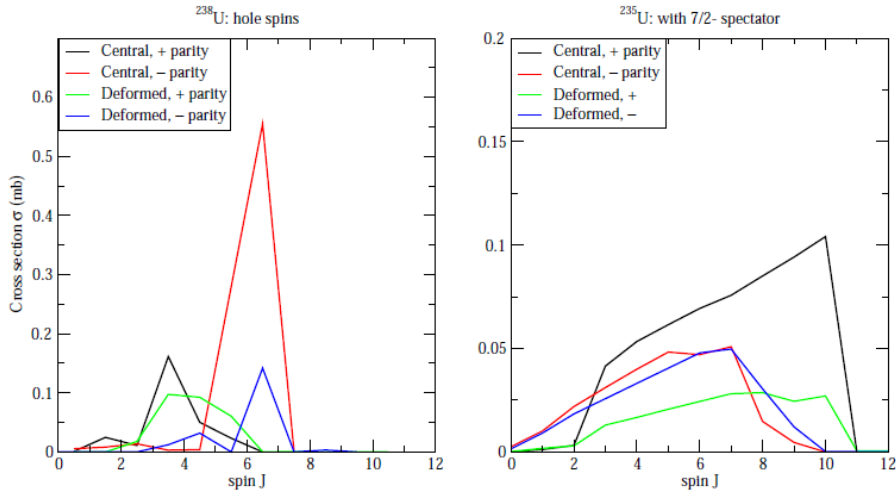
Figure 1.20: Left: Spin distributions of $^{237}U^*$ produced in the $^{238}U(^3He, \alpha)$ reaction.
Right: Similarly for $^{234}U^*$ after the $^{235}U(^3He, \alpha)$ reaction. The ground-
state spin of ^{235}U ($\frac{7}{2}^-$) is assumed to be spectator: this spin is not coupled
with the spins of all removed-neutron hole states in the calculations. The
neutron eigenstates have been determined with a spherical (central) and a
deformed potential ([Thompson 06]).

1.6.2 Branching ratios

Hauser-Feshbach calculations allow one to predict branching ratios for specific values of (E^*, J, Π) of the CN. These calculations provide realistic information on the $J\Pi$ sensibility of the branching ratios and predict when the Weisskopf-Ewing condition is fulfilled.

To study (n, f) cross sections, J. Escher et F. Dietrich ([Escher 06]) considered the reaction $n +^{235} U \rightarrow ^{236}U^*$ where the ^{235}U is a fissile nucleus. Note that the ground-state spin and parity of ^{235}U and ^{236}U are $\frac{7}{2}^-$ and 0^+, respectively. Figures 1.21 and 1.22 give the fission decay probabilities for various $J\Pi$ states of $^{236}U^*$ up to $J = 20\hbar$. Figure 1.21 focuses on spin range $J = [0; 5]$ and one observes that the fission decay probabilities depend on $J\Pi$ with a variation up to a factor 2 at low incident neutron energy. Nevertheless, above 1 MeV neutron energy, all the lines coincide by about 20%. The Weisskopf-Ewing approximation implies no $J\Pi$ dependence at all and this occurs at 4-5 MeV. The latter energy limit is often called the Weisskopf-Ewing limit. On other hand, figure 1.22 extends the latter calculations to spins up to $20\hbar$ and illustrates a crucial point: angular-momentum values larger than the spin-cutoff parameter ($6-7\hbar$ for actinides) invalidate the Weisskopf-Ewing assumption. We have seen before that for high spins, the spin dependence of the level density is not proportional to $(2I' + 1)$ anymore, and the spin-dependent part of the level density does not cancel in the derivation of the branching ratios.

Recently, J. Escher and F. Dietrich ([Escher 10a]) examined (n, γ) cross sections for spherical fission fragments and deformed rare-earth and actinide nuclei: Hauser-Feshbach calculations for $^{91}Zr(n, \gamma)$, $^{155}Gd(n, \gamma)$ and $^{235}U(n, \gamma)$ were carried out. Calculated γ-decay branching ratios $G_\gamma(E^*, J, \Pi)$ for values of J up to $12\hbar$ for $^{92}Zr^*$, $^{156}Gd^*$, and $^{236}U^*$are given in figure 1.23. In the energy regime considered, the decay of the $^{92}Zr^*$ CN proceeds only by γ or neutron emission. Due to the low level density in the residual nucleus ^{91}Zr, only few states are available after neutron emission. Actually, the access to each new state of the residual nucleus corresponds to a discontinuity in one or more γ-branching ratios.γ-decay probabilities are found to be very sensitive to the $J\Pi$ of the populated compound state (see panel (a)). It is clear that the Weisskopf-Ewing approximation is not valid in this region. The situation improves as one moves away from closed shells. For example, while ^{91}Zr has only one level below 1 MeV (the ground state), the well-deformed rare-earth nucleus ^{155}Gd has over 60, and the actinide nucleus ^{235}U has approximately 90. Consequently, the decay probabilities for $^{156}Gd^*$ and $^{236}U^*$ exhibit significantly less sensitivity to the $J\Pi$ values of the compound-nucleus. This is shown in panels (b) and (c) of figure 1.23. For $^{156}Gd^*$, the curve for the highest J-value, $J = 12\hbar$, is higher in magnitude than those for $J = 0 - 3\hbar$ by about a factor 3 in the higher-energy regime; for $^{236}U^*$, the difference is somewhat smaller, around 2. As a consequence, this important work indicates that high level densities present

in the deformed rare-earth and actinide regions reduce the sensitivity of the γ-decay probabilities to compound nuclear spin-parity distributions and nuclear-structure effects. Nevertheless, for low energies ($E_n < 1 - 2$ MeV), the conditions for the Weisskopf-Ewing approximation are not expected to be satisfied ([Escher 10b]).

An additional test of the Weisskopf-Ewing approximation was carried out by S. Chiba et al. ([Chiba 10]) which provided calculated decay probabilities for the fission and capture channels for various $J\Pi$ states of $^{239}U^*$ spins up to $J\Pi = 21/2^{\pm}$ and neutron energies up to 5 MeV (see figure 1.24). Contrary to the previous $^{236}U^*$ case, the fission barrier of ^{239}U (B_f^A=6.45 and B_f^B=6 MeV where B_f^A is the first fission barrier and B_f^B the second [Maslov 98]) is above the neutron binding energy (S_n=4.806 MeV). The calculations show that the fission decay probability varies depending on $J\Pi$ by about 15% at 5 MeV but the variation is about 50% at 1,5 MeV. The convergence is clearly much worse for the capture channel where the decay probabilities scatter by a factor of 8 at 5 MeV. The variation is much larger at lower energy and in this range, it appears that high spins favor the capture process at the expense of other decay channels. Above 2,5 MeV, one notes a systematic behavior: both, fission and capture probabilities increase monotonically as J increases. This trend was also present for the previous compound nuclei studied by J. Escher et al.

To conclude, for energies ($E_n < 1 - 2$ MeV), the conditions for the Weisskopf-Ewing approximation are not expected to be well satisfied. The Weisskopf-Ewing limit depends clearly on the structure of the compound-nucleus and of the residual nucleus after neutron emission. Also the dependence of the γ-branching ratios on the $J\Pi$ distribution is greater than that found for fission.
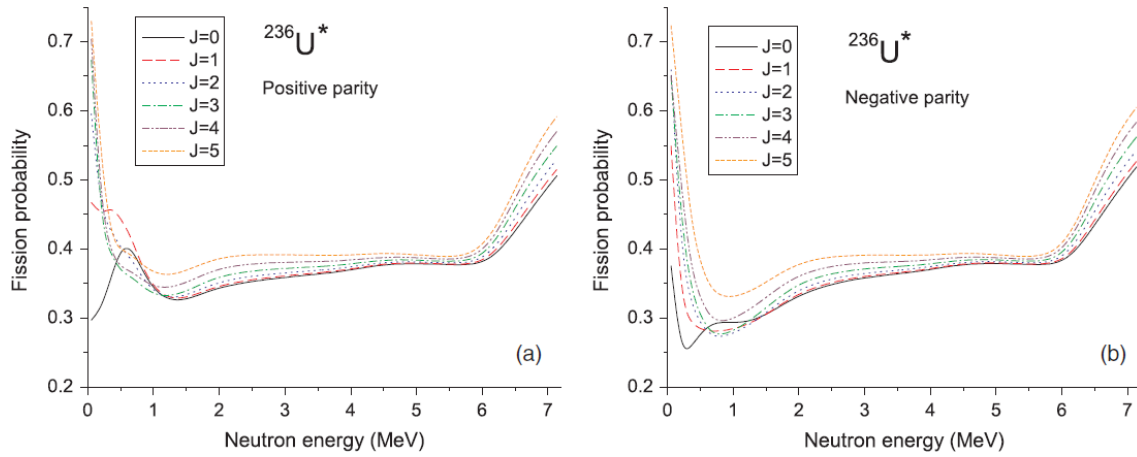
Figure 1.21: Calculated branching ratios $G_f(E^*, J, \Pi)$ for fission of ^{236}U, following $n +^{235}U$, as a function of neutron energy E_n. [Escher 06]
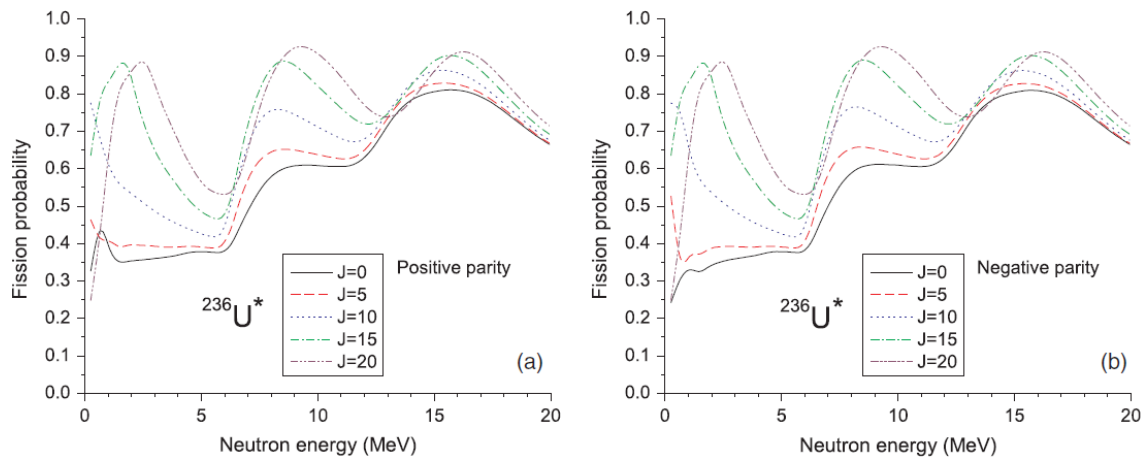
Figure 1.22: Same as 1.21 but with total angular momenta $J = 0, 5, 10, 15, 20$ in the compound-nucleus $^{236}U^*$.[Escher 06]
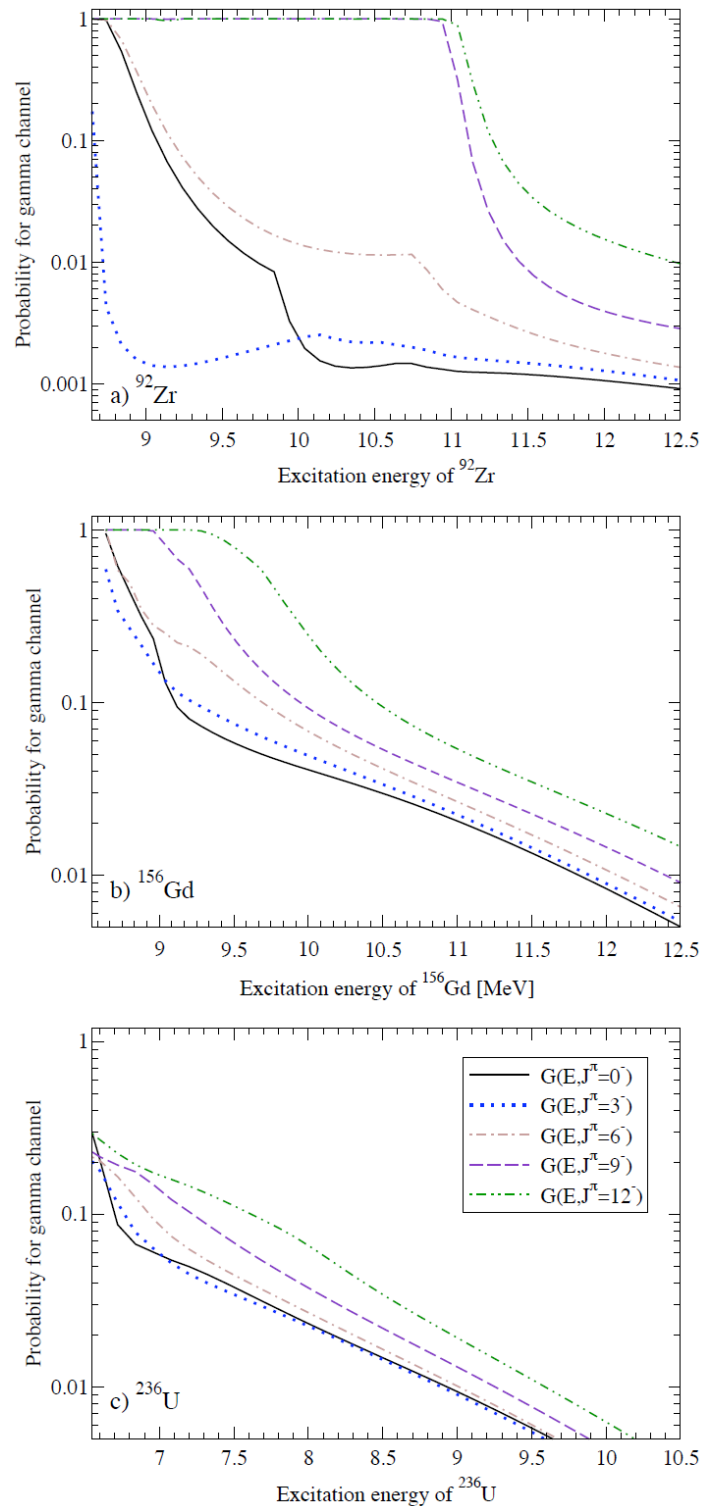
Figure 1.23: Calculated branching ratios $G_\gamma(E^*, J, \Pi)$ for $^{92}Zr^*$, $^{156}Gd^*$, and $^{236}U^*$. Shown is the probability that the compound-nucleus, when produced with a specific $J\Pi$ combination, decays via the γ-channel. The excitation energies shown correspond to incident-neutron energies of 0-4 MeV. Only negative parities are considered. ([Escher 10a])

45
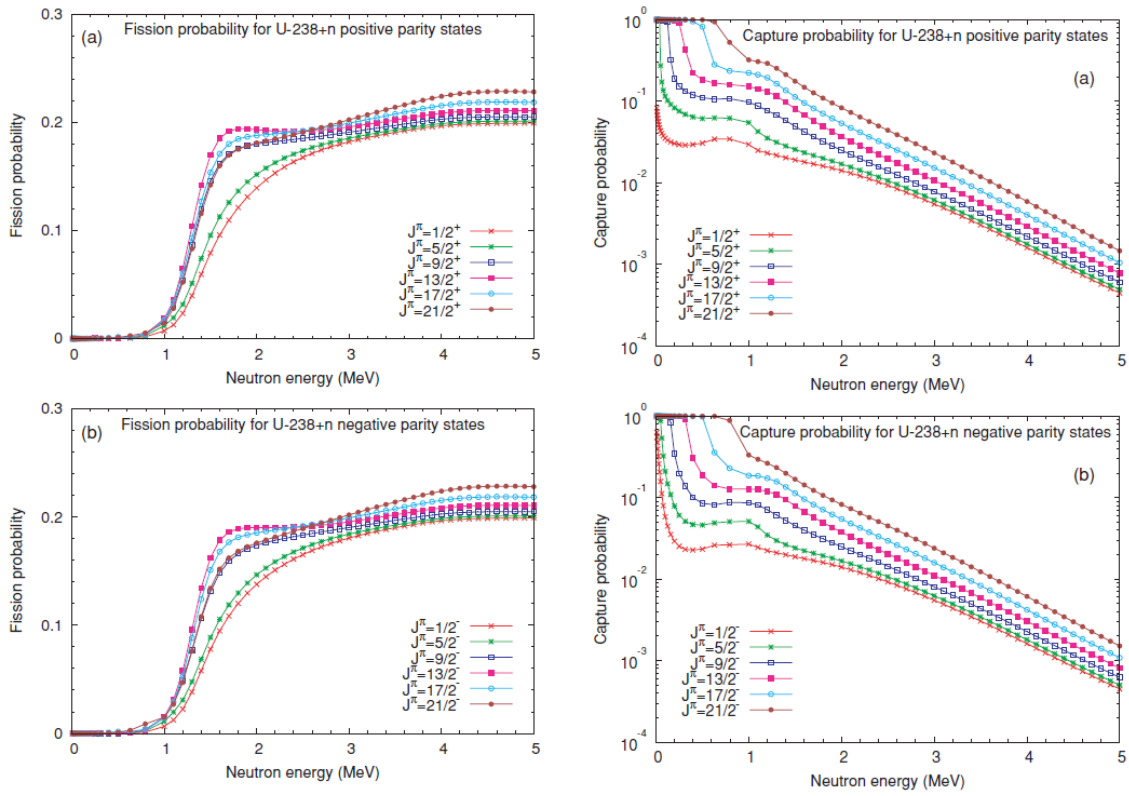
Figure 1.24: Branching ratios for the fission (left) and capture (right) channels for various $J\Pi$ states of ^{239}U. (a): positive-parity states. (b): negative-parity states. [Chiba 10]

1.7 The surrogate ratio method

Recently, an alternative to the standard surrogate approach, called the surrogate ratio method (SRM), has been developed ([Plettner 05]). This method relates the ratio of two neutron-induced cross sections to a ratio of measured decay probabilities from two surrogate reactions:

$$\frac{\sigma_{n,\chi}^{AX}(E_n)}{\sigma_{n,\chi}^{BY}(E_n)} = \frac{\sigma_{CN}^{A+1X^*}(E_n).P_\chi^{A+1X^*}(E_n)}{\sigma_{CN}^{B+1Y^*}(E_n).P_\chi^{B+1Y^*}(E_n)} \tag{1.71}$$

where:

- $\sigma_{n,\chi}^{AX}(E_n)$ and $\sigma_{n,\chi}^{BY}(E_n)$ are the cross sections for the reactions $^AX(n,\chi)$ and $^BY(n,\chi)$, respectively.

- $\sigma_{CN}^{A+1X^*}(E_n)$ and $\sigma_{CN}^{B+1Y^*}(E_n)$ are the compound-nucleus formation cross sections in the reactions $(^AX + n)$ and $(^BY + n)$ with energy E_n, respectively.

- $P_{s,\chi}^{A+1X^*}(E_n)$ and $P_{s,\chi}^{B+1Y^*}(E_n)$ are the measured surrogate decay probabilities for the compound nuclei $^{A+1}X^*$ and $^{B+1}Y^*$ with equivalent neutron energy E_n.

The SRM was initially developed for experimental reasons. The main advantage of the SRM is that under certain conditions it removes the need to measure the total number of reaction events, i.e. the «singles» events, which eliminates an important source of systematic uncertainty. This point will be discussed in section 2.2. Obviously the SRM requires one of the neutron-induced sections to be known in order to infer the desired one. Note that the ratio method is based on the Weisskopf-Ewing assumption and is therefore, in principle, only valid in this limit.

1.7.1 Theoretical investigation of the surrogate ratio method

Again the surrogate ratio method was investigated using Hauser-Feshbach calculations. Decay probabilities for particular values of (E^*, J, Π) were carried out in the same way as in section 1.6.2. Ratios of such quantities provide realistic information about the $J\Pi$ sensibility of the SRM.

In [Escher 06], F.S. Dietrich and J.E. Escher investigated under which conditions the SRM gives good results. They focused on the reactions $^{233}U(n, f)$ and $^{235}U(n, f)$. Figure 1.25 illustrates simulated results for surrogate experiments in which the compound nuclei $^{234}U^*$ and $^{236}U^*$ are populated with the $J\Pi$ distributions given by figure 1.26(a). For comparison, figure 1.26(b) shows angular-momentum distributions of the compound-nucleus ^{236}U populated in the neutron-induced reaction. Fission cross sections $\sigma_{n,f}^{234U^*}(E_n, J, \Pi)$ and $\sigma_{n,f}^{236U^*}(E_n, J, \Pi)$ have been obtained by calculating $\sum_{J\Pi} \sigma_{CN}^{234U^*}(E_n, J, \Pi) \times P_f^{234U^*}(E_n, J, \Pi)$ and $\sum_{J\Pi} \sigma_{CN}^{236U^*}(E_n, J, \Pi) \times P_f^{236U^*}(E_n, J, \Pi)$, respectively, using the latter angular-momentum distributions. Results are shown in figure 1.25(a)

and (b). The obtained cross sections are compared to calculated reference cross sections (adjusted to existing data). Deviations from the expected reference cross sections by up to 40% for neutron energies above 5 MeV, and up to a factor 2 at lower energies, are observed. In figure 1.25(c), the $\sigma_{n,f}^{235U}$ fission cross section obtained with the ratio $\frac{\sum_{J\Pi} \sigma_{CN}^{236U^*}(E_n,J,\Pi).G_f^{236U^*}(E_n,J,\Pi)}{\sum_{J\Pi} \sigma_{CN}^{234U^*}(E_n,J,\Pi).G_f^{234U^*}(E_n,J,\Pi)}$ and the reference $\sigma_{n,f}^{233U}(E_n)$ cross section is presented. The fission cross section is found to be in much better agreement with the neutron-induced cross section. One observes deviations of less than 50% at low energies and no more than 25% for the higher energies.

Similar statistical calculations have been done by S. Chiba et al. ([Chiba 10]) for $^{239}U^*$ and $^{237}U^*$. Branching ratio calculations were carried out for the fission and radiative capture channels. Figure 1.27 shows calculated fission $\frac{G_f^{239U^*}(E_n,J,\Pi)}{G_f^{237U^*}(E_n,J,\Pi)}$ and capture $\frac{G_\gamma^{239U^*}(E_n,J,\Pi)}{G_\gamma^{237U^*}(E_n,J,\Pi)}$ ratios for various $J\Pi$ states. The ratios are found to be in an astonishingly nice agreement with the neutron-induced evaluated ratios. For the fission ratio, the deviation is only at a level of 3% at 5 MeV. The largest deviation is of 15% at about 1,6 MeV while it was about 50% in figure 1.24. The convergence seems to be valid also for somewhat higher spin values. On the other hand, the capture ratios show important deviations ($\sim$30%) for lower energies but they have to be compared with the enormous $J\Pi$ dependence of the decay probabilities (see Fig. 1.24) where differences of a factor of 10 were observed. When $E_n>2$ MeV, one notices a good mutual convergence in Fig. 1.27, while we saw in Fig. 1.24 that the decay probabilities still depend on $J\Pi$ above this limit.

The agreement found highlights a reduction of the effects due to the spin-parity mismatch. When the two reactions that are analyzed are sufficiently similar, the spin-parity mismatch may affect both reactions in the same manner and it is likely that the angular-momentum effects partly cancel in the SRM. Also pre-equilibrium effects seem to cancel in the ratio approach. According to J. Escher and F. Dietrich, two reactions can be considered to be similar if:

- the same surrogate reaction (combination projectile-ejectile) is used to produce the compound nuclei in both cases.

- the same kind of decay (γ emission, charged-particle emission, or fission) is considered in both cases.

- the decays of the compound nuclei have similar properties (number and kind of open channels, separation energies for the various channels, level densities in the residual nuclei, etc).

If similarity is not fulfilled, uncorrelated effects and deviations may increase the discrepancies with respect to neutron-induced data.

$$\sum_{J\Pi} \sigma_{CN}^{234U^*}(E_n, J, \Pi).P_f^{234U^*}(E_n, J, \Pi) \qquad \sum_{J\Pi} \sigma_{CN}^{236U^*}(E_n, J, \Pi).P_f^{236U^*}(E_n, J, \Pi)$$

$$\sigma_{n,f}^{235U} = \frac{\sum_{J\Pi} \sigma_{CN}^{236U^*}(E_n, J, \Pi).P_f^{236U^*}(E_n, J, \Pi)}{\sum_{J\Pi} \sigma_{CN}^{234U^*}(E_n, J, \Pi).P_f^{234U^*}(E_n, J, \Pi)} \sigma_{n,f}^{233U}$$
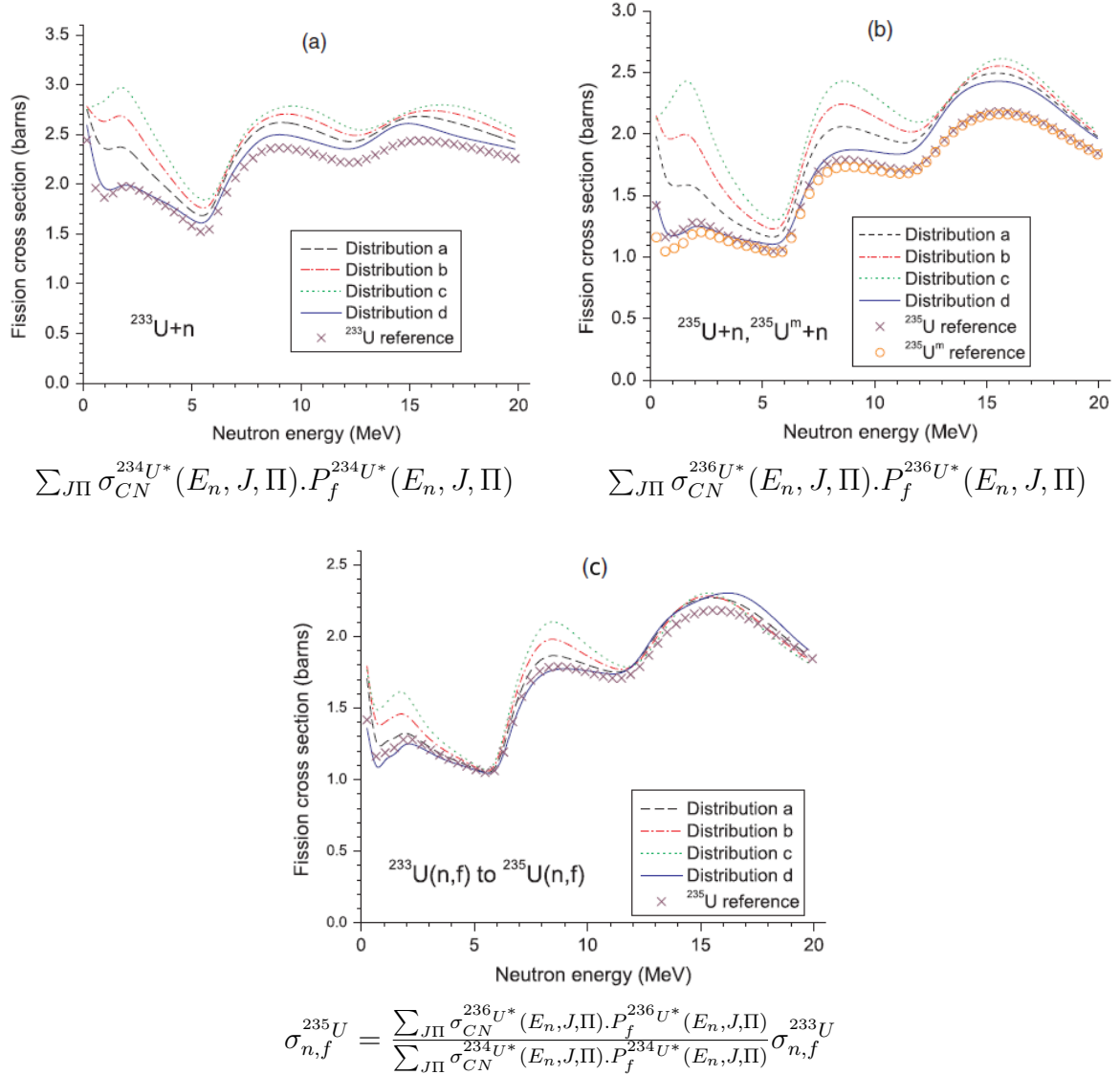
Figure 1.25: Calculated cross sections for $^{233}U(n, f)$ (a) and $^{235}U(n, f)$ (b) and $^{235m}U(n, f)$ (b), respectively, for the spin-parity distributions defined in figure 1.26(a). Calculations are compared with related reference cross sections. Estimates of the $^{235}U(n, f)$ cross section are obtained from the ratio method.[Escher 06]

(a)   (b)
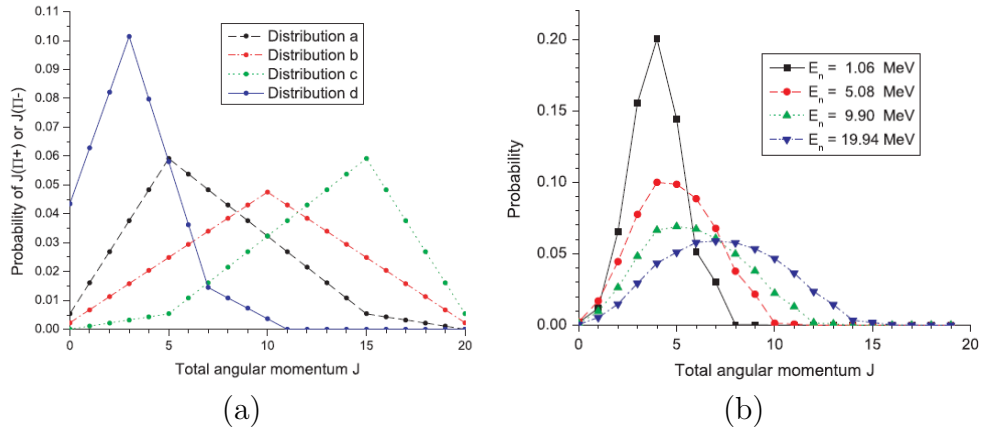
Figure 1.26: (a) Total angular momentum distributions for the compound nuclei con-
sidered in the studies presented in figure 1.25. (b) Angular-momentum
distribution of positive-parity states of the compound-nucleus ^{236}U follow-
ing neutron absorption for various neutron energies. The negative-parity
distribution is qualitatively similar. [Escher 06]
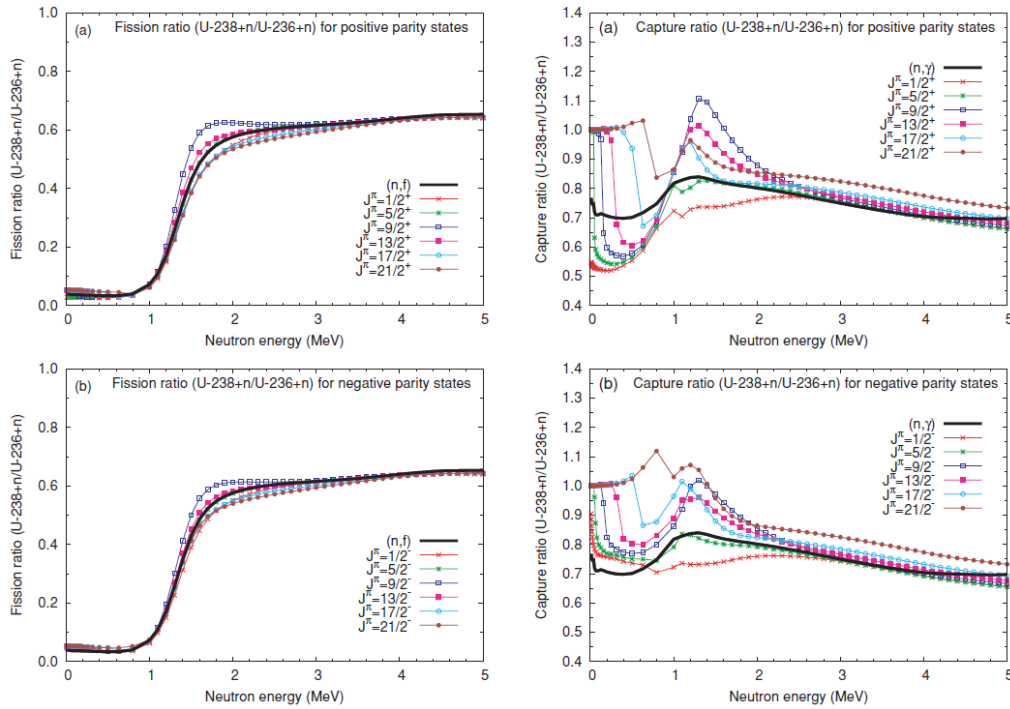
Figure 1.27: Calculated ratios of decay probabilities $\frac{G_{s,\chi}^{239U^*}(E_n,J,\Pi)}{G_{s,\chi}^{237U^*}(E_n,J,\Pi)}$ for the fission (left)
and capture (right) channels from various $J\Pi$ states of $^{239}U^*$ and $^{237}U^*$
obtained by S. Chiba et al. ([Chiba 10]). (a): positive-parity states. (b):
negative-parity states.

Chapter 2

Review of experiments based on the surrogate method

Measurements that test the validity of the Surrogate method are highly important. Applications of the method to (n, f) reactions have been tested in numerous experiments over the years. For (n, γ) reactions, only a few experiments exist. Still fewer have been designed to properly test the method. In order to provide useful information on the validity and limitations of the method, surrogate experiments need to yield cross section results that can be compared to direct measurements. This section is dedicated to experiments using both the standard surrogate method and the surrogate ratio method (SRM). To distinguish between the two surrogate applications the standard method is called «absolute» surrogate method (ASM) in literature;

2.1 The «absolute» surrogate method (ASM)

Let us recall equation 1.66 that describes how the decay probability $P_\chi^{CN}(E^*)$ for a given decay channel χ is obtained in the surrogate method:

$$P_\chi^{CN}(E^*) = \frac{N_{coinc}(E^*)}{N_{single}(E^*).\epsilon_\chi(E^*)} \tag{2.1}$$

where:

- $N_{coinc}(E^*)$ is the number of ejectiles detected in coincidence with the decay products of interest. Note that, at the excitation energies considered here, three exit channels χ can be observed: fission, radiative capture and neutron emission.

- $N_{single}(E^*)$ is the total number of ejectiles detected, namely the number of corresponding CN with excitation energy E^*. These are the so-called «singles» events.

- $\epsilon_\chi(E^*)$ is the detection efficiency for the exit channel χ.

In practise, the procedure of determining the decay probability can be a difficult task. If target contaminants are present, it becomes very difficult, if not impossible, to determine reliable values for N_{single} and N_{coinc}. That is why targets need to be pure and ideally self-supporting in order to avoid the subtraction of the background coming from the backing. The detection efficiency ϵ_χ needs to be determined very accurately. As mentioned before, the neutron induced cross section for the reaction $^A X(n, \chi)$ is obtained applying the Weisskopf-Ewing formula (equation 1.65).

2.1.1 The surrogate method applied to fission

Transfer reactions have been used for a long time in order to determine the structure of nuclear states and also to explore the fission barrier of actinide nuclei. In 1970, the surrogate method was developed in Los Alamos National Laboratory by J. Cramer and H. Britt ([Cramer 70b]). The first surrogate reactions were (t, p) and (t, d) using a 18 MeV triton beam. The ejectiles were detected by a silicon detector at 140° with a energy resolution of $\triangle E \approx 120 keV$ and the fission fragments were detected with 8 silicon detectors in the reaction plane. Fission cross section estimates for several isotopes of thorium, uranium and plutonium were obtained. Uncertainties were estimated to 10% for the fission probabilities and 5-20% for the optical model calculation of the CN formation cross section $\sigma_{CN}(E^*)$. This work was continued by studying the fission of several odd-A, doubly-odd ([Back 74a]) and doubly-even ([Back 74b]) actinide nuclei via new surrogate reactions as (d, p) or (p, p'). Few years later, H. Britt and J. Wilhelmy used $(^3 He, d)$ and $(^3 He, t)$ surrogate reactions on various actinide targets to infer (n, f) cross sections for 34 nuclei for $En \approx 0.5 - 6 MeV$ ([Britt 79]). Note that the compound-nucleus formation cross section was here approximated to $\sigma_{CN}(E^*) = 3, 1b$ and was assumed constant within a precision of 20%. A good agreement was observed with directly measured cross sections, where available, and uncertainties were similar to those of the previous work. However, below 1 MeV, there were in several cases serious discrepancies.

In 2001, the CENBG collaboration proposed to measure fission cross sections of very short-lived nuclei of interest for reactors based on the Thorium fuel cycle and for minor-actinide transmutation. Fission probabilities of $^{234}Pa^*$, $^{233}Pa^*$, $^{232}Pa^*$ and $^{231}Th^*$ were determined via the $^{232}Th(^3 He, pf)^{234}Pa^*$, $^{232}Th(^3 He, df)^{233}Pa^*$, $^{232}Th(^3 He, tf)^{232}Pa^*$ and $^{232}Th(^3 He, \alpha f)^{231}Th^*$ surrogate reactions, respectively. As detailed in Ref. [Petit 04], the 24 MeV $^3 He$ beam was provided by the Tandem of the IPN Orsay. The ^{232}Th target was prepared by electromagnetic separation and consisted of 100 $\mu g/cm^2$ ^{232}Th deposited on 50 $\mu g/cm^2$ carbon backing. The ejectiles were detected by 2 silicon telescopes ($\phi = 9mm$) placed respectively at 90° and 130° with respect to the beam axis. The fission-fragment detector was designed to achieve a large efficiency and good granularity for fission-fragment angular-distribution measurements, used to correct from fragments anisotropy. The system consisted of 15 photovoltaic cells (20x40 mm^2) placed mainly at forward angles. The left part of figure 2.1 shows the fission cross section of $^{233}Pa(n, f)$

obtained from the Weisskopf-Ewing analysis of the proton channel. The CENBG data are shown in comparison with the neutron-induced data. The lines represent the international evaluations. There is a reasonable agreement between the two sets of data at the fission threshold. The right part of the same figure illustrates results for $^{231}Pa(n,f)$ obtained from the Weisskopf-Ewing analysis of the triton transfer channel compared with the neutron-induced data. Again we find a good agreement between the surrogate results and the neutron-induced data at the fission threshold.

$$^{232}Th(^3He,pf)^{234}Pa^* \qquad ^{232}Th(^3He,tf)^{232}Pa^*$$
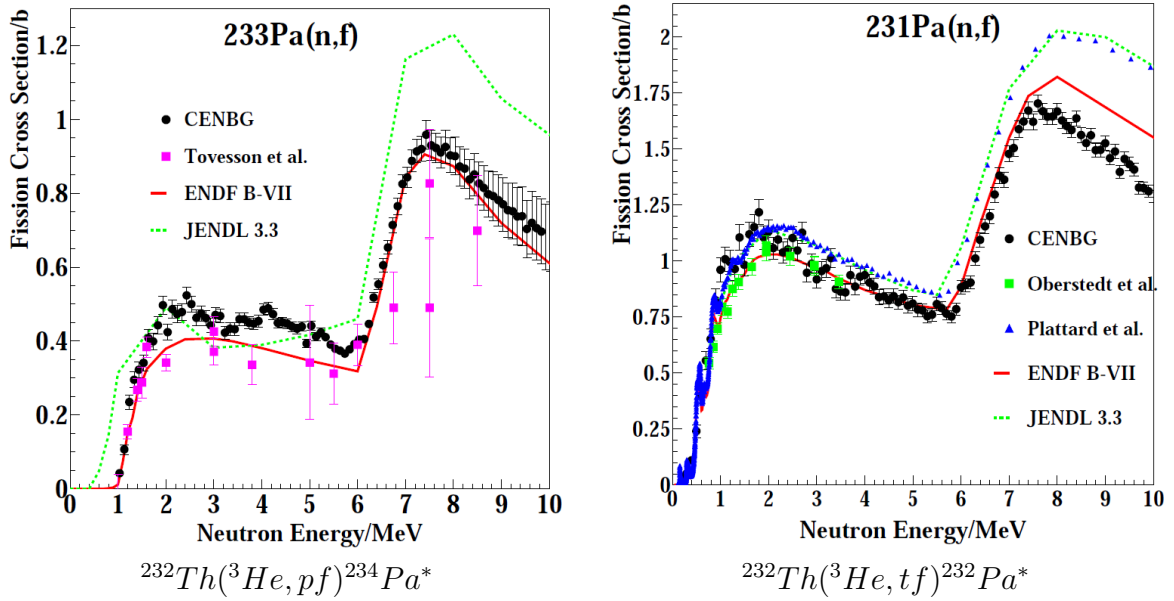
Figure 2.1: Comparison between the CENBG results for $^{233}Pa(n,f)$, $^{231}Pa(n,f)$ with existing direct measurements and the evaluations of the nuclear data libraries ENDF-B/VII and JENDL-3.3.

At that time, W. Younes and H. Britt investigated if nuclear models can be used to correct for $J\Pi$ population mismatch (see Refs. [Younes 03a] for the methodology used and [Younes 03b] for the detailed results). This work was based on previous fission probabilities measured via (t,p) surrogates for $^{240,241,243}Pu(n,f)$, $^{234,236,237,239}U(n,f)$, and $^{231,233}Th(n,f)$ ([Cramer 70b]). Firstly, considerable uncertainty in the neutron transmission coefficients (optical model) at low energy was shown as responsible for an over-estimation of the compound-nucleus cross section given by J. Cramer and H. Britt about twenty years before. Secondly, the (t,p) population probabilities $F_{(t,p)}^{CN}(E^*, J, \Pi)$ had been calculated in the meantime via a DWBA model by B. Back et al. ([Back 74b]), as shown previously in figure 1.19. Hence a Hauser-Feshbach approach of the surrogate method, based on equation 1.53, was used to correct for the $J\Pi$ population mismatch. The branching ratios for fission $G_f^{CN}(E^*, J, \Pi)$ were obtained using a statistical model to

reproduce the measured decay probabilities $P_f^{CN}(E^*)$. The use of realistic angular momentum and parity distributions for the entrance channel and the update of the optical model calculations allowed the authors to considerably improve the results. Only 20% of discrepancies with neutron-induced data were found at the lowest energies. Unfortunately, the population probabilities $F^{CN}(E^*, J, \Pi)$ for other surrogate reactions are still unknown. Consequently, no similar Hauser-Feshbach approach of the surrogate method has been applied until now.

In 2007, B. Lyles et al. measured the $^{236}U(n, f)$ cross section by performing the $^{238}U(^3He, \alpha)^{237}U^*$ reaction ([Lyles 07]). A 42 MeV ^3He-beam from the 88 Inch Cyclotron at Lawrence Berkeley National Laboratory was employed. Scattered α-particles were detected at forward angles using a $\triangle E - E_1 - E_2$ segmented detector ring called STARS (Silicon Telescope Array for Reaction Studies [Bernstein 05]). The obtained surrogate data are given in figure 2.2, the right part focuses on the low-energy region. The shape of the obtained cross section derived using the absolute surrogate technique trends within a factor 2 with direct measurements (represented by the recent evaluations of the library ENDF/B-VII) below 1.5 MeV. As shown on the right panel, the surrogate data were found to be sensitive to the detection angle of the ejectiles. The authors interpreted this angular dependence as a signature of the breakdown of the Weisskopf-Ewing approximation in this energy range. Note that according to the theoretical investigation of the surrogate method presented in section 1.6.2, a higher angular momentum sensibility is expected for doubly-even nuclei. A better agreement is found from 1.5 MeV to 3.3 MeV, above 3.3 MeV the data are spoiled by target contamination.
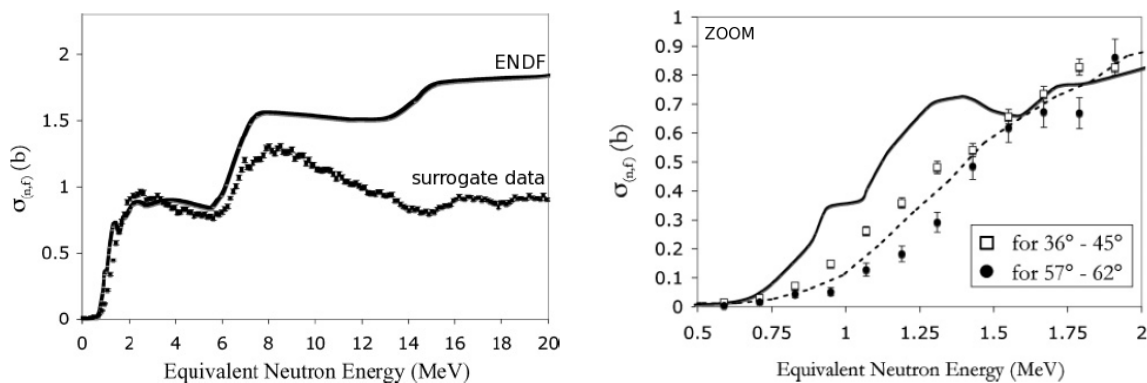
Figure 2.2: $^{236}U(n, f)$ cross section obtained from an ASM analysis (left). The low neutron-energy range is zoomed on the right part. [Lyles 07]

More recently, the CENBG collaboration performed a surrogate experiment to determine neutron-induced fission cross sections of $^{242,243}Cm$ and ^{241}Am via the ^3He-induced reactions $^{243}Am(^3He, df)^{244}Cm^*$, $^{243}Am(^3He, tf)^{243}Cm^*$ and $^{243}Am(^3He, \alpha f)^{242}Am^*$, respectively ([Kessedjian 10]). The experimental set-up, described in figure 2.3, was very similar to the one used previously for the $^{231,232,233}Pa$ and ^{232}Th fission measurements. As shown on the left part of figure 2.4, the results for $^{241}Am(n, f)$ are in very good agreement with those obtained in the neutron-induced measurements. The middle part shows the neutron-induced fission cross-sections of the doubly-even ^{242}Cm. The resulting fission cross section is found to be in excellent agreement at the fission threshold with the neutron-induced data of Vorotnikov et al. On the right part, the CENBG results for $^{243}Cm(n, f)$ are in good agreement with neutron-induced data up to about 0,7 MeV. Above this value, the CENBG data are well below those of Fursov. As explained in [Kessedjian 10], a detailed analysis shows that Fursov's data clearly over-predict this cross section. The general good agreement observed at the lowest neutron energies for these three nuclei indicates that the spin induced in the transfer reactions used was not so high and that the excitation energy of the decaying nuclei was high enough for the branching ratios to be insensitive to possible spin-parity differences. We will further comment these results in chapter 6.
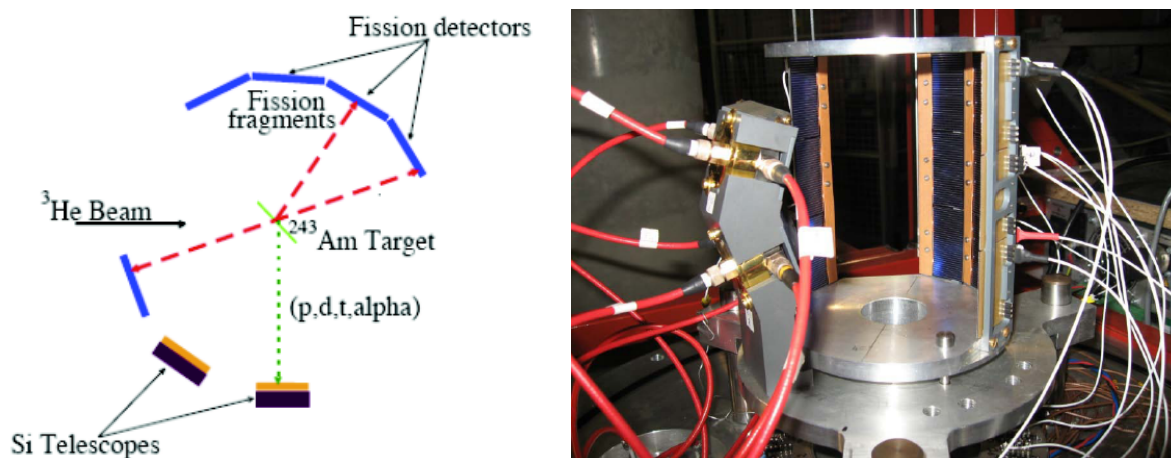
Figure 2.3: Top-view of the CENBG set-up for fission probability measurements.
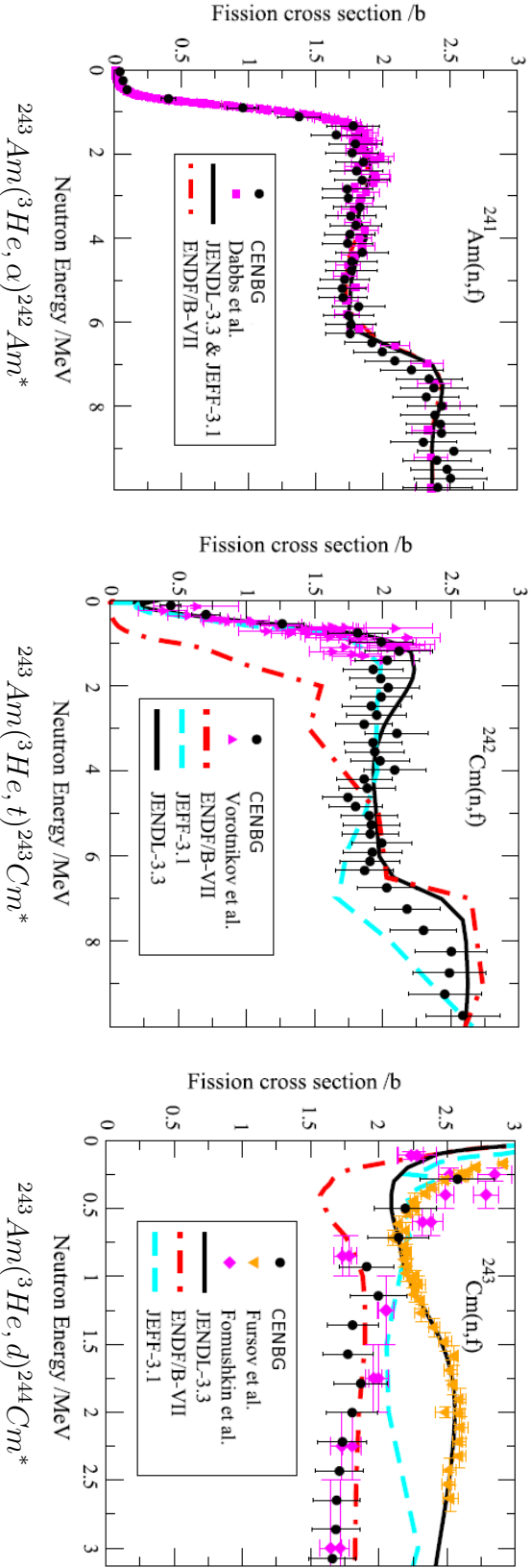
Figure 2.4: Fission cross sections for ^{241}Am, ^{242}Cm and ^{243}Cm as a function of neutron energy compared with neutron-induced data and the evaluations from several international libraries. The corresponding surrogate reaction is indicated below each diagram.([Kessedjian 10])

2.1.2 The surrogate method applied to radiative capture

Compared to fission, capture reactions are more sensitive to the differences between the spin-parity distributions. The reason is that the excitation energy range considered is lower than for fission. Moreover, radiative capture cross sections are expected to decrease very quickly. In the energy region where the radiative capture probability only represents few % of the decay, any variation of few % due to the spin-parity mismatch represents in relative several factors. In addition, fission probabilities are relatively easy to measure, due to the strong signature provided by the production of two fission fragments. However, capture probabilities are more difficult to measure. Firstly, one has to discriminate between capture and inelastic γ-rays coming from the residual nuclei after neutron emission. In addition, in the case of actinides above the fission threshold, one needs to distinguish between γ-rays originating from the nucleus of interest and from the fission fragments. It is also not evident to determine the detection efficiency for a radiative capture event. For all these experimental reasons, only few measurements have been done up to now applying the surrogate method to radiative capture.

In fact, the first one was done by the CENBG collaboration and results were published in 2006 ([Boyer 06]). The γ-ray emission probability of $^{234}Pa^*$ was measured using the transfer reaction $^{232}Th(^{3}He, p\gamma)^{234}Pa^*$ at an incident ^{3}He energy of 24 MeV. The experimental set-up was made of four liquid scintillator C_6D_6 detectors and four silicon telescopes arranged to detect γ rays and charged particles in coincidence. The silicon detectors were placed at backward angles (see figure 2.5). The total number of γ-ray cascades emitted by a given compound-nucleus was obtained via the total-energy detection principle coupled to the weighting function technique. This technique is also used in our work and will be described in detail later. Figure 2.6 gives the obtained $^{233}Pa(n, \gamma)$ capture cross section in the neutron-energy range from 0 to 1 MeV. We compared the obtained $^{233}Pa(n, \gamma)$ cross section with recent evaluations. According to us, the surrogate data are likely to be overestimated, perhaps by as much as a factor of 2. Unfortunately, no direct data exist for $^{233}Pa(n, \gamma)$ and the validity of the surrogate reaction method applied to radiative capture could not be checked.

In 2006, L. Bernstein et al. used the $(\alpha, \alpha'\gamma)$ inelastic scattering as surrogate reaction to infer $^{237}U(n, \gamma)$ cross sections (see Refs. [Bernstein 06] and [Browne 07]). Uranium targets were bombarded with 55 MeV α-particles from the 88-Inch Cyclotron at the Lawrence Berkeley National Laboratory. The ejectiles were detected at forward angles with STARS. The γ-ray detection array is called Livermore-Berkeley Array for Collaborative Experiments (LiBerACE). It consists of five clover-type high purity germanium ($HPGe$) detectors with bismuth-germanate-oxide (BGO) Compton-suppression shields. The experimental set-up is shown in figure 2.7. Here the capture probabilities were deduced from characteristic low-lying γ-ray transitions from the ground-state band of the compound-nucleus. The $^{237}U(n, \gamma)$ cross section deduced using a ASM analysis is
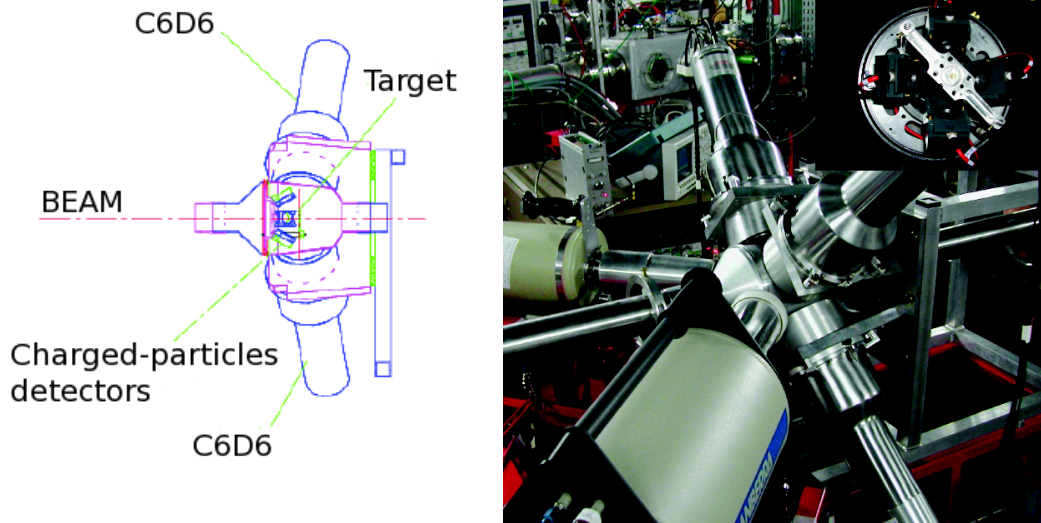
Figure 2.5: Layout of the experimental set-up at the IPN Orsay for the measurement of the ^{233}Pa γ-decay probability. The Germanium detectors were used for C_6D_6 calibration only. ([Boyer 06])
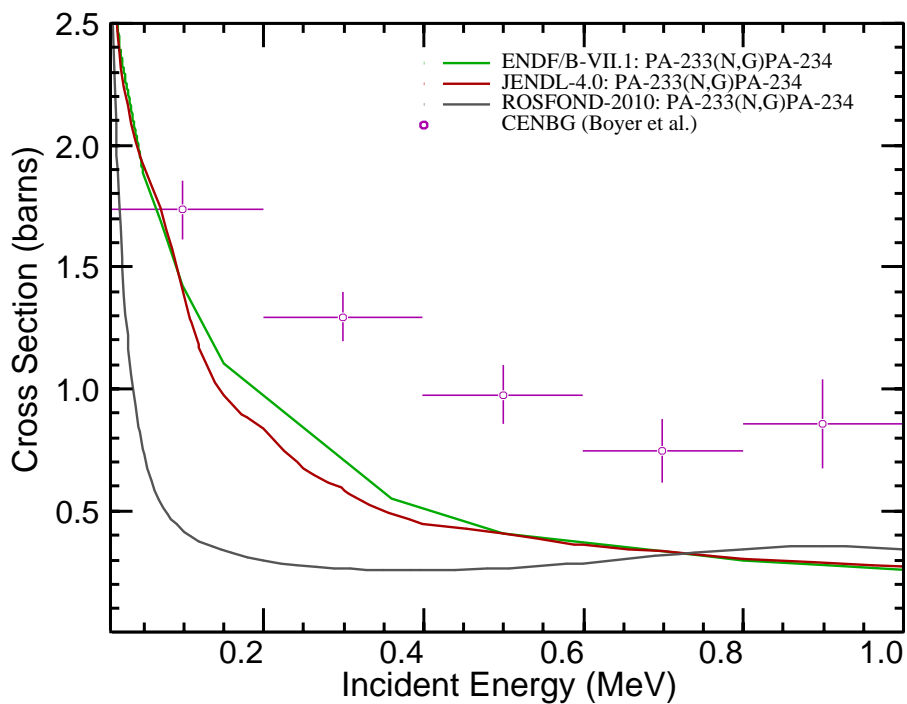
Figure 2.6: Neutron-induced radiative capture cross section of ^{233}Pa compared with the evaluations from several international libraries. ([Boyer 06])

presented in figure 2.8. The surrogate data appear to be about a factor of 2-4 too high. The observed discrepancies could be due to a mismatch of the spin distributions associated to the surrogate and the neutron-induced reactions. We should stress that this work remains unpublished for unknown reasons.
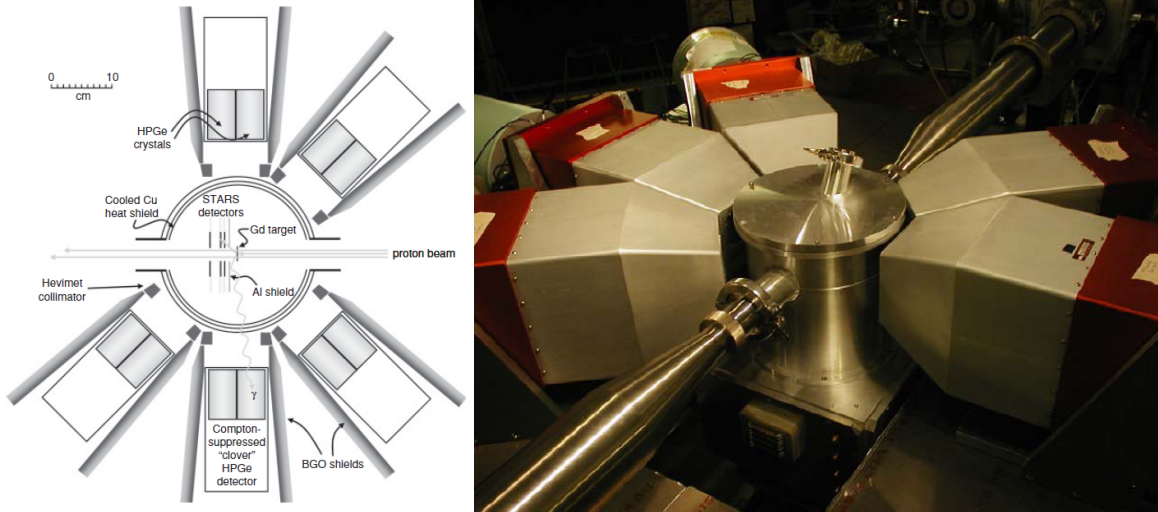
Figure 2.7: Layout of the experimental STARS/LiBerACE set-up. A picture of the *Ge* clovers is shown on the right. [Scielzo 10]
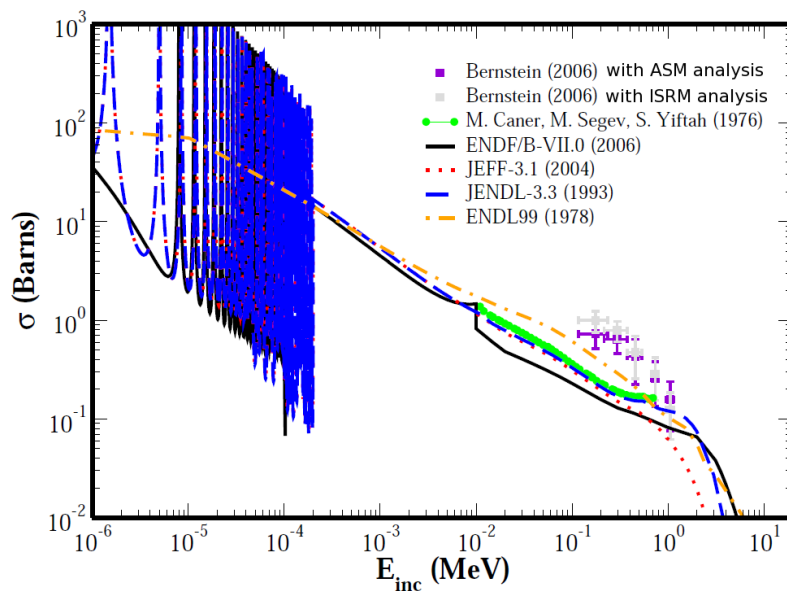
Figure 2.8: Radiative capture cross section for ^{237}U compared to existing neutron-induced data and to various predictions.[Bernstein 06]

In 2010, N. Scielzo et al. used the $(p, p'\gamma)$ inelastic scattering as surrogate reaction to infer $^{153,155,157}Gd(n,\gamma)$ cross sections ([Scielzo 10]). Gadolinium targets were bombarded with 22 MeV protons from the 88-Inch Cyclotron at the Lawrence Berkeley National Laboratory. The experimental set-up is the same as the one used by Bernstein et al. To detect the γ-rays in coincidence with scattered protons, the self-supporting $^{154,156,158}Gd$ targets were surrounded by the LiBerACE array. The obtained γ-decay probabilities yielded $^{155,157}Gd(n,\gamma)$ cross sections that were over-estimated by a factor of three with respect to the directly-measured cross section. Results are given in figure 2.9. To investigate the origin of such discrepancies, the authors performed several Hauser-Feshbach calculations for schematic spin-parity distributions representing possible (p, p') population probabilities $F_{(p,p')}^{CN}(E^*, J, \Pi)$. The characteristics of the Gaussian distributions used as $F_{(p,p')}^{CN}(E^*, J, \Pi)$ are given in table 2.1. The calculated cross sections for these distributions are compared to the surrogate data in figure 2.9. The first distribution centered on 2 $\hbar$ gives the best agreement with the neutron-induced data, whereas the other distributions centered on 5 and 8 $\hbar$ tend to reproduce the surrogate data. Therefore, it was deduced that the average spin populated in the (p, p') reaction is several times higher than the one populated in the neutron-induced reaction. We will come back to these important results later in chapter 6.

Spin distribution	$\overline{J}$	σ
1	2 $\hbar$	1.7 $\hbar$
2	5 $\hbar$	1.7 $\hbar$
3	8 $\hbar$	1.7 $\hbar$

Table 2.1: Mean value of J and standard deviation of the Gaussian distributions representing possible $F_{(p,p')}^{CN}(E^*, J, \Pi)$ in [Scielzo 10].

The radiative capture probability of ^{233}Th was determined with a method similar to the one used by CENBG ([Boyer 06]) using the CACTUS array at the Oslo Cyclotron Laboratory. The CACTUS array is made of 28 NaI γ-ray detectors, which intercept a solid angle of 15% of 4π (see Ref. [Guttormsen 90]). Charged-particle ejectiles were detected with eight segmented particle telescopes, each consisting of a front Si E detector and a back $Si(Li)$ E detector with thicknesses 140 and 3000 μm, respectively, placed at 128-142° with respect to the beam direction. The total-energy detection principle with the weighting function technique was used and the inelastic channel contribution was suppressed by putting a γ-detection threshold. Pictures of the experimental array are given in figure 2.10 and the obtained cross section is shown in figure 2.11. Important discrepancies with neutron-induced data have been found at low energy (below 500 keV). The observed discrepancies could be due to differences between the spin distribution of the (d, p) reaction and the one populated in the neutron-induced reaction. Nevertheless, above 500 keV a nice agreement is shown. This indicates that at these energies the differences in the populated spin distribution are smaller. Indeed, TALYS calculations
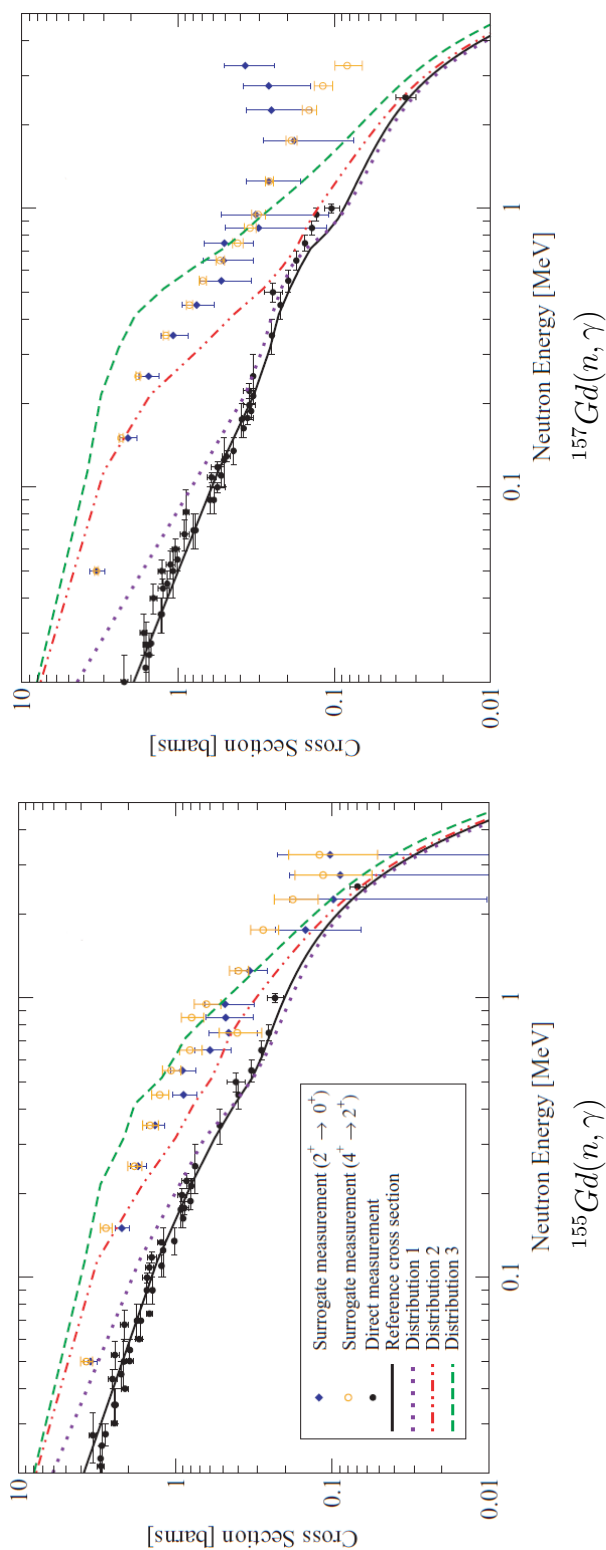
Figure 2.9: Cross sections obtained from (p, p') surrogate data (blue diamonds) are compared to direct measurements (black circles) and Hauser-Feshbach calculations (black solid lines) using the three spin-parity distributions defined in table 2.1. [Scielzo 10]

for $^{232}Th(n,\gamma)$ predict a spin distribution centered on 1 $\hbar$ with E_n=500 keV whereas Back et al. ([Back 74b], $\theta_{ejectile} = 90°$) and Hatarik et al. ([Hatarik 10], $\theta_{ejectile} = 44 - 77°$) predict an angular momentum distribution centered on 3 $\hbar$ for the (d,p) reaction.
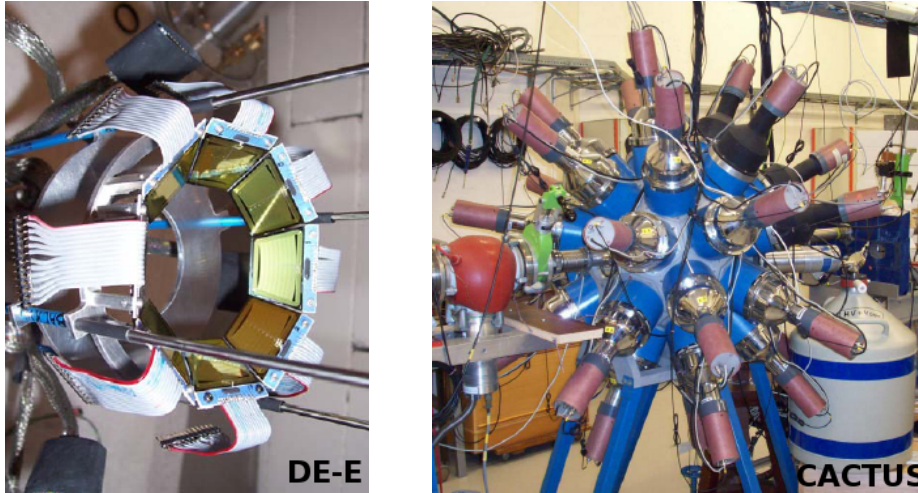
Figure 2.10: Experimental set-up used at the Oslo Cyclotron Laboratory to infer the ^{233}Th capture probability with the $^{232}Th(d,p)$ reaction.
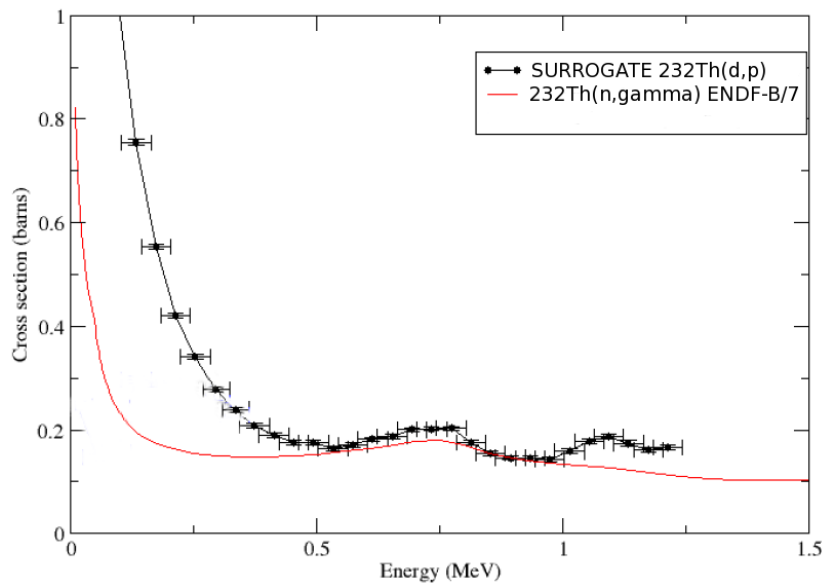
Figure 2.11: Cross sections for $^{232}Th(n,\gamma)$ obtained via the $^{232}Th(d,p)^{233}Th^*$ reaction compared to the ENDF-VII.0 evaluation. [Wilson 11]

2.2 The surrogate ratio approach

In 2005, a variation of the absolute surrogate method was developed by Plettner et al. to avoid the problem of contaminants in the singles spectrum ([Plettner 05]). We recall that the SRM principle has been introduced in section 1.7. In particular, eq. 1.71 relates the ratio of two neutron-induced cross sections to a ratio of measured decay probabilities from two surrogate reactions. Note that the SRM assumes the Weisskopf-Ewing approximation. By coupling eq. 1.71 with eq. 2.1 we have:

$$\frac{\sigma_{n,\chi}^{AX}(E_n)}{\sigma_{n,\chi}^{BY}(E_n)} = \frac{\sigma_{CN}^{A+1X^*}(E_n)}{\sigma_{CN}^{B+1Y^*}(E_n)} \cdot \frac{\frac{N_{coinc}^{A+1X^*}}{N_{single}^{A+1X^*} \cdot \epsilon_1}}{\frac{N_{coinc}^{B+1Y^*}}{N_{single}^{B+1Y^*} \cdot \epsilon_2}} \tag{2.2}$$

The latter equation can be considerably simplified if the following assumptions are valid:

- The two surrogate measurements are done under the same experimental conditions and both efficiencies are similar ($\epsilon_1 = \epsilon_2$).

- The two surrogate measurements involve neighbouring target nuclei and consequently one considers also that the compound-nucleus formation cross sections for $^{A+1}X^*$ and $^{B+1}Y^*$ are very close.

It is convenient to introduce an excitation-energy-independent factor F_{norm} :

$$F_{norm} = \frac{N_{single}^{B+1Y^*}}{N_{single}^{A+1X^*}} \tag{2.3}$$

This factor includes the cross sections for the transfer reactions, target thickness, beam intensity and the irradiation times. The factor F_{norm} can be estimated experimentally by comparison of the singles spectra in a E^* region free from contaminants. The final expression of a neutron-induced cross section obtained in SRM is:

$$\frac{\sigma_{n,\chi}^{AX}(E_n)}{\sigma_{n,\chi}^{BY}(E_n)} = \left[\frac{N_{coinc}^{A+1X^*}}{N_{coinc}^{B+1Y^*}} \cdot F_{norm} \right] \tag{2.4}$$

The advantage of this normalization is that it removes the need to measure the total number of single events N_{single}, which eliminates an important source of systematic uncertainty due to the effects of light contaminants, such as target backing materials and impurities. This is true for fission reactions. Note, however, that for radiative capture reactions the light contaminants may also emit γ-rays and spoil also the quantity N_{coinc}. In practice, the experiments required for a ratio analysis are simpler than those that need to be carried out with the ASM. However, the SRM requires one of the cross sections to be known in order to infer the desired one. As mentioned before, theoretical investigations

have shown that, under certain conditions, the ratio approach could also reduce the effect of spin-parity mismatch in the entrance channel. For this to be valid, the two involved reactions should be sufficiently similar; i.e., the projectile–ejectile combination should be the same and the compound nuclei should be close enough in A and Z to have similar properties. This implies severe limitations when one is interested in a region dominated by radioactive nuclei, such as minor actinide isotopes, for which, both, neutron-induced cross sections and targets are rather scarce.

There are three variants of the SRM:

- the external SRM (ESRM), where the same surrogate reaction is performed on two neighbouring nuclei. This is the variant that has been explained above with eq. 2.4. In this case, the compound-nucleus formation cross sections for the two compound nuclei are very similar. The advantage to proceed with the same surrogate reaction is to transfer similar angular momentum in both reactions. Nevertheless, the ESRM may be sensitive to nuclear-structure differences between the two target nuclei. Almost all applications of the SRM are based on the ESRM.

- the internal SRM (ISRM), where the particularity is to measure simultaneously two exit-channel probabilities of the same CN, e.g. capture and fission. The idea is to infer the radiative capture cross section with the known fission cross section. In this case, one should stress that the efficiency terms do not cancel in equation 2.2. The determination of the experimental detection efficiencies is therefore needed.

- the hybrid SRM (HSRM), where two different surrogate reactions are performed on the same target nucleus. This supposes similar spin-parity distributions populated in both reactions. However, the cross sections for the transfer reactions are expected to be different. Consequently, the factor F_{norm} cannot be deduced: the determination of the total number of reactions events N_{CN} in the two reactions is needed. Actually, the HSRM corresponds to applying two times the absolute surrogate method and normalizing the desired cross section with the reference one. One assumes that the deviations obtained between the surrogate results and the neutron-induced reactions for the well-known cross-section will be the same as the deviations of the unknown reaction.

The next sections present a review of the experimental results obtained with the surrogate ratio method.

2.2.1 The external surrogate ratio method (ESRM)

2.2.1.1 ESRM applied to fission

As mentioned before, in 2005, the first SRM experiment was leaded by Plettner et al. ([Plettner 05]). The $^{236}U(d,pf)^{237}U^*$ and $^{238}U(d,pf)^{239}U^*$ reactions served as surrogates for the well known $^{236}U(n,f)$ and $^{238}U(n,f)$ cross sections, respectively. Deuterium beams of 24 and 32 MeV energy were delivered by the ESTU tandem accelerator of Yale University. Ejectiles were identified using the STARS set-up (already mentioned) at forward angles. Fission fragments were detected in coincidence with a silicon detector. As shown in figure 2.12, a comparison of the surrogate ratio $\frac{^{236}U(d,pf)}{^{238}U(d,pf)}$ with the ratio $\frac{^{236}U(n,f)}{^{238}U(n,f)}$ showed a good agreement over a wide range of excitation energy, giving confidence in the ESRM. The $^{236}U(d,d'f)^{236}U^*$ and $^{238}U(d,d'f)^{238}U^*$ reactions were consequently used to determine the unknown $^{237}U(n,f)$ cross sections relative to the reference $^{235}U(n,f)$ cross section. The obtained ratio $\frac{^{238}U(d,d'f)}{^{236}U(d,d'f)}$ was compared to the low-energy surrogate data originating from the (t,pf) reaction ([Britt 79],[Younes 03a]) and a theoretical estimate based on an extrapolation of the same surrogate data ([Younes 03c]). As shown in figure 2.12, the comparison showed a relative good agreement over a wide range of excitation energy.
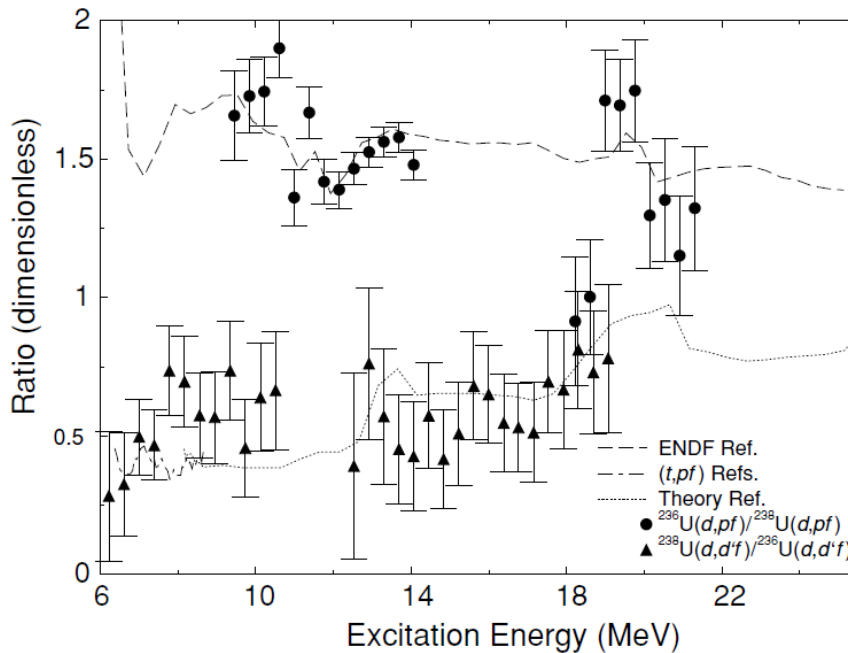
Figure 2.12: Fission probability ratios for the (d,pf) and $(d,d'f)$ reactions on ^{238}U and ^{236}U targets as a function of the excitation energy of the associated CN. Existing data and theoretical estimates are also indicated. [Plettner 05]

One year later, J. Burke et al. ([Burke 06]) employed a 55 MeV α-beam from the 88-inch cyclotron at the Lawrence Berkeley National Laboratory to induce fission via the following reactions: $^{238}U(\alpha, \alpha' f)^{238}U^*$ and $^{236}U(\alpha, \alpha' f)^{236}U^*$. The reaction on ^{238}U was a surrogate for $^{237}U(n, f)$, and the one on ^{236}U was used as a surrogate for $^{235}U(n, f)$. Scattered α-particles were detected using STARS at forward angles (35° to 60° with respect to the beam axis). The fission fragments were detected in a silicon detector located at backward angles (between 106° and 131°). The authors determined the $^{237}U(n, f)$ cross section in the following way:

- The energy scale for the $^{235}U(n, f)$ cross section was converted to excitation energy by adding the ^{236}U neutron separation energy (S_n =6544.5 keV).

- The product of the $\frac{^{238}U(\alpha, \alpha' f)}{^{236}U(\alpha, \alpha' f)}$ ratio and the shifted $^{235}U(n, f)$ spectrum yielded the $^{237}U(n, f)$ spectrum as a function of excitation energy.

- The $^{237}U(n, f)$ energy scale was shifted back by subtracting the ^{238}U neutron separation energy (S_n =6152.0 MeV) to obtain the $^{237}U(n, f)$ cross section at the appropriate neutron energy.

Figure 2.13 shows the nice agreement between the obtained $^{237}U(n, f)$ cross sections determined using the ratio approach and evaluated data by Younes et al. ([Younes 05]).
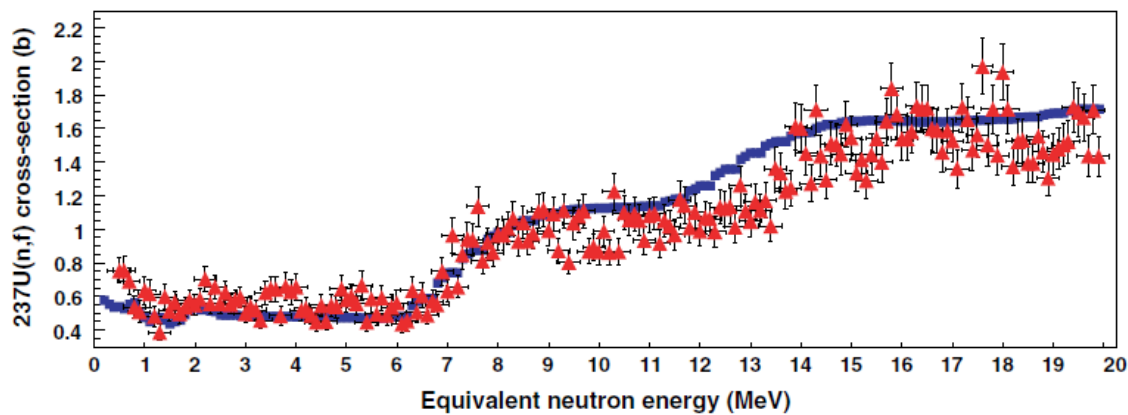
Figure 2.13: $^{237}U(n, f)$ cross section obtained with the SRM (red triangles) compared to theoretical estimates proposed by Younes et al. (blue squares, no error bars). [Burke 06]

The theoretical investigations of the SRM that have been detailed in section 1.7.1 were motivated by the latter experiments. Under the condition that the two involved reactions are sufficiently similar ([Escher 06]), the SRM is found to minimize uncertainties arising from pre-equilibrium decay and angular momentum effects. Note that, in the two previous experiments, the involved target nuclei have similar mass, deformation

and nuclear structure with equal GS spin and parity. If the angular momentum effects impact both reactions in a similar manner, their effects are expected to approximately cancel in the ratio method. However, if the two involved reactions are not sufficiently similar, the discrepancies may be enhanced.

In 2007, B. Lyles et al. applied the ESRM to determine the $^{236}U(n, f)$ cross section ([Lyles 07]). The $^{235}U(^3He, \alpha f)^{234}U^*$ and $^{238}U(^3He, \alpha f)^{237}U^*$ reactions were used as surrogates for $^{233}U(n, f)$ and $^{236}U(n, f)$, respectively. The ESRM was used to determine the $^{236}U(n, f)$ cross section. The results are compared to directly measured cross sections in figure 2.14. The SRM $^{236}U(n, f)$ cross section is consistent with evaluations from 3.5 to 20 MeV, but significant deviations are observed below 3.5 MeV. The discrepancies at low energy can be explained by the different nuclear structure of the two involved target nuclei ^{235}U $(GS = 7/2^-)$ and ^{238}U $(GS = 0^+)$. Moreover, we recall that the cross section for $^{236}U(n, f)$ determined via the ASM was found to be below the neutron-induced data for $E_n < 1.5$ MeV (cf figure 2.2). According to us, the cross sections for $^{233}U(n, f)$ obtained via the absolute surrogate measurement could be very useful to understand the origin of such discrepancies. Unfortunately, these data were not shown in [Lyles 07].

A similar ESRM experiment was done in 2009 by B. Goldblum et al. by performing a $(^3He, \alpha)$ reaction on targets of ^{232}Th and ^{236}U ([Goldblum 09]). The $^{232}Th(^3He, \alpha f)^{231}Th^*$ and $^{236}U(^3He, \alpha f)^{235}U^*$ were surrogates for $^{230}Th(n, f)$ and $^{234}U(n, f)$, respectively. Above 1.5 MeV, the shape of the $^{230}Th(n, f)$ cross section obtained using ESRM trends nicely with direct measurements. At low energies, important discrepancies are observed. Note also that low-energy resonances near 700 keV, 1.2 MeV, and 1.8 MeV observed in the Meadows and Muir data are not resolved in the surrogate measurement. Results are shown in figure 2.15.

Recently, Lesher et al. compared the surrogate fission-probability ratio $^{234}U(\alpha, \alpha' f)$ over $^{236}U(\alpha, \alpha' f)$ with the ratio of cross sections $^{233}U(n, f)$ over $^{235}U(n, f)$ ([Lesher 09]). The measured fission-probability ratio $\frac{P^{234U}_{(\alpha, \alpha' f)}}{P^{236U}_{(\alpha, \alpha' f)}}$ was compared with the corresponding ENDF cross section ratio in figure 2.16. These ratios were found to be in agreement above 1 MeV. Below this limit, the observed deviations of about 20% below 1 MeV are possibly the result of the Weisskopf-Ewing approximation not being satisfied. This work had the particularity to be related to two well-known cross sections. Moreover, the same ratio was studied within the theoretical investigations of J. Escher et al. ([Escher 06]). Comparison between theory and experiment provides evidence that the SRM reduces angular momentum effects in this case.

Very recently, Ressler et al. measured the $^{238}Pu(n, f)$ cross section using $^{239}Pu(\alpha, \alpha' f)$ $^{239}Pu^*$ as surrogate ([Ressler 11]). In this work the ratio analysis was made with two different reference fission cross sections $^{234}U(n, f)$ and $^{235}U(n, f)$, where the surrogate reactions used were $^{235}U(\alpha, \alpha' f)^{235}U^*$ and $^{236}U(\alpha, \alpha' f)^{236}U^*$. In figure 2.17, one observes
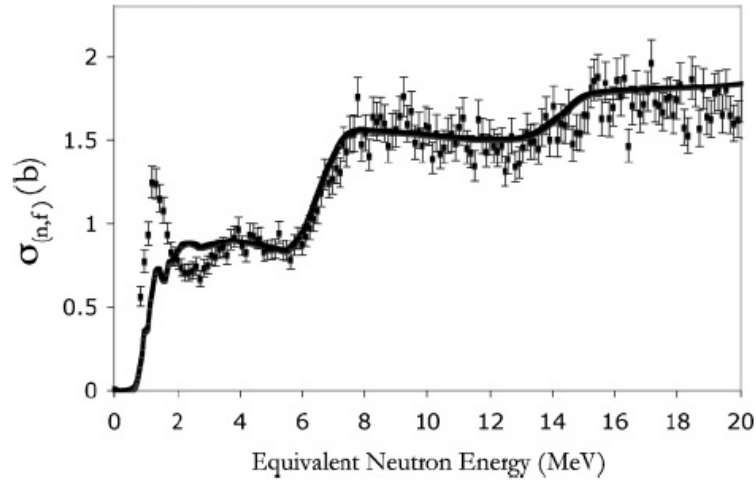
Figure 2.14: $^{236}U(n,f)$ cross section obtained from a ESRM analysis using $^{233}U(n,f)$ as reference cross section and $(^{3}He,\alpha)$ surrogate reactions. The black squares represent the experimental data and the solid line is the ENDF/B-VII evaluation. [Lyles 07]
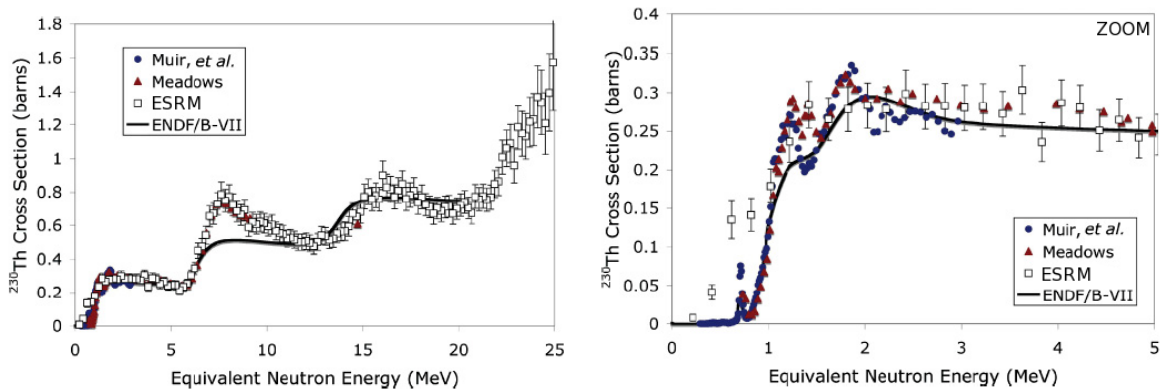
Figure 2.15: $^{230}Th(n,f)$ cross section obtained from a ESRM analysis using $^{235}U(n,f)$ as reference cross section and $(^{3}He,\alpha)$ surrogate reactions. The low neutron-energy range is zoomed on the right part. The squares represent the surrogate data, the coloured circles and triangles are the existing neutron-induced data and the solid line is the ENDF/B-VII evaluation. [Goldblum 09]
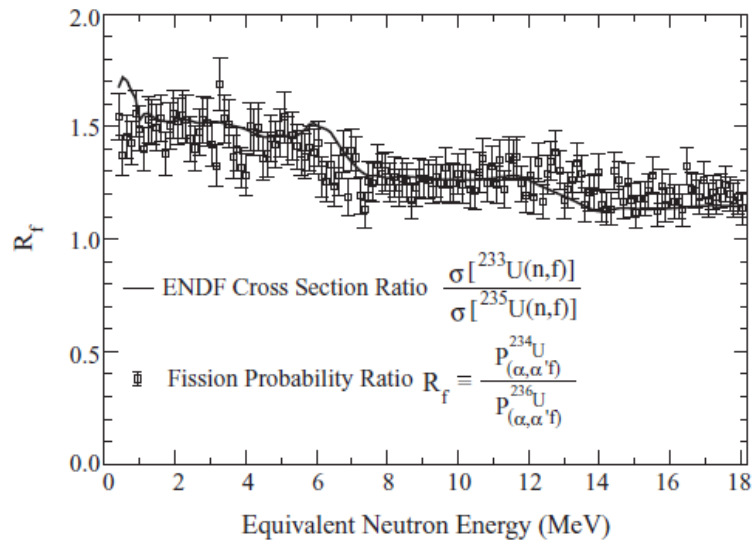
Figure 2.16: Surrogate fission probability ratio $\frac{P^{234U}_{(\alpha,\alpha'f)}}{P^{236U}_{(\alpha,\alpha'f)}}$ compared to the evaluated $\frac{\sigma^{234U}_{(n,f)}}{\sigma^{236U}_{(n,f)}}$ cross section ratio. [Lesher 09]
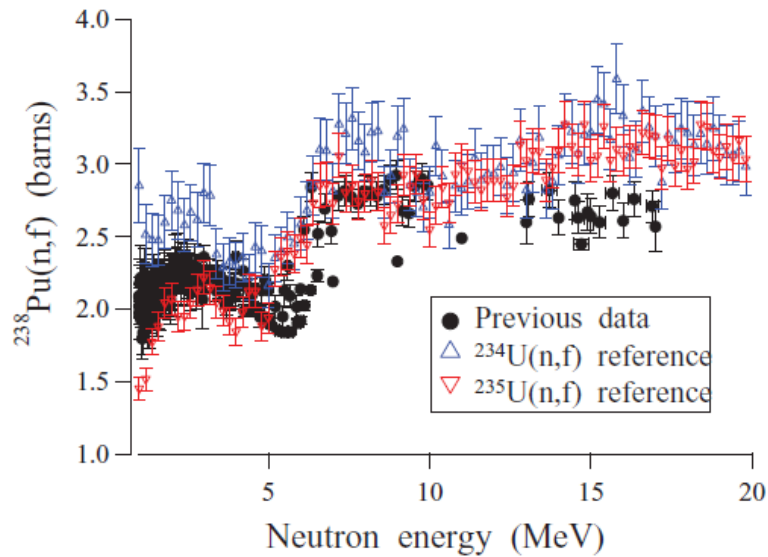
Figure 2.17: Neutron-induced fission cross sections of ^{238}Pu using two (α, α') surrogate ratio measurements (relative to $^{234}U(n,f)$ and $^{235}U(n,f)$) compared to neutron-induced data. [Ressler 11]

at lowest energies deviations of the measured SRM cross sections for $^{238}Pu(n,f)$ with respect to the neutron-induced data depending on the reference used. Angular momentum effects may be responsible for these deviations because of important differences of GS spin and parity in the target nuclei ($\frac{1}{2}^+$ for ^{238}Pu, $\frac{7}{2}^-$ for ^{235}U and 0^+ for ^{234}U). The difference in the neutron-binding energy and the mass of the reference nucleus may also play an important role. Actually, higher-mass Pu isotopes may probably be better to use as reference but such radioactive targets are very difficult to obtain. Nevertheless, this work confirms that for higher neutron energies, the differences in mass and proton number of the reference isotopes do not play a significant role. Note that the over-estimation found at the highest energies is not explained in [Ressler 11].

2.2.1.2 ESRM applied to radiative capture

In [Goldblum 08], an experimental set-up close to the one used by the CENBG ([Boyer 06]) was used to determine (n,γ) cross sections via the ESRM. The $^{170}Yb(n,\gamma)$ cross section in the neutron energy range of 165-465 keV was inferred from the experimental γ-decay probabilities of $^{171}Yb^*$ and $^{161}Dy^*$. Two types of surrogate reactions were used:

- $^{171}Yb(^3He,^3He'\gamma)$ relative to $^{160}Dy(n,\gamma)$ via $^{161}Dy(^3He,^3He'\gamma)$ and,

- $^{172}Yb(^3He,\alpha\gamma)$ relative to $^{160}Dy(n,\gamma)$ via $^{162}Dy(^3He,\alpha\gamma)$.

According to the authors, the inelastic-scattering $(^3He,^3He'\gamma)$ mode has a tendency to populate low-lying collective states (such as the ones of the ground-state rotational band) and compound-nuclear resonances, whereas single-nucleon pickup processes $(^3He,\alpha\gamma)$ tend to populate states via particle-hole excitations with a wide range of spins. For us, another important aspect is the difference in the GS spin-parity with respect to the reference nucleus. The $(^3He,^3He'\gamma)$ is performed on even-Z, odd-N targets of ^{171}Yb and ^{161}Dy with GS of $1/2^-$ and $5/2^+$, respectively, while the $(^3He,\alpha\gamma)$ surrogate reaction is performed on even-even targets with $GS = 0^+$. The difference in mass may also be a potential issue between the Yb and Dy isotopes ([Ressler 11]). The results are presented in figure 2.18 and one observes that the surrogate cross section extracted using the $(^3He,^3He'\gamma)$ reaction overlaps within the systematic error with the cross section extracted using the $(^3He,\alpha\gamma)$ reaction, indicating no significant entrance-channel effects. This observation is in contradiction with the theoretical studies of J. Escher et al. ([Escher 06]). In any case, this can not be attributed to the validity of the Weisskopf-Ewing approximation in this low excitation-energy range. The agreement found strongly suggests that the dependence of the γ-decay probabilities on angular momentum are at least partially canceled in the surrogate ratio analysis.
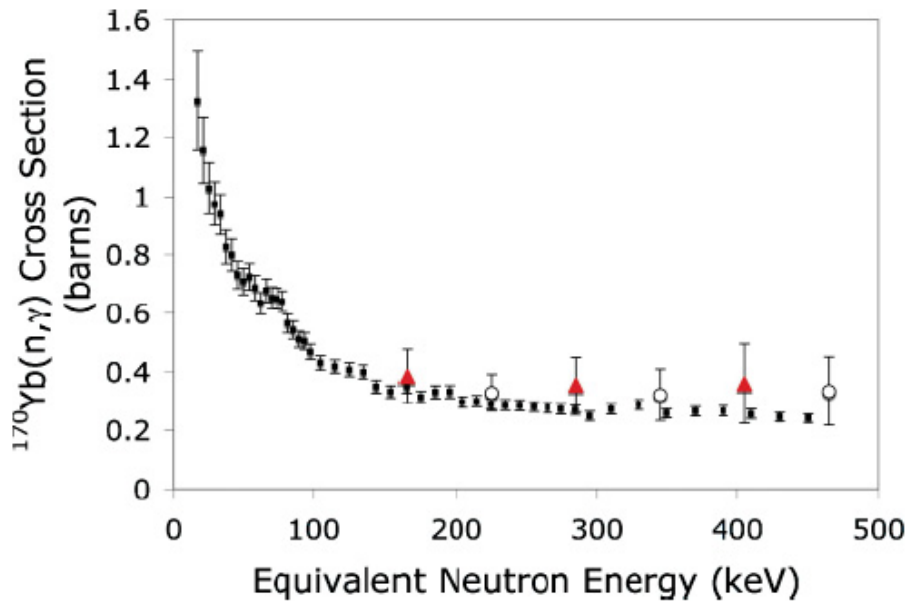
Figure 2.18: $^{170}Yb(n,\gamma)$ cross section as a function of equivalent neutron energy. The results were extracted using the SRM relative to the well known $^{160}Dy(n,\gamma)$ cross section. The data corresponding to the $(^3He,^3He')$ surrogate reaction are represented by the open circles and the ones corresponding to the $(^3He,\alpha)$ reaction by the red triangles. For comparison, the directly measured $^{170}Yb(n,\gamma)$ cross section is denoted by filled squares. [Goldblum 08]

In [Goldblum 10], the same ratio methodology as above was applied to infer capture cross sections for $^{161}Dy(n,\gamma)$ via two different means:

- $^{162}Dy(^3He,^3He'\gamma)$ relative to $^{160}Dy(n,\gamma)$ via $^{161}Dy(^3He,^3He'\gamma)$ and,

- $^{163}Dy(^3He,\alpha\gamma)$ relative to $^{160}Dy(n,\gamma)$ via $^{162}Dy(^3He,\alpha\gamma)$.

In parallel, the same capture cross section was deduced via:

- $^{162}Dy(^3He,^3He'\gamma)$ relative to $^{163}Dy(n,\gamma)$ via $^{164}Dy(3He,3He'\gamma)$.

As shown in the left part of figure 2.19, the ESRM cross section of $^{161}Dy(n,\gamma)$ is given using two different γ-ray energy thresholds, namely 500 keV and 2 MeV. The ESRM $^{161}Dy(n,\gamma)$ cross section was again found to be independent of the type of surrogate reaction employed, within the total uncertainty, indicating as previously no significant entrance-channel effects. The authors applied a 500-keV γ-ray energy threshold to exclude contributions from the $(n,n'\gamma)$ channel up to an equivalent neutron energy of 500 keV. The surrogate data are systematically lower by a factor 2 than the evaluated result. With a 2-MeV γ-ray energy threshold, the $^{161}Dy(n,\gamma)$ surrogate cross section agrees with the evaluation within big uncertainties. Note that the SRM involves in this case dissimilar (in spin and parity) target pairs ($^{161-160}Dy$). With a similar target pair ($^{161-163}Dy$), one may expect to apply the SRM with better confidence. The right part of figure 2.19 shows a better agreement between the surrogate data and the direct measurement. One should stress that the surrogate data with a 500 keV γ-energy threshold was again found to be under-estimated. With application of the 2 MeV threshold, the average deviation between the surrogate and evaluated data was approximately 12%. According to the authors, the agreement is increased by putting a higher gamma threshold because above the pairing gap (which is particularly high for ^{162}Dy and ^{164}Dy, $\triangle = 1,85$ MeV and $\triangle = 1,70$ MeV, respectively). The fraction of γ-decays that proceed through resolved states is diminished or suppressed. Only γ rays from the first-generation statistical cascade (called statistical gamma-rays in literature) are detected and the Weisskopf-Ewing approximation can be applied. According to us, this interpretation needs to be discussed. We will see later how our work can bring a new point of view on these results.

ESRM with $^{160}Dy(n,\gamma)$ ESRM with $^{163}Dy(n,\gamma)$
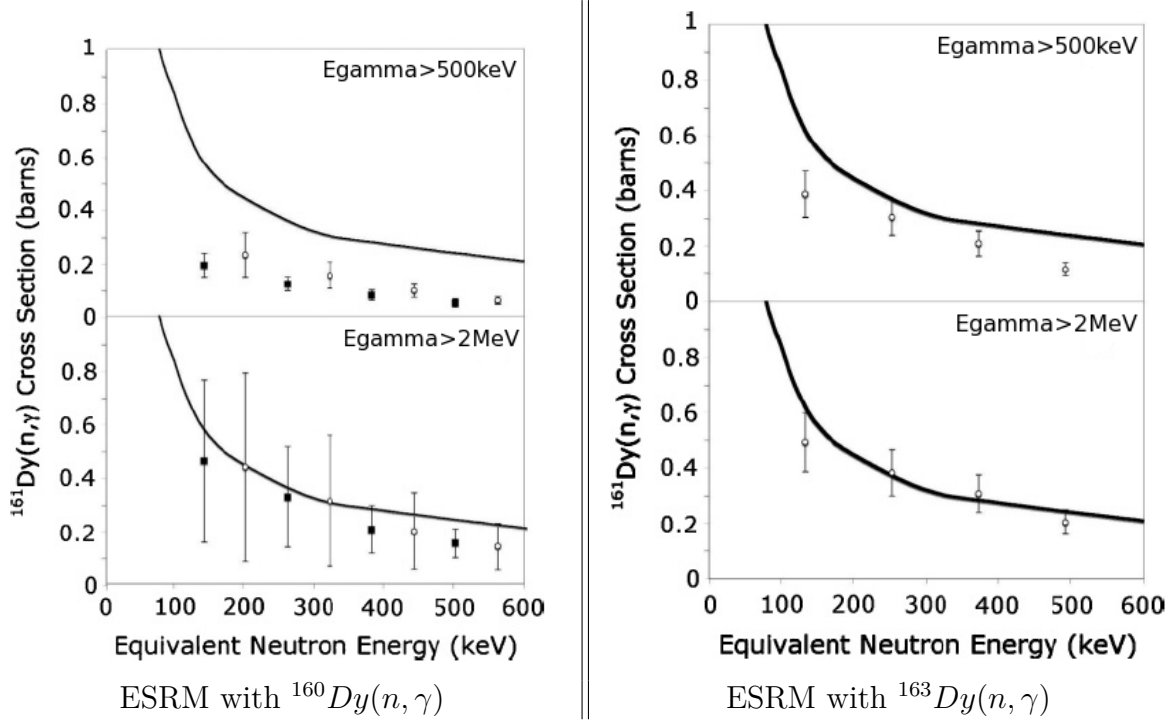
Figure 2.19: $^{161}Dy(n,\gamma)$ cross section extracted using the ESRM with the evaluated $^{160}Dy(n,\gamma)$ and $^{163}Dy(n,\gamma)$ cross sections (ENDF/B-VII.0) as references. The results corresponding to the $(^3He,^3He')$ surrogate reaction are represented by the open circles and the ones corresponding to the $(^3He,\alpha)$ reaction by the solid squares. The evaluated $^{161}Dy(n,\gamma)$ cross section is denoted by solid lines. On the upper part , a γ-ray energy threshold of 500 keV was applied, while a 2 MeV threshold was used for the data shown in the lower part. [Goldblum 10]

Let us now recall the ASM performed by Scielzo et al. ([Scielzo 10]) where (p, p') surrogate reactions were used to infer $^{155,157}Gd(n, \gamma)$ cross sections. As illustrated in figure 2.9, the data and the statistical calculations highlighted the effects of the $J\Pi$ mismatch between the desired and surrogate reactions; discrepancies of the order of a factor of 2 were observed. Since the ^{155}Gd and ^{157}Gd nuclei are structurally very similar (they are well-deformed and both have ground-state spin and parity $\frac{3}{2}^-$), a ESRM was applied. Results are shown in figure 2.20. The cross-section ratios (deduced from the $2^+ \rightarrow 0^+$ and $4^+ \rightarrow 2^+$ transition intensities) are seen to differ from the desired ratio by a factor 2 for energies below about $E_n = 0.7$ MeV. Above this energy, they rapidly converge (within huge error bars) to the reference ratio. Thus, the ratio approach seems to somewhat reduce the effect of the $J\Pi$ mismatch on the extracted cross sections for energies where the WE approximation is not valid ([Scielzo 10]).

Finally, in 2010, $^{171,173}Yb(d, p\gamma)$ reactions were measured by Hatarik et al. using the STARS/LiBerACE array ([Hatarik 10]). In this ESRM application, the capture ratio was deduced from measured ground-state band low-lying transition intensities. In addition, the intensities of the selected γ-ray transitions were simulated using the DICEBOX code. Each simulation was done for an excitation energy of 100 keV above the neutron separation energy, with one simulation for each spin-parity combination from $J\Pi = 0^-$ to $J\Pi = 7^+$. The comparison of the simulation with the observed intensities for the $6^+ \rightarrow 4^+$ and $4^+ \rightarrow 2^+$ transitions indicates that the average angular momentum transferred in the (d, p) reaction is about 3 $\hbar$, whereas neutron capture in the keV region is mostly dominated by s-wave capture (where the average angular momentum is about $\frac{1}{2}$ $\hbar$). To correct for the $J\Pi$ mismatch, the intensity of the $4^+ \rightarrow 2^+$ transition was determined with the $6^+ \rightarrow 4^+$ transition intensity subtracted. According to the authors, subtracting the feeding from the 6^+ state to the 4^+ state will likely select a compound-nuclear $J\Pi$ distribution closer to the one populated by the neutron-induced reaction. Indeed, above 100 keV, the surrogate cross-section ratios deduced from the $^{171,173}Yb(d, p\gamma)$ measurements agree with the neutron capture results within 15% (see figure 2.21). Note that the studies of the (d, p) reactions are of interest for the use of the surrogate method using inverse kinematics.

74
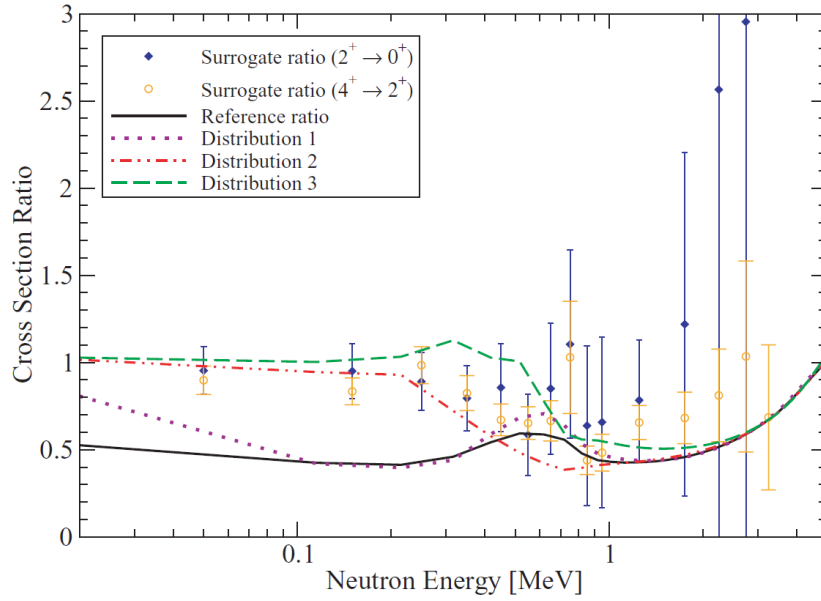
Figure 2.20: Ratio of $^{157}Gd(n,\gamma)$ and $^{155}Gd(n,\gamma)$ cross sections compared to the ratio of the reference cross sections (black solid line). Also shown are the ratios of the calculated probabilities for the distributions given in table 2.1. [Scielzo 10]
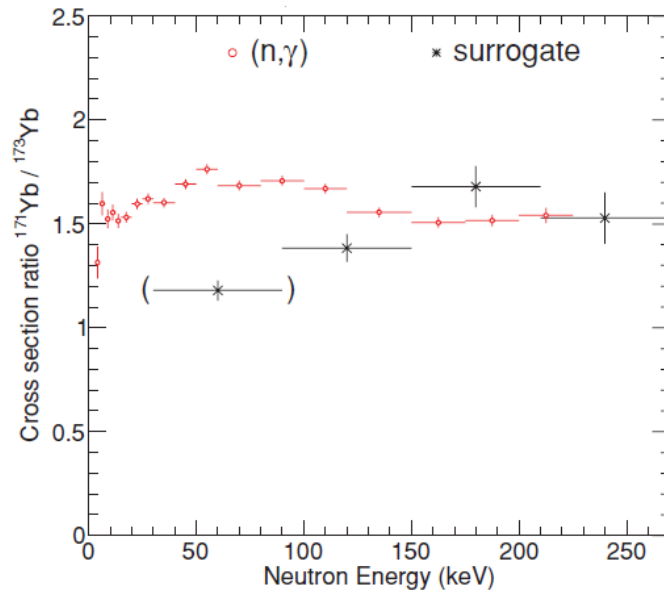
Figure 2.21: Comparison of the cross-section ratio obtained in neutron-induced reactions with the results from $(d,p\gamma)$ measurements using the $4^+ \to 2^+$ transition intensity with the $6^+ \to 4^+$ transition intensity subtracted. [Hatarik 10]

2.2.2 The internal surrogate ratio approach

In the internal surrogate ratio method (ISRM), for a given surrogate reaction, two exit-channel probabilities (e.g. fission and radiative capture) are measured. In [Allmond 09], the $^{235}U(d,p\gamma)$ and (d,pf) surrogate reactions were used to test the validity of the ISRM by comparing their probability ratios to the known $^{235}U(n,\gamma)$ and (n,f) cross-section ratios. Note that γ yields are inferred from the $1^- \rightarrow 2^+$ low-lying transition intensity in $^{236}U^*$. Results are shown in figure 2.22. The average deviation is 23% for $0.9MeV < E_n < 3.3MeV$.
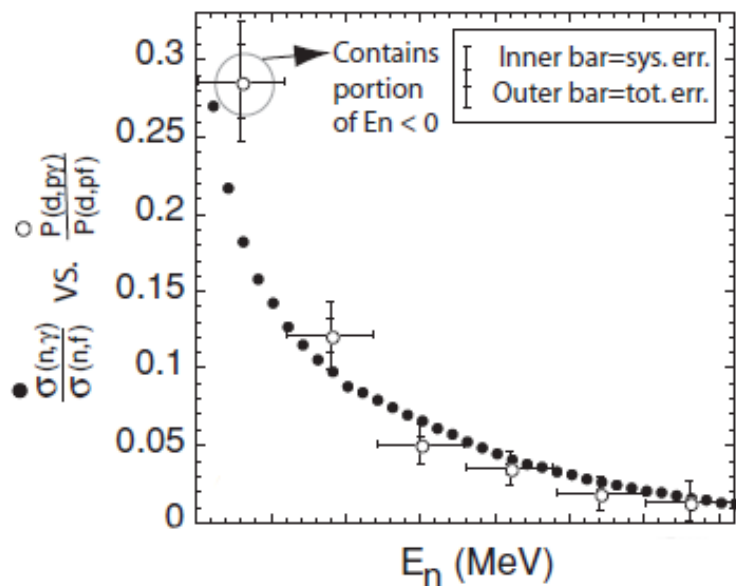
Figure 2.22: ^{235}U probability ratios $\frac{(d,p\gamma)}{(d,pf)}$ (ISRM) compared to the reference ratio $\frac{(n,\gamma)}{(n,f)}$ (given by ENDF) [Allmond 09]

We recall the studies of L. Bernstein et al. and J. Burke et al. relative to the same (α, α') surrogate experiment:

- in Ref. [Bernstein 06], the $^{237}U(n,\gamma)$ was deduced via an ASM analysis.

- in Ref. [Burke 06], the $^{237}U(n,f)$ cross section was determined applying the ESRM with $^{235}U(n,f)$ as reference.

The coupling of both data enables to extract the $^{237}U(n,\gamma)$ cross sections using an «internal ratio» to the fission probability. As illustrated in figure 2.8, the obtained ISRM cross section is found to be lower than the cross section obtained in the ASM analysis. However, the ISRM data are still a factor of 2 too high. We stress again that this work remains unpublished. According to us, a comprehensive theoretical and experimental «benchmarking» of the ISRM remains to be done.

2.2.3 The hybrid surrogate ratio approach (HSRM)

In 2008, the $^{233}Pa(n,f)$ cross section was determined relative to the $^{235}U(n,f)$ cross section by applying the HSRM with the two surrogate reactions $^{232}Th(^6Li,\alpha)^{234}Pa$ and $^{232}Th(^6Li,d)^{236}U$ ([Nayak 08]). Measurements were done at equivalent-neutron energies above 12 MeV where the Weisskopf-Ewing assumption should be valid. However, at these energies, no neutron-induced data are available for comparison. As illustrated in figure 2.23, the HSRM data are in good agreement with a calculation that was adjusted to reproduce M. Petit et al. data ([Petit 04]) at lower energies. According to us, the conditions under which the HSRM will work are very unclear. Firstly, there is still no knowledge on the difference of spin-parity populated in the transfer reactions used. Secondly, the decaying compound nuclei are dissimilar and there is no reason to expect that the deviations with respect to the neutron-induced reactions will be the same for the two surrogate reactions.
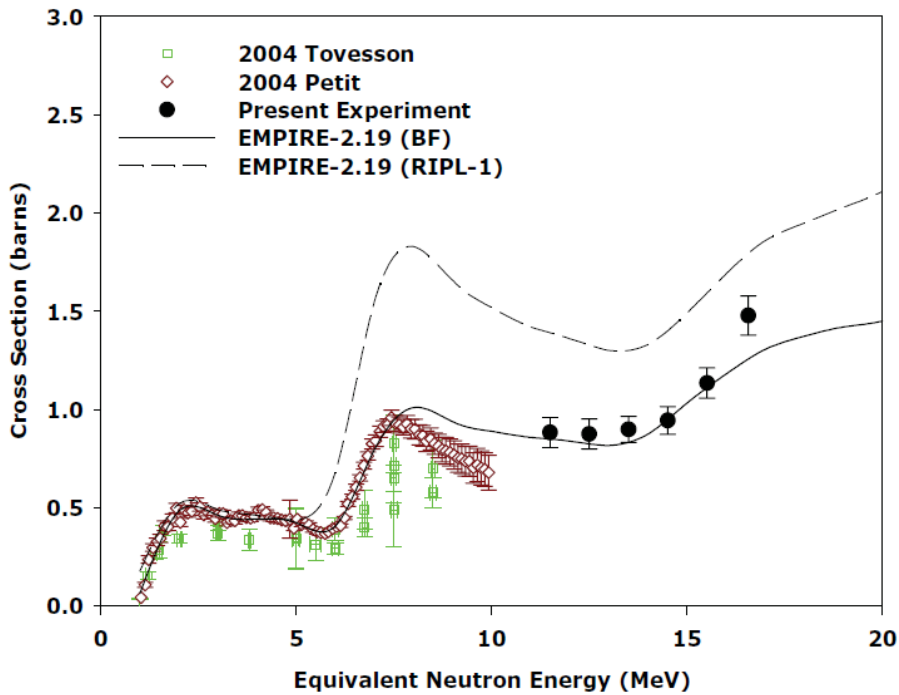
Figure 2.23: Experimental $^{233}Pa(n,f)$ cross section using the HSRM compared to EMPIRE calculations. [Nayak 08]

2.3 Summary and context of our experiment

The state-of-the-art of surrogate experiments is summarized in tables 2.2 and 2.3.

Neutron-induced fission cross sections (n, f) obtained with the absolute surrogate method (ASM) are in general good agreement at the fission threshold with the neutron-induced data. However, in the case of fissile nuclei, an important over-estimation (about 50%) is predicted at low neutron energies, namely $E_n \lesssim 500$ keV. Above this limit, fission cross sections can be extracted within 10-20% uncertainties.

Neutron-induced capture (n, γ) cross sections are very difficult to obtain with the ASM. Moreover, there is a general lack of neutron-induced data and a-posteriori comparison with ASM capture cross sections is often not possible. Since the energy range of interest for radiative capture is located at low excitation energies, theoretical investigations predict that the capture channel is more sensitive to the $J\Pi$ mismatch than fission. One should not forget that radiative capture cross sections are expected to decrease very quickly. In the region where capture only represents few % of the decay, any variation of few % due to the $J\Pi$ mismatch represents in relative several factors. Over-estimations of the neutron-induced capture cross-sections by a factor 3 have been observed recently (see Ref. [Scielzo 10]) using a (p, p') surrogate reaction in the rare-earth region. At the lowest energies important discrepancies have also been observed using the (d, p) reaction in the actinide region but a nice agreement has been obtained above 500 keV neutron energy (see Ref. [Wilson 11]). Therefore, further investigations need to be done.

Initially developed to reduce systematic uncertainties, the «external» SRM (ESRM) is the most commonly used of the SRM variants. Both, calculations and experiments show that the angular momentum effects can be compensated in the SRM. When the two reactions used are sufficiently similar, the spin-parity mismatch could affect both reactions in the same manner. Nevertheless, many ESRM experiments applied to fission are found to fail at the fission threshold (see Refs. [Lyles 07], [Goldblum 09] and [Ressler 11]). The reason is that in some cases, using dissimilar compound nuclei, angular momentum effects are enhanced and the SRM fails. In general, fission cross sections are found to be in good agreement with direct measurements above about 2 MeV. Because of the insensitivity of the ratio to pre-equilibrium effects and to contaminants, ESRM measurements give better results than the ASM from the first-chance fission up to about 12 MeV. Uncertainties are about 5-15%.

The ESRM has also been recently used for the determination of capture cross sections. The results, with certain restrictions on γ detection (transitions and/or energies), tend to show a convergence within 20% with direct data. The Weisskopf-Ewing breakdown observed in the ASM is compensated in the SRM. When the two compound nuclei used

in the ratio are similar enough, the SRM works well above 600 keV neutron energies using a (α, α') reaction for instance (see Ref. [Scielzo 10]). However, in Ref. [Goldblum 08], even though the two compound nuclei of the ratio have different ground-state $J\Pi$ and masses, an excellent agreement is found between SRM and neutron-induced data even at the lowest energies. According to us, the conditions under which the SRM can be used with confidence are still very unclear.

As mentioned before, ISRM and HSRM need a comprehensive theoretical and experimental «benchmarking». In our opinion, the reasons why these two methods give suitable results are still unclear.

As a conclusion, we believe that it is important to investigate the surrogate method independently from the Ratio approach. In the latter, angular momentum effects might cancel and a straightforward interpretation is rather difficult. We would like to stress that, in a phase of understanding, the ASM is the best way to investigate the spin-parity mismatch in the entrance channel and the associated effects. That is why we have chosen to investigate the surrogate method applied to capture in its standard form. In addition, we use target nuclei in the rare-earth region instead of actinides to avoid the contamination caused by the γ-rays emitted by the fission fragments. Also, there exist high-quality data for the neutron-induced cross sections associated to the nuclei that we investigate in this work.

Surrogate reaction	Desired reaction	Reference	Agreement with neutron-induced data
(t,pf), (d,pf), (t,df) $(^3He,df)$, $(^3He,tf)$ $(p,p'f)$, $(^3He,pf)$	$230-234Th(n,f)$, $229-232Pa(n,f)$ $232-240U(n,f)$, $232-238Np(n,f)$ $236-244Pu(n,f)$, $238-247Am(n,f)$ $244-250Cm(n,f)$, $244-248Bk(n,f)$ $252-253Cf(n,f)$, $255-256Es(n,f)$	J.D. Cramer et al.[Cramer 70b][Cramer 70a][Britt 70] H.C. Britt et al.[Britt 80][Britt 79] (LANL) B.B. Back et al.[Back 74a][Back 74b]	√ within 30%
$232Th(^3He,pf)234Pa*$	$233Pa(n,f)$	S. Boyer et al. [Boyer 06] (CENBG)	?
$232Th(^3He,tf)232Pa*$	$231Pa(n,f)$	M. Petit et al.[Petit 04] (CENBG)	√
$232Th(^3He,\alpha f)231Th*$	$230Th(n,f)$		
$232Th(^3He,p\gamma)234Pa*$	$233Pa(n,\gamma)$		
$238U(\alpha,\alpha')238U*$	$237U(n,\gamma)$	L. Bernstein et al. [Bernstein 06] (LLNL/LLBL)	Ø by a factor 3
$238U(^3He,\alpha f)237U*$	$236U(n,f)$	B.F. Lyles et al. [Lyles 07] (LLNL/LLBL)	$E_n \gtrsim 1.5$ MeV
$238U(^3He,tf)238Np*$	$237Np(n,f)$	M.S. Basunia et al. [Basunia 09] (LLNL/LLBL)	√
$243Am(^3He,df)244Cm*$	$243Cm(n,f)$		√
$243Am(^3He,tf)243Cm*$	$242Cm(n,f)$	G. Kessedjian et al. [Kessedjian 10] (CENBG)	√
$243Am(^3He,\alpha f)242Am*$	$241Am(n,f)$		√
$154Gd(p,p'\gamma)154Gd*$	$153Gd(n,\gamma)$		?
$156Gd(p,p'\gamma)156Gd*$	$155Gd(n,\gamma)$	N.D. Scielzo et al. [Scielzo 10] (LLNL/LLBL)	Ø by a factor 3
$158Gd(p,p'\gamma)158Gd*$	$157Gd(n,\gamma)$		Ø by a factor 5
$232Th(d,p\gamma)233Th*$	$232Th(n,\gamma)$	J. Wilson et al. [Wilson 11] (OSLO/IPNO)	Ø
$174Yb(^3He,p\gamma)176Lu*$	$175Lu(n,\gamma)$		$E_n \gtrsim 500$ keV
$174Yb(^3He,d\gamma)176Lu*$	$174Lu(n,\gamma)$		
$174Yb(^3He,t\gamma)176Lu*$	$173Lu(n,\gamma)$	(this work)	
$174Yb(^3He,\alpha\gamma)176Lu*$	$172Yb(n,\gamma)$		

Table 2.2: Overview of ASM applications (until 2011). The symbol √ indicates an overall good agreement with neutron-induced data and the symbol Ø indicates important discrepancies. In the case where the surrogate data could not be compared with neutron-induced data, the symbol ? is used.

Desired reaction	Surrogate reaction	Reference reaction	Surrogate reaction for reference reaction	Reference	Agreement with neutron-induced data
$^{236}U(n,f)$	$^{236}U(d,pf)$	$^{238}U(n,f)$	$^{238}U(d,pf)$	C. Plettner et al. (Yale/LLNL)	poor
$^{237}U(n,f)$	$^{238}U(d,d'f)$	$^{235}U(n,f)$	$^{236}U(d,d'f)$	[Plettner 05]	statistics
$^{237}U(n,f)$	$^{238}U(\alpha,\alpha'f)$	$^{235}U(n,f)$	$^{236}U(\alpha,\alpha'f)$	J.T. Burke et al. (LLNL/LLBL)[Burke 06]	$E_n \gtrsim 500$ keV
$^{236}U(n,f)$	$^{238}U(^3He,\alpha f)$	$^{233}U(n,f)$	$^{235}U(^3He,\alpha f)$	B.F. Lyles et al. (LLNL/LLBL) [Lyles 07]	$E_n \gtrsim 3$ MeV
$^{170}Yb(n,\gamma)$	$^{171}Yb(^3He,^3He'\gamma)$	$^{160}Dy(n,\gamma)$	$^{161}Dy(^3He,^3He'\gamma)$	B.L. Goldblum et al. (LLNL/LLBL/OSLO)	$E_n \gtrsim 150$ keV
$^{170}Yb(n,\gamma)$	$^{172}Yb(^3He,\alpha\gamma)$	$^{160}Dy(n,\gamma)$	$^{162}Dy(^3He,\alpha\gamma)$	[Goldblum 08]	$E_n \gtrsim 150$ keV
$^{233}U(n,f)$	$^{234}U(\alpha,\alpha'f)$	$^{235}U(n,f)$	$^{236}U(\alpha,\alpha'f)$	S.R. Lescher et al. (LLNL/LLBL)[Lesher 09]	$E_n \gtrsim 1$ MeV
$^{231}Th(n,f)$	$^{232}Th(^3He,^3He'f)$	$^{235}U(n,f)$	$^{236}U(^3He,^3He'f)$	B.L. Goldblum et al. (LLNL/LLBL)	?
$^{230}Th(n,f)$	$^{232}Th(^3He,\alpha f)$	$^{234}U(n,f)$	$^{236}U(^3He,\alpha f)$	[Goldblum 09]	$E_n \gtrsim 1$ MeV
$^{161}Dy(n,\gamma)$	$^{162}Dy(^3He,^3He'\gamma)$	$^{163}Dy(n,\gamma)$	$^{164}Dy(^3He,^3He'\gamma)$	B.L. Goldblum et al.	$E_n \gtrsim 150$ keV
$^{161}Dy(n,\gamma)$	$^{162}Dy(^3He,^3He'\gamma)$	$^{160}Dy(n,\gamma)$	$^{161}Dy(^3He,^3He'\gamma)$	(LLNL/LLBL/OSLO)	$E_n \gtrsim 150$ keV
$^{161}Dy(n,\gamma)$	$^{163}Dy(^3He,\alpha\gamma)$	$^{160}Dy(n,\gamma)$	$^{162}Dy(^3He,\alpha\gamma)$	[Goldblum 10]	$E_n \gtrsim 150$ keV
$^{171}Yb(n,\gamma)$	$^{171}Yb(d,p\gamma)$	$^{173}Yb(n,\gamma)$	$^{173}Yb(d,p\gamma)$	R. Hatarik et al. (LLNL/LLBL)[Hatarik 10]	$E_n \gtrsim 100$ keV *
$^{238}Pu(n,f)$	$^{239}Pu(\alpha,\alpha'f)$	$^{235}U(n,f)$	$^{236}U(\alpha,\alpha'f)$	J.J. Resler et al. (LLNL/LLBL)	$E_n \gtrsim 1$ MeV
$^{238}Pu(n,f)$	$^{239}Pu(\alpha,\alpha'f)$	$^{234}U(n,f)$	$^{235}U(\alpha,\alpha'f)$	[Ressler 11]	$E_n \gtrsim 3$ MeV
$^{239}Np(n,f)$	$^{238}U(^3He,pf)$	$^{237}Np(n,f)$	$^{236}U(^3He,pf)$	E. Norman et al. (LLNL/LLBL) (to be published)	

Table 2.3: List of ESRM experiments (until 2011). (* data corrected from spin-parity mismatch)

81

Experiment & Data analysis

Chapter 3

Experiment

In this work we investigated the interaction of a ^3He beam with a ^{174}Yb target. The main reactions considered are shown in figure 3.1:
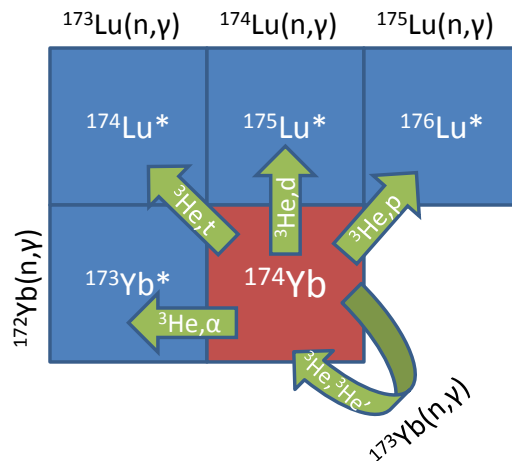
Surrogate reaction	CN	$\sigma(n,\gamma)$	$T_{1/2}$
$^{174}Yb(^3He, p\gamma)$	$^{176}Lu^*$	$^{175}Lu(n,\gamma)$	stable
$^{174}Yb(^3He, d\gamma)$	$^{175}Lu^*$	$^{174}Lu(n,\gamma)$	3,31y
$^{174}Yb(^3He, t\gamma)$	$^{174}Lu^*$	$^{173}Lu(n,\gamma)$	1,37y
$^{174}Yb(^3He, ^3He'\gamma)$	$^{174}Yb^*$	$^{173}Yb(n,\gamma)$	stable
$^{174}Yb(^3He, \alpha\gamma)$	$^{173}Yb^*$	$^{172}Yb(n,\gamma)$	stable

Figure 3.1: Transfer channels available in our experiment and corresponding (n,γ) cross sections that can be in principle inferred via the surrogate method.

In principle, this surrogate experiment can be used to determine several neutron-induced cross sections. The experiment was realized at the tandem accelerator of the IPN Orsay during winter 2010.

3.1 Beam energy
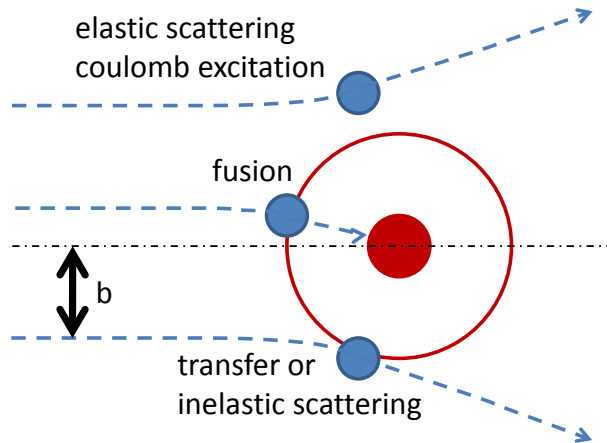
Figure 3.2: Representation of different reaction mechanisms as a function of the impact
parameter *b*.

When a charged projectile approaches a target, it experiences the long range repulsive
Coulomb force that is proportional to the charges of the two nuclei and the attractive nu-
clear force that only acts over short distances. The reaction mechanisms are determined
by the impact parameter *b* (cf. figure 3.2). For high impact parameters, the effect of
the nuclear potential can be be neglected in comparison with the Coulomb force. Under
these conditions one says that the particle undergoes Rutherford scattering or Coulomb
excitation. For lower impact parameters, when the projectile gets very close to the tar-
get, both nuclear and Coulomb forces play a role and nuclear reactions can occur. When
the collision is central, the predominant reaction is the fusion of the projectile with the
target nucleus. When the collision is peripheral, the probability to exchange only few
nucleons increases. In this case, inelastic and transfer reactions are predominant.

Obviously, it is not possible to control the impact parameter experimentally but one
can favour the mechanism of transfer by adjusting the beam energy. At energies close
to the Coulomb barrier, defined as the threshold kinetic energy for nuclear interactions,
the transfer rate is known to be maximized ([Derkx 10]). Actually the Coulomb barrier
is given by:

$$B_C = \frac{e^2}{4\pi\epsilon_0} . \frac{Z_{projectile}.Z_{target}}{R_c} \tag{3.1}$$

where $\frac{e^2}{4\pi\epsilon_0} = 1,44$ MeV.fm is a term relative to the charge of the electron and R_c corre-
sponds to the distance of closest approach in absence of nuclear interactions. Assuming
that R_c is independent of energy and is characteristic of the system considered, R_c is
determined with systematics given by ([Bass 80]):

$$R_c \approx R_{projectile} + R_{target} + 3.2 \tag{3.2}$$

with

$$R_i = 1.12 \times A_i^{1/3} - 0.94 \times A_i^{-1/3} \tag{3.3}$$

Hence, the Coulomb barrier relative to the reaction $^3He +^{174}Yb$ is:

$$B_c = 19,67 MeV \tag{3.4}$$

In our case we have chosen a projectile energy of 24 MeV:

$$E_{^3He} = 24 MeV \tag{3.5}$$

The ^3He beam was provided by the tandem accelerator of the IPN Orsay. Its nominal voltage is 15 MV and the accelerated ion beams range from protons to gold. In our case, the beam intensity was 20 particles nA.

3.2 Experimental set-up: overview

The principle of an absolute surrogate experiment has been explained previously in section 2.1. For completeness, we recall how the radiative capture probability is experimentally obtained:

$$P_\gamma^{CN}(E^*) = \frac{N_{coinc}(E^*)}{N_{single}(E^*).\epsilon_\gamma} \tag{3.6}$$

where:

- $N_{single}(E^*)$ is the total number of different ejectiles, each being associated to a compound-nucleus. The identification of the ejectiles was performed by two telescopes $\triangle E - E$.

- $N_{coinc}(E^*)$ is the number of γ-cascades detected in coincidence with an ejectile. To determine the number of capture events we used four C_6D_6 scintillators. They have the advantage of allowing for a good discrimination between photons and neutrons. The ^{174}Yb target was also surrounded by six germanium detectors.

- ϵ_γ is the detection efficiency of our experimental set-up for capture events.

Figure 3.3 illustrates our experimental set-up. The telescopes and the target were located in a thin aluminium reaction chamber with internal vacuum. The stable ^{174}Yb target was fabricated at the SIDONIE facility (mass separator) of the CSNSM laboratory. The ^{174}Yb sample had a thickness of 250 $\mu g/cm^2$ and was deposited onto a carbon foil of 50 $\mu g/cm^2$.
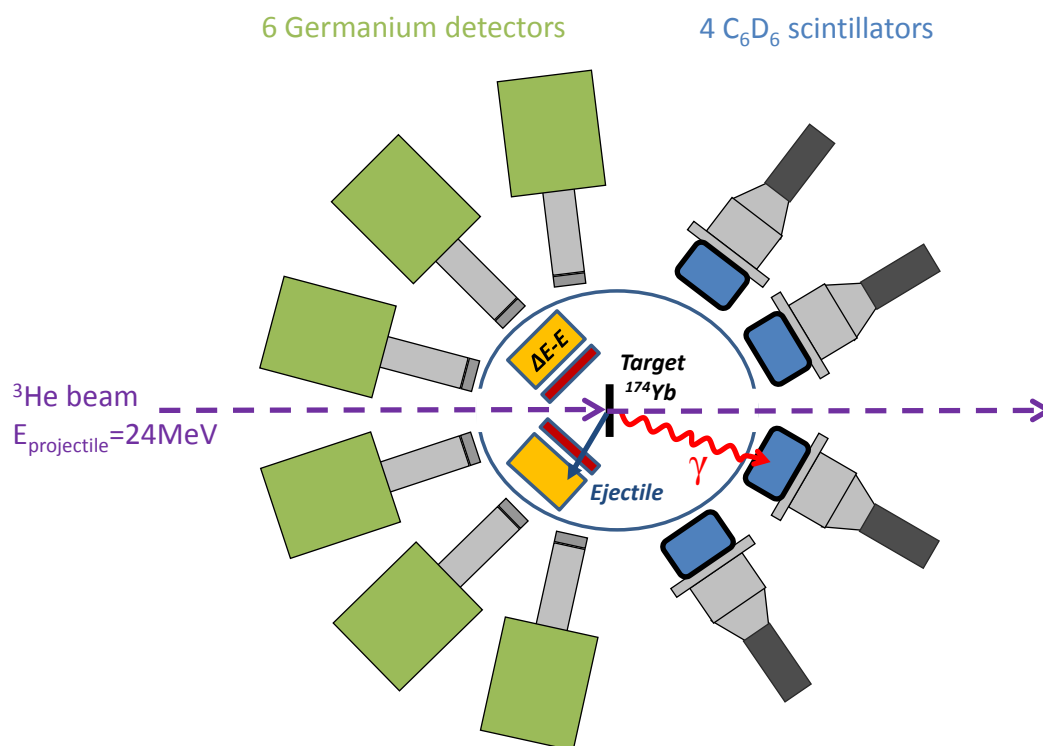
Figure 3.3: Top view of our experimental set-up.

3.3 Identification of decaying nuclei

3.3.1 Identification of the transfer channels with $\Delta E - E$ telescopes

The ^3He beam interacts with the ^{174}Yb target leading to a panel of nuclear reactions. In order to identify the compound-nucleus formed, it is necessary to identify the associated transfer channel, namely the corresponding ejectile. For instance, the detection of a proton signs the production of the compound-nucleus $^{176}Lu^*$. The ejectiles are fully identified by two large area $\Delta E - E$ telescopes placed symmetrically at 130° with regard to the ^3He beam. The ejectiles are detected at backward angles for two important reasons:

- to avoid detector saturation caused by the detection of the elastic scattered ^3He beam.

- to keep the excitation-energy range of interest free from events arising from the interaction of the beam with the carbon backing or target impurities. Note that this kind of considerations is very important for applications of the absolute surrogate method. If ejectiles produced in transfer reactions on the carbon backing or on impurities contaminate the spectra, we make a wrong identification of the decaying nucleus and determine a wrong number of compound nuclei. The events originating from the carbon backing are usually subtracted, however it is crucial to minimize this contribution which is an important source of systematic uncertainty.

The ΔE detectors were two 300 μm silicon detectors of design W1 from the company Micron Semiconductors. The 16x16 X-Y strips configuration provides the angle of the detected particle with an angular coverage of 107° to 150°. This 50×50 mm^2 double-sided p-on-n silicon structure has been extensively studied in [Soisson 10]. The intrinsic energy resolution $\sigma_{\Delta E}$ as determined with a non-collimated standard 3α source, is 19.25 keV for the ^{241}Am alpha (cf left part of figure 3.4). During the beam time, the detectors were shielded against δe^- coming from the target with a thin Mylar(Al) foil polarized at -300V. This electrostatic screen is used to prevent any decrease of the amplitude signal and the energy resolution. To avoid border effects and electrostatic perturbations a nickel frame of 2 mm thickness was positioned in front of the ΔE detectors. As a consequence, the strips at the edges of the detector could not be used, see the outer area of the red square of figure 3.5. The E detectors were two $Si(Li)$ detectors of 3 mm thickness with a 58x58 mm^2 active surface. At ambient temperature, the intrinsic energy resolution σ_E, as determined with a non-collimated standard 3α source, is 40.46 keV for the ^{241}Am alpha (cf right part of figure 3.4). The final geometry of our telescopes is given in figure 3.6 and a front view of the reaction chamber is shown in figure 3.7.

Isotope	Average E_α(MeV)
^{239}Pu	5.149
^{241}Am	5.480
^{244}Cm	5.795

ΔE: FWHM$\approx$45keV E: FWHM$\approx$95keV
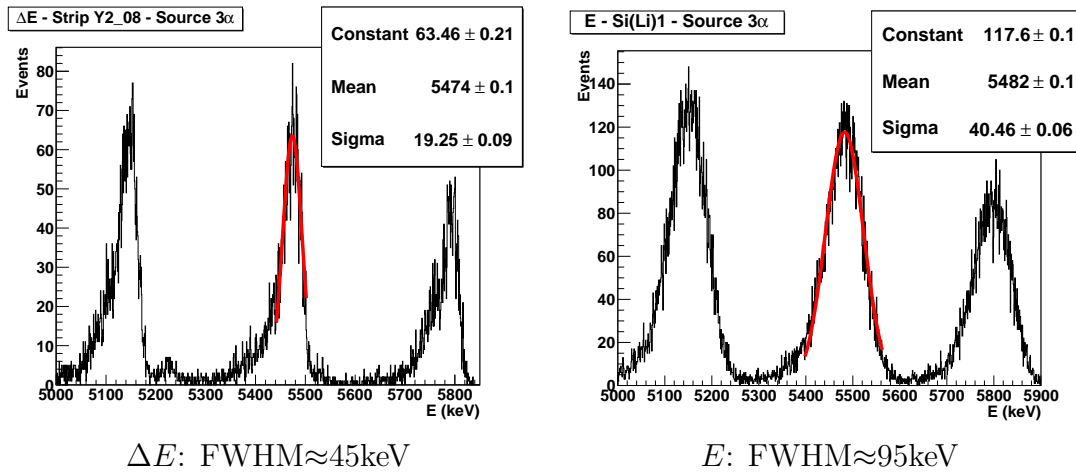
Figure 3.4: Intrinsic energy resolution of the ΔE and E detectors obtained with a standard 3α source, see text for details.
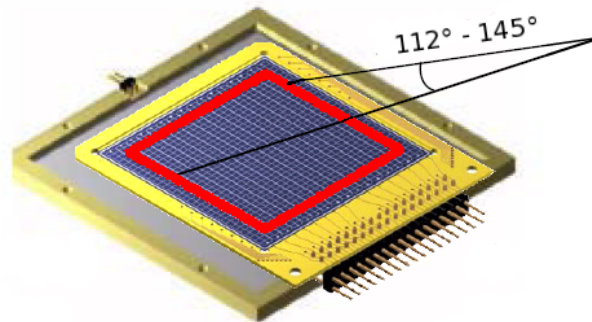
Telescope $\Delta E - E$ assembly

Figure 3.5: Telescope detector. The red frame illustrates the real active area and opening angles taking into account the nickel collimator.
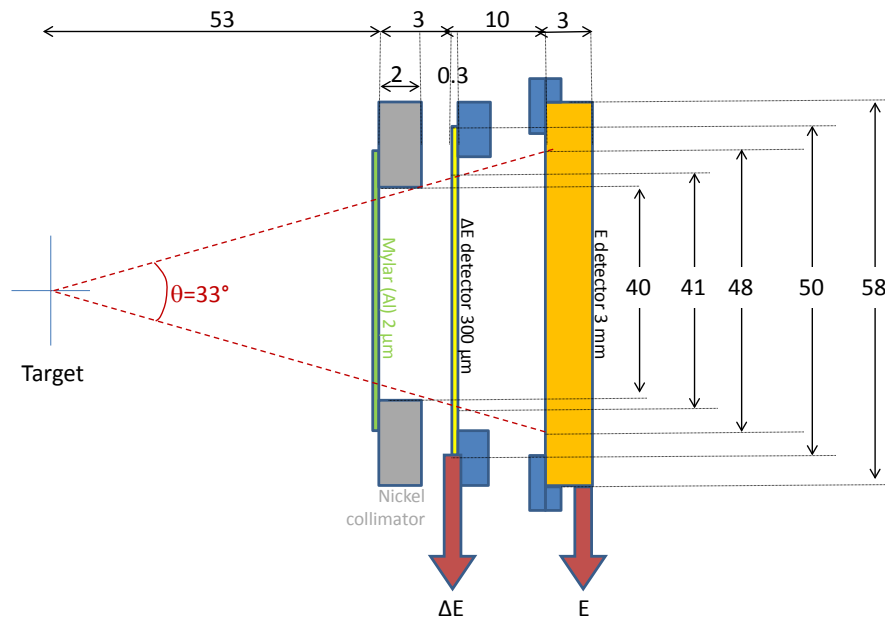
Figure 3.6: Geometry of the telescopes.
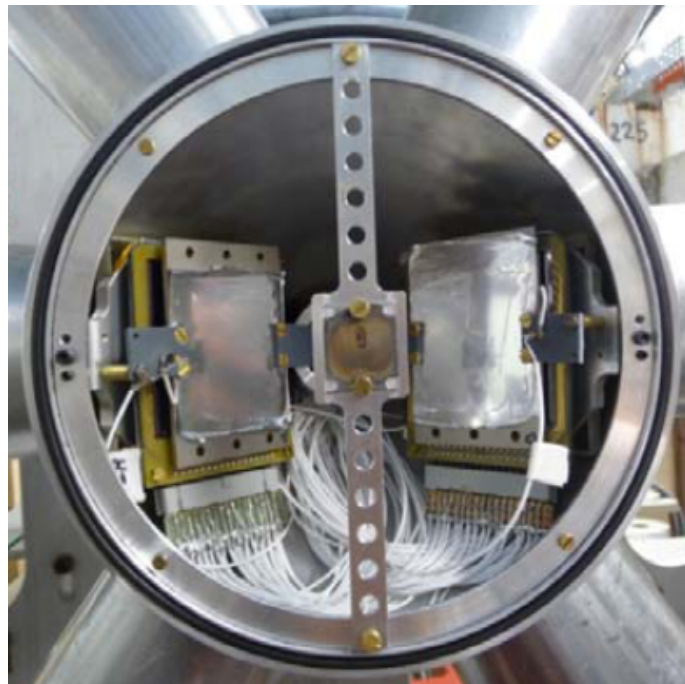
Figure 3.7: Front view of the reaction chamber. At the centre, one distinguishes the ^{174}Yb target surrounded by the two telescopes shielded with nickel frames and thin Mylar(Al) foils. The support for the telescopes and the reaction chamber have been designed and constructed at the CENBG.

91

The principle of the $\Delta E - E$ identification of the ejectile is based on the Bethe and Bloch formula [Leo 87], the energy loss ΔE of a nucleus in matter depends on its kinetic energy E_c , its charge Z and its mass A:

$$\Delta E \propto \frac{AZ^2}{E_c} \tag{3.7}$$

Representing ΔE vs. the residual energy E, which is directly related to E_c, one obtains different hyperbolas corresponding to the different ejectiles. These hyperbolas are separated by a factor proportional to AZ^2(cf. figure 3.8).
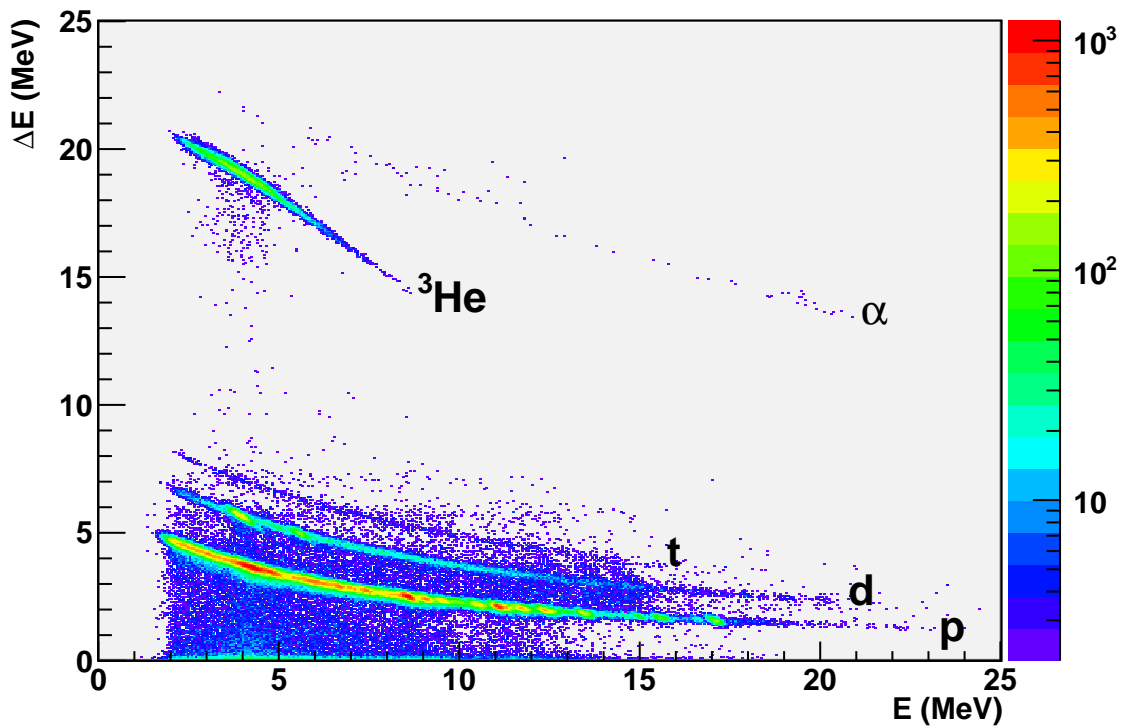
Figure 3.8: Identification matrix $\Delta E - E$ for the strip Y2_08 ($\theta = 130, 19°$).

3.3.2 Excitation energy of the compound-nucleus

The kinetic energy of the ejectile E_c is given by the total energy loss in the telescope:

$$E_c = \triangle E + E \tag{3.8}$$

To be rigorous, one should also use Ziegler tables to compensate for the energy loss in the 2 μm Mylar(Al) foil. For example, the corresponding energy loss is nearly 7 keV for protons at 20 MeV. As we will see later, these values are negligible in comparison with the excitation-energy resolution of our detectors. Therefore, we decided to neglect this correction. The emission angle is precisely given by the position of the pixel XY of the $\triangle E$ detector that has been traversed by the ejectile. Nevertheless, to ensure enough statistics, we prefer working only with the vertical strips of our $\triangle E$ detectors. This choice involves a larger angular uncertainty for the strips which correspond to large angles. The strips identification is given in figure 3.9. The average emission angle of the ejectiles hitting the different Y-strips and the angular standard deviation were obtained with a Monte-Carlo simulation and are listed in table 3.1.
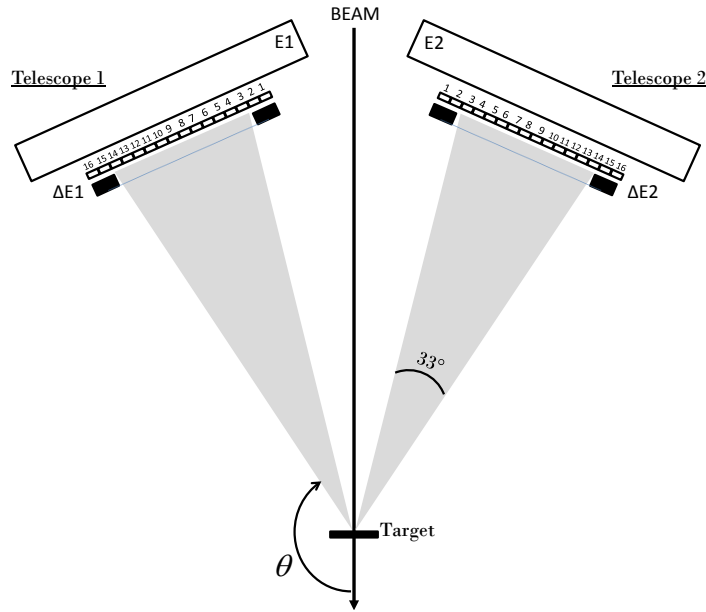
Figure 3.9: Schematic view of the telescopes setup. The vertical (Y) strip number is given.

Applying two-body kinematics, the excitation energy of the compound-nucleus can be deduced from the kinetic energy and emission angle of the corresponding ejectile. In the case of a transfer reaction $X(a,b)Y$, the characteristics of each particle are listed in table 3.2, where M corresponds to the atomic mass, E_c is the kinetic energy and $\vec{v}$ is the velocity vector of the particle. Note that the recoiling nucleus Y is here the compound-nucleus formed in the transfer reaction.

Strip Y_i	Mean angle: θ_{Yi} (°)	$\sigma_{\theta_{Yi}}$(°)	Mean thickness d_{Yi} (μm)	$\sigma_{d_{Yi}}$(μm)
1	150.008911	2.310522	331.541	12.980
2	147.429443	2.188386	326.966	8.384
3	144.729294	2.072329	321.922	8.397
4	141.962967	1.957487	317.596	8.368
5	139.095444	1.843308	314.117	8.385
6	136.177231	1.736199	311.473	8.424
7	133.195618	1.627700	309.721	8.428
8	130.191895	1.523163	308.852	8.425
9	127.165871	1.418898	308.830	8.438
10	124.151871	1.324940	309.705	8.441
11	121.160835	1.231485	311.460	8.416
12	118.198067	1.145601	314.140	8.478
13	115.302895	1.058899	317.613	8.338
14	112.467880	0.986202	321.918	8.402
15	109.722717	0.916909	326.974	8.397
16	107.065254	0.848750	331.637	12.717

Table 3.1: Mean angle and mean thickness of Y strips, with associated errors, determined with a Monte-Carlo calculation.

Particles	Parameters
X (target)	M_X
a (projectile)	M_a, E_{ca}, $\vec{v_a}$
b (ejectile)	M_b, E_{cb}, $\vec{v_b}$
Y (recoiling nucleus)	M_Y, E_{cY}, $\vec{v_Y}$
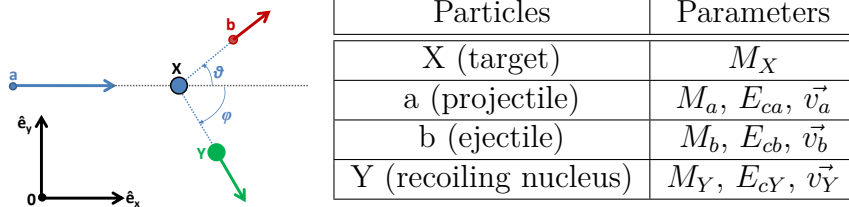
Table 3.2: Two-body $X(a,b)Y$ nuclear reaction scheme and associated parameters.

The conservation of the total energy (shared between kinetic and excitation energies) gives :

$$E_{ca} = (E_{cb} + E_b^*) + (E_{cY} + E_Y^*) - Q \qquad (3.9)$$

where Q is the Q-value of the reaction and E_b^*, E_Y^* are the excitation energies of the ejectile b and the recoiling nucleus Y, respectively. The highly asymmetric projectile-target combination presents the advantage that the excitation of the ejectile can be neglected. We assume that the excitation energy is fully transferred to the recoiling nucleus which has a much higher level density.

The conservation of the total momentum gives:

- in $\vec{x}$ direction:

$$M_a v_a = M_b v_b cos\theta + M_Y v_Y cos\phi \qquad (3.10)$$

- in $\vec{y}$ direction

$$0 = M_b v_b sin\theta + M_Y v_Y sin\phi \qquad (3.11)$$

Using the non-relativistic formula $Mv = \sqrt{2ME_c}$, one obtains:

- in $\vec{x}$ direction:

$$\sqrt{2M_a E_{ca}} = \sqrt{2M_b E_{cb}}cos\theta + \sqrt{2M_Y E_{cY}}cos\phi \qquad (3.12)$$

- in $\vec{y}$ direction:

$$0 = \sqrt{2M_b E_{cb}}sin\theta + \sqrt{2M_Y E_{cY}}sin\phi \qquad (3.13)$$

Using equations 3.12 and 3.13, equation 3.9 can be written as:

$$E_{ca}(M_a - M_Y) + E_{cb}(M_Y + M_b) - 2\sqrt{M_a M_b E_{ca} E_{cb}}cos\theta - M_Y(Q - E_Y^*) = 0 \qquad (3.14)$$

In the context of a surrogate experiment, we are interested in the determination of the excitation energy E_Y^* of the compound-nucleus (i.e. the recoiling nucleus) as a function of the emission angle θ and energy E_{cb} of the ejectile:

$$E^* = E_Y^* = \frac{M_Y Q - E_{ca}(M_a - M_Y) - E_{cb}(M_Y + M_b) + 2\sqrt{M_a M_b E_{ca} E_{cb}}cos\theta}{M_Y} \qquad (3.15)$$

The equivalent neutron energy can then be deduced from:

$$E_n = \frac{M_Y}{M_Y - 1}\left(E^* - S_n\right) \qquad (3.16)$$

where, as explained before, S_n is the one-neutron separation energy for the compound-nucleus Y. Reaction parameters for each transfer channel are reported in table 3.3.

Reaction	X	a	b	Y	Q-value (MeV)	S_n(MeV)
$^{174}Yb(^{3}He, p)^{176}Lu*$	^{174}Yb	^{3}He	p	$^{176}Lu*$	+4,080	6,288
$^{174}Yb(^{3}He, d)^{175}Lu*$	^{174}Yb	^{3}He	d	$^{175}Lu*$	+0,017	7,667
$^{174}Yb(^{3}He, t)^{174}Lu*$	^{174}Yb	^{3}He	t	$^{174}Lu*$	-1,393	6,761
$^{174}Yb(^{3}He,^{3}He')^{174}Yb*$	^{174}Yb	^{3}He	^{3}He	$^{174}Yb*$	0	7,465
$^{174}Yb(^{3}He, \alpha)^{173}Yb*$	^{174}Yb	^{3}He	^{4}He	$^{173}Yb*$	+13,113	6,368

Table 3.3: Reaction parameters and S_n values

The total error on the ejectile energy $(\sigma_{E_{cb}})$ is given by the quadratic sum of the intrinsic resolution of the $\triangle E$ and E detectors:

$$(\sigma_{E_{cb}}) = \sqrt{(\sigma_{\triangle E})^2 + (\sigma_E)^2} \tag{3.17}$$

which gives approximately 44,8 keV. We remind that these values have been determined with a standard 3α source. This gives a good estimate for $(\sigma_{E_{cb}})$ even if we expect some differences for more energetic particles. Moreover, the energy loss and straggling due to the traverse of the target, carbon backing and Mylar foil are not taken into account. Finally, the total error on the excitation energy (σ_{E^*}) as a function of the detector energy $(\sigma_{E_{cb}})$ and the the angular resolution (σ_θ) can be written as:

$$(\sigma_{E^*})^2 = \left(\frac{M_Y + M_b}{M_Y}\right)^2 (\sigma_{E_{cb}})^2 + \frac{M_a M_b E_{ca} E_{cb}}{(M_Y)^2} \cdot \left(\cos^2(\theta) \cdot \left(\frac{\sigma_{E_{cb}}}{E_{cb}}\right)^2 + \sin^2(\theta) \cdot (\sigma_\theta)^2\right) \tag{3.18}$$

where we have neglected the errors related to the beam energy $(\sigma_{E_{ca}})$, the Q-value of the reaction (σ_Q), and the energy calibration. Table 3.4 illustrates the kinematic calculations for the $^{174}Yb(^3He,p)^{176}Lu^*$ reaction for various excitation energies E^* at different emission angles θ of the ejectile. Calculations for the other transfer channels are given in appendix B.

(MeV)	$\theta_{Y14} = 112,46°$		$\theta_{Y8} = 130,19°$		$\theta_{Y3} = 144,73°$	
E^*	E_{cb}	σ_{E^*}	E_{cb}	σ_{E^*}	E_{cb}	σ_{E^*}
0	27,3219		27,1895		27,1036	
5	22,3684		22,2485		22,1708	
S_n=6,288	21,0927	0,0470	20,9763	0,0487	20,9008	0,0489
10	17,4170		17,3112		17,2426	
15	12,4688		12,3792		12,3211	
20	7,5259		7,4562		7,4111	

Table 3.4: Kinematic calculations for the $^{174}Yb(^3He,p)^{176}Lu^*$ transfer channel.

The error in the excitation energy is dominated by the ejectile energy resolution $(\sigma_{E_{cb}})$. It is important to note that for heavy recoiling nuclei (rare earths or actinides), the angular dispersion term becomes very weak ($\sim$10keV/°) in comparison with a variation of $\sim$100keV/° for lighter recoiling nuclei originating from reactions on the carbon support and the light target impurities.

3.3.3 Excitation-energy range accessible with our experimental set-up

Ejectile identification is only possible if the ejectile goes through the ΔE detector. $E_{threshold-300\mu m}$ is defined as the minimal energy for the ejectile to traverse the ΔE detector. Since we are studying the validity of the surrogate method to infer neutron-induced cross sections, the excitation-energy range of interest is just above S_n. A comparison between the ejectile energy E_{cb} corresponding to the formation of a compound-nucleus with $E^* = S_n$ and the threshold energy $E_{threshold-300\mu m}$ is shown in table 3.5.

Ejectiles	$E_{threshold-300\mu m}$	E_{cb} for $E^* = S_n$	$\Delta E(300\mu m)$	$E(3mm)$
p	6.129	21.0927	1.416	19.6
d	8.124	15.5518	3.2804	12.271
t	9.542	14.9219	4.7558	10.166
^3He	21.786	15.5938	15.5938	0
α	24.494	29.2424	16.113	13.13

Table 3.5: LISE++ energy-loss calculations in the $\Delta E - E$ telescopes.

For the $(^3He, p)$, $(^3He, d)$, $(^3He, t)$ and $(^3He, \alpha)$ transfer channels, the excitation-energy range above S_n is accessible. Unfortunately, the kinematics of the inelastic scattering $(^3He, {}^3He')$ reaction is not favorable. Because of a zero Q-value and a higher charge, most of the $^3He'$ scattered ejectiles are stopped in the ΔE detector. For this reason, the $(^3He, {}^3He')$ cannot be analysed[1]. Note that the $(^3He, \alpha)$ transfer channel can be analysed due to a high Q-value which permits to produce high-energy ejectiles and associated compound nuclei with excitation energies above S_n.

3.3.4 The contaminants issue

Absolute surrogate experiments need pure targets. The presence of unknown impurities is responsible for transfer reactions that lead to decaying nuclei different than the desired compound-nucleus. Unfortunately, it is very difficult to completely eliminate contaminants. The main contaminants arise from reactions on ^{12}C and ^{13}C from the 50 $\mu g/cm^2$ carbon backing. In addition, the oxydation of the target pollutes the energy spectrum because of transfer reactions on ^{16}O. The consequence is the presence of broad resonances in the singles spectrum. These structures correspond to the population of the ground states and first excited states of the residual nuclei populated in the contaminant transfer reaction, as detailed in table 3.6.

It is possible to correct for part of the contaminant events by subtracting the carbon contribution. The latter is obtained from a measurement with a bare carbon backing

---

[1]Surrogate experiments using the $(^3He, {}^3He')$ reaction need higher beam energies and thinner ΔE detectors (150 μm for example).

Reaction	Nucleus	E of first excited states (MeV)			Q-value (MeV)
$^{12}C(^3He,p)$	$^{14}N^*$	2.3129	3.9478	4.915-5.1059	4.779
$^{13}C(^3He,p)$	$^{15}N^*$	5.2704-5.2989	6.3239	7.1554	10.666
$^{16}O(^3He,p)$	$^{18}F^*$	0.9371-1.119	1.701	2.1007	2.032
$^{12}C(^3He,d)$	$^{13}N^*$	2.365	3.511-3.547	6.36	-3.550
$^{13}C(^3He,d)$	$^{14}N^*$	2.3129	3.9478	4.915-5.1059	2.057
$^{16}O(^3He,d)$	$^{17}F^*$	0.4953	3.104	3.857	-4.893

Table 3.6: Excited states of the compound nuclei produced through transfer reactions on target contaminants.

(coming from the same carbon layer) which can, after proper normalisation, be subtracted directly to the measurement done with the ^{174}Yb target. Nevertheless, this subtraction is firstly an important source of systematic uncertainty and secondly, it does not remove the events coming from reactions on ^{16}O. For these reasons, kinematic calculations need to be done (cf figures 3.10 and 3.11 relative to the $(^3He,p)$ and $(^3He,d)$ channels, respectively) in order to prevent for contamination coming from reactions on oxygen and if possible, minimize the contribution of the carbon backing in the excitation energy range of interest. From 110° to 150°, reactions on ^{12}C and ^{13}C pollute the singles (and eventually the coincidence) spectrum in the range $S_n < E^* < S_n + 2$ MeV. However, they are less important than in the region from 50° to 100°. Note that the $(^3He,t)$ reaction is also corrected from a small background contribution coming from the carbon backing and impurities. The $(^3He,\alpha)$ channel is not polluted at backward angles. Details are given in Chapter 4.
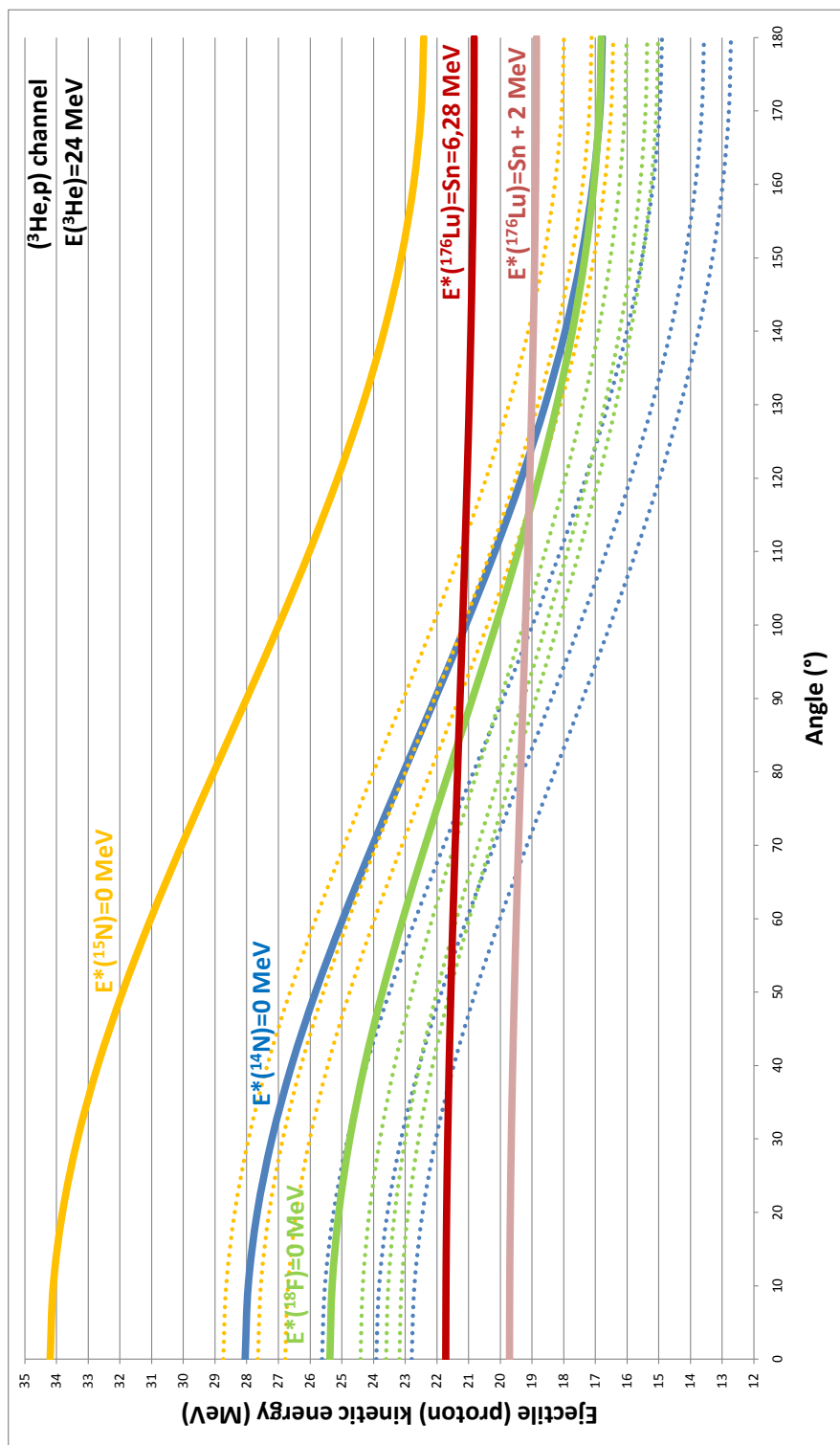
Figure 3.10: Kinetic energy of the ejectiles (protons) as a function of the detection angle for the reaction $^{174}Yb(^{3}He,p)^{176}Lu^{*}$ (full lines in red) for $E^{*} = S_{n}$ and $E^{*} = S_{n} + 2$ MeV; and for the ground (full lines) and first excited states (dotted lines) of the nuclei $^{14}N^{*}$(blue), $^{15}N^{*}$(orange) and $^{18}F^{*}$(green) produced in the parasitic reactions $^{12}C(^{3}He,p)$, $^{13}C(^{3}He,p)$ and $^{16}O(^{3}He,p)$, respectively.
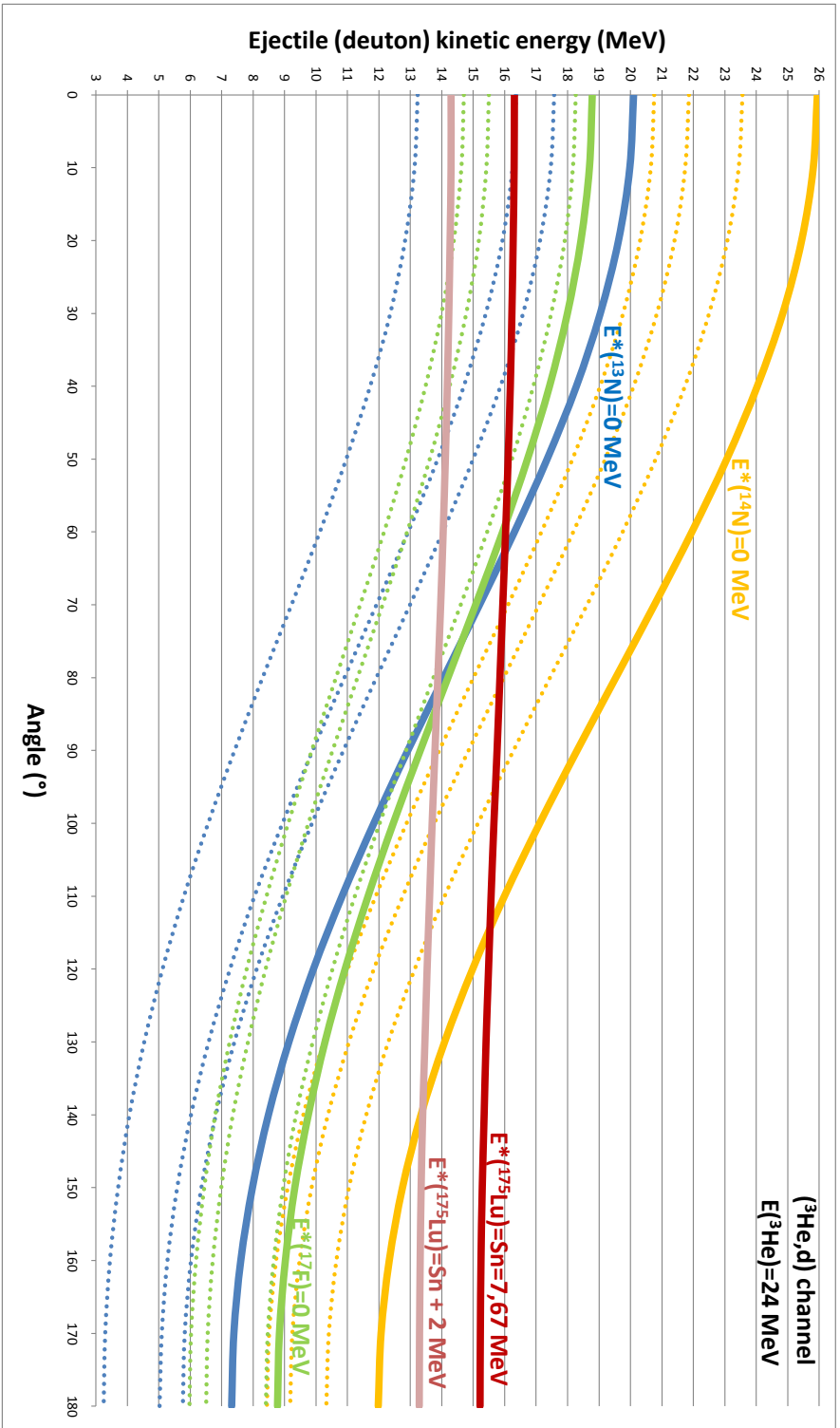
Figure 3.11: Kinetic energy of the ejectiles (deuterons) as function of the detection angle for the reaction $^{174}Yb(^{3}He,d)^{175}Lu^{*}$ (full lines in red) for $E^{*} = S_{n}$ and $E^{*} = S_{n} + 2$ MeV; and for the ground (full lines) and first excited states (dotted lines) of the nuclei $^{13}N^{*}$(blue), $^{14}N^{*}$(orange) and $^{17}F^{*}$(green) produced in the parasitic reactions $^{12}C(^{3}He,d)$, $^{13}C(^{3}He,d)$ and $^{16}O(^{3}He,d)$, respectively.

3.4 Gamma-ray detection

As shown by equation 3.6, one needs to determine the number of radiative capture events in coincidence with ejectiles.

3.4.1 Overview on experimental techniques used for capture measurements

3.4.1.1 Total γ-cascade detection with a 4π array

A way to overcome many of the difficulties related to capture measurements (see section 2.1.2) is to detect the complete γ-cascade with a 4π geometry and almost 100% efficiency detector array. The most performing multi-sectional detector is the DANCE detector at the Los Alamos National Laboratory. It consists of 160 inorganic high-density scintillators BaF_2. The γ-cascade detection efficiency is around 98%. Its high segmentation enables gamma multiplicity measurements. The fast timing allows for precise γ-γ coincidence and time-of-flight measurements. Similar 4π BaF_2 arrays have been built at CERN (n_TOF) and at Forschungszentrum Karlsruhe for measuring neutron capture cross sections up to 200 keV. Due to the difference of multiplicity and total energy of the detected cascades originating from (n,γ), $(n,n'\gamma)$ and $(n,f\gamma)$ events, one can get rid of most of the contaminant reactions. For the same reason, it is also possible to distinguish the «internal» γ-rays coming from the Baryum itself. Unfortunately, this kind of 4π arrays is prohibitively expensive.

3.4.1.2 Non 4π arrays with low energy-resolution detectors

An alternative way to determine (n,γ) cross sections is to use organic or inorganic scintillators as γ-ray counters in an ensemble with relatively low efficiency. An important drawback of these detectors is that one cannot distinguish between the γ-rays coming from the reaction of interest from the ones coming from other background reactions. We can denote four contaminants:

- γ-rays coming after neutron emission. Hauser-Feshbach models can be used to correct from the inelastic $(n'\gamma)$ contribution. However, an adequate γ-ray detection threshold is probably the best way to correct for this contribution.

- γ-rays following fission. This only the case for heavy nuclei. A veto on fission fragments is needed to remove this contribution. Such measurements are very challenging.

- γ-rays coming from radiative capture (n,γ) inside the detector itself or in the surrounding materials. Resonant radiative capture can occur in many materials. In

particular, iodine detectors NaI and CsI are especially sensitive to these «internal» radiative capture. Organic and inorganic scintillators, as BaF_2 or C_6H_6, are in general also sensitive.

- neutrons originating from elastic and inelastic scattering or fission fragments. Two methods are widely used to discriminate between events induced by neutrons and by γ-rays. Since γ-rays travel faster than neutrons one can measure the difference in time-of-flight between the target and the detector. A good time resolution implies large target-detector distances. By using organic scintillators, discrimination using the difference in the detected pulse shape can also be utilized. This technique is used in this work and is extensively studied in appendix E. Since the pulse widths for neutrons are wider in time than those for photons[2], pulse shape discrimination (PSD) is possible. For example, figure E.2 illustrates how PSD is applied using an Am/Be source as a n-γ source.

Moxon-Rae detectors

A method for determining the cascade efficiency of an array which is not 4π was suggested by Moxon and Rae ([Moxon 63]) who proposed a particular design for a γ-ray detector that fulfills the proportionality between the gamma energy E_{γ_i} and the detection efficiency ε_{γ_i}:

$$\varepsilon_{\gamma_i} = k.E_{\gamma_i} \tag{3.19}$$

For such a system, the efficiency ϵ_c for detecting a γ-cascade can be expressed as:

$$\epsilon_c = \sum_i \varepsilon_{\gamma_i} + \sum_i \sum_j \varepsilon_{\gamma_{i,j}} + ... \tag{3.20}$$

where the first term corresponds to the efficiency to detect only one of the constituting γ-rays, the second term corresponds to the efficiency to detect two γ-rays of the cascade in coincidence, etc. If the γ-ray efficiency of such detector is very small $\varepsilon_\gamma \ll 1$, the probability to detect two or more γ-rays coming from the same cascade can be considered as negligible. Under these conditions we have:

$$\epsilon_c \approx \sum_i \varepsilon_{\gamma_i} \tag{3.21}$$

Inserting eq. 3.19 into eq. 3.21, ϵ_c becomes proportional to the cascade energy E_c:

---

[2]The light emission of scintillators is dominated by a single fast decay component (fluorescence) and a substantial slow component (phosphorescence). Thus, the overall decay time of the emitted light pulse will vary with the type of exciting radiation, depending of the proportion of metastable excited states (relative to the slow component).

$$\epsilon_c \approx \sum_i \varepsilon_{\gamma_i} = k. \sum_i E_{\gamma_i} = k.E_c \qquad (3.22)$$

The final consequence is that the detection efficiency for a capture event ϵ_c is directly proportional to the total energy released in the capture event. In practice, the proportionality factor k is known for the Moxon-Ray detector used and the energy of the cascade E_c corresponds to the excitation energy of the compound-nucleus. The detection efficiency becomes here totally independent of the cascade path. The determination of the radiative capture efficiency in this way is known as «total-energy detection principle». Unfortunately, the so-called Moxon-Ray detector, which was designed to achieve the latter conditions, was abandoned due to its inherently low efficiency and its non-proportionality below 1 MeV. ([Macklin 63]).

The total energy detection principle applying the Pulse Height Weighting Technique

An alternative to the Moxon-Rae detector is the Pulse-Height Weighting Technique (PHWT). Developed by Macklin and Gibbons ([Macklin 67]), the idea is to use non-proportional detectors and achieve the proportionality of the detection efficiency with energy mathematically by weighting the response function of the detector with an appropriate function. The PHWT technique is often used in neutron-induced capture cross-section measurements in the resonance region, for example at the IRMM (Geel) ([Borella 07]) and n_TOF(CERN) ([Plag 03],[Tain 04]). The same technique has been recently investigated by the CENBG group ([Wilson 03]) for the $^{233}Pa(n,\gamma)$ cross-section measurement (cf section 2.1.3, [Boyer 06]).

In this work we used this technique to determine the radiative capture probability using four C_6D_6 scintillators. Details on the γ-cascade efficiency determination are given in section 4.3.1. On the other hand, we will present an alternative method to determine the efficiency based on the constant-efficiency hypothesis, which can be easily applied to radiative-capture measurements using surrogate reactions. The two methods will be compared in section 4.4.

3.4.1.3 Non 4π arrays with high energy-resolution detectors

The principal application of germanium detectors is γ-ray spectroscopy. Because of the high atomic number (Z=32), the photoelectric cross section is very high and consequently, germanium detectors offer the highest energy resolution available for γ-ray energies from a few keV up to 10 MeV. Capture cross sections can be determined by measuring all primary γ-rays depopulating the CN state or by gating only on γ-ray transitions feeding the ground state[3]. The energy-dependent efficiencies ε_γ for these

---

[3]In this case, we assume that all decay paths go through these transitions.

transitions are determined using calibrated γ sources. Note that ε_γ is also corrected for internal conversion via calculations. As mentioned in section 2.1.2, this technique can be used to measure (n, γ) cross sections via the surrogate method. However, the experiments usually involve well-known even-even compound nuclei with particularly simple level schemes. This technique has not yet been applied to odd compound nuclei. The main problem is that gating only on few γ-ray transitions induces very low statistics. Another important drawback is the relatively high $Ge(n, \gamma)$ cross section. Neutron emission competes with capture and the emitted neutrons may interact with the Ge detector. However, due to the high resolution, the sensitivity to neutrons is not an issue in terms of gamma-neutron discrimination. Nevertheless, semiconductor detectors are relatively sensitive to neutron damage. Under a high neutron flux, the main effect on the detector performance is an increase of the leakage current that leads to a degradation of the energy resolution. All details about semi-conductor principles applied to γ-ray measurements can be found in [Leo 87].

In this work we also used this approach to determine the radiative capture probability using six *Ge* detectors. Details are given in section 4.8.

3.4.2 Experimental set-up for gamma-ray detection

As mentioned before, four C_6D_6 liquid scintillators, based on purified deuterated benzene, were used for measuring the radiative capture events. The C_6D_6 detectors are also known as NE-230: it is an alternative to the very usual NE-213, which are C_6H_6 liquid scintillators. The replacement of hydrogen by deuterium strongly suppresses γ-rays originating from neutron captures inside the detector itself[4]. We stress that this detector is very sensitive to fast neutrons. However, C_6D_6 scintillators are known for their very good PSD properties that allow for a neutron-gamma discrimination. These scintillators surrounded the reaction chamber, which was very thin (1mm aluminium) so one can neglect the interaction of γ-rays with the chamber. The C_6D_6 detectors were placed in a propeller formation at front angles, each one was set at an angle of 45° with respect to the horizontal plane and titled 30° with respect to a perpendicular plane to the beam axis. The target-C_6D_6 distance was about 90 mm. Each scintillator cell cavity had a diameter of 106 mm and a thickness of 76.2 mm. Additional technical data are given in appendix C. As illustrated in figure 3.12, each C_6D_6 detector consists of a liquid scintillating organic material which is optically coupled to a photomultiplier via a light guide. Because of the very low atomic numbers, Compton scattering is the predominant γ-interaction process inside the cavity cell. The incident photon collides with an electron in the scintillator. Then this «Compton» electron excites the atoms and molecules making up the scintillator which deexcite emitting light. This light is transmitted to the photocathode where it is converted into a weak current of photo-electrons which is

---

[4]In particular, one wants to avoid the 2,2 MeV γ-ray produced in the reaction $H(n, \gamma)D^*$.

then further amplified by a photomultiplier (PM). The amplitude of the electric signal is directly proportional to the Compton-electron energy. The latter varies with angle and is given by the formula:

$$E_{e^-} = E_0 - E_\gamma = E_0 - \frac{E_0}{1 + E_0.(\frac{1-cos\theta}{m_e.c^2})} \tag{3.23}$$

where:

- E_{e^-} is the energy of the recoiling electron.

- E_0 is the energy of the incident photon.

- E_γ is the energy of the outgoing photon.

- $m_e.c^2$=0,511 MeV is the rest energy of the electron.

- θ is the angle of deflection for the photon (see figure 3.13).

When θ approaches zero, no energy is transferred to the electron. The maximum amount of energy is transferred when θ approaches π and is called the «Compton edge»:

$$E_{compton} = E_{e^-}(\theta = \pi) = \frac{2.(E_0)^2}{m_e.c^2 + 2.E_0} \tag{3.24}$$

Consequently, C_6D_6 detectors are clearly not suitable as γ-ray spectrometers: the output response for a given input γ-ray is a distribution covering all possible energies (the «Compton plateau») up to the «Compton edge». Note there is no photoelectric peak. Figure 3.13(b) shows the response for a γ-ray with E_0=611 keV.

The reaction chamber is also surrounded by six high-volume germanium detectors, coming from the ORGAM array[5]. The *Ge* detectors were placed at backward angles and the target-detector distance was about 90.5 mm. Each *Ge* crystal was coaxial with 70% efficiency. An engineering drawing is given in appendix D. They were used to measure low-lying γ-ray transition intensities as a function of the compound-nucleus excitation energy, which is an additional way to infer the capture probability and to investigate the difference in spin distributions between transfer and neutron-induced reactions. We will see later that *Ge* detectors were also needed to perform energy calibrations as well as efficiency and response function measurements of the C_6D_6 scintillators. The positions of the detectors are illustrated in figures 3.14 and 3.15. The aluminium support of the C_6D_6 has been integrally designed by the engineering group of CENBG.

---

[5]The Compton-suppressed BGO were removed.

(a)   (b)
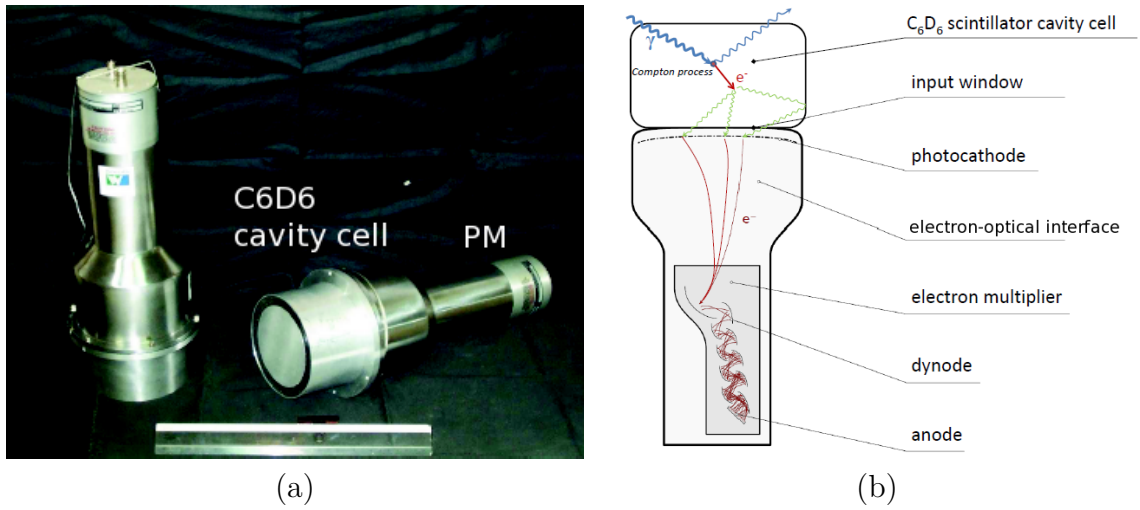
Figure 3.12: (a) Picture of the C_6D_6 detectors used: a module consists of a C_6D_6 cavity cell, a photomultiplier tube and a voltage divider. (b) Generation of the electronic signal in the anode for a Compton event.

(a)   (b)
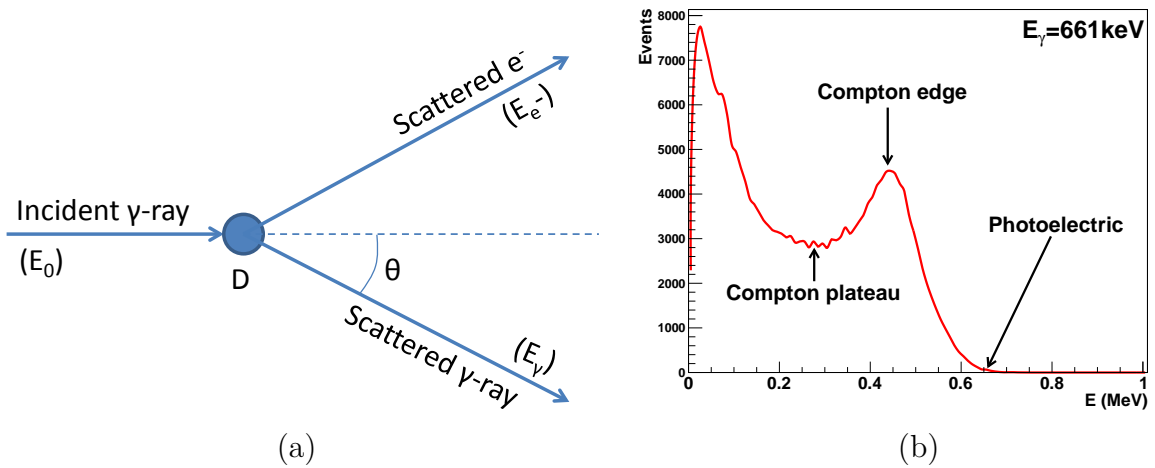
Figure 3.13: (a) Compton scattering diagram (b) Example of an experimental C6D6 energy spectrum for an incident γ-ray with E_0=611 keV.

| Front angles: C_6D_6 scintillators | Back angles: *Ge* detectors |
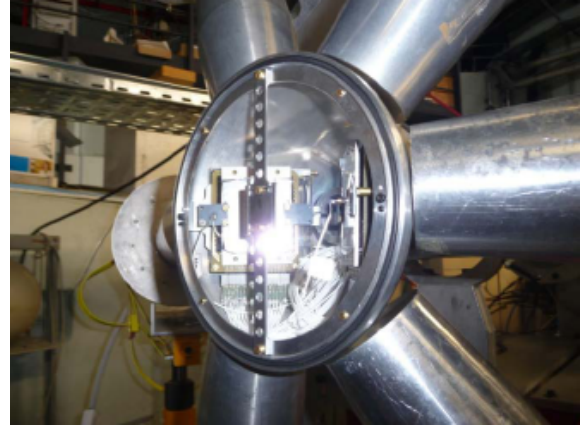
Figure 3.14: Geometry of the γ-ray detectors used in this experiment.
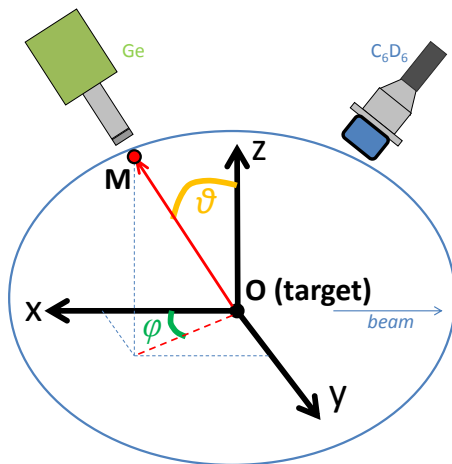
	θ (deg)	φ (deg)
C6D61	150	135
C6D62	150	225
C6D63	30	225
C6D64	30	135
GE1	148	290
GE2	90	290
GE3	32	290
GE4	32	70
GE5	90	70
GE6	148	70

Figure 3.15: Absolute position in spherical coordinates of the C_6D_6 scintillators and the *Ge* detectors in our surrogate experiment.

3.5 Summary of the experimental conditions

Below a practical summary of the experimental conditions (table 3.7) and two pictures of the set-up (figures 3.16 and 3.17) are shown.

Beam ^3He	
Energy	24 MeV
Current	20 nAe with ^{174}Yb target / 50 nAe with ^{12}C target

	Targets	Carbon Backing	Measurements time
^{174}Yb	250 $\mu g/cm^2$	50 $\mu g/cm^2$	98 hours
^{12}C	x	50 $\mu g/cm^2$	38 hours

Telescopes	
ΔE Si	300 μm
E Si(Li)	3000 μm
Distance target-collimator	53 $\pm$0.5 mm
Ni Collimator dim.	32 x 32 mm²
Distance target-ΔE	56$\pm$0.5 mm
Active ΔE surface	33.2 x 33.2 mm²
Opening angles	112°$\rightarrow$145°
Solid angle covered by one telescope	$\sim$0.36 sr
Geometric efficiency for one telescope	$\sim$2.8 %
Total geometric efficiency	$\sim$5.6 %
Mylar(Al) [polarized at -300V]	2 μm

C_6D_6 scintillators and Ge detectors	
Mean distance target-C_6D_6	90 mm
Dimensions of the cavity cell	106 x 76.2 mm²
Geometric efficiency for one C_6D_6	8.67 %
Mean distance target-Ge	90.5 mm
Spherical coordinates of the detectors	see figure 3.15

Table 3.7: Practical summary of the experimental conditions
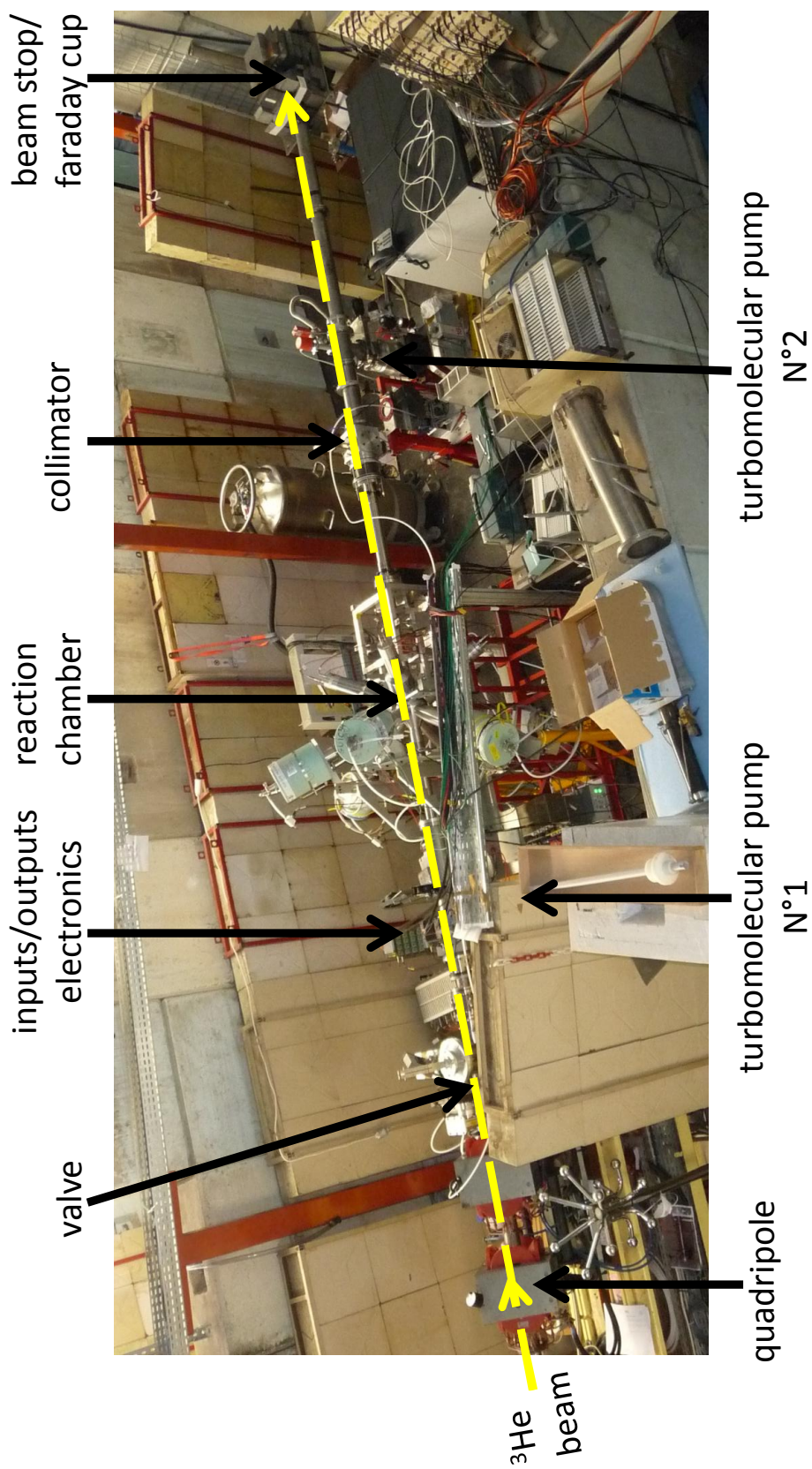
Figure 3.16: Picture of the whole experimental set-up.
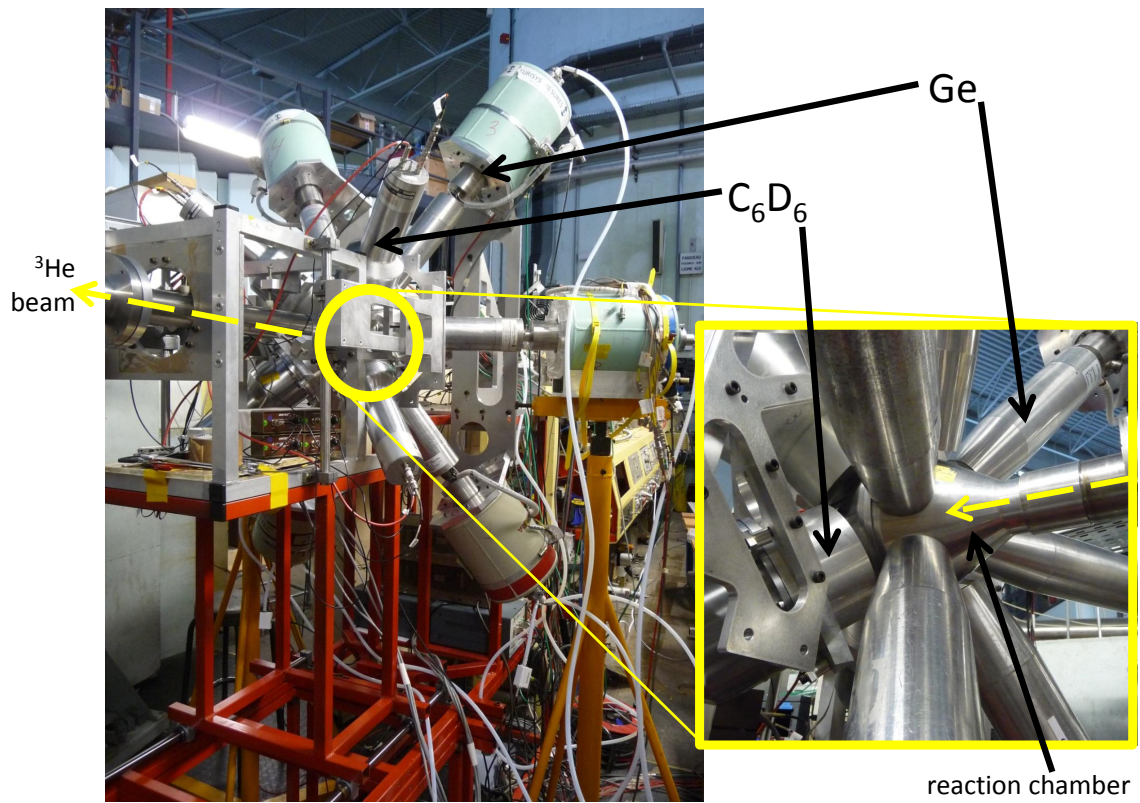
Figure 3.17: Picture of the surrounding of the reaction chamber.

3.6 Electronics and data acquisition

Details about the electronics used for this experiment can be found in figures 3.18, 3.19 and 3.20 for the read out of the telescopes, the C_6D_6 and the Ge, respectively.

Data were processed via the GANIL acquisition system. Several VME cards were used: two 32-channel ADC, one 16-channel ADC, one 16-channel TDC (CAEN V785, V785N and V775N, respectively). The acquisition was triggered via a TGV module (Trigger Generic VME), which permits handling single and coincidence events for each detector in different possible experimental configurations. For the $\triangle E$ detectors the polarization and the pre-amplification of the output signal for each XY strip was operated by a 16-channel motherboard, developed at the CENBG. The **A** output (see fig. 3.18) was made by the logical OR of all the vertical Y strips for both detectors, the logical signals were generated by two CFDs (VME V812 modules with 20 ns delay). Using standard electronics, an OR of the logical signals associated to $Si(Li)$ 1 and 2 was generated and defined as the **B** output (see fig. 3.18). Finally, for the γ-emission probability measurements, the acquisition was triggered by **(A&B)** which corresponds to the equivalent logical OR of signals from any of the two telescopes (logical AND from $\triangle E$ and E signals). When a trigger signal arrived, a time window of 4 μs was generated to register the eventual signals from the C_6D_6 and Ge detectors. A VME (CAEN V560) scaler gave on-line counting rates of the telescopes. Note that the end-line Faraday cup was coupled to an integrator in order to monitor the ^3He current during the different measurements.

Gamma measurements with C_6D_6 scintillators and Ge detectors were carried out using standard NIM modules. For the C_6D_6, the neutron/gamma discrimination was made with a PSD of the anode output signal using the Mesytec MPD-4 module, whereas the energy signal was obtained in parallel via the output signal of the seventh dynode. The electronics used for the PSD analysis is fully detailed in appendix E. In the case of the C_6D_6 calibration, the acquisition can be triggered by **D** (see fig. 3.19), namely the logical OR of signals from any of the four C_6D_6 scintillators. The Ge output signals were amplified with a 16-channel main amplifier. The trigger **C**, which is the logical OR of the Ge signals, permits to obtain γ-spectra for the Ge detectors. TDC outputs were generated for each γ detector providing the time difference (within a dynamical range of 1.2 μs) between the start signal, given by the detection of an ejectile in one of the telescopes, and the stop signal either from the C_6D_6 scintillators or the Ge detectors.

Each detected event was coded into 4096 channels and was recorded sequentially in list mode. The PHWT was applied offline.
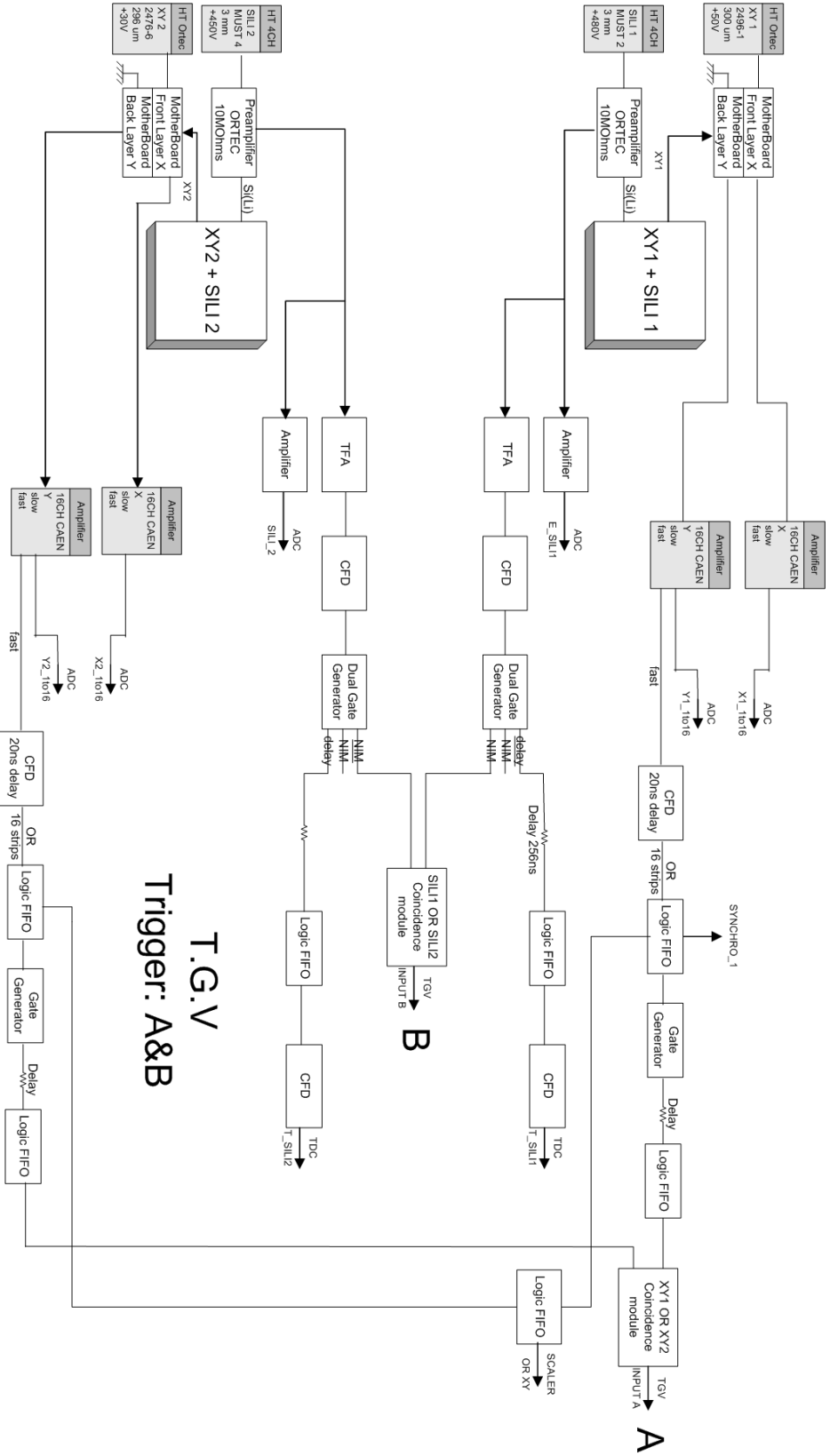
Figure 3.18: Block diagram used for our $\Delta E - E$ telescopes. The coincidence was made with a TGV module, controlled via a VME interface.
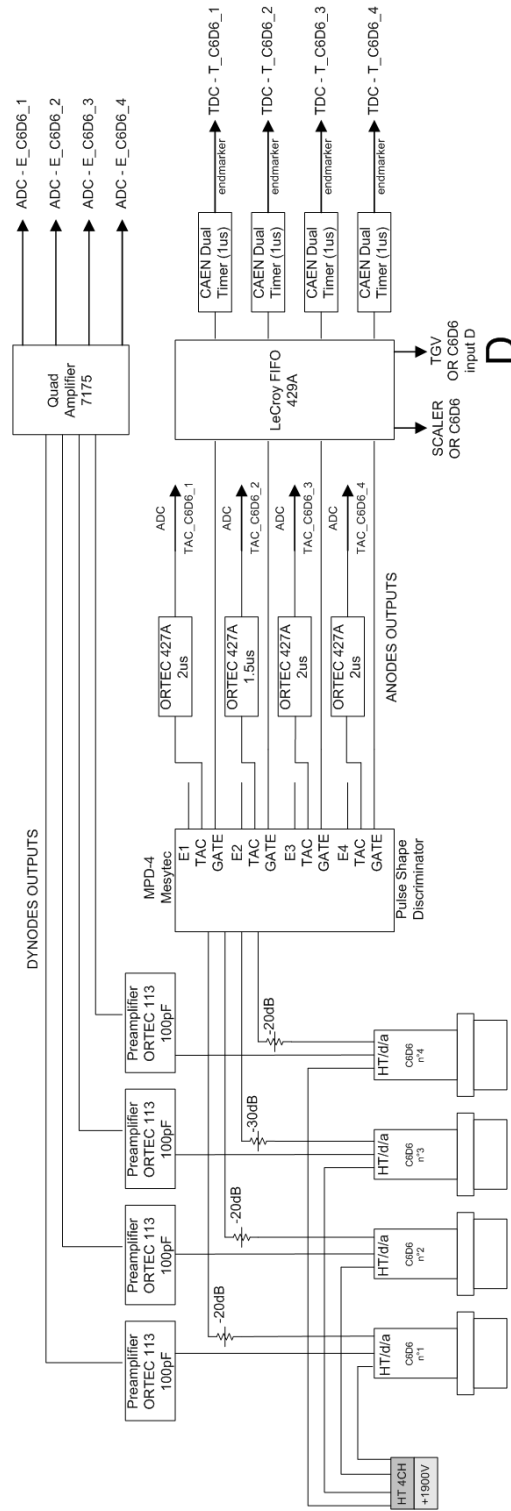
Figure 3.19: Block diagram of the electronics used for the C_6D_6 scintillators. Note that the PSD is made via an integrated NIM module, called MPD-4, which plays the role of four standard zero-crossing pulse shape discrimination circuits.
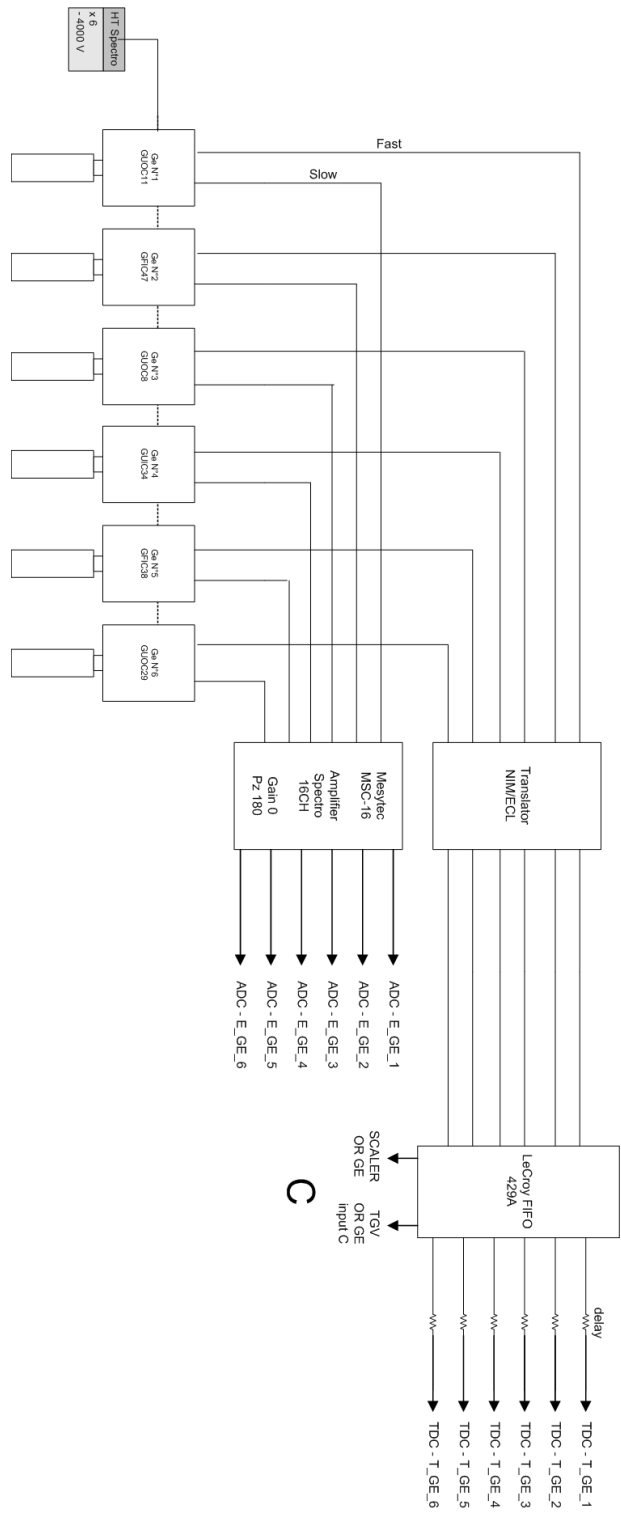
Figure 3.20: Block diagram of the electronics used for the *Ge* detectors.

Chapter 4

Data Analysis

4.1 Singles-spectra analysis

4.1.1 Energy calibration of the telescopes

The energy calibration of the telescopes was performed using the transfer reactions $^{208}Pb(^3He,d)^{209}Bi^*$ and $^{208}Pb(^3He,\alpha)^{207}Pb^*$. The incident energy of the ^3He beam was 24 MeV. The target consisted of 200 $\mu g/cm^2$ of ^{208}Pb deposited on a carbon backing. These reactions allow us to populate the first excited states of $^{209}Bi^*$ and $^{207}Pb^*$ whose energies are very well known. When one of these states is populated, the ejectile (d or α) has a well defined energy which can be easily calculated from the reaction kinematics. The advantage of this calibration method with respect to the use of standard α-sources is that we can calibrate the Si-detectors with different incident particles and with energy ranges similar to the ones encountered in the surrogate reactions of interest. The $\triangle E - E$ identification matrix relative to the reaction $^3He +^{208} Pb$ is given in figure 4.1. Each exited state was selected with a contour. Then, the RMS deviation of its projection in channels onto the ΔE and E axis is associated to the calculated energy losses, as illustrated for strip Y8 in table 4.1. Each vertical (Y) strip was calibrated independently. We recall that the horizontal (X) strips are not used in this work. The Si(Li) detectors were calibrated in association with each strip to avoid errors due to a non-uniformity of the charge collection. Finally, we extracted linear calibration coefficients for each vertical ΔE strip and the corresponding area of the Si(Li) in its shadow. The charge collection in a silicon detector depends on the atomic number Z of the detected particle ([Leo 87]). The set of calibration parameters determined with the $^{208}Pb(^3He,d)$ reaction is used for the excitation-energy determination of the compound nuclei associated to surrogate reactions with the ejectiles p,d and t. The second set obtained with the $(^3He,\alpha)$ reaction is used for reactions with heavier ejectiles as ^3He and α particles. Calibration parameters and errors are presented in appendix F.
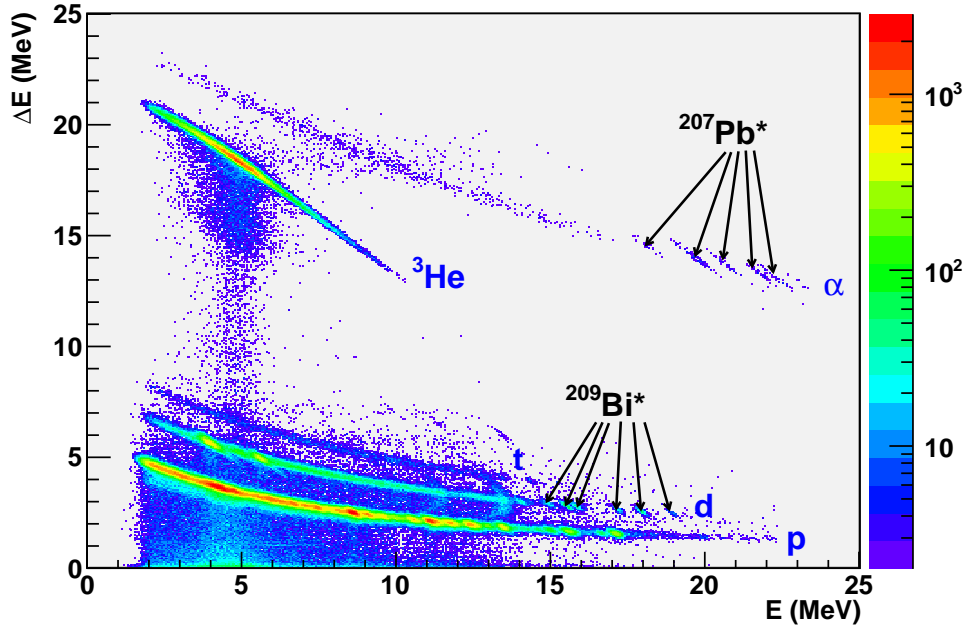
Figure 4.1: Identification matrix relative to the reaction $^3He +^{208} Pb$. The first excited states of $^{207}Pb^*$ and $^{209}Bi^*$ are indicated.

Reaction	Q-value (MeV)	E^* of the excited states (MeV)	$\theta_{Y8} = 130, 19°$		
			Ejectile energy (MeV)	Energy loss (LISE++) (MeV)	
				$E_{mylar-2\mu m}$	$\triangle E$	E
$^{208}Pb(^3He,d)^{209}Bi^*$	-1,696	0	21.4083	0.011545	2.4832	18.914
		0,896	20.5278	0.011981	2.5729	17.943
		1,608	19.8283	0.012301	2.6502	17.166
		2,826	18.6319	0.012955	2.7957	15.823
		3,119	18.3441	0.013130	2.8337	15.497
		3,638	17.8344	0.013415	2.9045	14.916
$^{208}Pb(^3He,\alpha)^{207}Pb^*$	+13,21	0	35.5377	0.053634	12.659	22.825
		0,570	34.9833	0.054399	12.885	22.044
		0.898	34.6643	0.054835	13.017	21.593
		1.633	33.9496	0.055601	13.331	20.563
		2.340	33.2622	0.056668	13.655	19.550
		3.475	32.1597	0.058342	14.226	17.875

Table 4.1: Energies of ejectiles for the different excited states of $^{209}Bi^*$ and $^{207}Pb^*$ and corresponding energy losses in the different layers of matter for the ejectiles traversing the strip Y8 of the ΔE detector.

4.1.2 Experimental excitation-energy resolution

After calibration, the experimental excitation-energy resolution σ_{E*} can be inferred from the calibrated E^* spectra of ^{209}Bi and ^{207}Pb. Figure 4.2 shows the E^* spectra for ^{209}Bi and ^{207}Pb that result from the sum of the spectra associated to each strip. The matching in excitation energy is very good since the calibration is precisely based on these excited states. The total resolution has been found to be around 60 keV and 80 keV for the $(^3He, d)$ and $(^3He, \alpha)$ channels, respectively. These values are higher than the predictions presented in table 3.4. However, the experimental determination of σ_{E*} has the advantage to integrate all the possible sources of errors. That is why, for the determination of radiative-capture probabilities, the excitation energy was chosen to be divided in energy bins of 80 keV to reduce the statistical error and to avoid to take possible narrow statistical structures in the spectra for physical.

$^{208}Pb(^3He, d)^{209}Bi^*$ $^{208}Pb(^3He, \alpha)^{207}Pb^*$
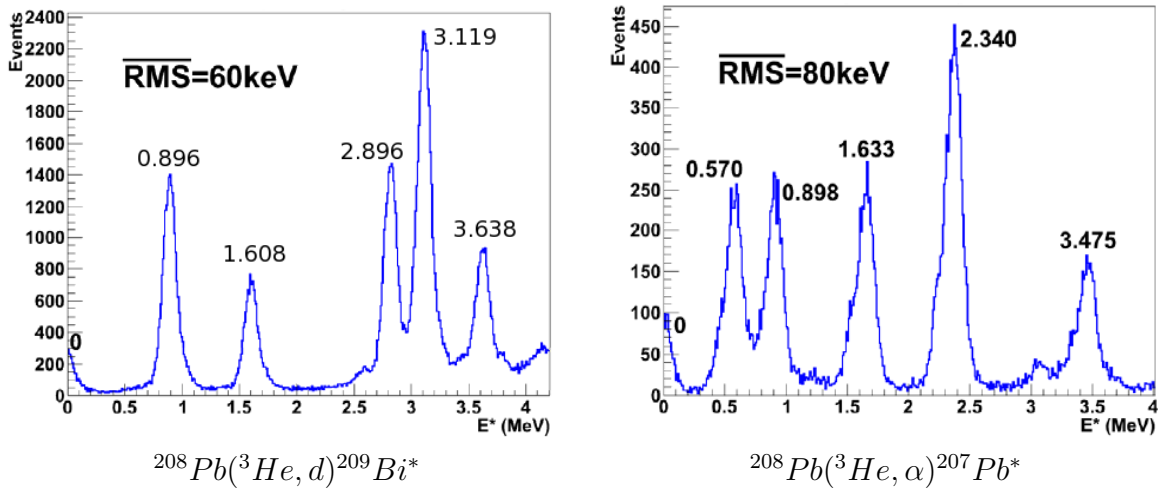
Figure 4.2: Excitation-energy spectra for $^{209}Bi^*$ and $^{207}Pb^*$. The experimental values for the E^* of the different excited states are indicated.

4.1.3 Singles spectra and contaminants subtraction

The first ingredient in the determination of the radiative capture probabilities is the energy spectrum of the ejectiles, which is commonly called the singles spectrum. The singles events are corrected from the random events under the coincidence peak in the time spectra for $\triangle E - E$. As explained previously, the relation between the energy of the ejectile and the excitation energy of the associated compound-nucleus is given by the kinematics. Figure 4.3 illustrates how equation 3.15 is applied to a singles spectrum.

We observe clearly the presence of large peaks in the energy spectra originating mainly from transfer reactions on the carbon backing. We performed a measurement with a carbon target of $50\ \mu g/cm^2$ under the same experimental conditions in order to determine

Proton spectrum   Excitation energy spectra
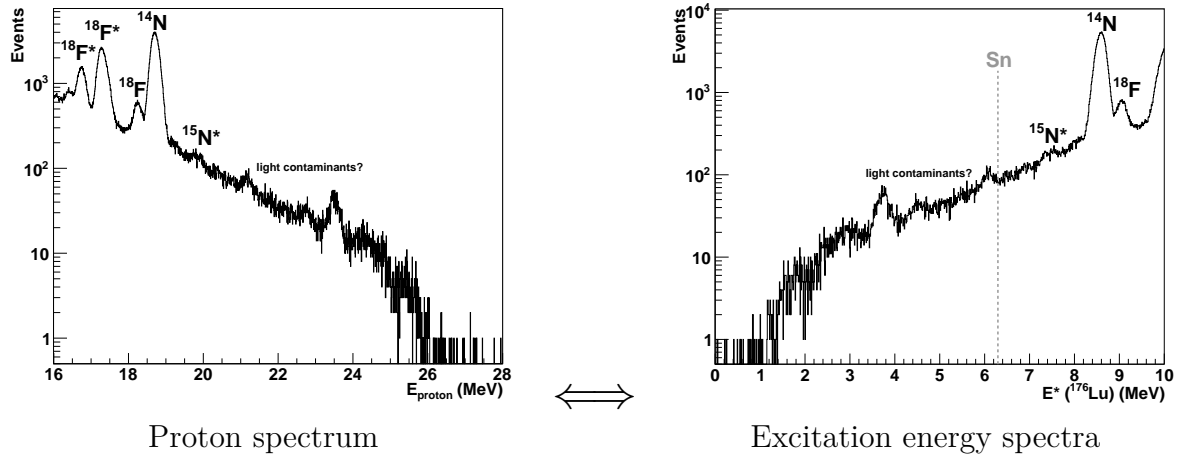
Figure 4.3: Singles spectrum for the reaction $^{174}Yb(^3He,p)^{176}Lu^*$ as a function of the ejectile energy (left) and as a function of E^* of $^{176}Lu^*$(right).

the background events coming from the backing. For the background subtraction, the two data sets have to be normalized. Two possibilities exist:

- via the integration of the ^3He current across the end-line Faraday cup during the two measurements.

or

- by using the most intense proton peak of the $^{12}C(^3He,p)^{14}N_{g.s}$ reaction.

In our case, the first method failed. The distance between the Faraday cup and the target was about five meters and part of the beam did not hit the Faraday cup. Consequently we applied the second method. The subtraction is directly done via the following relation:

$$N^x_{single}(E^*) = N^x_{part}(E^*) - f_{norm}.N^x_{bkg}(E^*) \tag{4.1}$$

where:

- $N^x_{single}(E^*)$ is the number of ejectiles x in the surrogate reaction involving only the nucleus ^{174}Yb as function of the excitation energy E^* of the corresponding CN.

- $N^x_{part}(E^*)$ is the number of ejectiles x detected in the surrogate experiment, including reactions in the target ^{174}Yb and in the backing.

- $N^x_{bkg}(E^*)$ is the number of ejectiles x detected in the background measurement using a carbon backing.

- f_{norm} is the normalization factor and is equal to 2,25. This value corresponds to the average ratio of the area under the $^{14}N_{g.s}$ peak in the two data sets. Note that this value was the same within 1% fluctuations for all strips and for all transfer reactions.

Unfortunately, in the measurement of $N^x_{part}(E^*)$, the ejectiles produced in the carbon backing interacted with the lutetium layer before its detection but this was not the case for $N^x_{bkg}(E^*)$. This lead to a small broadening and an energy shift between $N^x_{part}(E^*)$ and $N^x_{bkg}(E^*)$. The subtraction is done individually for each strip. Proton singles spectra before and after carbon-background subtraction for three detection angles are shown in figure 4.4. The small $^{13}C(^3He, p)^{15}N^*$ contribution that is present in the excitation energy range from $[S_n; S_n + 1]$ MeV is well suppressed. However, because of important fluctuations resulting from the subtraction of two big numbers, the region corresponding to the highest background peak has been excluded from the analysis. In addition, we have excluded several few regions where unidentified contaminants were present. The obtained total singles spectra for protons, deuterons, tritons and alphas are given in figure 4.5. These spectra have been obtained by summing the spectra associated to each strip for both telescopes.
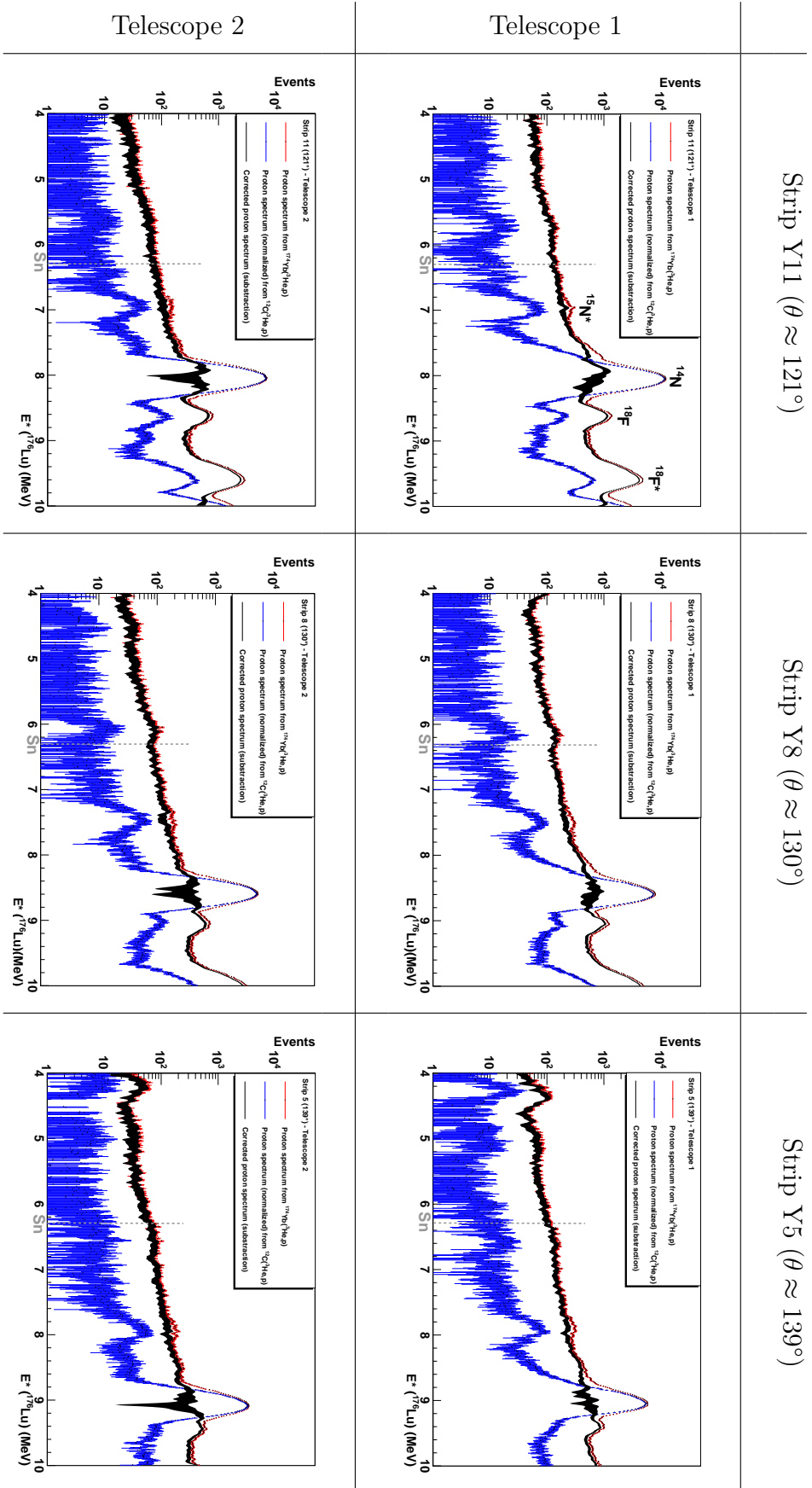
Figure 4.4: Singles spectra for protons for several emission angles before and after the subtraction of events coming from the carbon support. The normalized singles spectra of ^{14}N is also shown.
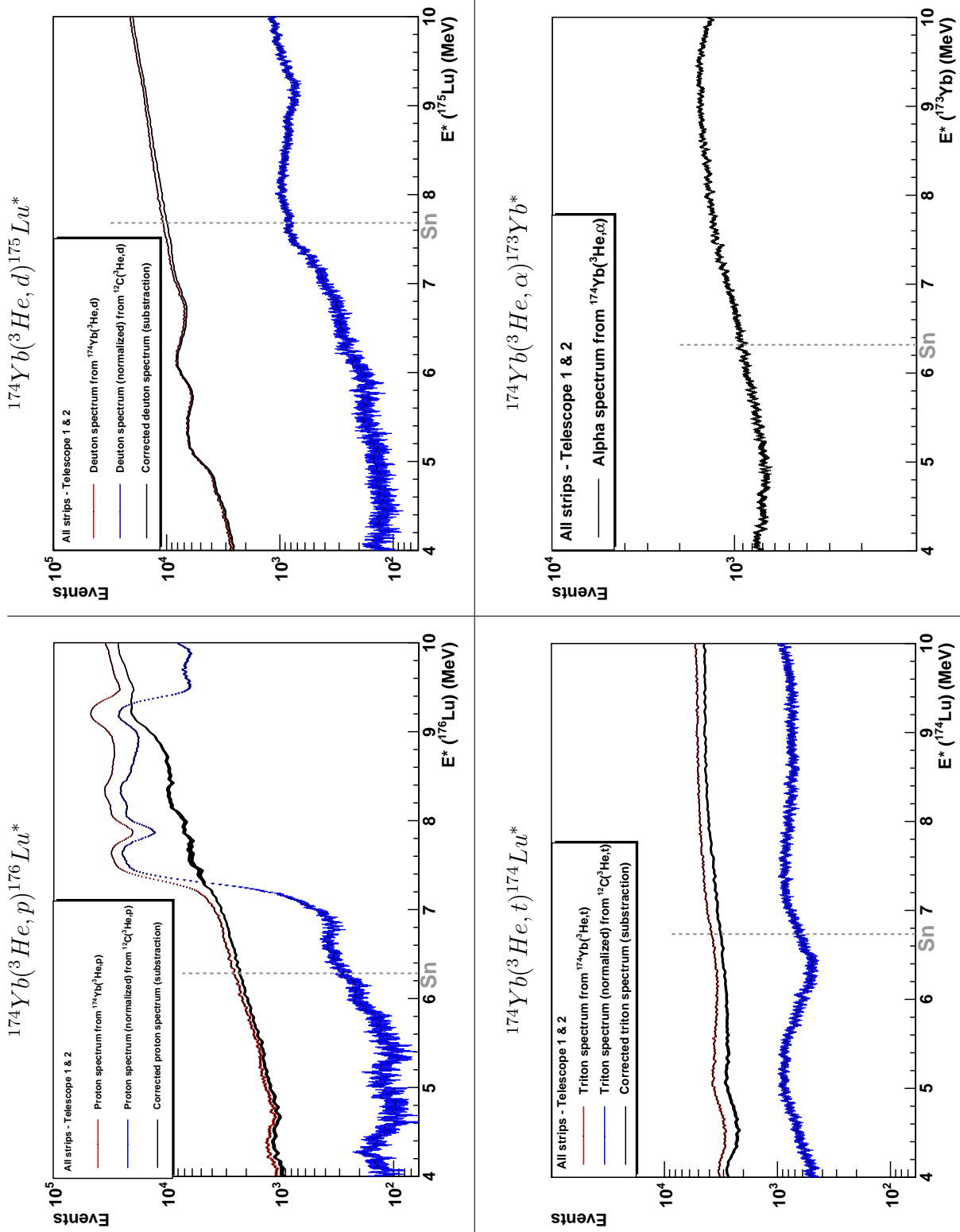
Figure 4.5: Total singles spectra for protons, deuterons, tritons and alphas.

4.2 Coincidence-spectra analysis

The second ingredient in the determination of the radiative capture probabilities is the energy spectra of the ejectiles in coincidence with gamma rays detected by one of the C_6D_6 scintillators. The γ-detection threshold was raised to 200 keV for each C_6D_6 detector in order to simplify the shape of the γ-spectra at the electronic threshold. To generate the coincidence spectra we selected the ejectiles for which the time difference telescope-C_6D_6 lies in the coincidence peak and for which the associated C_6D_6 signal corresponds to a γ-ray and not to a neutron. As illustrated in figure 4.6, the width of the coincidence peak between the telescope and the C_6D_6 detectors was about 37 ns. The small amount of random coincidences under the peak was subtracted. An example of contour used to disentangle γ-rays from neutrons is shown in figure 4.7.
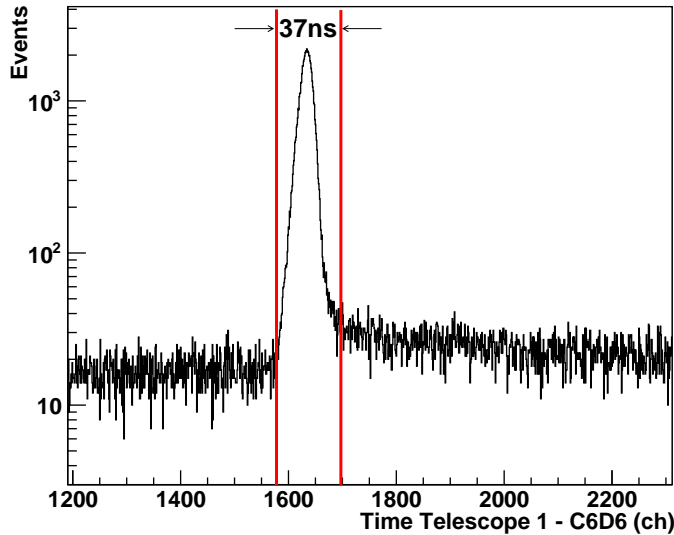
Figure 4.6: Time spectrum between telescope 1 and C_6D_6 1.

As for the singles spectra, the contribution of γ-rays coming from the excited states of $^{15}N^*$ was subtracted from the coincidence spectra using the carbon-backing coincidence spectra. The subtraction was done individually for each strip in coincidence with each C_6D_6 detector. In the same manner as eq. 4.1, the subtraction was done via the following relation:

$$N_{coinc}^x(E^*) = N_{gamma}^x(E^*) - f_{norm}.N_{gamma-bkg}^x(E^*) \tag{4.2}$$

where:

- N_{coinc}^x is the number of coincidences between an ejectile x and a γ-ray in the surrogate reaction involving only the nucleus ^{174}Yb.

- N^x_{gamma} is the number of coincidences detected in the surrogate experiment, including γ-rays originating from the target ^{174}Yb and the backing.

- $N^x_{gamma-bkg}$ is the number of coincidences detected in the background measurement using the carbon backing.

- f_{norm} is the normalization factor and is equal to 2.25, as defined previously.

The obtained total coincidence spectra for protons, deuterons, tritons and alphas are given in figures 4.8, 4.9, 4.10 and 4.11, respectively. They are the result of adding the coincidence spectra of each Y strip. These spectra first increase with E^* and then show a step decrease at $E^* = S_n$ indicating a drastic reduction of the γ-rays emitted due to the competition with neutron emission. The S_n-values found experimentally are in good agreement with the tabulated values for all the compound nuclei (cf. table 3.3).
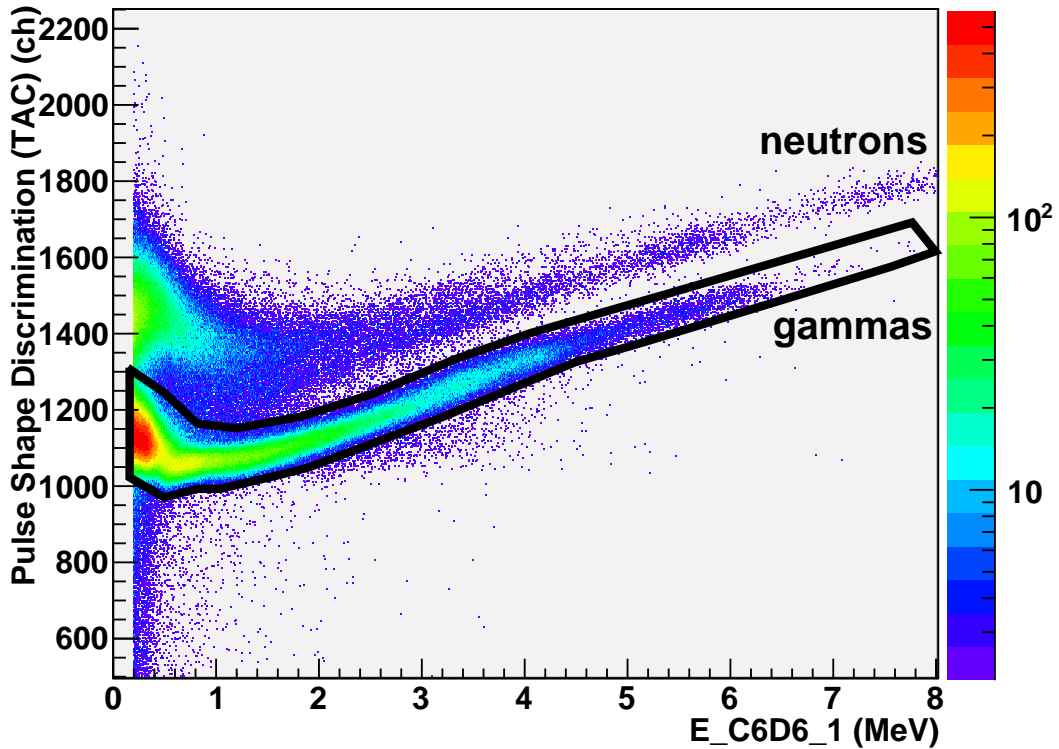
Figure 4.7: Pulse Shape Discrimination (PSD) signal vs. deposited energy in a C_6D_6. The contour indicates the selection of γ-rays.
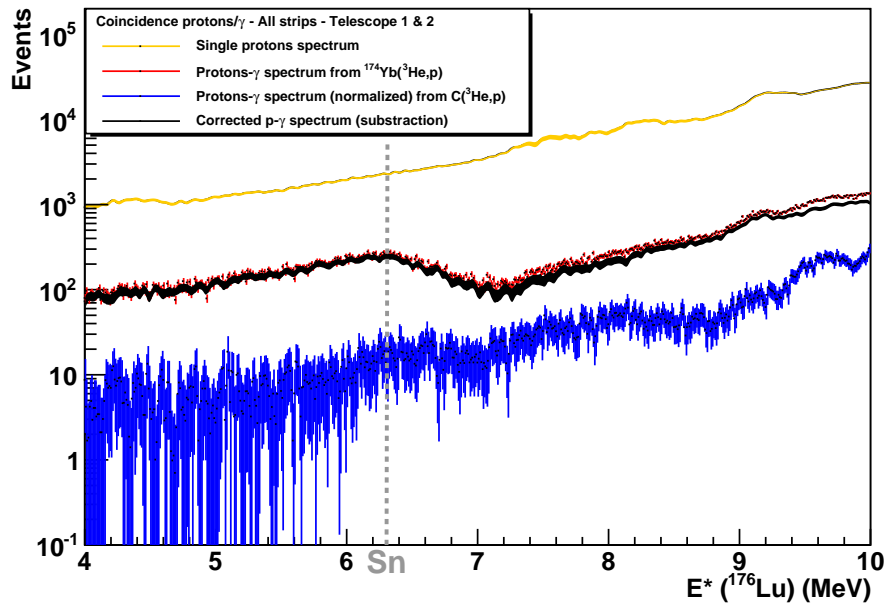
Figure 4.8: Coincidence spectrum for protons before and after the subtraction of coincident events coming from the carbon support. The normalized coincidence spectrum of ^{14}N is given. The dashed vertical line indicates the tabulated neutron-separation energy of the corresponding CN. For completeness, the singles spectrum for protons is also shown.
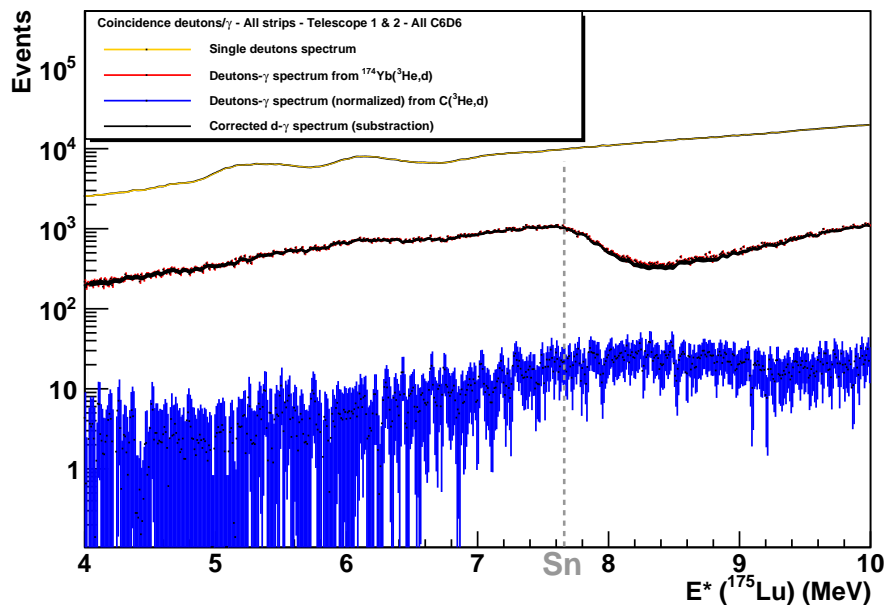
Figure 4.9: The same as in Fig. 4.8, but for deuterons.
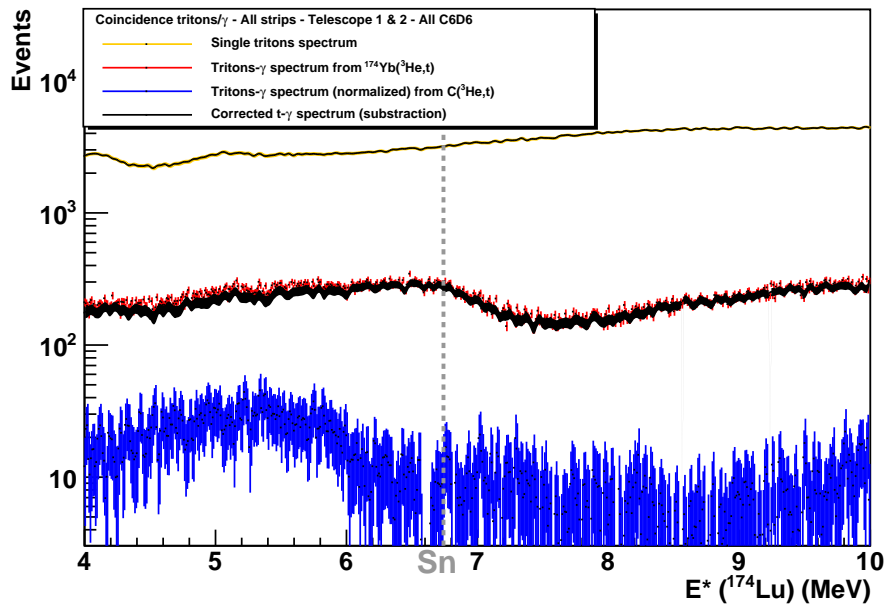
Figure 4.10: The same as in Fig. 4.8, but for tritons.
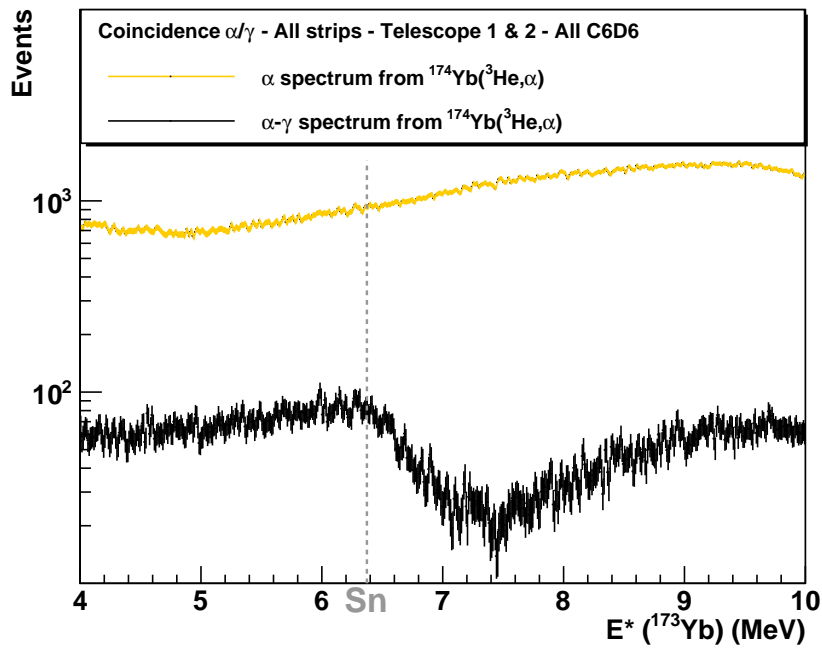
Figure 4.11: The same as in Fig. 4.8, but for alphas.

4.3 Gamma-cascade detection efficiency

The last ingredient in the determination of the radiative capture probabilities is the γ-cascade detection efficiency. As introduced in section 3.4.1.2, we applied the total-energy principle using the PHWT. For completeness, we recall that the total-energy principle needs two important conditions:

- a low detection efficiency ($\epsilon_i \ll 1$).

- the proportionality between the gamma energy E_γ and its detection efficiency ε_γ ($\varepsilon_\gamma = k.E_\gamma$).

The first condition ensures that the probability to detect two γ-rays coming from the same cascade is negligible, and consequently, the detection efficiency of any cascade ϵ_c is equal to the sum of the efficiencies for detecting the individual γ-rays in the cascade:

$$\epsilon_c \underset{\epsilon_i \ll 1}{\approx} \sum_i \varepsilon_{\gamma_i} \tag{4.3}$$

To ensure the validity of eq. 4.3 with our experimental set-up, events with more than one C_6D_6 fired were counted only once and the corresponding C_6D_6 energy signal was randomly selected between the touched detectors. The measured proportion of dual counts was always below 3.8%[1]. The proportionality condition yields:

$$\epsilon_c \underset{\varepsilon_\gamma = k.E_\gamma}{=} k.\sum_i E_{\gamma_i} \longrightarrow \epsilon_c = k.E_c \tag{4.4}$$

where the energy of the γ-cascade E_c corresponds to the excitation energy E^* of the compound-nucleus. The γ-cascade-efficiency becomes independent of the γ-path within the cascade. For example, this means that the probability to detect a γ-cascade of total energy $E_c = 5$ MeV is the same if the γ-cascade is made of a single γ-ray of energy $E_{\gamma_i} = 5$ MeV or of five γ-rays of energy $E_{\gamma_i} = 1$ MeV. However, our γ-ray detectors do not fulfill the proportionality condition. The PHWT was hence applied to achieve the proportionality of the detection efficiency with γ-energy. In this work, we have developed an alternative method to determine the γ-cascade detection efficiency. This method is based on the hypothesis that the γ-cascade efficiency is independent of E^*. The two methods will be compared.

---

[1]The proportion of dual counts in our C_6D_6 detection set-up was also investigated using $^{176}Lu^*$ γ-cascade simulations with DICEBOX. The average γ-ray energy and multiplicity were about 1 MeV and 6, respectively. At $E^* = 6.29$ MeV, dual and triple counts were estimated to reach 4.1% and 0.08%, respectively.

4.3.1 The PHWT

4.3.1.1 Methodology of the PHWT

The PHWT achieves the proportionality of the detection efficiency ϵ_i with γ-energy E_i mathematically weighting the response function of the detector with an appropriate function. The application of the method requires the determination of a set of response distributions for γ-ray energies up to about 10 MeV. Since it is not possible to determine them all experimentally for such a broad range of γ-energies, we measured the responses for several γ-rays and obtained the rest by interpolation through Monte-Carlo simulations. The detector response function $R(E_d, E_i)$ is nothing but the probability that an incident γ-ray with an energy E_i deposits an energy E_d in the detector. In our case, since the gamma-ray interacts with a C_6D_6 scintillator primarily via the Compton scattering process, the detected energies lie in a distribution, $R(E_d)$, covering all energies up to the Compton-edge. For a given γ-ray with incident energy E_i, the sum of the response function over E_d verifies:

$$\sum_{E_d} R(E_d, E_i) = \varepsilon_i^{exp} \tag{4.5}$$

where ε_i^{exp} is the experimental detection efficiency. We introduce a «weighting function» $W(E_d)$ that weights the response function $R(E_d, E_i)$:

$$\sum_{E_d} W(E_d).R(E_d, E_i) = \varepsilon_i^{weighted} \tag{4.6}$$

where $\varepsilon_i^{weighted}$ is the weighted detection efficiency that fulfills the proportionality with the corresponding γ-ray energy:

$$\varepsilon_i^{weighted} = \varepsilon_i^{desired} = k.E_i \tag{4.7}$$

The combination of equations 4.6 and 4.7 yields:

$$\sum_{E_d} W(E_d).R(E_d, E_i) = k.E_i \tag{4.8}$$

The latter equation has to be verified for each incident γ-ray energy E_i. Figure 4.12 illustrates how the weighting of the response function modifies the experimental efficiency function $\varepsilon_i^{exp}(E_i)$, represented schematically by the black full circles. The desired efficiency function $\varepsilon_i^{desired}(E_i)$ corresponds to a linear function determined by the proportionality factor k (blue dashed line). As shown in figure 4.12, the weighting function is independent of the energy of the γ-cascade considered. $W(E_d)$ is a unique function that weights the response functions $R(E_d, E_i)$ for each E_i in order to fulfill eq. 4.7. The solution of the weighting function $W(E_d)$ is obtained by χ^2 minimization over

E_i:

$$minimize\left(\chi^2 = \sum_{E_i}\left[\sum_{E_d}\left(W(E_d).R(E_d,E_i)\right) - k.E_i\right]^2\right) \tag{4.9}$$

where the weighting function is adequately parametrized with a fifth-degree polynomial:

$$W(E_d) = \sum_{n=1}^{N=5} a_n.\left(E_d\right)^n \tag{4.10}$$

Then, combining equations 3.6 and 4.8, the radiative capture probability is given by:

$$P_\gamma^{WF}(E^*) = \frac{N_{coinc}(E^*)}{N_{singles}(E^*).\epsilon_\gamma(E^*)} = \frac{\sum_{E_d}\left[N_{coinc}^{C_6D_6}(E^*,E_d).W(E_d)\right]}{N_{singles}(E^*).\epsilon_\gamma^{WF}(E^*)} \tag{4.11}$$

where $N_{coinc}^{C6D6}(E^*,E_d)$ is the C_6D_6 γ-spectrum associated to the coincidence spectrum $N_{coinc}(E^*)$. The γ-cascade efficiency $\epsilon_\gamma^{WF}(E^*)$ is given by eq. 4.4 in the framework of the total-energy detection principle. Finally, this yields:

$$P_\gamma^{WF}(E^*) = \frac{\sum_{E_d}\left[N_{coinc}^{C_6D_6}(E^*,E_d).W(E_d)\right].F_{corr}}{N_{singles}(E^*).k.E^*} \tag{4.12}$$

where the proportionality coefficient k is usually taken equal to 1 MeV^{-1}. A correction term F_{corr} is added to take the experimental γ-ray detection threshold into account. It will be discussed in section 4.3.1.8.

Weighting functions depending on the excitation energy

In equation 4.9, the χ^2-value was determined from a minimization over the whole range of incident γ-energies. We know that the upper limit for the incident γ-ray energy E_i is given by the total energy E_c of the γ-cascade which corresponds to the excitation energy E^* of the compound-nucleus. In order to optimize the quality of the weighting functions, one can perform the χ^2 minimization only for incident γ-ray energies below the excitation energy of interest. That is why the weighting functions are usually calculated for a set of different excitation energies. Thus for a given γ-cascade of energy $E_c = E^*$, eqs. 4.9 and 4.12 become:

$$minimize\left(\chi^2 = \sum_{E_i=0}^{E_i=E_c=E^*}\left[\sum_{E_d}\left(W_{E^*}(E_d).R(E_d,E_i)\right) - k.E_i\right]^2\right) \tag{4.13}$$

$$P_\gamma^{WF}(E^*) = \frac{\sum_{E_d}\left[N_{coinc}^{C_6D_6}(E^*,E_d).W_{E^*}(E_d)\right].F_{corr}}{N_{singles}(E^*).k.E^*} \tag{4.14}$$

where $W_{E^*}(E_d)$ is the weighting function for the excitation energy E^*.
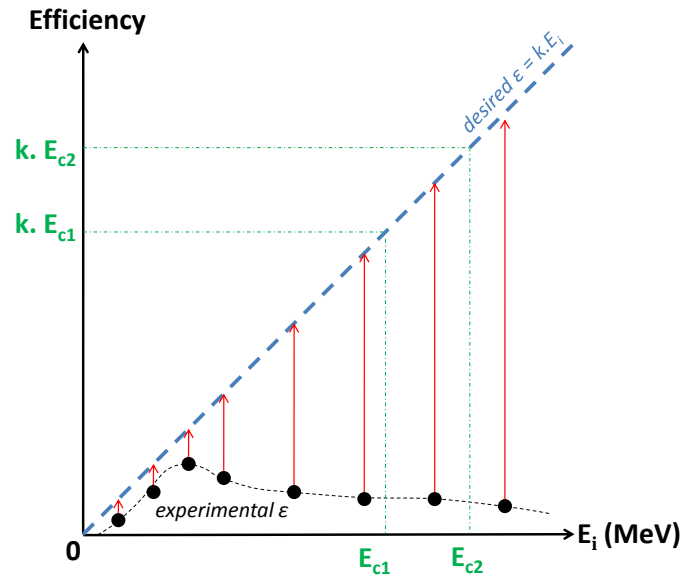
Figure 4.12: Principle of the weighting function technique for $k = cst$. The black points represent the experimental efficiency $\varepsilon_{\gamma i}$ for a given E_i. The red arrows show how the deduced weighting function $W(E_d)$ applies. The two examples (for two different γ-cascade energies) show that the weighting function $W(E_d)$ determination is independent on the γ-cascade energy considered.
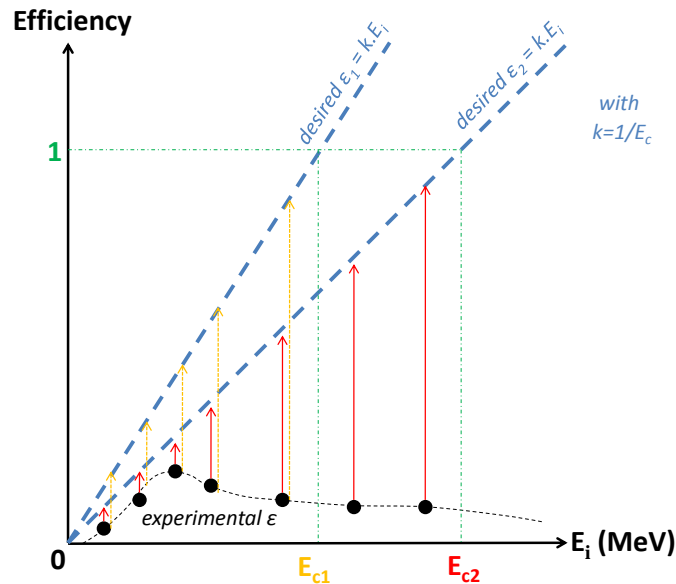
Figure 4.13: The same as Fig. 4.12 but for $k = \frac{1}{E_c}$ MeV^{-1}. The two examples (for two different γ-cascade energies) show how the weighting function $W_{E^*}(E_d)$ determination depends on the γ-cascade energy considered.

Our approach

In our case , the proportionality factor k was taken equal to $\frac{1}{E_c}$ or $\frac{1}{E^*}$ MeV^{-1}. Consequently the desired efficiency $\varepsilon_i^{desired}$ is found to be equal to 1 independently of the γ-cascade considered and equation 4.14 can be written as:

$$P_\gamma^{WF}(E^*) = \frac{\sum_{E_d} \left[N_{coinc}^{C_6D_6}(E^*, E_d).W_{E^*}(E_d) \right].F_{corr}}{N_{singles}(E^*)} \qquad (4.15)$$

where the number of capture events is directly deduced by multiplying the detected gamma spectrum $N_{coinc}^{C_6D_6}(E^*, E_d)$ with the associated weighting function $W_{E^*}(E_d)$. Practically, that gives a weighted spectrum whose integral corresponds to the number of capture events. One should stress that the dependence of the desired efficiency function $\varepsilon_i^{desired}(E_i)$ with the γ-cascade energy requires to determine the weighting functions for each γ-cascade energy using eq. 4.13. As illustrated in figure 4.13, the higher the γ-cascade energy, the lower is the weight $W_{E^*}(E_d)$. In our case we determined a set of weighting functions $W_{E^*}(E_d)$ for excitation energy bins of 80 keV.

Forewarned is forearmed

The PHWT analysis is made of several parts, each corresponding to the next subsections:

- Determination of experimental efficiencies and response functions for each C_6D_6 detector, in the 0.1-7 MeV γ-energy range. Energy calibration and resolution for each C_6D_6 detector were determined by comparing the experimental response functions with simulations.

- Simulation of the total response function (sum of the four C_6D_6) for several γ-rays in the range of γ-energies of interest, namely up to 10 MeV.

- Verification of the simulation by comparison with experimental efficiencies and response functions.

- Determination of a continuous response function matrix $R(E_d, E_i)$ by interpolation.

- Determination of weighting functions through minimisation.

- Determination of the threshold correction term F_{corr}.

4.3.1.2 Experimental response functions and efficiencies

In our experiment, we are interested in excitation energies up to about 10 MeV. Therefore, we expect γ-ray energies from few keV to 10 MeV. That is why we need the response functions of the C_6D_6 scintillators for such a wide range of energies.
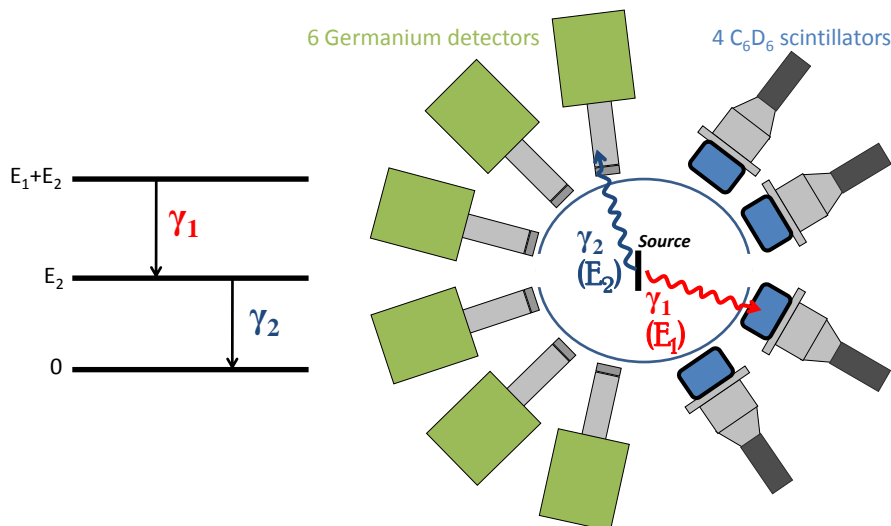
Figure 4.14: Principle of the «Corvi» technique [Corvi 88] applied using our set-up. The detection of $\gamma_1(E_1)$ in one of the C_6D_6 scintillators is made in coincidence with $\gamma_2(E_2)$ detected in one of the Ge detectors. The level scheme corresponding to a γ-cascade of multiplicity 2 is shown on the left.

Response functions can be obtained experimentally by using mono-energetic γ-sources up to 1 MeV. Unfortunately, we only disposed of two of such sources (cf table 4.2). To study the detector response functions for higher γ energies one can use multi-γ sources or nuclear reactions. An experimental method was proposed in [Corvi 88] to infer mono-energetic γ-ray spectra with multi-γ sources. This method requires identifying a γ-cascade of multiplicity 2. A second detector is required for the identification of one of the gamma rays from the cascade. In our case, we use one of our Ge detectors. The measurement of $\gamma_1(E_1)$ in one of the C_6D_6 scintillators is made in coincidence with $\gamma_2(E_2)$ detected in the Ge, as illustrated in figure 4.14. In this way we know the energy of the γ-ray impinging in the C_6D_6 detector. The experimental γ-ray spectra before and after the coincidence technique obtained with a ^{60}Co γ-source are shown in figure 4.15. Note that signals were defined to be coincident if the detector timing pulses arrived within 40 ns of each other. γ-sources and particular proton-induced reactions that can be used with this method are presented in table 4.3.

With our experimental set-up it was possible to use an alternative method to infer mono-energetic γ-ray spectra. It consisted in using inelastic scattering or transfer reactions on light nuclei (^{12}C, ^{13}C and ^{19}F) to populate the first excited states of compound

nuclei that decay directly to the ground state via a single photon emission. The detection of the ejectile gives the excitation energy E^* of the compound-nucleus. We considered the response of the C_6D_6 scintillators in coincidence with the ejectile associated to the excited state of interest, as shown in figure 4.16. The γ-energies considered are reported in table 4.4. Targets of ^{12}C (60 $\mu g/cm^2$), and ^{19}F (105 $\mu g/cm^2$ of CaF_2 on 10 $\mu g/cm^2$ carbon backing) were used with proton-induced (E_p=12 MeV) and ^3He-induced ($E_{^3He}$=24 MeV) reactions.

Source	E_γ(keV)	Duration of measurement
^{137}Cs	661	∼10 minutes
^{54}Mn	834	∼10 minutes

Table 4.2: Mono-energetic γ-sources used for C_6D_6 calibration and efficiency determination.

Source / Reactions	E_1(keV)	E_2 tagged in coincidence (keV)	Duration of measurement
^{152}Eu	344	867	∼1 hour
^{60}Co	1173	1333	∼1 hour
^{60}Co	1333	1173	∼1 hour
^{88}Y	1836	898	∼2 hours
^{232}Th $(^{208}Pb^*)$	2614	860	∼5 hours
$^{34}S(p,\gamma)^{35}Cl^*$	3164	4386	[Corvi 88]
$^{34}S(p,\gamma)^{35}Cl^*$	4386	3164	[Wilson 03]
$^{27}Al(p,\gamma)^{28}Si^*$	5922	6878	cf. Appendix G

Table 4.3: Multi-energetic γ-sources and proton-induced reactions used for C_6D_6 calibration and efficiency determination with the «Corvi» technique shown in fig. 4.14.

Reactions	First excited state (keV)	Duration of measurement
$^{12}C(^3He,p)^{14}N^*$	2313	∼34 hours
$^{12}C(p,p')^{12}C^*$	4440	∼6 hours (20nA)
$^{19}F(p,\alpha)^{16}O^*$	6915 - 7117	∼10 hours (20nA)

Table 4.4: Transfer-induced or inelastic scattering reactions used for C_6D_6 calibration and efficiency determination.

Note that the $^{34}S(p,\gamma)^{35}Cl^*$ and $^{27}Al(p,\gamma)^{28}Si^*$ reactions were not used to extract high energy gamma-rays in the present experiment. However, a preliminary experiment was dedicated to the characterisation of our detectors at the AIFIRA facility of the CENBG using these reactions. This study is presented in appendix G. Finally, a total of ten response functions for each C_6D_6 detector has been obtained for the energies reported in previous tables.

Experimental efficiencies were deduced from the response functions. By using mono-energetic γ-sources of known activity A, the detector efficiency $\epsilon_{C6D6}^{mono-\gamma}$ can be deduced from the number of gamma rays N^γ observed in a given time t. A correction has to be applied to subtract the contribution N^{bkg} coming from the environmental γ-rays.

$$\epsilon_{C6D6}^{mono-\gamma} = \frac{N^\gamma - N^{bkg}}{A.t} \tag{4.16}$$

When using γ-cascades with multiplicity 2, the determination of the efficiency for a photon energy E_1 can be deduced from the area under the Ge photo-peak at energy E_2. More precisely we define:

$$N_{photopeak2}^{TOTAL} = N_0.\epsilon_{germanium}^{\gamma2} \tag{4.17}$$

and

$$N_{photopeak2}^{COINC} = N_0.\epsilon_{germanium}^{\gamma2}.\epsilon_{C6D6}^{\gamma1} \tag{4.18}$$

where:

- $N_{photopeak2}^{TOTAL}$ is the area under the photo-peak at E_2 in the germanium.

- $N_{photopeak2}^{COINC}$ is the area under photo-peak at E_2 in the germanium in coincidence with the C_6D_6.

- N_0 is the number of photons emitted from the source or the number of excited nuclei during the measurement.

- $\epsilon_{germanium}^{\gamma2}$ is the efficiency of Ge detector for E_2.

- $\epsilon_{C6D6}^{\gamma1}$ is the efficiency of C_6D_6 detector for E_1.

Then, an elegant way to determine the efficiency $\epsilon_{C6D6}^{\gamma1}$ is given by:

$$\epsilon_{C6D6}^{\gamma1} = \frac{N_{photopeak2}^{COINC}}{N_{photopeak2}^{TOTAL}} \tag{4.19}$$

Note that the number of emitted photons from the source N_0 and the efficiency of the Germanium detector $\epsilon_{germanium}^{\gamma2}$ are not needed.

Nevertheless, some corrections have to be applied:

- for the anisotropy of the intensity distribution within the solid angle of the detectors due to the angular correlations. Because the angles between the two emitted gamma-rays have been chosen to minimize correlations, no angular distribution corrections have been applied. The appendix H is dedicated to angular correlations and shows under which experimental conditions angular corrections can be neglected.

- for contaminants or missing intensity if the γ-cascade of interest has a little branching in or out of the intermediate level. This correction is not needed when the γ-sources of table 4.3 are used.

In the case of inelastic scattering or transfer reactions, the determination of the efficiency ϵ_{C6D6}^{γ} at the photon energy E_γ is given by the ratio:

$$\epsilon_{C6D6}^{\gamma} = \frac{N_\gamma^{E*}}{N_{ejectile}^{E*}} \tag{4.20}$$

where:

- $N_{ejectile}^{E*}$ is the number of ejectiles detected corresponding to the first excited state E_1^*.

- N_γ^{E*} is the number of ejectiles corresponding to E_1^* in coincidence with a γ-ray detected in a C_6D_6 scintillator.

The experimental efficiencies are shown in figure 4.17.

The experimental spectra will be used to calibrate our detectors. The Compton edge for each γ-ray energy is given in appendix I using eq. 3.24. Unfortunately, the experimental determination of the Compton-edge is imprecise because of the bad resolution of C_6D_6 detectors. A simple way to calibrate the detectors is to assume the position of the Compton-edge at half-height of the maximum of the Compton distribution. In our case, a simultaneous iteration procedure that compares the experimental spectra to Monte-Carlo simulations was used:
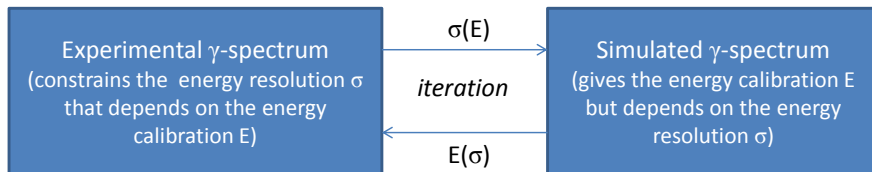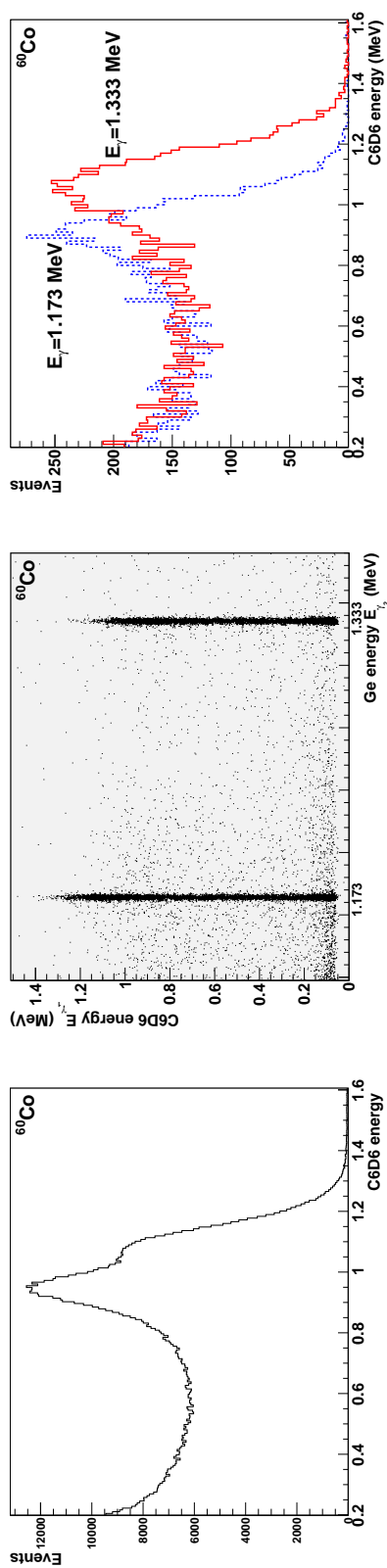
Figure 4.15: From left to right: a raw C_6D_6 response to a ^{60}Co γ-source, a bi-dimensional spectrum representing the measured γ-energy in the C_6D_6 detector vs. the measured γ-energy in the Ge, and the two mono-energetic spectra deduced from the $\gamma_1 - \gamma_2$ coincidence measurement.
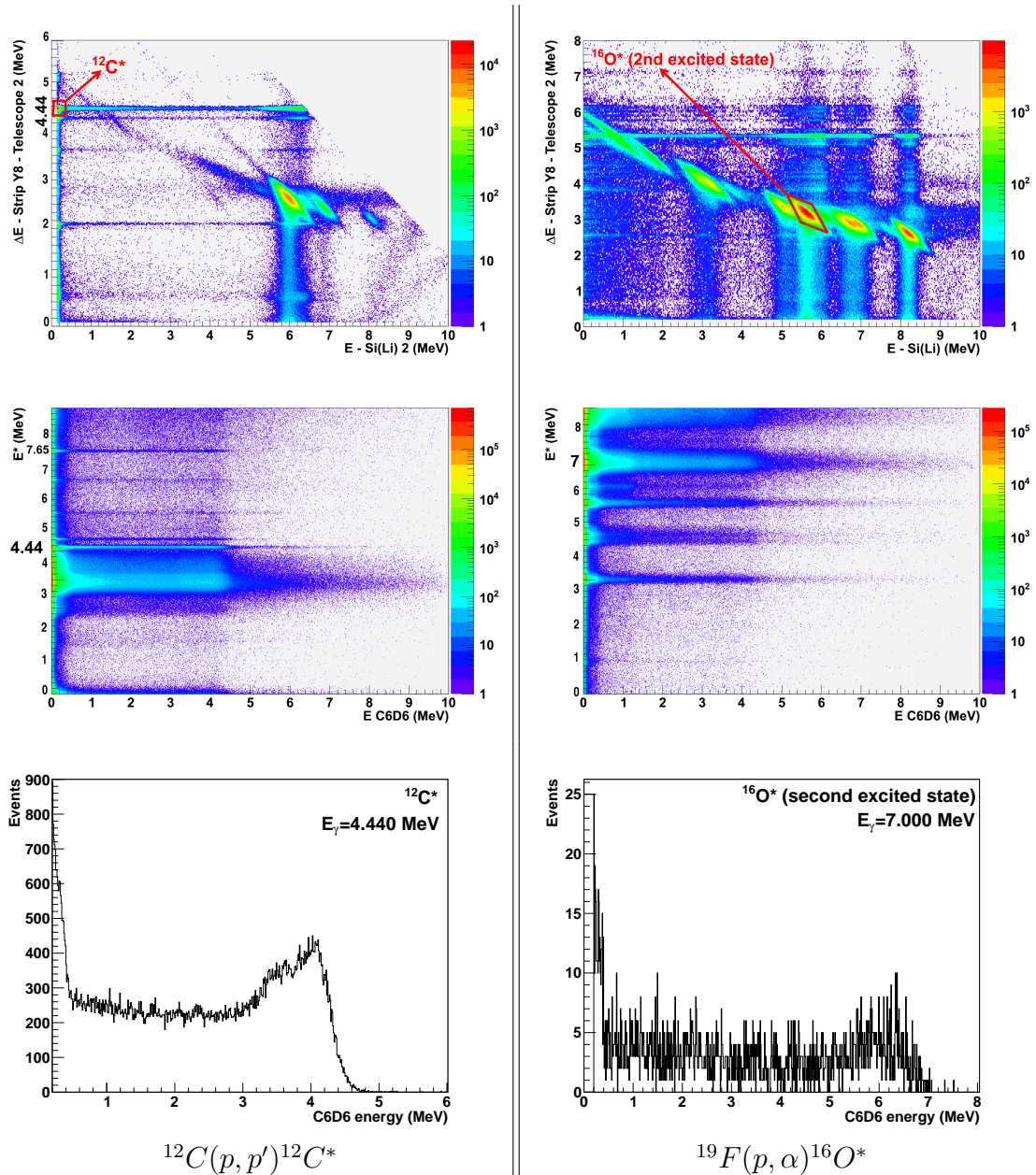
Figure 4.16: Determination of experimental response functions for high-energy γ-rays produced in $^{12}C(p,p')^{12}C^*$(left) and $^{19}F(p,\alpha)^{16}O^*$ (right) reactions. The mono-energetic γ-ray spectra (bottom panels) are obtained in coincidence with the ejectile by selecting the excited state of interest in a $\triangle E - E$ identification matrix (upper panels) or alternatively with a bidimensional plot representing the excitation energy vs. the deposited energy in the C_6D_6 (middle panel).
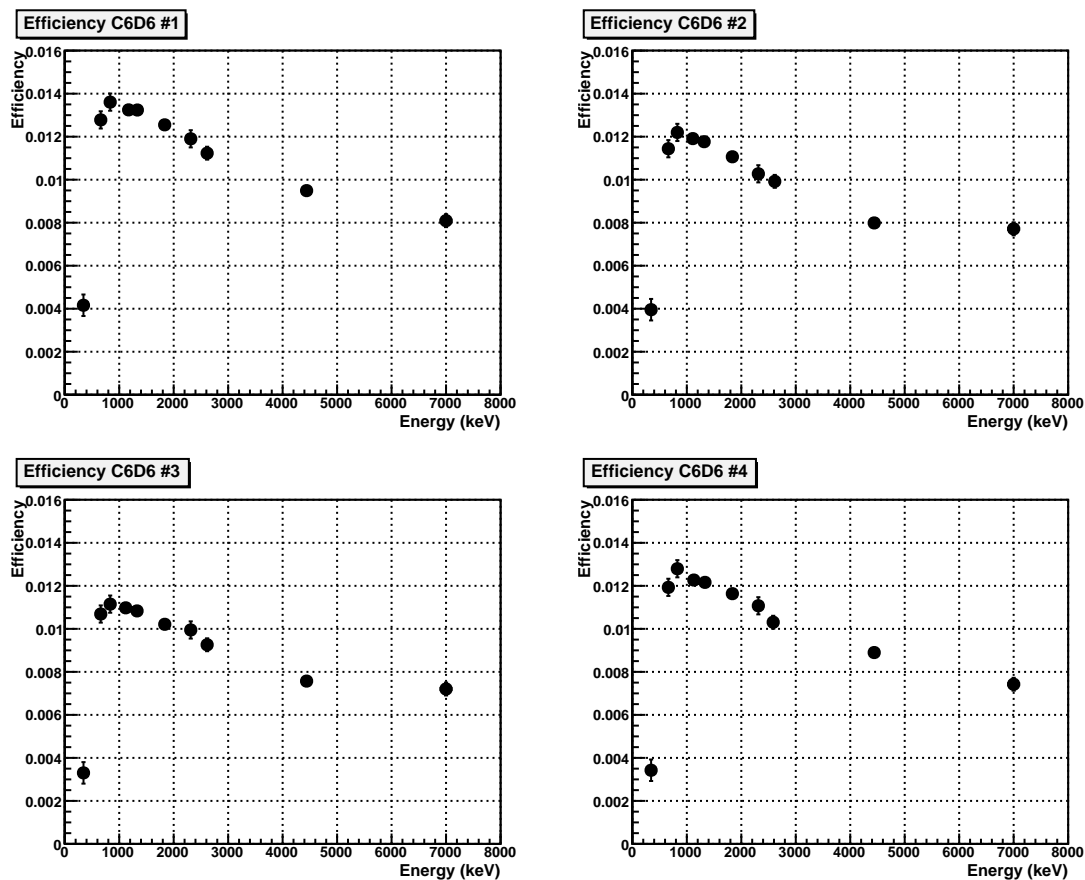
Figure 4.17: Experimental efficiency as a function of the incident γ-energy for the four C_6D_6 detectors used in our experiment.

4.3.1.3 Simulation of the response function

The present simulations have been realized with GEANT4 ([Agostinelli 03]) in combination with the powerful CLHEP (mathematical) and ROOT (analysis) libraries that can easily be included in the code. In our work, only the photon and electron transport in the target and the detection system were simulated. The light production and its propagation in the scintillator were not taken into account. To be as realistic as possible, not only the active C_6D_6 set-up was included, but also the detector housing, the target, the silicon telescopes, the reaction chamber, the tubes and the Germanium detectors. These materials contribute to the overall efficiency since γ-rays can interact with them. The sensitivity of the response functions to these materials has been investigated in appendix G. The complete geometry as used in our GEANT4 simulations is shown in figure 4.18. Note that the source was supposed to be a point source and no energy threshold was applied.

Figure 4.18: Three-dimensional geometry visualisation of our experimental set-up as defined in the GEANT4 simulation.
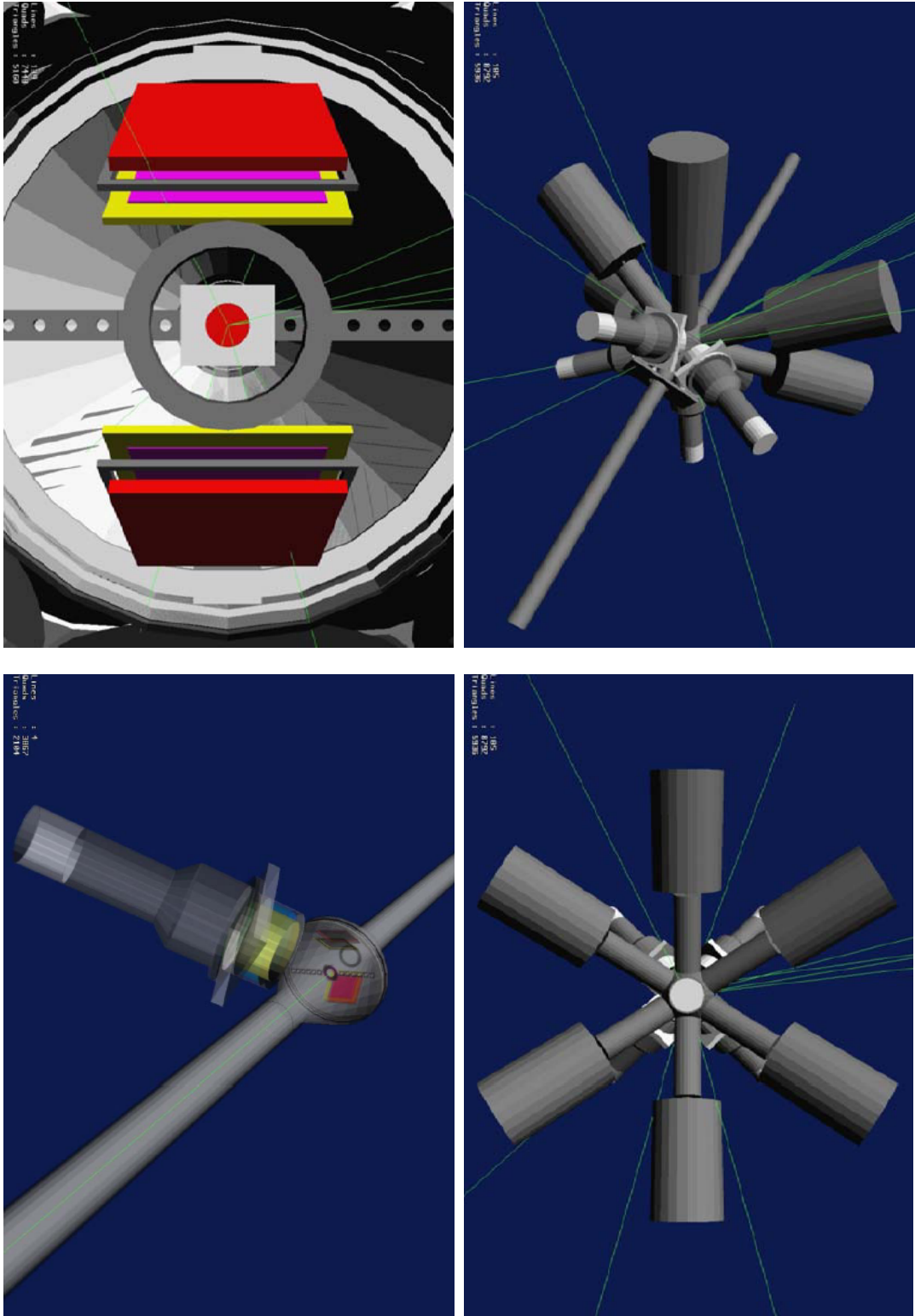
In the simulations, the response of each detector was treated separately but taking into account the whole environment. The simulated response $R_{simu}(E_{simu}, E_\gamma)$ represents the energy deposited in the detector E_{simu} by a γ-ray of energy E_γ. Response functions $R_{simu}(E_{simu}, E_\gamma)$ for a set of incident γ-ray energies E_γ are given in figure 4.19. One clearly observes the various contributions to the shape of the detector response. In particular, we highlight the important contribution of the pair-production process when the incident γ-ray energy increases. The very sharp peak, called «double escape peak», corresponds to the energy deposited by the e^-/e^+ pair and the escape of the photons originating from the e^+ annihilation. Note that the two annihilation photons have energy $m_e c^2$. By losing them, the deposited energy is $E_\gamma - 2m_e c^2$.

To obtain a realistic representation, the simulated responses $R_{simu}(E_{simu}, E_\gamma)$ need to be widened by a Gaussian convolution $G(E_d, E_{simu})$ representing the energy resolution function of the detector. The convoluted response function $R(E_d, E_\gamma)$ can be written as:

$$R(E_d, E_\gamma) = \int R_{simu}(E_{simu}, E_\gamma).G(E_d, E_{simu})dE_{simu} \qquad (4.21)$$

where the energy E_d corresponds to the energy E_{simu} of each simulated event randomly shifted following a Gaussian distribution with σ equal to the detector energy resolution[2]. Figure 4.20 illustrates the final response functions $R(E_d, E_\gamma)$ for a set of incident γ-ray energies E_γ. Usually, the energy resolution of the C_6D_6 scintillators as a function of the deposited energy E_d (in MeV) is given by the relation:

$$\sigma_{instru}^2 = \left[\alpha.E_d^2 + \beta.E_d + \eta \right] \qquad (4.22)$$

where the coefficients are obtained from a fit to the experimental energy resolution. To obtain σ at different energies, we adjusted the upper portion (the tail of the Compton edge) of the simulated spectrum to the measured spectrum for several mono-energetic γ-sources. In our case, two fits were obtained for the C_6D_6 1-2 and 3-4, respectively. In the table of figure 4.21, our α, β and η coefficients are compared with existing coefficients quoted in literature, while the plot compares our results with the resolution broadening σ obtained in other experiments using C_6D_6 scintillators. The resolution of the C_6D_6 detectors is found to be similar at low energy but important discrepancies on σ are observed in the high-energy range. Nevertheless, a good agreement has been found between our results and those obtained by G. Aerts et al. ([Aerts 06]) using FZK detectors (made of a high-volume, 1 liter, C_6D_6 liquid scintillator). The energy resolution used for BICRON scintillators in previous experiments ([Tain 04]) is different to the one we determined in this work.

---

[2]In our case, we included the RandomGauss() function of the CLHEP library in the GEANT4 simulation.
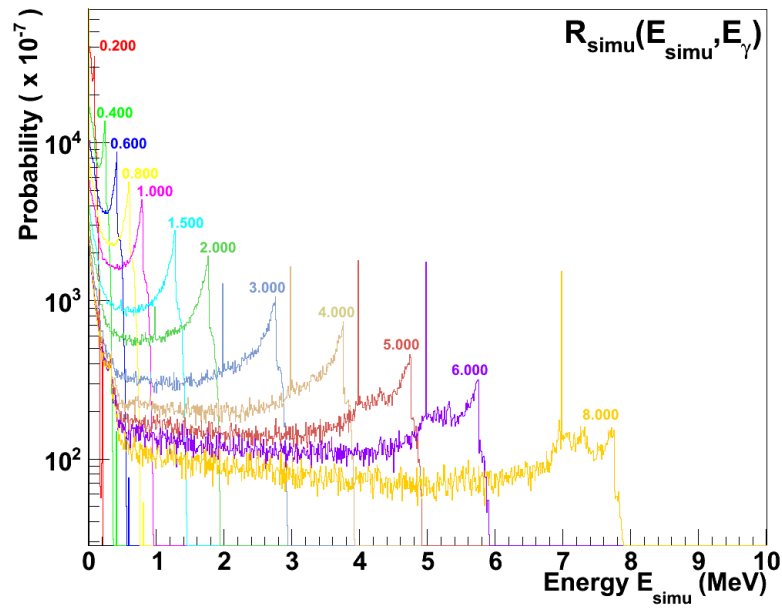
Figure 4.19: Simulated response functions $R_{simu}(E_{simu}, E_\gamma)$ for a set of incident γ-ray energies before convolution of the spectrum with the energy resolution σ.
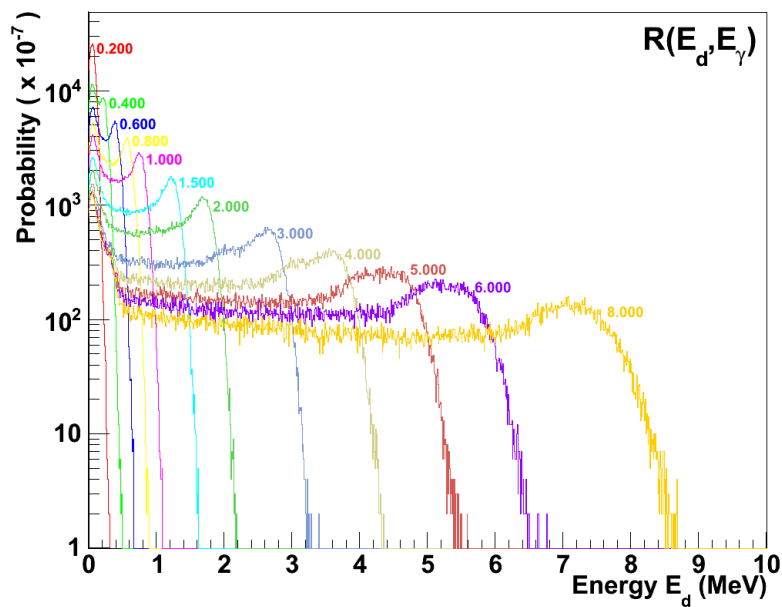
Figure 4.20: Simulated response functions $R(E_d, E_\gamma)$ for a set of incident γ-ray energies after convolution of the spectrum with the energy resolution σ.

Reference	α	β	η
Naqvi et al. [Naqvi 96] (50x50 mm cell)	$2,5.10^{-4}$	$1,62.10^{-2}$	4.10^{-6}
Tain et al. [Tain 04] (BICRON)	0	3.10^{-3}	0
Tain et al. [Tain 04] (FZK)	0	6.10^{-3}	0
Aerts et al. [Aerts 06](FZK)	$1,87.10^{-3}$	$3,75.10^{-3}$	0
Borella et al. [Borella 07](IRMM cells)	$1,87.10^{-6}$	$1,43.10^{-2}$	$3,16.10^{-1}$
Our work : C6D6 1 & 2 (CENBG)	2.10^{-3}	1.10^{-5}	1.10^{-3}
Our work : C6D6 3 & 4 (CEA Saclay)	3.10^{-3}	1.10^{-5}	1.10^{-3}
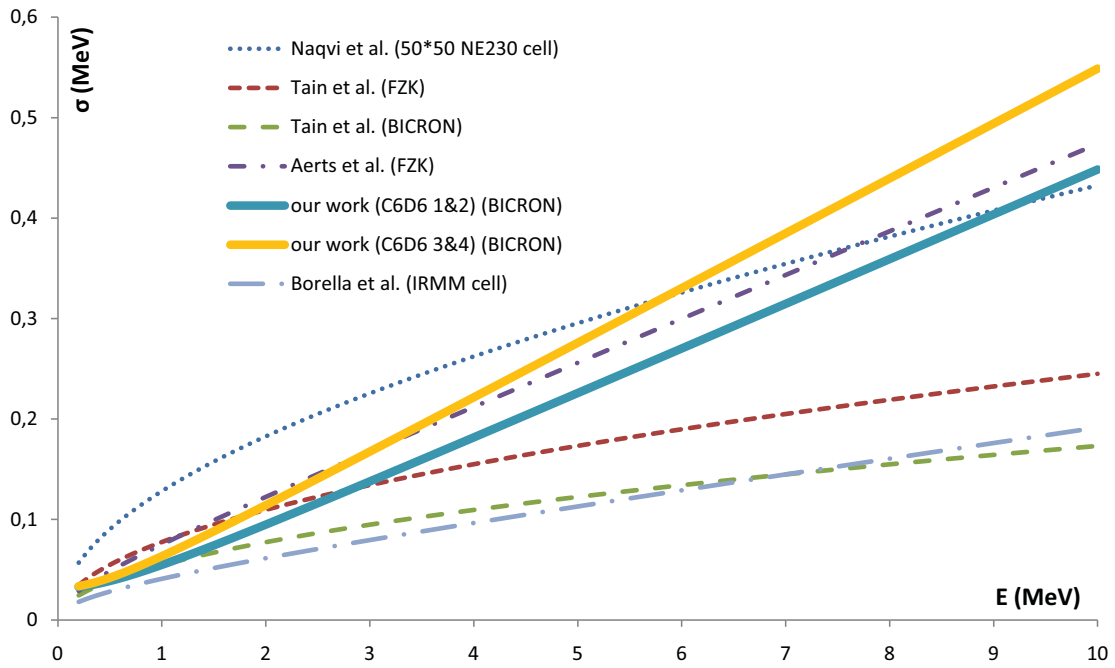
Figure 4.21: Our results for the resolution broadening σ compared to previous experiments using C_6D_6 scintillators.

As shown before, the comparison of the experimental and simulated responses has been used in a first step to obtain the instrumental widening necessary to convolute the resolution. The same procedure also allowed us to calibrate the energy deposited in the detectors. As illustrated in figure 4.22, the position of the Compton edge is deduced from the intersection between the experimental spectra and the simulated spectra before convolution. It was found at about 80% of the maximum at the upper part of the Compton distribution. Finally, a non-linear calibration was done using all the available experimental response functions. The calibrated experimental response functions are found to be in good agreement with simulations, as shown in Fig. 4.22 for a set of different γ-ray energies. We stress that the nice agreement of the spectra, in particular at high energy, is also a proof of the robustness of our resolution broadening σ. Calibration parameters for the scintillators are given in appendix J.
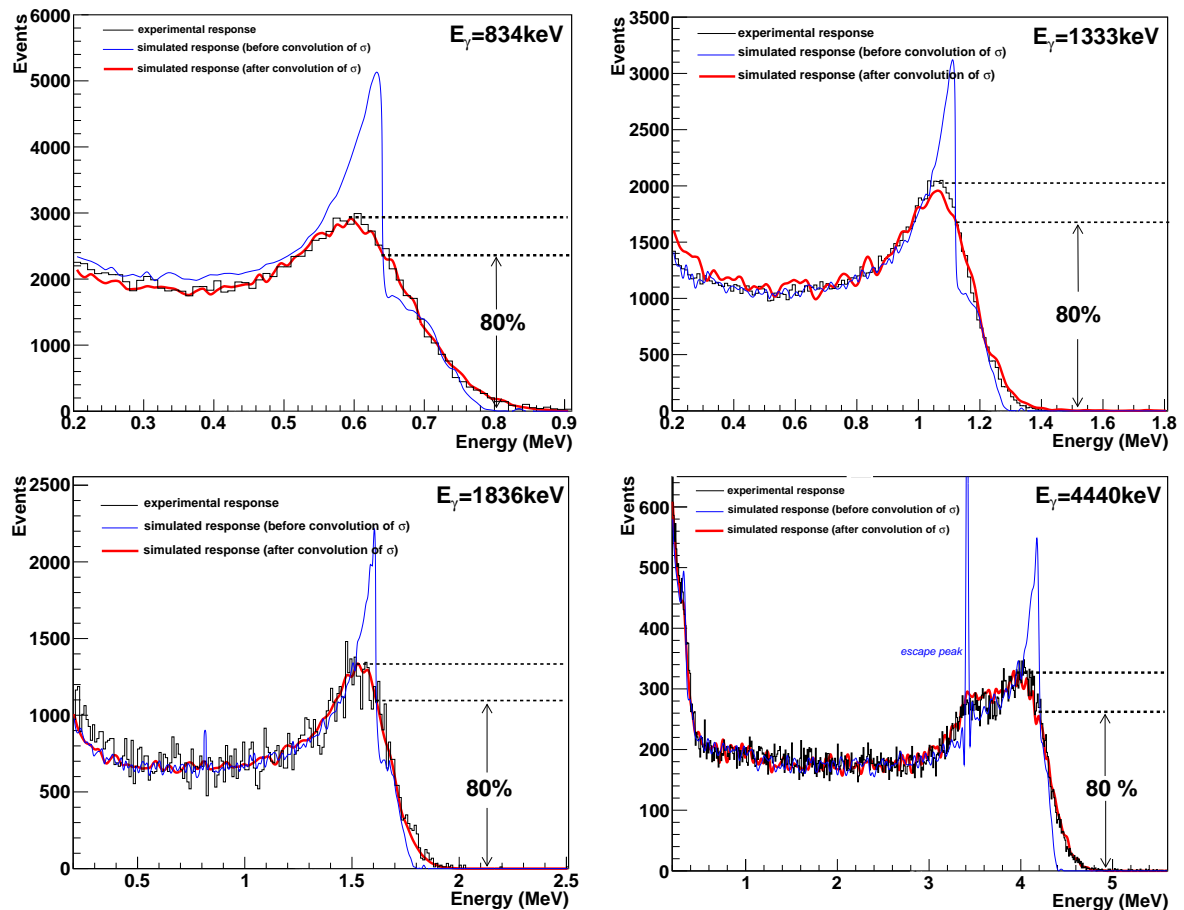
Figure 4.22: Comparison of experimental and simulated responses (C_6D_6 1) spectra for various γ-ray energies.

4.3.1.4 Simulation of the response functions and validation

It is crucial to verify the simulations. To test the veracity of our simulations, we checked that experimental efficiencies and response functions are well reproduced. In figure 4.23, the total efficiency (the sum of the four individual detector efficiencies) is compared to the simulated one. Note that the efficiency calculations were realized with a 200 keV deposited-energy threshold to be compared with experimental data.
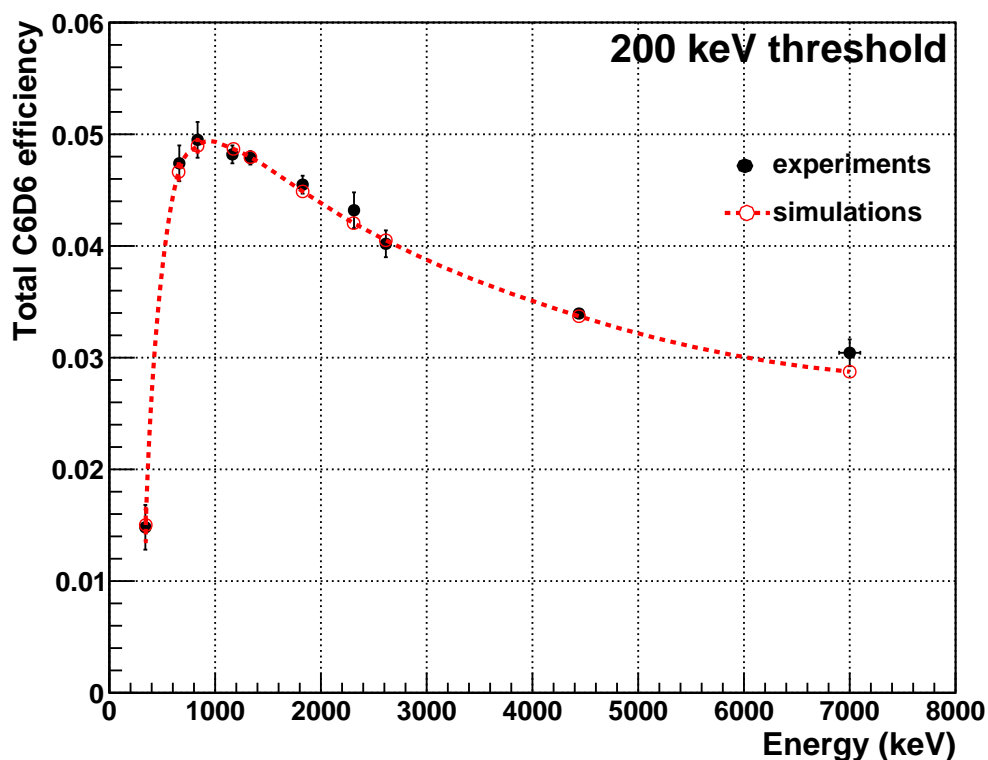
Figure 4.23: Comparison of the simulated and experimental total efficiency as a function of γ-ray energy.

Total experimental response functions (the sum of the four individual detector response functions) for several gamma-ray energies are compared to simulated values in figure 4.24. A very nice reproduction of the measured response distributions is found. Once our simulation was validated, we used it to obtain the response functions for γ-ray energies ranging from 0.1 MeV to 0.4 MeV in steps of 50 keV and from 0.4 MeV to 10 MeV in steps of 100 keV. A large number of events (10^7) was simulated for each energy.
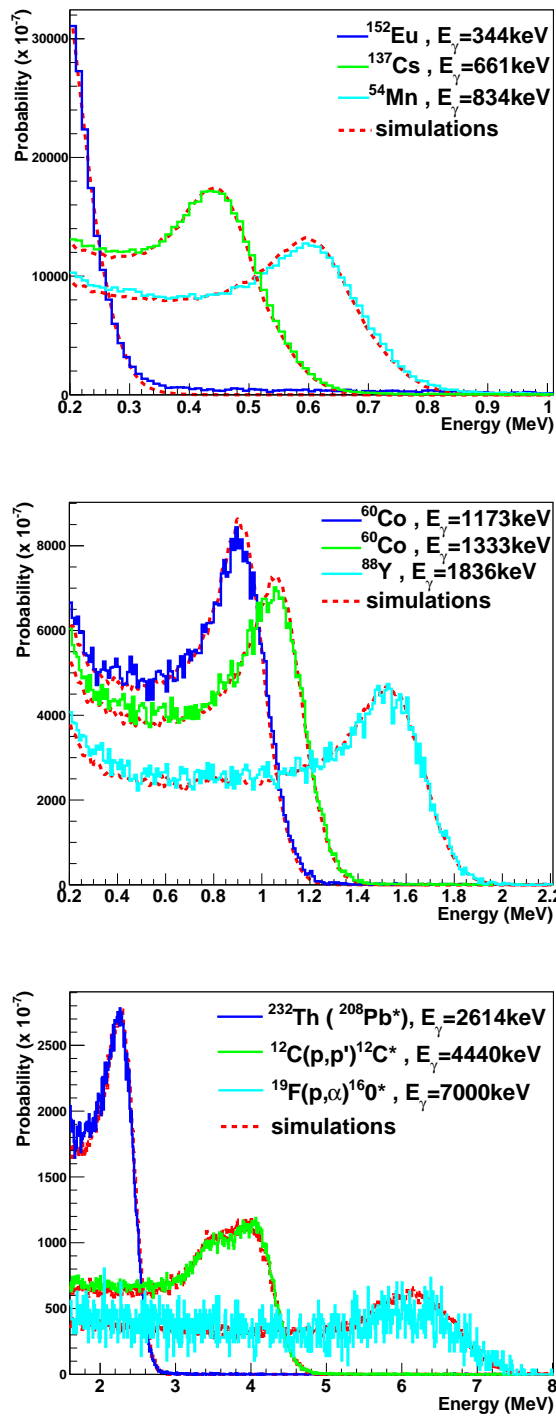
Figure 4.24: Comparison of experimental and simulated total response functions in the 0.2-7 MeV gamma-energy range. A 200 keV threshold has been applied.

4.3.1.5 Interpolation and response-function matrix

We need to build the response matrix $R(E_d, E_\gamma)$ continuously over the full range of energy. Obviously it is possible to simulate the response functions for all the possible E_γ, namely from 10 keV to 10 MeV in steps of 10 keV. However this method is very much time consuming, although it may become possible in the near future with parallelized jobs. An alternative way is to interpolate the $R(E_d, E_\gamma)$ between each pair of simulated response distributions obtained previously. In our case, we applied the second solution by using an algorithm developed by J. Wilson et al. that is explained in details in Ref. [Wilson 03]. The interpolation is performed for all E_γ with a bin of 10 keV all over the energy range from 0 to 10 MeV. An unknown response function $R(E_d, E_j)$ can be deduced directly from the adjacent simulated $R(E_d, E_n)$ and $R(E_d, E_{n+1})$. Firstly, $R(E_n)$ is stretched with a gain coefficient $a_{n+1} = E_j/E_{n+1}$ and $R(E_{n+1})$ is diminished with another coefficient $a_n = E_j/E_n{}^3$. Then $R(E_j)$ is extracted from the linear combination:

$$R(E_j) = p.a_{n+1}.R(E_n) + q.a_n.R(E_{n+1}) \qquad (4.23)$$

where the two normalization coefficients can be defined as follows:

$$p = (E_n - E_j)/(E_n - E_{n+1}) \qquad (4.24)$$

$$q = 1 - p \qquad (4.25)$$

Unfortunately, a complication arises for $E_i > 1022$ keV since the double escape peak cannot be well reproduced. This peak is always 1022 keV below E_i and that is why it is forbidden to stretch this part of the spectrum in the re-mapping stage. For bins whose $E_d < (E_{n+1} - 1022)$ keV and $E_d < (E_n - 1022)$ keV respectively, $R(E_n)$ is stretched with $a_{n+1} = (E_j - 1022)/(E_{n+1} - 1022)$ and $R(E_{n+1})$ is diminished with $a_n = (E_j - 1022)/(E_n - 1022)$. The junction with the part of the spectrum below the double escape peak (at $E_d < (E_j - 1022)$) is ensured by renormalization with the original number of counts. Consequently, the interpolated double escape peak is just shifted and this method permits us to interpolate $R(E_j)$ also for high energies. To illustrate the accuracy of the interpolation, an interpolated spectrum $R(E_j)$ with $E_j = 3000$ keV is extracted firstly (a) from the two adjacent simulated spectra $R(E_n)$ and $R(E_{n+1})$ with $E_n = 2500$ keV and $E_{n+1} = 3500$ keV, respectively, and secondly (b) from $R(E_n)$ and $R(E_{n+1})$ with $E_n = 2000$ keV and $E_{n+1} = 4000$ keV. As illustrated in figure 4.25, the interpolation shows a very good agreement with the simulated 3000 keV response, with a overestimation of 1% for case (a) and 4% for case (b). Obviously, the closer the two adjacent simulated spectra are, the more accurate is the interpolation. In our case, steps of 100 keV in the simulations provide a very precise interpolated response matrix.

---

[3]Note that the stretching/diminishing re-mapping preserves the total number of counts of the original spectrum.
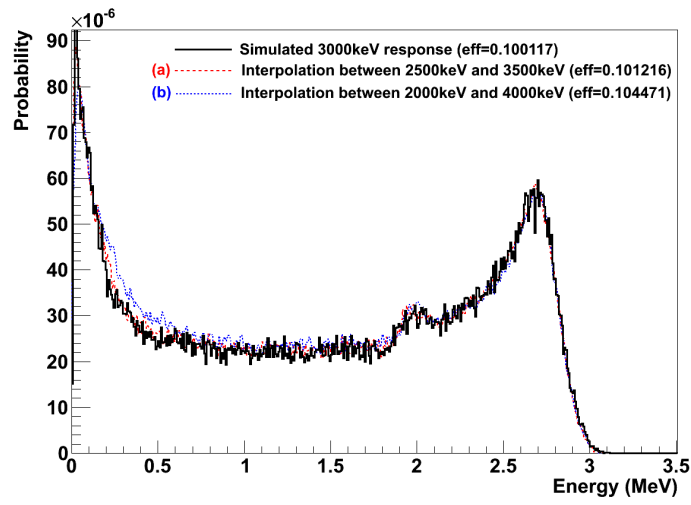
Figure 4.25: Comparison between interpolated and simulated responses at E_i=3000 keV.
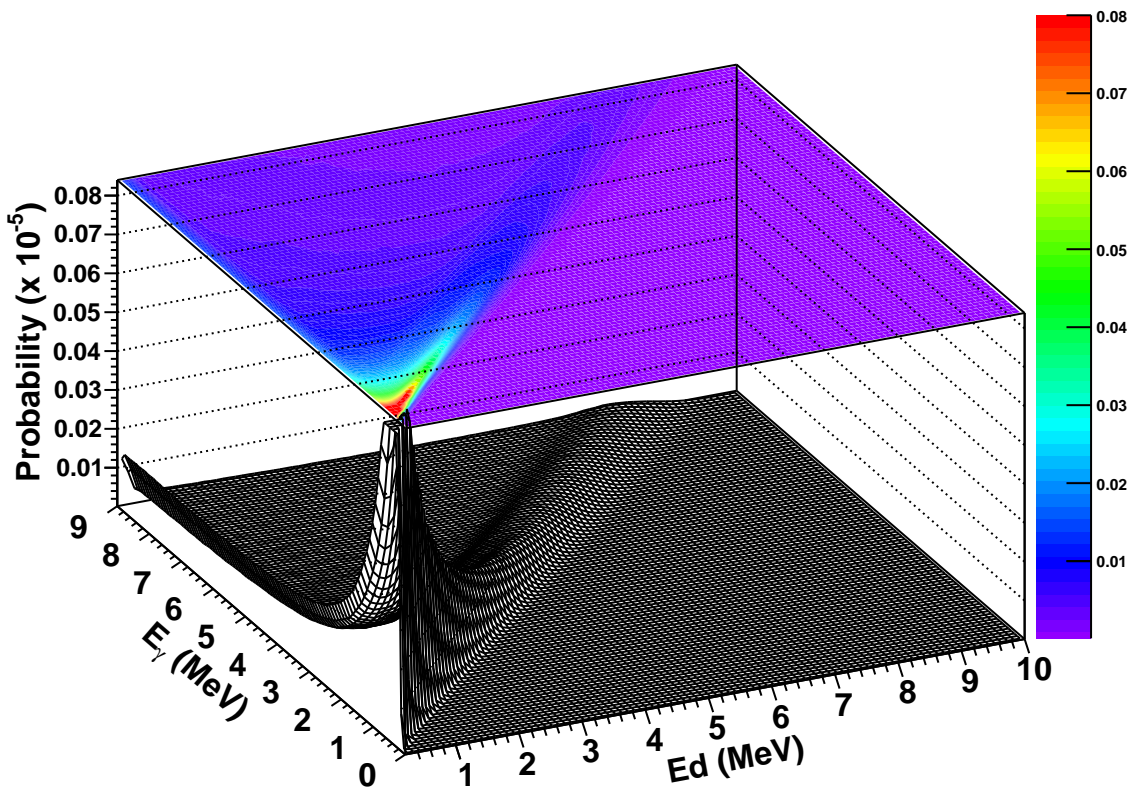
Figure 4.26: Three-dimensional response matrix $R(E_d, E_i)$.

A final response matrix with 1000 x 1000 elements was determined. The X axis corresponds to the deposited energy E_d in the scintillator and the Y axis corresponds to the incident γ-ray energy E_i. The bin size was 10 keV/channel for both axis. The Z axis shows the number of events per source particle, namely the probability to fill the corresponding pair (E_d, E_γ). In figure 4.26, a three-dimensional view gives the $R(E_d, E_i)$ values of the response matrix. For completeness, we recall that for a given incident γ-ray energy E_i, the projection over E_d gives the response function of the detector for this incident energy. The integral of the obtained response function corresponds to the total efficiency for this incident energy. Thus, the projection of the efficiency-values for each E_i provide the total efficiency function for our experimental set-up, as given in Fig. 4.23. A two-dimensional response matrix with its projections is shown just below in figure 4.27.
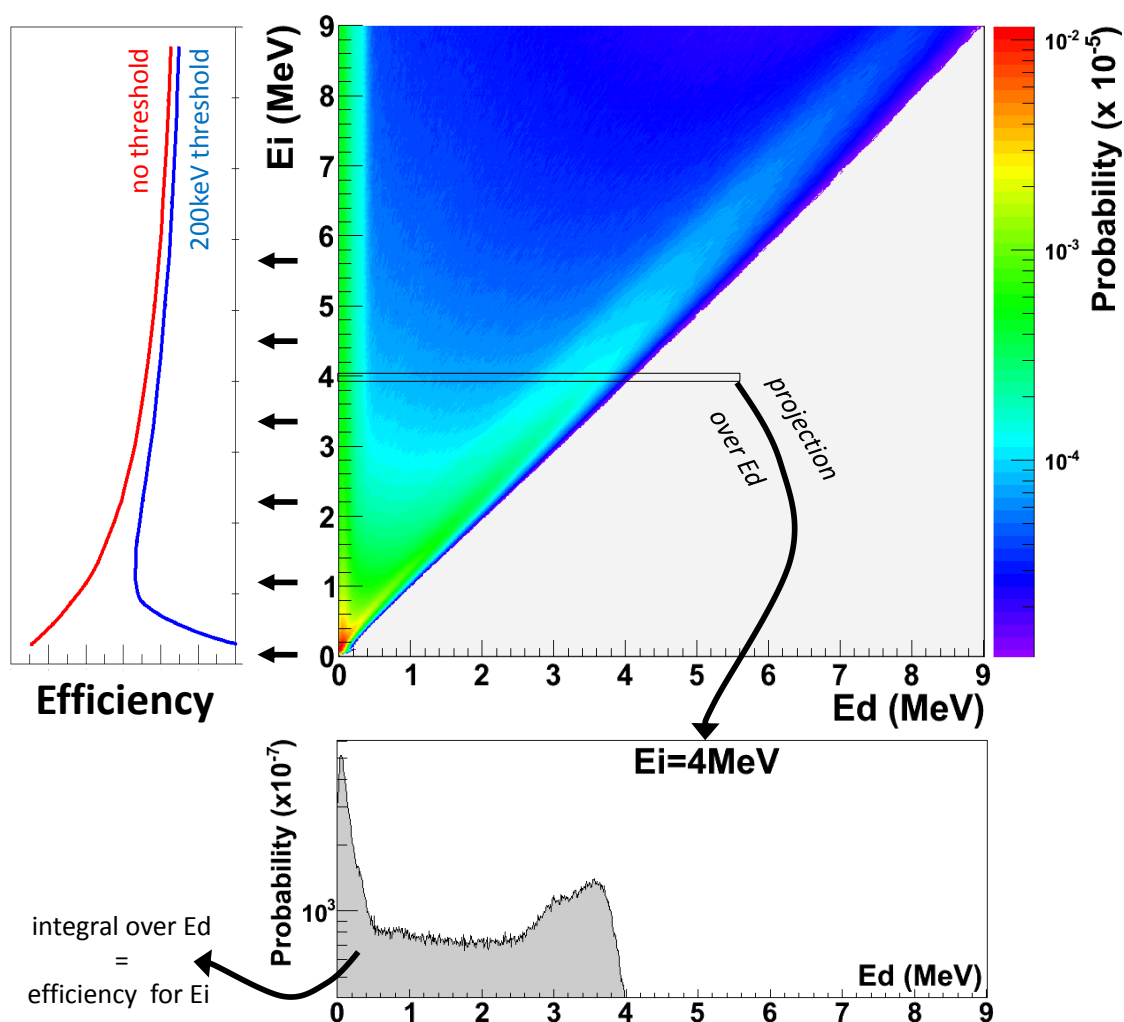
Figure 4.27: Two-dimensional response matrix and its projections.

4.3.1.6 Weighting-function determination

At this stage, we have confidence in our response matrix $R(E_d, E_i)$ and we want to solve equation 4.13. We recall that the proportional factor k was taken equal to $\frac{1}{E_c}$ MeV^{-1} and the weighting functions can be parametrized as a polynomial of order 5 (see eq. 4.10). The χ^2 is hence described as a function $f(x)$ depending on the polynomial coefficients $x = [a_1, a_2, a_3, a_4, a_5]$. To find x that minimizes $f(x)$, we used the Downhill Simplex Method [Nelder 65], which is also called Amoeba in reference to the basic movements of the little animal. It proceeds by choosing a set of points (the simplex) forming here a five-dimensional triangle (one degree of liberty for each polynomial coefficient). Then the triangle is transformed so that the worst point is improved, either by stretching, shrinking or reflecting it about the center of the triangle. At each iteration, the algorithm tends to make progress toward a minimum. In our case, the solution x is determined when the local optimum is stabilized with a tolerance of 0,0000000001. We performed the minimization using the Interactive Data Language (IDL) 8.0. The determination of the weighting functions was done for a set of γ-cascade energies that correspond to the excitation energies for each compound-nucleus, namely from $(S_n - 1.6)$ MeV to $(S_n + 2)$ MeV in steps of 80 keV. The polynomial coefficients of the weighting functions are given in appendix K. Figure 4.28 shows the weighting functions obtained for three excitation energies. The quality of the weighting functions can be verified by testing equation 4.8. We calculated the ratio:

$$Q = \frac{\sum_{E_d} W_i(E_d).R(E_d, E_i)}{k_i.E_i} = \frac{\epsilon_i^{weighted}}{\epsilon_i^{desired}} \tag{4.26}$$

which has an expected value of 1, for each simulated response corresponding to an incident γ-ray with energy E_i. This ratio is nothing but the ratio of the efficiency after application of the weighting function $\epsilon_i^{weighted}$ and the desired one $\epsilon_i^{desired}$ that is linear, as illustrated in the top panels of figure 4.29. The bottom panels show the deviation of the new efficiency from linearity. On the average, the deviations from linearity are negligible. The ratio Q reflects some experimental limitations at lower energies because of the impossibility to extrapolate the detector response below 50 keV.

4.3.1.7 Application of the weighting functions

The experimental γ-spectra were histogrammed with a deposited-energy bin of 10 keV. Then, for excitation-energy bins of 80 keV, the PHWT was applied to the corresponding detected C_6D_6 spectrum. Since in our case (k=$\frac{1}{E_c}$ MeV^{-1}), the number of capture events is directly deduced by multiplying the detected C_6D_6 γ-spectrum $N_{coinc}^{C_6D_6}(E^*, E_d)$ with the associated weighting function $W_{E^*}(E_d)$. The obtained weighted spectrum is devoid of any physical meaning but its integral corresponds to the total number of capture events for the given E^* bin. It is clear that the higher the deposited energy the more weighted is the detected spectrum. An illustration of how the PHWT practically applies
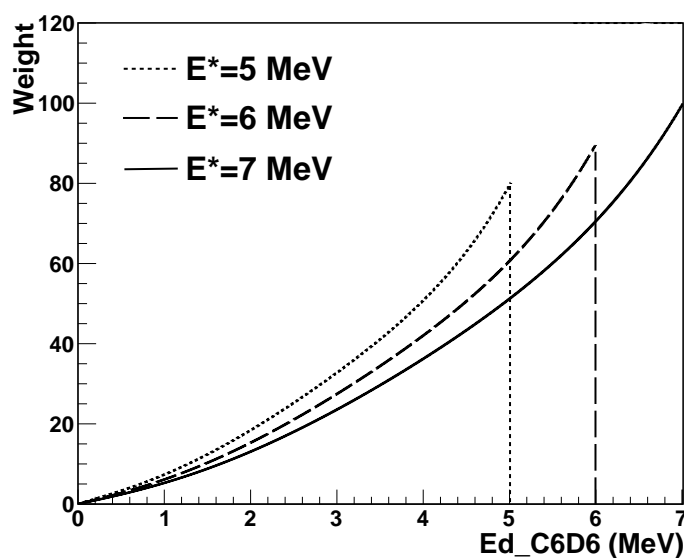
Figure 4.28: Weighting functions for various excitation energies.
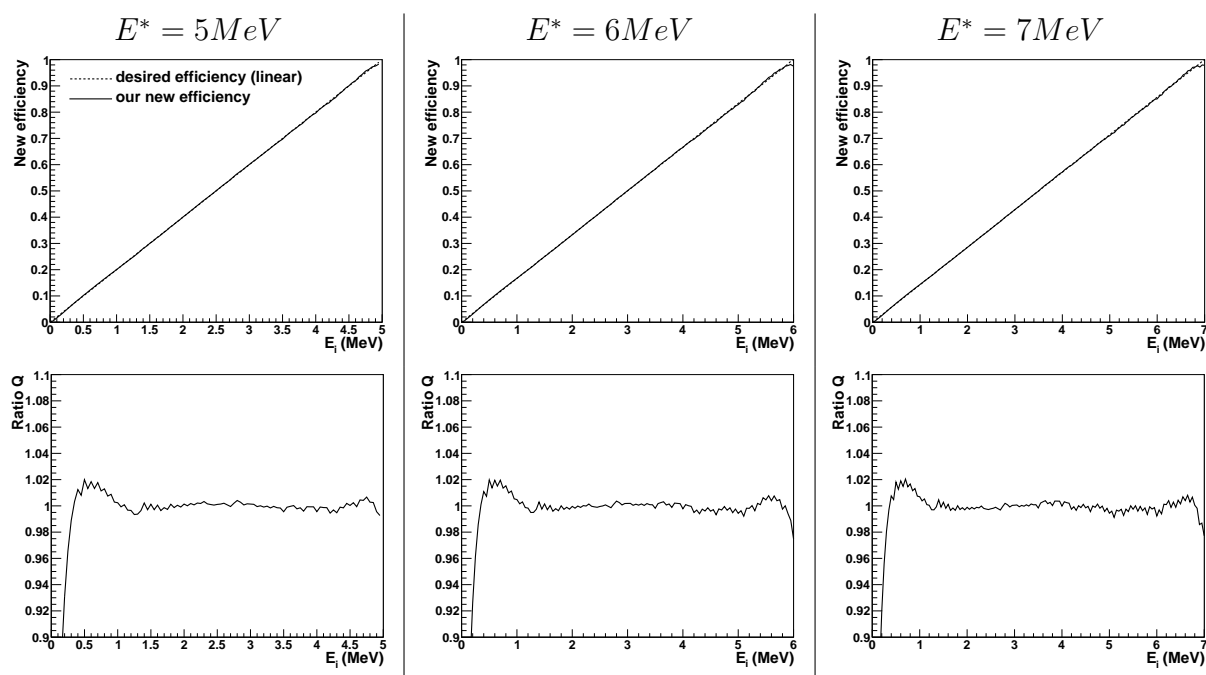
Figure 4.29: Upper figures: comparison of the obtained and desired efficiency for different E^*. Lower figures: ratio Q (eq. 4.26) as a function of the incident γ-ray energy E_i.
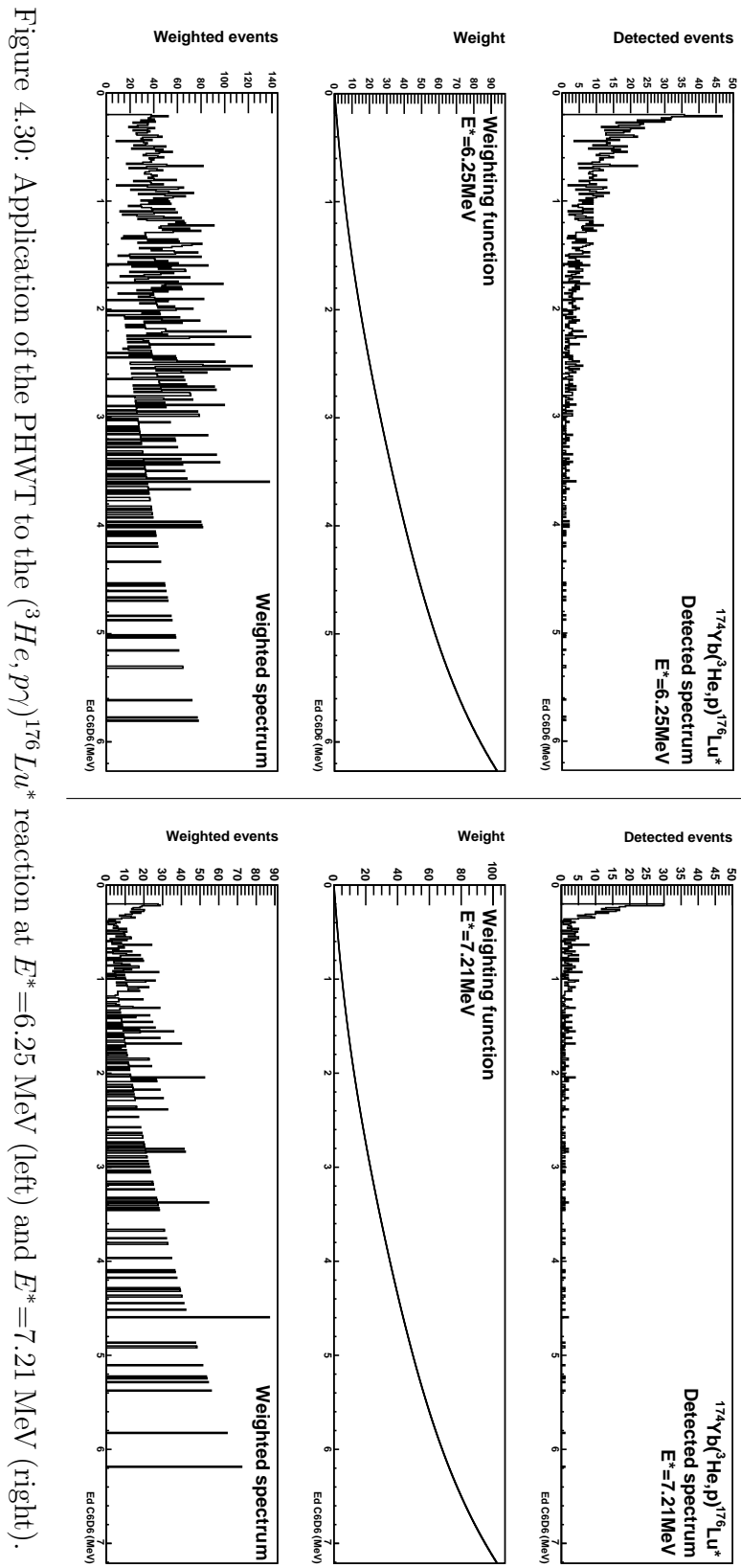
Figure 4.30: Application of the PHWT to the $(^3He, p\gamma)^{176}Lu^*$ reaction at E^*=6.25 MeV (left) and E^*=7.21 MeV (right).

for the $(^3He, p\gamma)^{176}Lu^*$ channel is given in figure 4.30. On the left panel, the analysis is done at $E^* = 6.25$ MeV, namely just below $S_n = 6.29$ MeV. Below this limit, the detected spectrum corresponds only to radiative capture events. On the right panel, $E^* = 7.21$ MeV and the shape of the experimental C_6D_6 γ-spectrum is found to be different than the other one. This point will be discussed later.

4.3.1.8 Threshold correction factor

While the experimental γ-ray spectra always present an electronic threshold, the proportionality hypothesis is fulfilled over the full energy range and the weighting functions are determined without any threshold considerations. In figure 4.30, the weighting functions are applied even below 200 keV where the detected-spectrum values are zero. A correction needs to be applied to account for the missing part of the experimental spectrum. To correct for this, we proceeded as in [Tain 04] where the missing contribution of γ-rays below the threshold is estimated with Monte-Carlo simulations of the statistical decay of the compound-nucleus. We used the DICEBOX code [Becvar 98] to generate γ-ray cascades of $^{176}Lu^*$ at $E^* = S_n = 6,29$ MeV. The generation is based on the experimental level scheme at low excitation energy and levels and branching ratios obtained from the statistical model at high excitation energies. Another code, called CASGAM, that is developed in CEA DAM DIF has been used for comparison. Then the γ-cascades were inputted and the response of our set-up was simulated with GEANT4. A comparison between the simulated spectrum and the experimental spectrum in the vicinity of S_n is given in figure 4.31. A reasonable agreement is observed. The simulation gave us the detected spectrum with no detection threshold. Statistical errors can be neglected due to the large number of γ-cascades simulated. The weighting function determined for $E^* = S_n$ was then applied on the simulated response. The weighted spectrum provided the events lying below the threshold. The missing contribution of γ-rays below the threshold can be estimated through the ratio of the weighted counts below and above the energy threshold. The correction factor F_{corr}, as defined in equation 4.15 , can be written as:

$$F_{norm} = 1 + \frac{N_{counts}^{weighted}(E_\gamma < E_{threshold})}{N_{counts}^{weighted}(E_\gamma \geq E_{threshold})} \qquad (4.27)$$

This factor has been determined for two detection thresholds (200 keV and 400 keV). Contrary to neutron-induced reactions where the angular momentum distributions of the compound-nucleus are well known, the angular momentum distributions populated in transfer reactions are not known *a priori*. Consequently, γ-cascades have been generated for a set of initial spins using DICEBOX (spins 3 and 8) and CASGAM (spins 3,4,7 and 8). The factors obtained with DICEBOX and CASGAM are in good agreement within 15 % uncertainties. Because of the angular momentum issue, the correction factor was defined as the average value of F_{norm} obtained from the six simulations, as detailed in table 4.5. Note that higher spins tend to favour γ-ray energies below the detection

threshold. Deduced normalization factors are given in the table. As a conclusion, the lower the threshold the smaller is the threshold correction.

$^{176}Lu^*$Spin	$\frac{N_{counts}(E_\gamma < 200keV)}{N_{counts}(E_\gamma \geq 200keV)}$		$\frac{N_{counts}(E_\gamma < 400keV)}{N_{counts}(E_\gamma \geq 400keV)}$	
	DICEBOX	CASGAM	DICEBOX	CASGAM
3	8.87%	7.60%	15.18%	15.18%
4	⊘	8.40%	⊘	16.62%
7	⊘	8.58%	⊘	17.22%
8	7.58%	8.21%	15.54%	16.88%
Mean value	8.21%		16.10%	
Correction factor	1.0821		1.1610	

Table 4.5: Fraction of events below the detection threshold according to DICEBOX and CASGAM for different initial spins and two different thresholds. The obtained correction factors are also given.

4.3.1.9 Test of the PHWT

The uncertainty of the PHWT can be obtained by simulating a known number N_c of γ-cascades with a fixed cascade energy $E_c = E^*$ using the same codes employed previously. As said above, the integral of the simulated energy spectrum after applying the weighting function should be equal to the number of cascades N_c. The difference between the two terms gives a measure of the uncertainty in the PHWT. For example, this difference was extracted from the simulations shown in figure 4.31 where the number of computed γ-cascades was **800000** and the area below the weighted spectrum was **811100**. This gives a deviation of 1,39%. Using several simulations with different spins, the average deviation is about 1%. We also investigated the sensitivity of the instrumental energy width used to convolute the simulated response. To do this we varied σ to produce new response functions and weighting functions. This leads to very weak variations of the simulated weighted spectrum in agreement with [Tain 04]. Finally, we considered for this work a value of 1% as the systematic uncertainty associated with the weighting functions. Actually, this value is negligible in comparison to statistical uncertainties, which are particularly important when weighting the high-energy part of the experimental spectra.
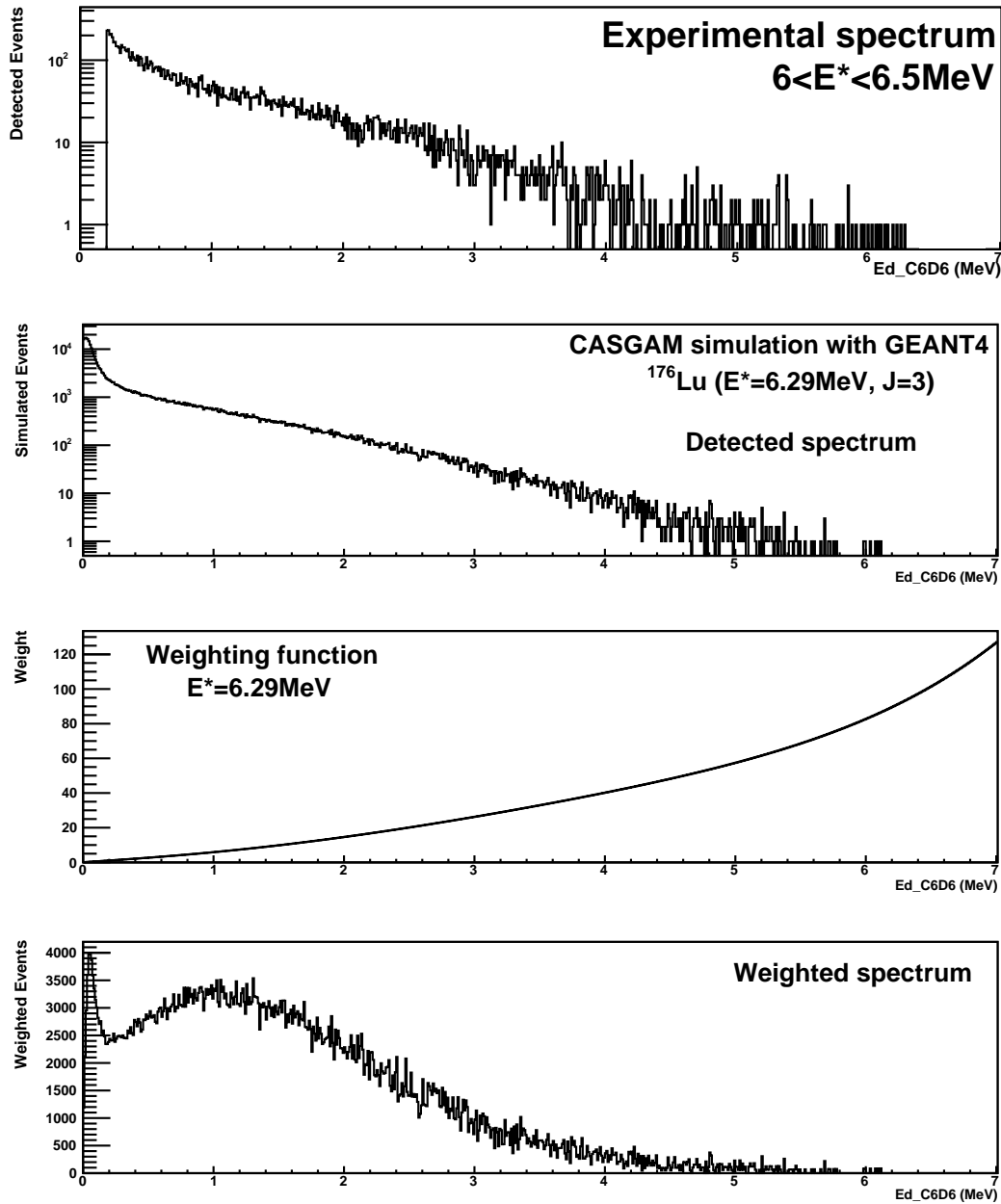
Figure 4.31: Example of the determination of the threshold correction factor with CAS-
        GAM.

4.3.2 The constant-efficiency method

The PHWT is usually applied in neutron-induced reaction measurements. In our case, since the decaying nuclei are formed by a transfer reaction, it is possible to populated excitation energies below the neutron separation energy S_n. In this context, we propose a method to determine the efficiency of our detection system that is much simpler than the PHWT.

4.3.2.1 Principle

This method is based on the hypothesis that the γ-cascade detection efficiency is independent of the excitation energy. To verify this, we performed a TALYS calculation to infer the average γ-ray energies E_γ^{avg} and multiplicities M_γ in the neutron-induced reaction $^{175}Lu(n,\gamma)^{176}Lu^*$. As illustrated in figure 4.32, these quantities vary only very weakly above S_n. In the rare earth region, the neutron separation energy is generally above 6 MeV. This high excitation energy ensures a high level density that explains the constancy of the latter γ-decay quantities. Thus, it is reasonable to assume a constant γ-cascade detection efficiency in the vicinity of the neutron separation threshold for nuclei in the rare-earth region. Note that since the heavier the nucleus, the higher is the level density at S_n, this assumption should be also valid in the actinide region.
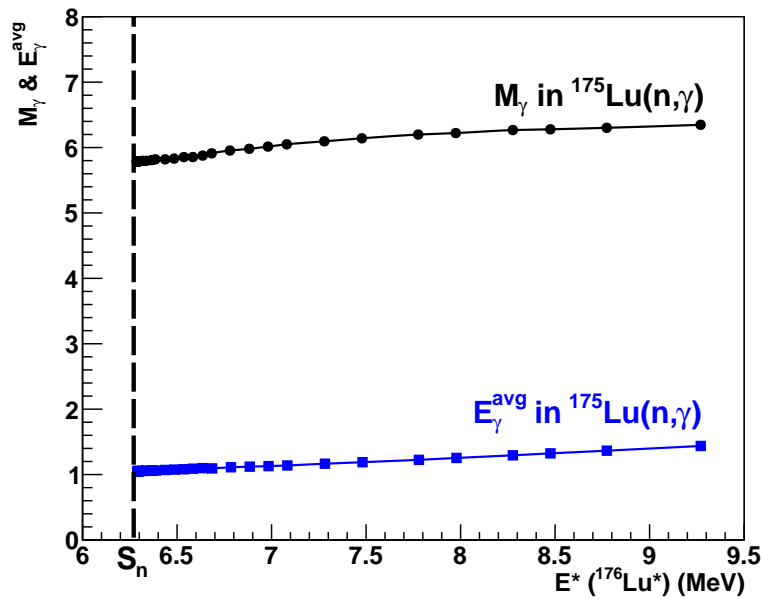
Figure 4.32: TALYS calculations of the average gamma-ray energies E_γ^{avg} and multiplicities M_γ in the $^{175}Lu(n,\gamma)^{176}Lu^*$ reaction.

Below S_n, only γ-rays can be emitted and consequently the measured capture proba-

bility P_γ should be **1**:

$$1 = P_\gamma(E^* < S_n) = \frac{N_{coinc}(E^* < S_n)}{N_{singles}(E^* < S_n).\epsilon_\gamma} \qquad (4.28)$$

Therefore the total efficiency of the C_6D_6 detectors for detecting a γ-cascade is given by:

$$\epsilon_c^{CST} = \frac{N_{coinc}(E^* < S_n)}{N_{singles}(E^* < S_n)} \qquad (4.29)$$

4.3.2.2 Determination of the capture-event efficiency

The capture-event efficiencies for each transfer channel have been determined for a set of γ-energy detection thresholds. The ratio $\frac{N_{coinc}}{N_{singles}}$ remains essentially constant below S_n, as illustrated in figure 4.33. The efficiency and the corresponding error are determined by fitting the ratio $\frac{N_{coinc}}{N_{single}}$ in this energy range. Only energy ranges free from contaminants were used for the fit.

4.4 Comparison of the obtained gamma-cascade efficiency

The γ-cascade detection efficiencies have been determined by using independently the two previous methods. In the PHWT, the γ-cascade efficiency term is not explicitly determined. However, according to eq. 4.15, this quantity is given by the ratio of coincidence events before and after applying the weighting functions:

$$\epsilon_c^{PHWT}(E^*) = \frac{N_{coinc}(E^*)}{N_{cascade}(E^*)} = \frac{N_{coinc}(E^*)}{\sum_{E_d}\left[N_{coinc}^{C_6D_6}(E^*, E_d).W_{E^*}(E_d)\right].F_{corr}} \qquad (4.30)$$

In figure 4.34, we compare the efficiencies obtained for the $^{174}Yb(^3He, p)^{176}Lu^*$ channel according to both methods. The error bars are higher for the efficiencies obtained via the PHWT because of the important statistical-uncertainty propagation in the weighting stage. The efficiencies are in excellent agreement in the vicinity of S_n. However, one observes some discrepancies for excitation energies above 6.9 MeV. The origin of the discrepancies is due to $(n'\gamma)$ inelastic events. Above the neutron emission threshold S_n, neutron evaporation may compete with γ-ray emission of the compound-nucleus. γ-rays can also be emitted after neutron evaporation and it is not possible to distinguish them from the capture events. In figure 4.30, we presented the experimental γ-spectra obtained for the $(^3He, p\gamma)^{176}Lu^*$ channel analysis at $E^* = 6.25$ MeV (just below $S_n = 6.29$ MeV) and at $E^* = 7.21$ MeV. In the first case, the detected spectrum corresponds only to radiative capture events, while at higher E^*, $(^3He, pn\gamma)^{175}Lu^*$ is the predominant
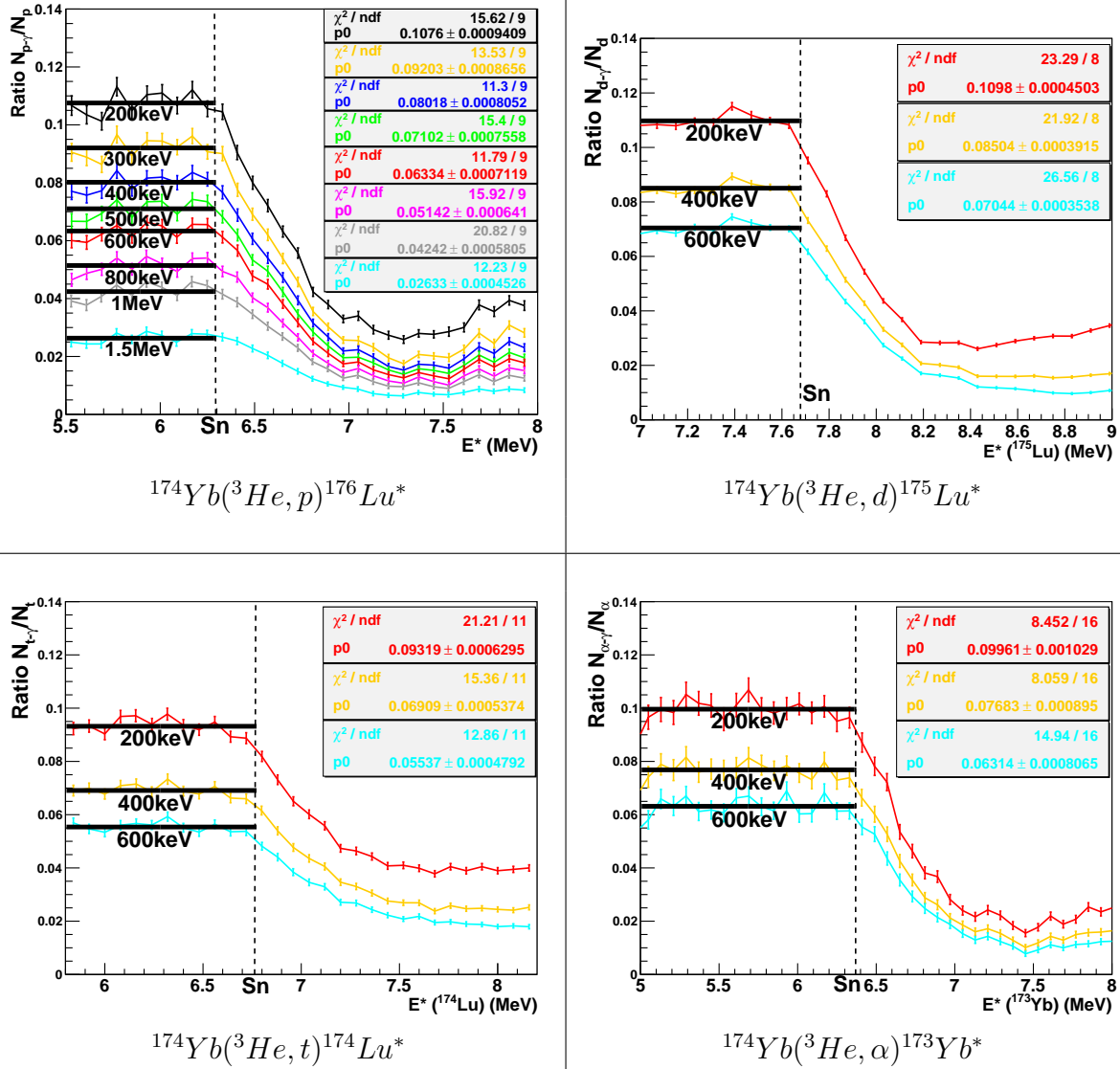
Figure 4.33: Determination of the capture-event efficiencies for a set of detected γ-energy detection thresholds using the constant-efficiency method. The full horizontal lines are the results of the fit.

decay channel. The two experimental spectra have different shapes. When the inelastic channel becomes predominant, γ-rays originating from radiative capture events are highly suppressed, while the γ-rays originating from the inelastic $(n'\gamma)$ events which have low energies dominate. The γ-ray energy of inelastic events is limited by the available excitation energy of the residual nucleus after neutron evaporation, which is $(E^* - Sn)$ MeV. When the weighting function is applied to an $(n'\gamma)$-spectra, the low γ-energies are poorly weighted and the number of equivalent cascades is less important than when the weighting is applied to a γ-spectrum corresponding to capture events. The wrong weighting comes from the fact that we apply a weighting function calculated for an E^* that is much higher (by S_n) than the actual E^* of the decaying nucleus after neutron emission. This leads to an increase of the ratio $\frac{N_{coinc}}{N_{cascade}}$. It becomes clear that the discrepancies between the efficiencies are due to the contamination of our γ-spectra with γ-rays originating from the $(n'\gamma)$ channel. With a γ-ray energy threshold of 200 keV, the efficiency obtained with the PHWT increases at about 600 keV above the neutron-separation threshold. This limit corresponds to the minimum excitation energy for the residual nucleus after neutron evaporation that allows the emission of a γ-ray of energy higher than 200 keV. By putting a higher threshold, we expect to suppress the $(n'\gamma)$ contribution in the excitation-energy range considered. Indeed, with a threshold equal to 400 keV, the efficiencies are found to be in better agreement in the excitation-energy range of figure 4.34. As a conclusion, our constant γ-cascade efficiency is clearly confirmed by the PHWT. These results give an excellent confidence in the use of the constant-efficiency method.
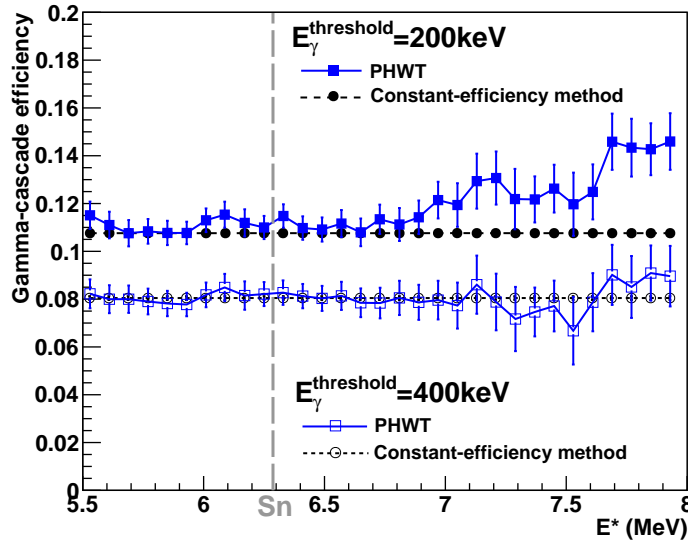
Figure 4.34: Comparison of the efficiencies determined with the PHWT and the constant-efficiency method for two different γ-energy detection thresholds.

4.5 Correction of inelastic events

As mentioned before, it is not possible to distinguish the inelastic $(n'\gamma)$ events from the capture events. This is particularly true for high excitation energies where the $(n'\gamma)$ channel is predominant. Boyer et al. [Boyer 06] used a model-dependent correction for the $(n'\gamma)$ contribution based on the predictions of the cross section ratio $\frac{\sigma(n,\gamma)}{\sigma(n,n'\gamma)}$ using a statistical model. In our case, we preferred to apply a threshold to the detected gamma-energy in order to suppress the contribution of the $(n'\gamma)$ channel. Since the maximum energy of inelastic γ-rays is limited to $(E^* - Sn)$ MeV, this can be done with the help of contours, as illustrated in figure 4.35. This figure shows the evolution of the γ-spectra with the excitation energy of the compound-nucleus. As can be seen in Fig. 4.35, the application of a threshold that increases with E^* highly reduces the statistics at the highest E^*. That is why, in this work, the investigation of the radiative capture probabilities will be limited to E^* below (S_n+1) MeV.

In these conditions, the excitation energy of the residual nucleus after neutron emission should not exceed 1 MeV. Using the level schemes available in literature (NNDC), the maximum γ-ray energy coming from $^{175,173}Lu^*$ and $^{172}Yb^*$ nuclei is about 400keV and maybe 100 keV more for the case of $^{174}Lu^*$. These values have been verified with the Germanium detectors (see section 4.8). In order to test the γ-energy detection threshold on the rejection of the inelastic events, radiative capture probabilities have been determined using the constant-efficiency method for three thresholds 200 keV, 400 keV and 600 keV. Gamma emission probabilities based on the PHWT have also been obtained for two different γ-ray energy thresholds: 200keV and 400 keV. Results are given in figure 4.36. First of all, one observes a very good agreement between the two methods. Below S_n, the gamma emission probability remains constant. Some deviations can be observed when the PHWT is applied but these may be due to statistical effects. Above the neutron binding energy (in average), the gamma probabilities are in very good agreement up to $(S_n + 600)$ keV. Neither the method to determine the efficiency nor the threshold seem to have an influence on the shape of the probability. After this limit, the probabilities obtained with the constant-efficiency method and a 200 keV threshold are systematically higher than those using a higher threshold or given by the PHWT analysis. Below approximately $(S_n + 600)$ keV, the 200 keV electronic threshold suppress all γ-rays with incident energy lower than 350 keV [4] because of the Compton process. Nevertheless, above this limit, a 200 keV threshold is not enough to reject all $(n'\gamma)$ events. As a direct consequence, the gamma emission probability starts to rise. By putting a 400 keV threshold, all gamma transitions below 580 keV are suppressed. For $E^*<(S_n + 1)$ MeV no inelastic γ-rays are expected to exceed this limit: the 400 keV threshold was hence a suitable choice for the determination of the radiative capture probability. This is confirmed by the probability obtained with a higher threshold (600 keV for example) which is very similar to the one obtained with a 400 keV threshold. We should stress that

---

[4]The incident γ-energy is higher than the electronic threshold because of the Compton process.

the radiative capture probability obtained with the PHWT using a 200 keV γ-energy threshold is particularly low whereas the $(n'\gamma)$ events are not suppressed. As explained in previous section, the γ-cascade efficiency is over-estimated (cf. fig. 4.34). That leads in this case to a diminution of the radiative capture probability. In contrast, we know that the PHWT using a 400 keV detection threshold rejects all the $(n'\gamma)$ events.

This study confirms that a 400 keV detected γ-energy threshold is enough high to suppress the $(n'\gamma)$ contribution in the excitation energy range $S_n < E^* < (S_n + 1)$ MeV. However, to minimize the statistical errors, we have used a γ-threshold that depends on the excitation energy E^*. A 200 keV and a 400 keV threshold have been applied below $E^* = S_n + 600$ keV and above this limit, respectively.
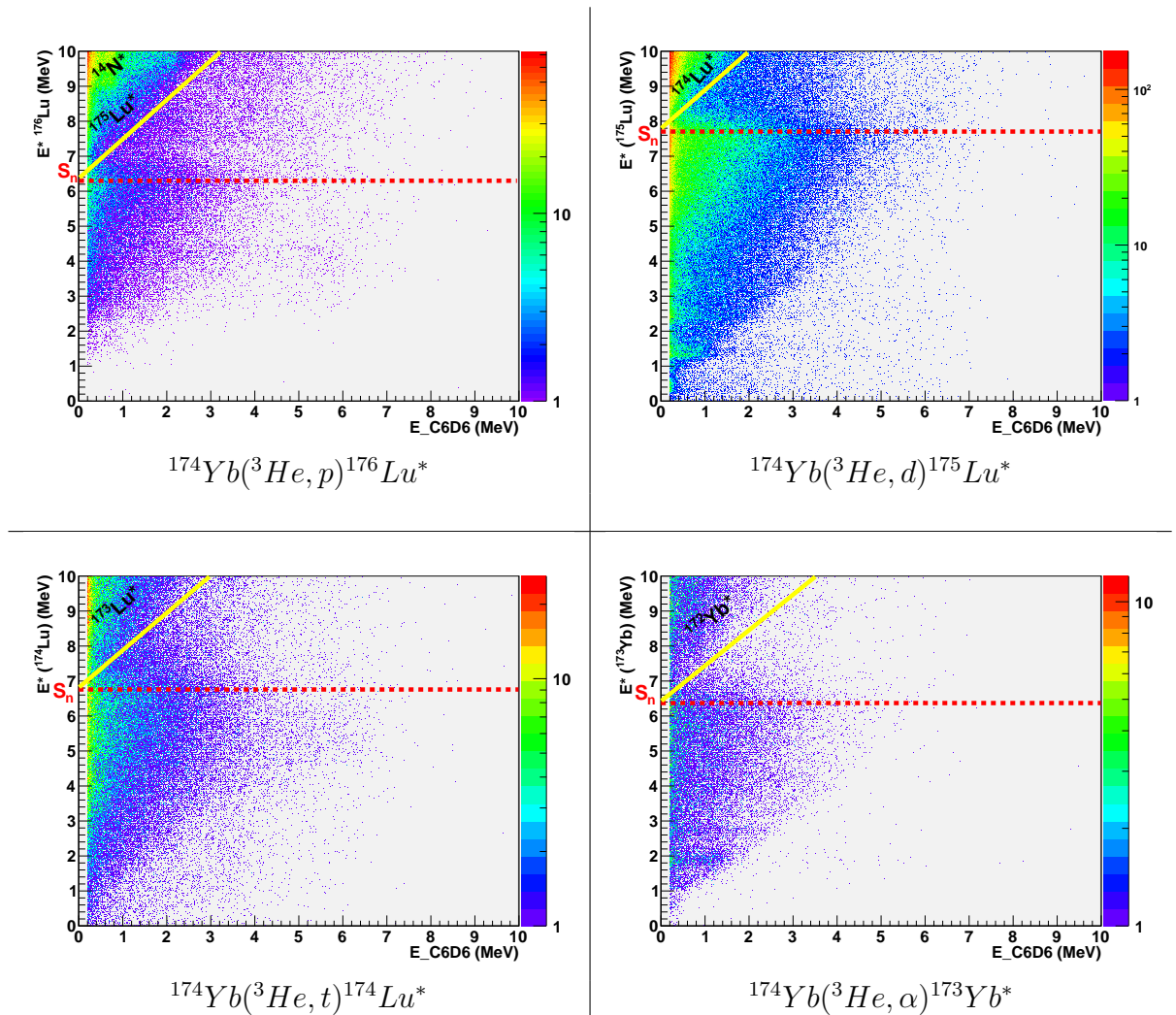
Figure 4.35: E^* vs. deposited energy in the C_6D_6 detectors. The events located on the right of the diagonal line are free from $(n'\gamma)$ events.
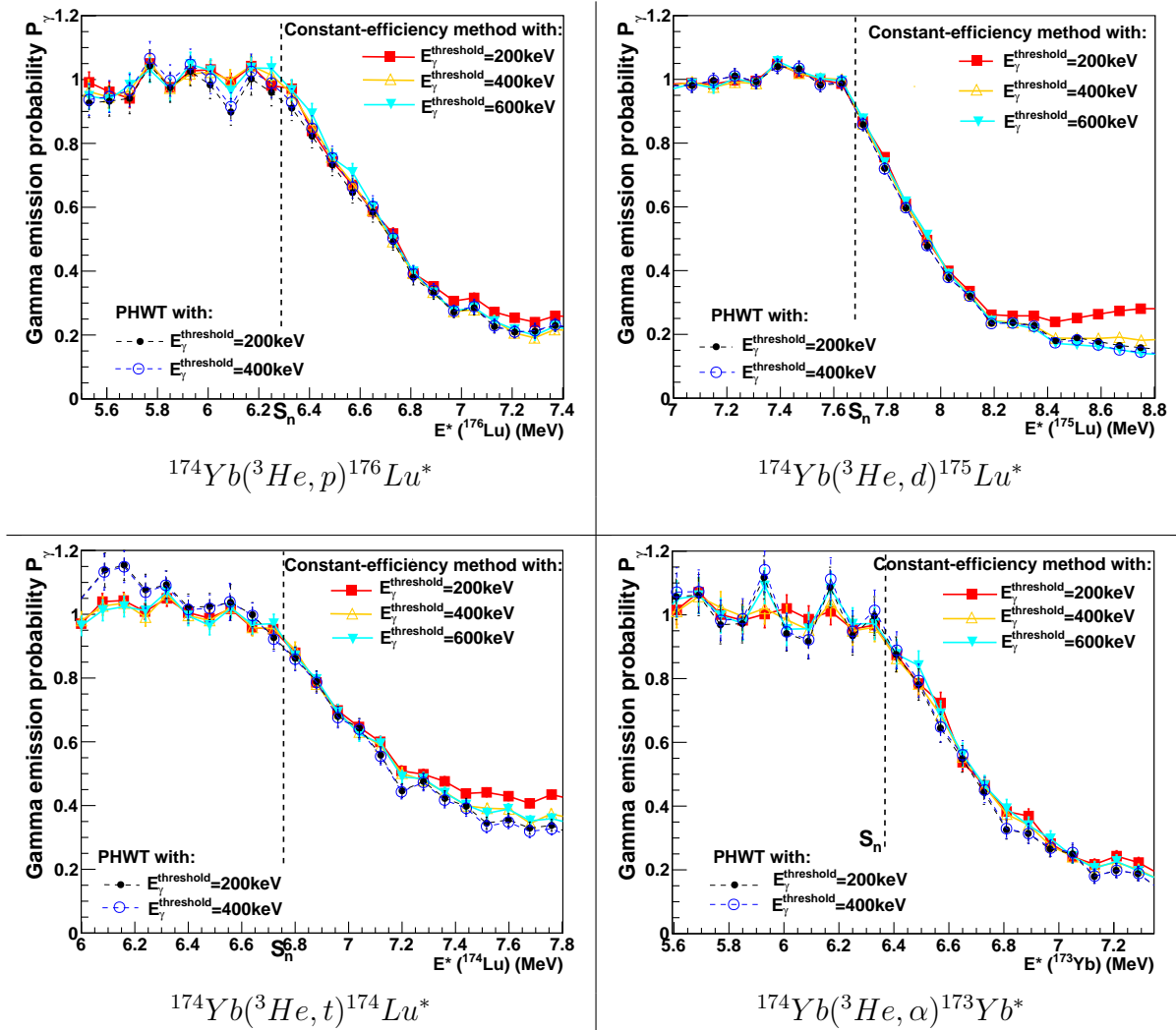
Figure 4.36: Capture probability as function of the excitation energy of the compound-nucleus for different γ-energy thresholds.

4.6 Gamma emission probabilities

The constant-efficiency method was preferred to infer the radiative capture probability. The first argument is the reduction of the statistical and systematic errors, which are clearly not negligible in the PHWT. The second point is the ease for applying an E^*-dependent threshold to eliminate the $(n\gamma')$ events. Radiative capture probabilities are presented in figure 4.37 for each transfer channel. In appendix L, the values for the experimental gamma decay probabilities of $^{176}Lu^*$, $^{175}Lu^*$, $^{174}Lu^*$ and $^{173}Yb^*$ and the associated errors are reported.

$^{174}Yb(^3He,p)^{176}Lu^*$

$^{174}Yb(^3He,d)^{175}Lu^*$

$^{174}Yb(^3He,t)^{174}Lu^*$

$^{174}Yb(^3He,\alpha)^{173}Yb^*$
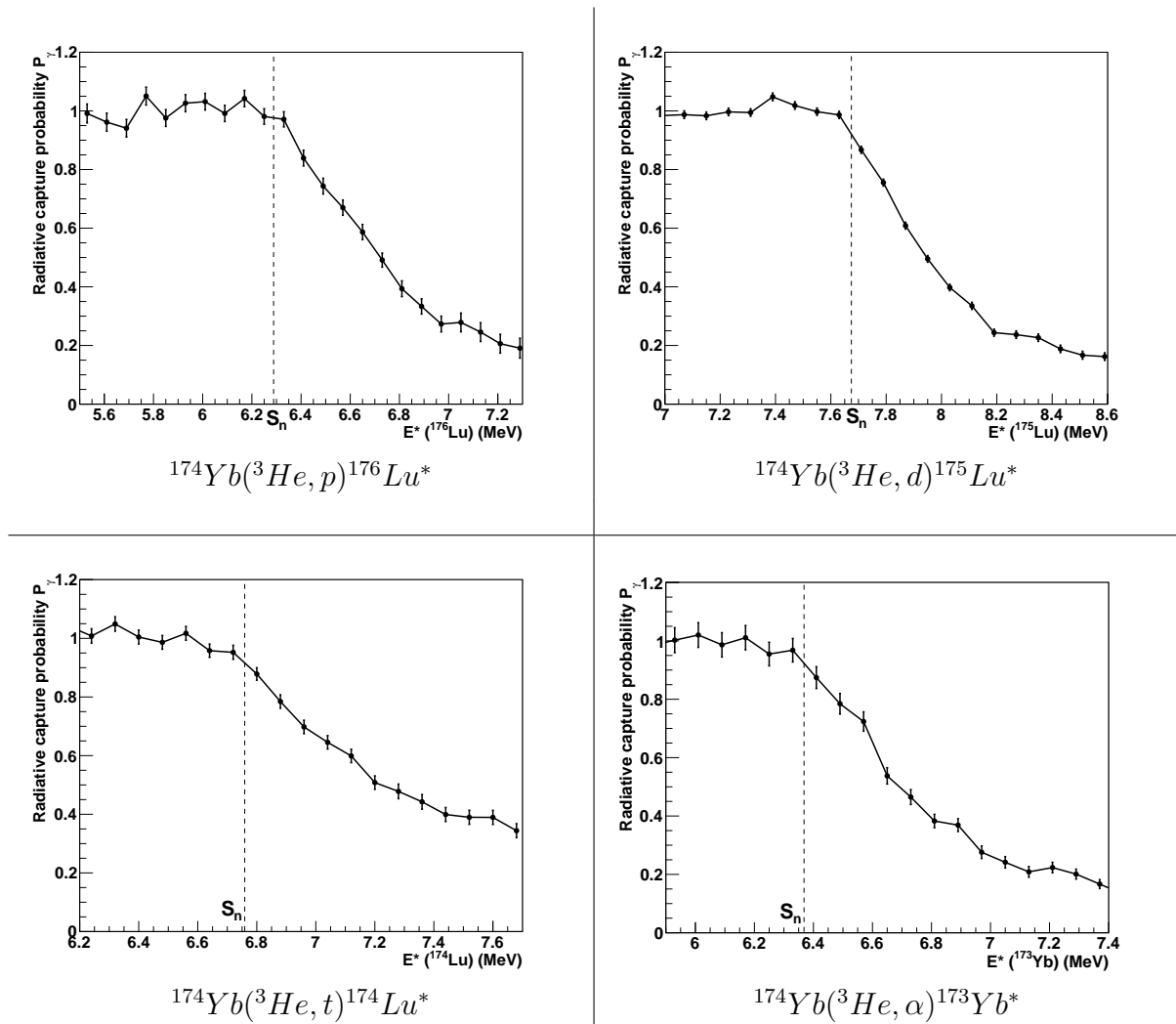
Figure 4.37: Radiative capture probabilities obtained in our surrogate experiment.

4.7 Variance-covariance analysis

In the following, we infer the errors associated to the final radiative capture probability which are obtained from the weighted mean of the results obtained for each strip. The error analysis of the radiative capture probability is based on eq. 3.6. The probability depends on two statistical parameters $\{N_{single}, N_{coinc}\}$ and one systematic parameter $\{\epsilon_c\}$. However, N_{single} and N_{coinc} are deduced from eqs. 4.1 and 4.2, respectively. Thus, the probability is actually a function of four statistical parameters $\{N_{part}, N_{bkg}, N_{gamma}, N_{gamma-bkg}\}$ and the systematic parameter $\{\epsilon_c\}$. Let us estimate the correlations between these parameters. Since, except for the very small ^{13}C contribution, the regions used of our singles and coincidence spectra are free from contaminants, the error due to a bad identification of the compound-nucleus is negligible: the covariance term $Cov(N_{single}, N_{coinc})$ can be taken equal to 0. The background measurement corresponding to N_{bkg} was done under the same experimental conditions as the one corresponding to the ^{174}Yb target. However, systematic errors on the counting rates are negligible and the covariance term $Cov(N_{bkg}, N_{part})$ and $Cov(N_{gamma-bkg}, N_{gamma})$ can hence be taken equal to 0. Thus, the statistical parameters are not correlated in this experiment and one can write (according to eq. 4.1):

$$\sigma_{N_{single}}^2 = \sigma_{N_{part}}^2 + f_{norm}^2 . \sigma_{N_{bkg}}^2 \qquad (4.31)$$

Similarly we have for the coincidence events (according to eq. 4.2):

$$\sigma_{N_{coinc}}^2 = \sigma_{N_{gamma}}^2 + f_{norm}^2 . \sigma_{N_{gamma-bkg}}^2 \qquad (4.32)$$

We need to consider the covariance terms $Cov(N_{coinc}, \epsilon_c)$ and $Cov(N_{single}, \epsilon_c)$ that link the γ-cascade efficiency with the ratio $\frac{Ncoinc}{Nsingle}$ given in eq. 4.29. There is *a priori* a correlation because these three quantities have been measured with the same set-up. However, there are no systematic errors and $Cov(N_{coinc}, \epsilon_c)$ and $Cov(N_{single}, \epsilon_c)$ can be neglected. Finally, the error for the radiative capture probability is given by:

$$\left(\frac{\sigma_{P_\gamma}}{P_\gamma}\right)^2 = \left(\frac{\sigma_{N_{coinc}}}{N_{coinc}}\right)^2 + \left(\frac{\sigma_{N_{single}}}{N_{single}}\right)^2 + \left(\frac{\sigma_{\epsilon_c}}{\epsilon_c}\right)^2 \qquad (4.33)$$

where $\left(\frac{\sigma_{P_\gamma}^{stat}}{P_\gamma}\right)^2 = \left(\frac{\sigma_{N_{coinc}}}{N_{coinc}}\right)^2 + \left(\frac{\sigma_{N_{single}}}{N_{single}}\right)^2$ is the statistical error and $\left(\frac{\sigma_{P_\gamma}^{syst}}{P_\gamma}\right)^2 = \left(\frac{\sigma_{\epsilon_c}}{\epsilon_c}\right)^2$ is the systematic error. Finally, one has to consider the correlations between the radiative capture probabilities as a function of the excitation energy because the same efficiency has been used over all the E^* range considered. The correlation matrix for our measurement is defined as:

$$Corr(P_\gamma(E_i^*); P_\gamma(E_j^*)) = \frac{\sigma_{P_\gamma}^{syst}(E_i^*) . \sigma_{P_\gamma}^{syst}(E_j^*)}{\sigma_{P_\gamma}(E_i^*) . \sigma_{P_\gamma}(E_j^*)} \qquad (4.34)$$

The correlation matrices for each probability are given in appendix M. The one for the $^{176}Lu^*$ radiative capture probability is shown in figure 4.38. The decrease of correlations above $S_n = 6.29$ MeV means that the systematic errors become negligible in comparison with the statistical errors that are principally governed by $\sigma_{N_{coinc}}$. Correlation matrices are important for evaluators as they are used to define the degree of interdependence between our data points.
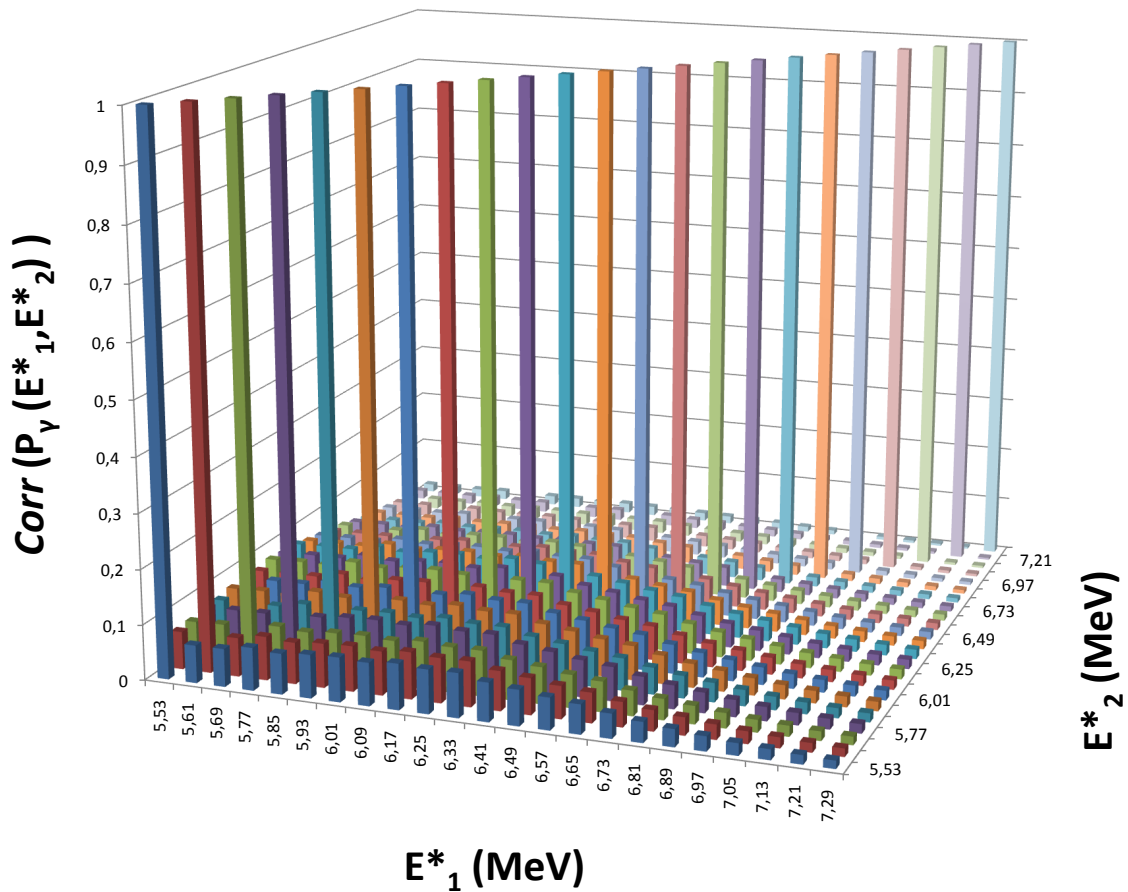
Figure 4.38: Correlation matrix for the γ-decay probability of $^{176}Lu^*$.

4.8 Analysis of data taken with the Ge detectors

4.8.1 Germanium calibrations and efficiencies

Our six *Ge* detectors were not only used for calibration purposes but also for providing an alternative analysis to this surrogate experiment. Gamma-spectra have been obtained in a γ-ray energy range from 50 keV to about 1.5 MeV. Each detector was calibrated using a ^{152}Eu γ-source, then the individual γ-spectra were summed. Figure 4.39 shows the calibrated total γ-spectrum for the latter γ-source. The experimental efficiency and resolution was measured for each *Ge* detector. Assuming that the γ-ray auto-absorption in the ^{174}Yb target was negligible, the total efficiency for the *Ge* detection set-up as a function of E_γ is given in the left part of figure 4.40. As can be seen on the right part of this figure, the resolution remains relatively constant in the range from 0 to 500 keV. The average value is about 2 keV in this energy range.
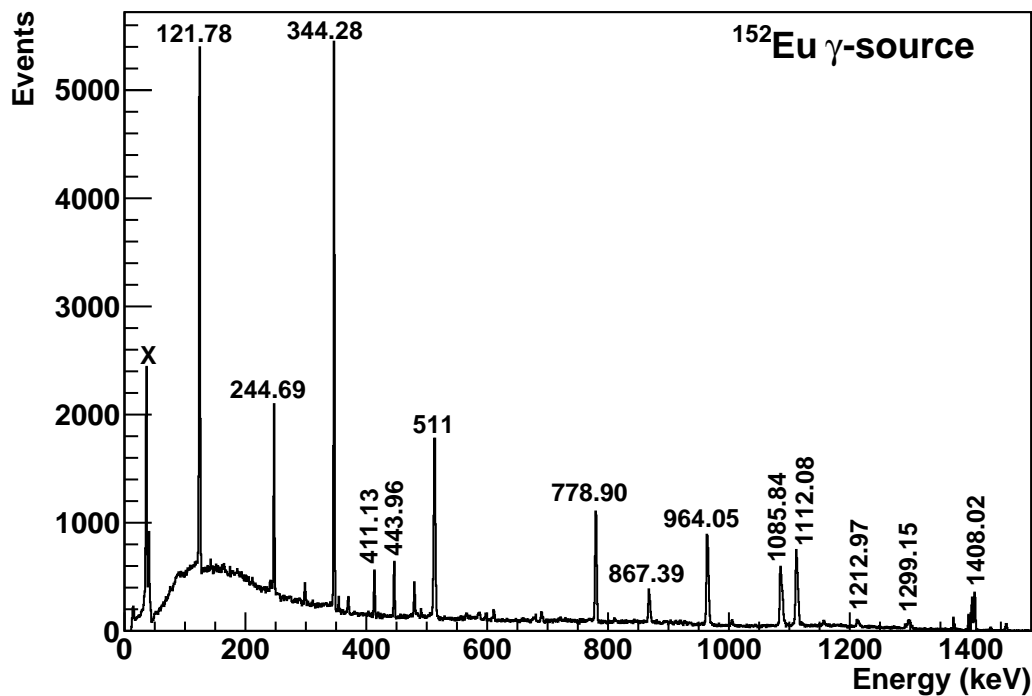
Figure 4.39: Sum of the 6 Germanium spectra obtained with a ^{152}Eu γ-source.
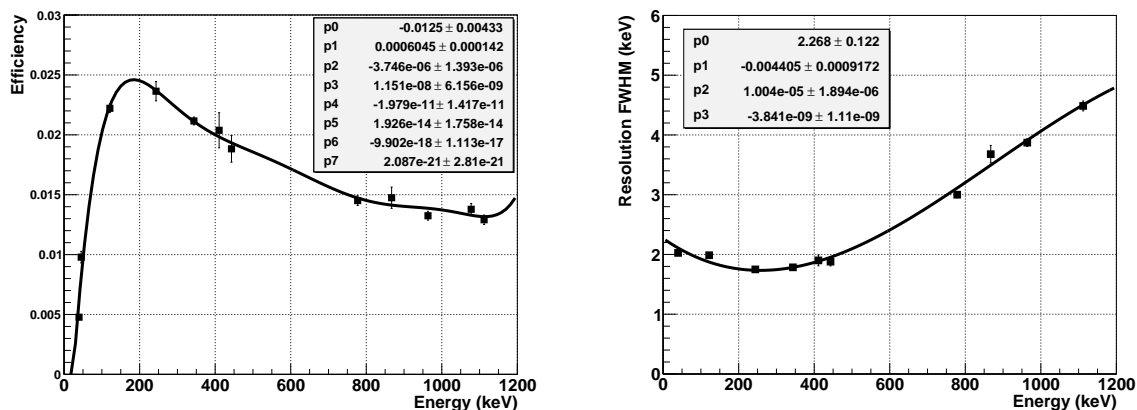
Figure 4.40: Efficiency and energy resolution of the Germanium set-up as a function of γ-ray energy.

4.8.2 Identification of the decaying nuclei

A spectroscopy analysis was realized by looking at the γ-rays detected by *Ge* detectors in coincidence with an ejectile detection in the $\triangle E - E$ telescopes. A selection in the *Ge*-telescope time spectra could have been applied in order to distinguish between prompt and delayed γ-transitions. This is particularly interesting when the extraction of nano-second isomeric transitions is needed. However, for statistical reasons, we included prompt and delayed γ-transitions in the analysis by using a 160 ns time window (cf. Fig. 4.41).
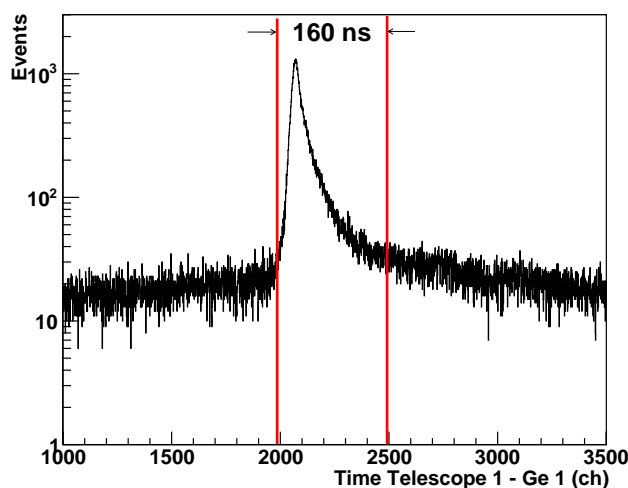
Figure 4.41: Time spectrum between telescope 1 and *Ge* 1. The vertical lines indicate the limits of the time window used to extract the spectra shown in Figs. 4.42, 4.43, 4.44 and 4.45.

For each transfer channel, the *Ge* energy spectra have been analysed for three excitation energy ranges:

- from 0 to S_n, where the only decay channel for the compound-nucleus is γ-ray emission.

- from S_n to $(S_n + 600)$ keV, where the neutron emission channel $(n'\gamma)$ competes with γ-ray emission.

- from (S_n+600) keV to (S_n+2) MeV, where the decay channel $(n'\gamma)$ is predominant: γ-ray emission from the compound-nucleus cannot be observed anymore.

Figures 4.42, 4.43, 4.44 and 4.45 show coincidence γ-spectra for the above-mentioned excitation energy ranges relative to the $(^3He, p)$, $(^3He, d)$, $(^3He, t)$ and $(^3He, \alpha)$ reactions, respectively. Gamma-transitions from the compound-nucleus can be nicely identified below the neutron binding energy, while above (S_n+600) keV, all the observed γ-transitions correspond to the residual nucleus after neutron evaporation. Each spectrum is associated to a table given in appendix N which gives the characteristics of the identified γ-transitions, as given by the NNDC database. The assignment was realized for all the nuclei formed before and after neutron emission, namely $^{176,175,174,173}Lu$ and $^{173,172}Yb$. Each gamma transition is identified with its energy E_γ, the energy of the initial level E_{level}, the initial and final spin-parity states $(J\Pi \rightarrow J'\Pi')$ and its half-life $T_{1/2}$. This permitted us to verify the nature of the most important observed gamma-transitions and we therefore believe that our identification of the transitions is robust. In addition, the fact that we could assign the main γ-ray transitions to the expected nucleus (before and after neutron emission) reflects that the target used was isotopically pure.

4.8.3 Radiative-capture probabilities obtained with the Ge detectors

An alternative method to infer radiative-capture probabilities consists in measuring ground-state band low-lying transition intensities. This method has been used in LLNL experiments, as presented in chapter 2. Nevertheless, up to now, this method was limited to even-even well-known decaying nuclei. In this case, it is assumed that all decay paths go through the yrast $4^+ \rightarrow 2^+$ or $2^+ \rightarrow 0^+$ transitions. This makes detection efficiencies associated to these transitions independent of E^*. For an odd-odd compound-nucleus like ^{176}Lu, it is not obvious to choose a low-lying γ-transition that is supposed to collect all the decays due to the spreading of the γ-decay path over a large number of transitions. In this case, the feeding of the low-lying transitions may depend on E^*. We determined the ratio between the sum of the intensities of several selected transitions and the corresponding number of ejectiles as a function of E^*. Since the detection efficiency is low
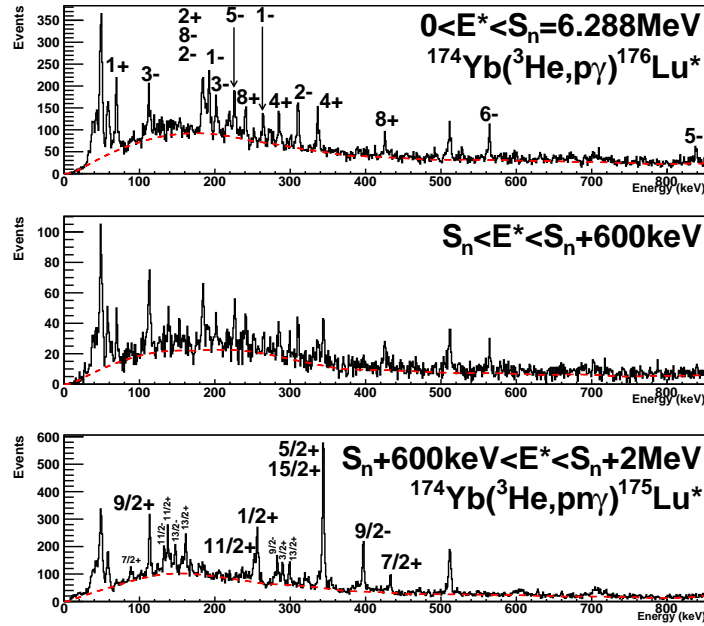
Figure 4.42: *Ge γ-ray spectra relative to the $(^3He,p)^{176}Lu^*$ and $(^3He,pn)^{175}Lu^*$ channels for different excitation energies of $^{176}Lu^*$. The initial spin-parity states $J\Pi$ of each transition are given.*
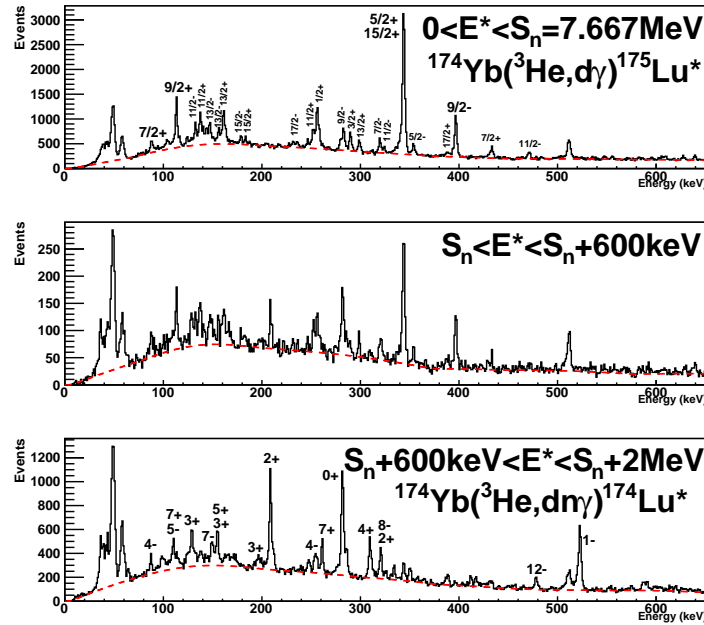
Figure 4.43: The same as in fig. 4.42 but for the $(^3He,d)^{175}Lu^*$ and $(^3He,dn)^{174}Lu^*$ channels.

167
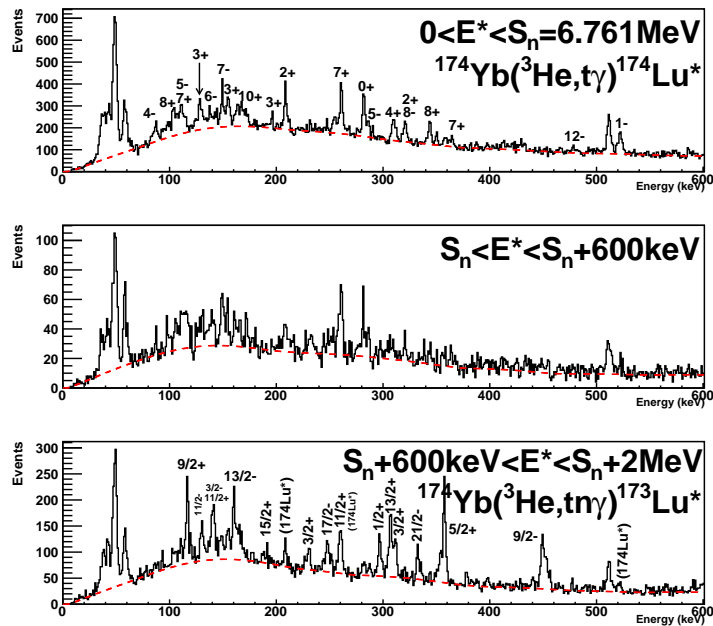
Figure 4.44: The same as in fig. 4.42 but for the $(^3He, t)^{174}Lu^*$ and $(^3He, tn)^{173}Lu^*$ channels.
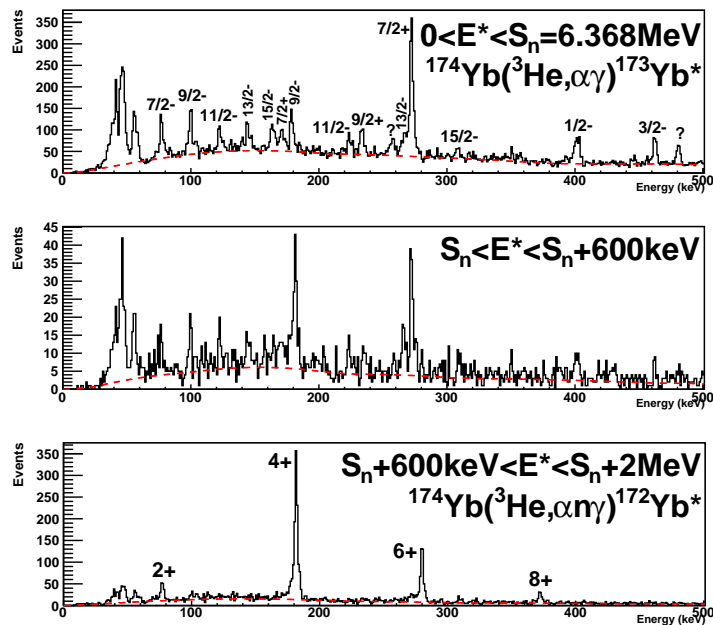
Figure 4.45: The same as in fig. 4.42 but for the $(^3He, \alpha)^{173}Yb^*$ and $(^3He, \alpha n)^{172}Yb^*$ channels.

($<$2%), the probability to detect two γ-rays from the same γ-cascade is negligible. Note that the *Ge* detectors have the advantage that one can select only γ-transitions relative to the compound-nucleus of interest. No correction for inelastic events ($n'\gamma$) is therefore needed. In order to reduce statistical errors, the size of the excitation-energy bin used was 200 keV. To obtain the γ-decay probability, the measured ratio was normalized to 1 below S_n. The gamma transitions selected for the analysis are given in table 4.6:

Reaction channel	Selected gamma transitions
$^{174}Yb(^3He,p)^{176}Lu^*$	$1^+ \to 1^-$ (71.51 keV) , $8^- \to 7^-$ (184.13 keV)
$^{174}Yb(^3He,d)^{175}Lu^*$	$\frac{5}{2}^+ \to \frac{7}{2}^+$ (343.7 keV) , $\frac{9}{2}^- \to \frac{7}{2}^+$ (396.32 keV)
$^{174}Yb(^3He,t)^{174}Lu^*$	$2^+ \to 3^-$ (208.36 keV) , $2^+ \to 1^-$ (320.09 keV) , $0^+ \to 1^-$ (281.16 keV), $8^+ \to 7^+$ (340.69 keV)
$^{174}Yb(^3He,\alpha)^{173}Yb^*$	$\frac{9}{2}^+ \to \frac{9}{2}^-$ (233.6 keV) , $\frac{7}{2}^+ \to \frac{7}{2}^-$ (272.1keV), $\frac{1}{2}^- \to \frac{5}{2}^-$ (398.9keV), $\frac{3}{2}^- \to \frac{5}{2}^-$ (461.5keV)

Table 4.6: Gamma-transitions selected for the analysis.

The γ-spectra were unfolded using Gaussian fits for the peaks and a quadratic fit for the background. Unfortunately, this approach was abandoned because of the lack of statistics. To overcome this problem, we used a one-dimensional background estimation function already implemented in ROOT. After twenty iterations, the backgrounds were found to follow polynomial of second order (see dotted red lines on the identification γ-spectra). The transition intensities were then defined as the residual area of the peak after background subtraction. In addition to statistical errors, we assumed a systematic error of 10% in order to take into account the uncertainties in the background determination/subtraction and the probability normalization below the neutron-binding energy. The obtained probabilities are compared to those obtained previously via the analysis of the C_6D_6 scintillators in figure 4.46. The radiative capture probabilities are rather well reproduced with the *Ge* analysis. This indicates that either the feeding of the selected transitions does not depend on E^* or the selected transitions collect all the decays. In addition, this good agreement shows several important points concerning the C_6D_6 analysis:

- There is no contaminant issue or severe systematic error for all the transfer channels.

- The ($n'\gamma$) channel has been well subtracted.
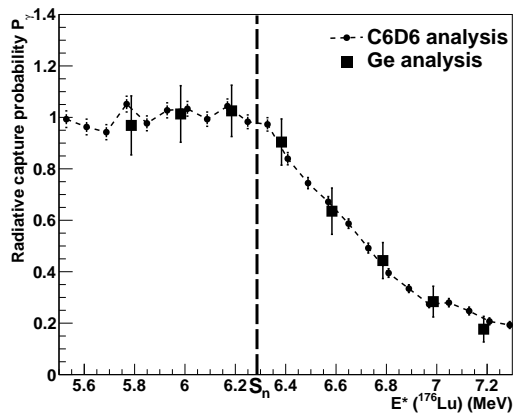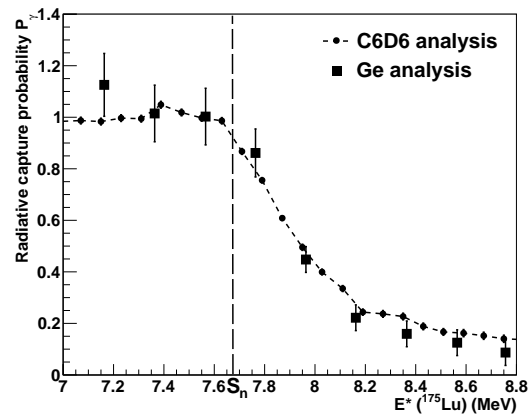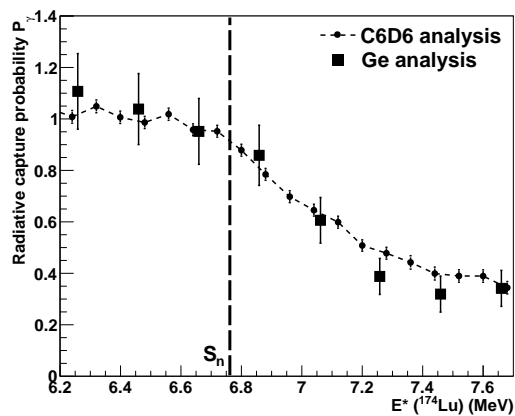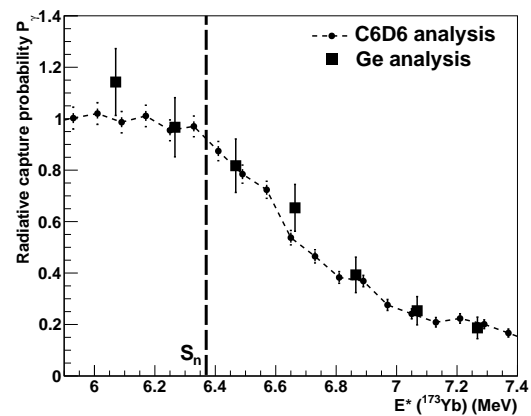
Figure 4.46: Radiative capture probabilities obtained in the surrogate experiment by using the *Ge* detectors in comparison with the results obtained with the C_6D_6 detectors.

To conclude, we would like to stress that, reducing considerably the statistical errors, this new technique could be envisaged to infer radiative capture cross sections in future surrogate experiments. Nevertheless, further investigations are needed to understand under which conditions:

- the feeding of the selected γ-transitions is independent of E^*.

$$\text{or}$$

- all the decay paths go through the selected γ-transitions.

Interpretation & Consequences

"L'esprit n'use de sa faculté
créatrice que quand l'expérience
lui en impose la nécessité."

(Henri Poincaré (1854-1912))

Chapter 5

Interpretation of results

5.1 Study of the $^{174}Yb(^3He, p\gamma)^{176}Lu^*$ reaction as a surrogate for $^{175}Lu(n, \gamma)$

5.1.1 TALYS calculations for the compound-nucleus formation cross section

A TALYS calculation using an optimized deformed optical potential was realized by Pascal Romain (CEA DAM DIF). Level density and strength function parameters were adjusted to reproduce the known s-wave resonance spacings, average radiative widths, and measured neutron-induced cross sections. Similar work has already been done for the neighbouring hafnium isotopes in [Noguere 09]. Pre-equilibrium neutron emission, width-fluctuation corrections and electron conversion are included in TALYS. To ensure that we have reliable parameters in TALYS, we performed a neutron-induced experiment ($^{175}Lu + n$). This is detailed in appendix O. The statistical calculations were found to reproduce all the measured observables. In order to infer the neutron-induced radiative cross sections using the surrogate method, the compound-nucleus formation cross section of the reaction $^{175}Lu + n$ was calculated. An error of 5% was assumed. Figure 5.1 shows the different types of cross sections related to the $^{175}Lu + n$ reaction as a function of the incident neutron energy. Below 1 MeV, the decay proceeds mainly through a compound-nucleus. It is therefore reasonable to neglect the direct and pre-equilibrium contributions since they are more than one order of magnitude lower than the CN contribution to the total cross section.

5.1.2 Comparison with neutron-induced data and with calculations

Applying equation 2.1, the (n, γ) capture cross section of ^{175}Lu, in the neutron-energy range from 0 to 1 MeV, was deduced via the product of the measured γ-decay probability $P_\gamma(E^*)$ of $^{176}Lu^*$ with the calculated compound-nucleus formation cross section in the
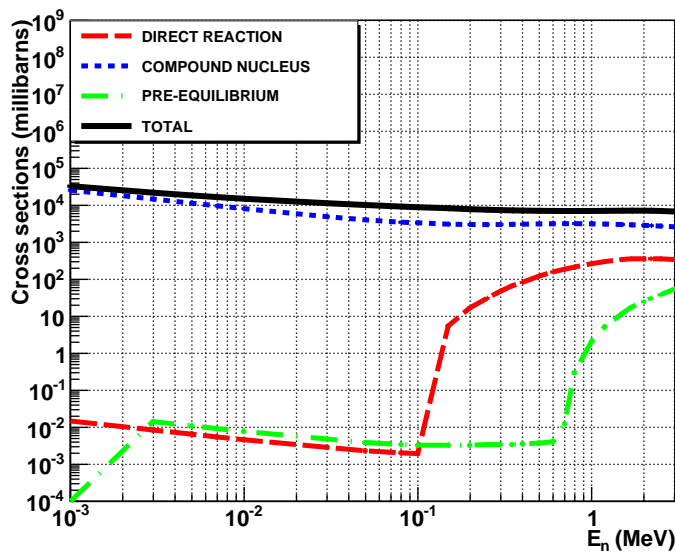
Figure 5.1: TALYS calculation for the different contributions to the total reaction cross section in $^{175}Lu + n$.

neutron-induced reaction. The result is shown in figure 5.2 in comparison with neutron-induced data, the ENDF/B-VII evaluation and the TALYS calculation from which we extracted the CN cross section. Our surrogate cross section is too large on average by roughly a factor 4. The assumption that the spin distributions populated in the $^{174}Yb(^3He, p\gamma)$ and $^{175}Lu(n, \gamma)$ reactions are the same is questioned. This will be further investigated in next section.

5.1.3 Comparison of the experimental radiative capture probability with TALYS calculations

The experimental γ-decay probability is compared with TALYS calculations for the neutron-induced capture probability of ^{175}Lu and for the photon-induced capture probability of ^{176}Lu. Note that the parameters of the TALYS code have been tuned to exactly reproduce the experimental data for the $^{175}Lu(n, \gamma)^{176}Lu^*$ cross sections, see fig. 5.2. As can be seen in figure 5.3, our surrogate data present big discrepancies with respect to the neutron-induced data, while we observe a much better agreement with the $^{176}Lu(\gamma, \gamma')^{176}Lu^*$ calculation at low energies. This indicates that the $J\Pi$ distribution populated in the $^{174}Yb(^3He, p)$ surrogate reaction is close to the one populated in the photon-induced reaction. The ground-state $J\Pi$ of ^{175}Lu and ^{176}Lu are respectively $\frac{7}{2}^+$ and 7^-. On the other hand, the spin of a neutron and a E1 photon are respectively $\frac{1}{2}$
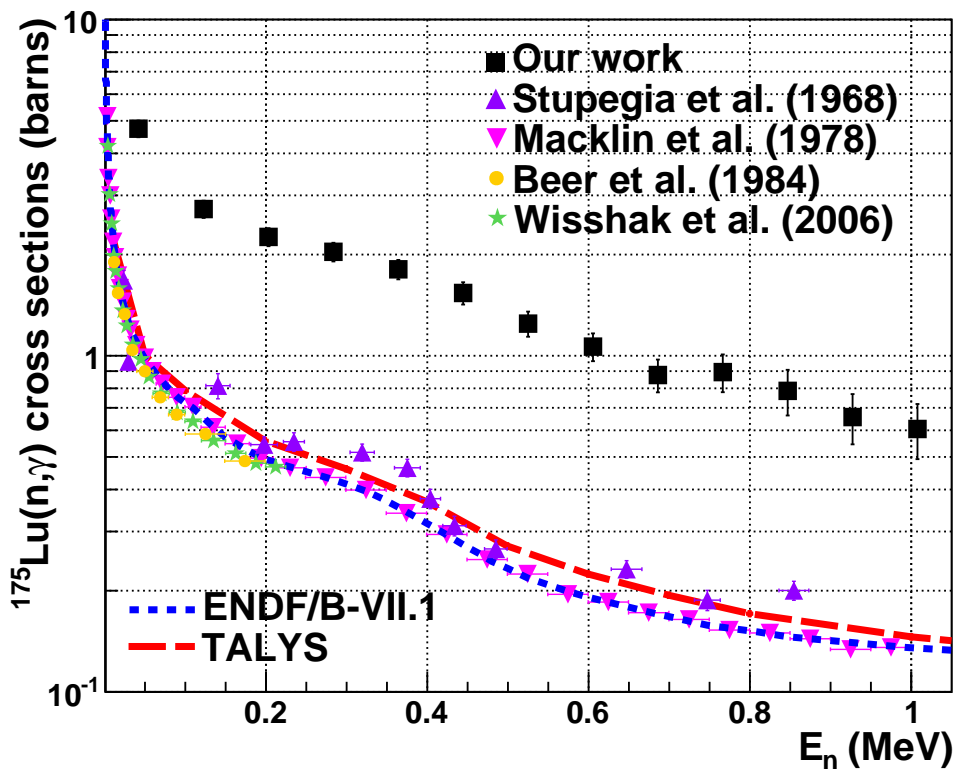
Figure 5.2: Radiative capture cross section of ^{175}Lu obtained from $^{174}Yb(^{3}He, p\gamma)^{176}Lu^{*}$ compared to existing neutron-induced data and to various evaluations. Details on the neutron-induced measurements can be found in [Stupegia 68],[Macklin 78], [Beer 81], [Beer 84] and [Wisshak 06].

and 1. The angular momentum composition gives:

$$\vec{I} + \vec{i} + \vec{l} = \vec{J} \qquad (5.1)$$

where $\vec{I}$ is the spin of the target, $\vec{i}$ is the spin of the captured particle, $\vec{l}$ is the orbital angular momentum transferred in the reaction and $\vec{J}$ is the spin of the compound-nucleus. In the case of neutron-induced reactions, the orbital angular momentum transferred increases with the neutron energy. For s-wave neutrons, only $\vec{l} = 0$ can occur. In the case of photons, E1 transitions are predominant. That is why the angular momentum of ^{176}Lu populated by low-energy neutrons is mainly centered between 3 and 4 $\hbar$ $(\frac{7}{2} \pm \frac{1}{2}\ \hbar)$, while the angular momentum populated in the photon-induced reaction is much higher $(7 \pm 1\ \hbar)$. Consequently, the big discrepancies found at low E^* can be explained by the differences between the spin distributions populated in photon- or transfer-induced reactions and neutron-induced reactions. For excitation energies after neutron emission below the first excited state of ^{175}Lu (113keV,$\frac{9}{2}^+$), the (n, γ) decay channel is only in competition with the compound-elastic channel (n, n), where the residual nucleus is left in its ground state after neutron emission. The nucleus can only decay to one state with a well-defined $J\Pi$ $(\frac{7}{2}^+)$ that corresponds to the spin of the target $\vec{I}$. This particular exit channel is extremely sensitive to the spin of the compound-nucleus $^{176}Lu^*$. The compound elastic channel (n, n) is allowed since for low energy neutrons the spin of the compound-nucleus verifies $\vec{I} \pm \frac{1}{2} = \vec{J} \approx \vec{I}$. Hence, the emission of slow s-neutrons leaves the residual nucleus in its ground state $\vec{I}$. In the left part of figure 5.4, TALYS calculations for the neutron-induced reaction show clearly that the (n, n) channel is the dominant decay channel right above S_n. Moreover, it remains rather strong up to about 8 MeV excitation energy. The (n, n') channel sets in above $S_n + 113$ keV and becomes predominant at higher energies. Consequently, the (n, γ) radiative capture is expected to decrease very quickly at S_n because of the openned (n, n) and (n, n') decay channels. However, as said above, the angular momentum induced by the $(^3He, p)$ transfer reaction seems to be also centered around 7 $\hbar$, which is about two times higher than the angular momentum of the ^{175}Lu ground state $\frac{7}{2}^+$. Under these conditions, $\vec{J} \neq \vec{I}$ and the population of the ground state of ^{175}Lu after neutron emission is very improbable. The same strong spin selectivity is also expected for the first excited states of the residual nucleus. Therefore, at the lowest energies above S_n, γ-emission is the dominant decay channel. This is illustrated on the right part of figure 5.4. In conclusion, the differences in populated spins and the high selectivity of the (n, n) and (n, n') decay channels are at the origin of the large discrepancies observed between surrogate and neutron-induced measurements.
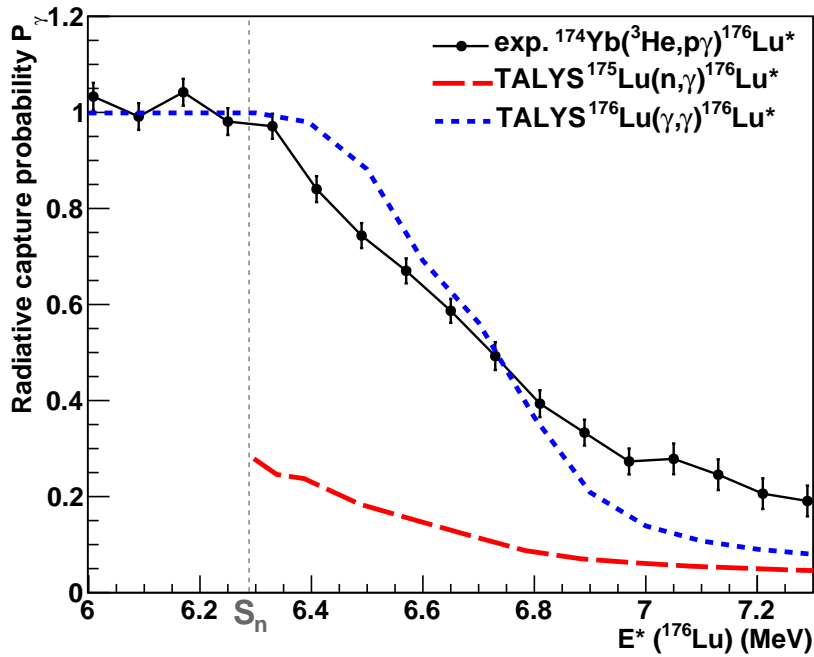
Figure 5.3: Radiative capture probability measured in the $^{174}Yb(^3He,p\gamma)^{176}Lu^*$ reaction as a function of the E^* of ^{176}Lu (black dots) compared to predictions performed with TALYS. The red dashed-line is the neutron-induced capture probability (n,γ) of ^{175}Lu. The blue dotted-line is the photon-induced capture probability (γ,γ) of ^{176}Lu.
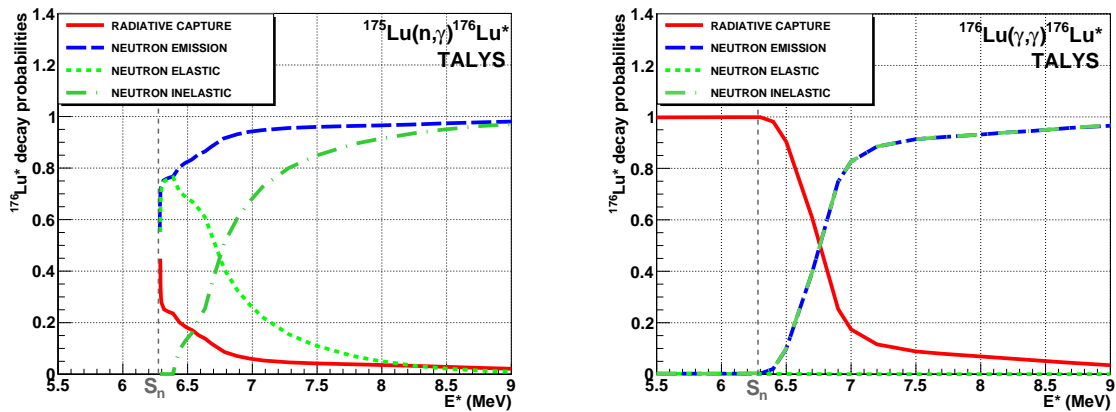
Figure 5.4: TALYS calculations for the different decay probabilities in $^{175}Lu(n,\gamma)^{176}Lu^*$ (left) and $^{176}Lu(\gamma,\gamma)^{176}Lu^*$ (right).

5.1.4 Determination of the populated angular momentum distribution using TALYS

Since the gamma decay probability of $^{176}Lu^*$ is very sensitive to $J\Pi$, we investigated a method to extract the populated $J\Pi$ distribution from a fit to the experimental decay probability using the branching ratios calculated by TALYS. Figure 5.5 shows TALYS calculations for the γ-decay probabilities for various spin/parity states as a function of the excitation energy of $^{176}Lu^*$. The calculation included 54 discrete levels of ^{176}Lu. The lower limit of the continuum is the energy of the last discrete level at 772 keV. In addition, 19 discrete levels for the residual nucleus after neutron evaporation ^{175}Lu were taken into account. Figure 5.5 clearly illustrates the sensitivity of γ-decay probabilities to the $J\Pi$ of the decaying compound state. The clear drop just above S_n due to the competition with the (n, n) channel is only observed for spin values of 3 to 4 $\hbar$. For all the other spins P_γ remains close to 1 near S_n. Note also that for the highest spins, P_γ remains equal to 1 over several keV. This is due to the impossibility to populate the first-excited states of ^{175}Lu after neutron emission. At these excitation energies it is very unlikely that the emitted neutron carries high angular momentum. It is clear that the Weisskopf-Ewing approximation is not valid in this region.

According to equation 2.1, the experimental gamma-decay probability $P_\gamma(E^*)$ can be written as:

$$P_\gamma(E^*) \approx \sum_{J,\Pi} \left[\frac{1}{2\sigma\sqrt{2\pi}} e^{-\frac{(J-\bar{J})^2}{2\sigma^2}} \right] . G_\gamma^{TALYS}(E^*, J, \Pi) \qquad (5.2)$$

where the angular momentum distribution $F_s^{CN}(E^*, J, \Pi)$ is expressed as a Gaussian without dependence on the excitation energy. The two parities are assumed to be equally populated. The two unknown parameters $\overline{J}$ and σ correspond to the average value and the standard deviation of the spin distribution. These quantities are obtained by fitting eq. 5.2 to the experimental radiative capture probability using the branching ratios $G_\gamma^{TALYS}(E^*, J, \Pi)$. By fitting our data from 5.5 to 7.4 MeV, as shown in figure 5.6, we obtained a spin distribution centered at $< \overline{J} >= 7.1\hbar$ with $\sigma = 2.3\hbar$. A high χ^2-value (close to 2) was obtained which is due to discrepancies above $E^* > 7$ MeV. By fitting our data only up to 7 MeV, the χ^2-value becomes excellent (close to 1): the obtained spin distribution had still $< \overline{J} >= 7.1\hbar$ but with a lower $\sigma = 1.8\hbar$. For comparison, the spin distribution populated in a neutron-induced reaction for $E_n = 1$ MeV has $< \overline{J} >= 4\hbar$ with $\sigma = 1.3\hbar$, see fig. 5.7. It should be investigated to which extent the obtained angular momentum distribution can be extrapolated to heavier target nuclei (e.g. actinides). It would be more than desirable to have the support of theoreticians to evaluate how much does the populated spin distributions depend on the target nucleus. More precisely, one needs to study for example the influence of the single-particle structure of the target nucleus on the angular momentum distribution.
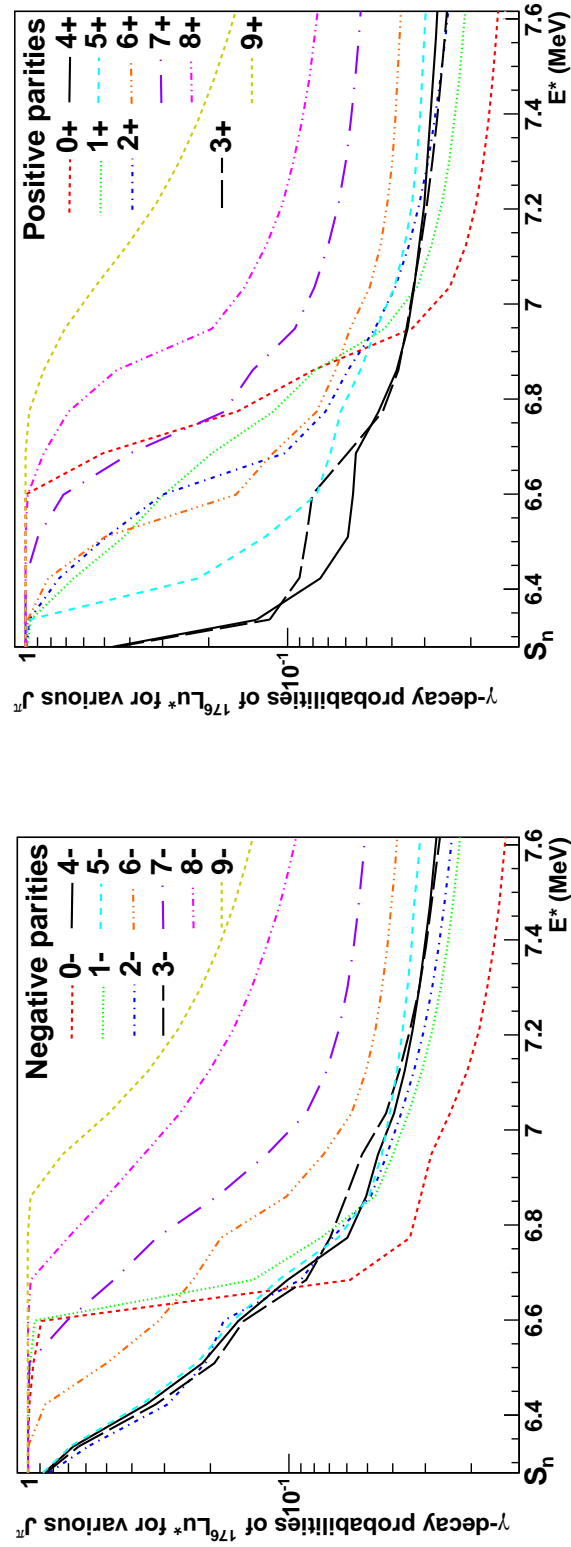
Figure 5.5: Calculated γ-decay probabilities $G_{\gamma}^{TALYS}(E^{*},J,\Pi)$ of ^{176}Lu for a specific $J\Pi$ combination. The excitation energies shown correspond to incident neutron energies of 0-1,2 MeV. The left and right parts are dedicated to negative and positive parities, respectively.
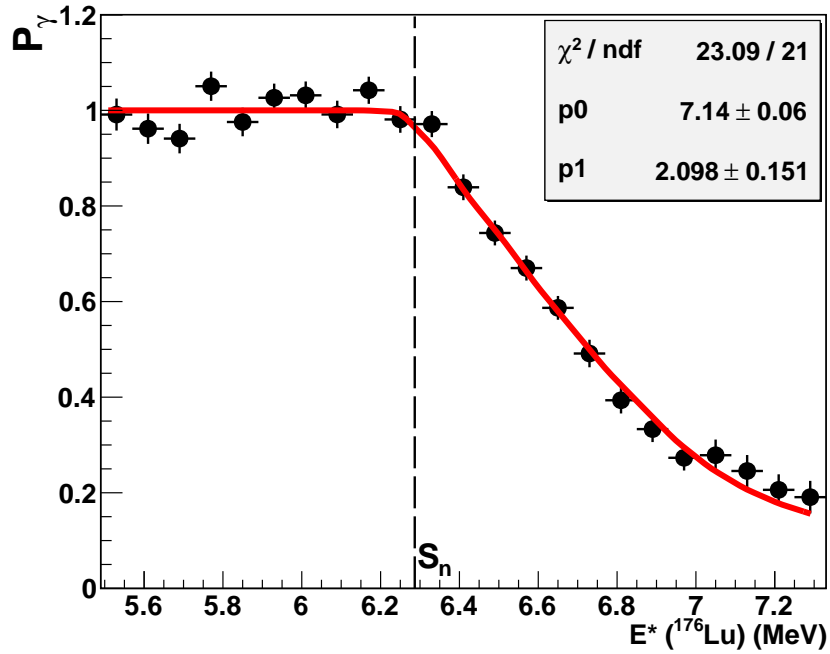
Figure 5.6: Fit of the experimental P_γ with eq. 5.2. The parameters $p0$ and $p1$ correspond to the average spin-value $\overline{J}$ and the σ of the Gaussian spin distribution, respectively.
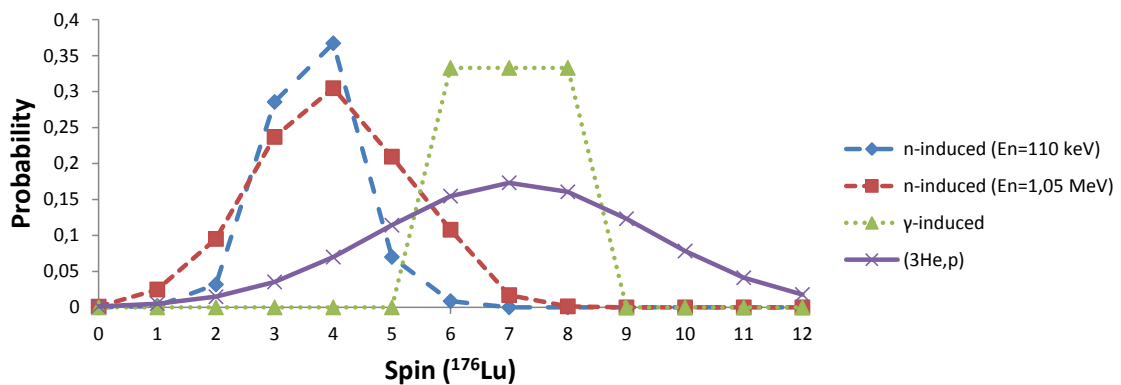
Figure 5.7: Spin distributions of $^{176}Lu^*$ populated in different reactions.

5.1.5 Determination of a more realistic populated angular momentum distribution

In the following, we investigate a formalism to extract the transferred angular momentum and spin distributions through a more realistic approach that does not assume equal probability for positive and negative parities. We know that direct reactions predominantly excite particular states in the compound-nucleus: single-neutron-states in (d, p) reactions, single-proton-states in $(^3He, d)$ reactions or quasi-particle states in (t, p) reactions. The analysis of the angular-dependent cross sections of these reactions is one of the most important ways for the determination of the structure of nuclear states in the low excitation-energy range. In the excitation-energy region of interest in this work (above S_n=6.29 MeV), the particular single-particle states $J\Pi_{sp}$ are predominantly mixed to many complex overlapping compound states $J\Pi_c$ described by the statistical model. This is confirmed by our measured singles spectrum that varies very smoothly with the excitation energy. If we consider one of the particular states $J\Pi_{sp}$, this state is mixed to the neighbouring complex states $J\Pi_c$. In other words, the strength of single-particle level is spread over a large number of complex states $J\Pi_c$ having excitation energies roughly between $E_{sp} + \Gamma_s$ and $E_{sp} - \Gamma_s$, where Γ_s is the mixing width of the considered single-particle states. The damping of the particular single-particle state into the continuum is usually described by the strength function concept. Unfortunately, these strength functions are very difficult to be obtained. To overcome these problem, B.L. Andersen and B.B. Back ([Andersen 70]) defined a similar function that describes the spreading as a function of the excitation energy E^* and the discrete energy E_{sp} of the particular state $J\Pi_{sp}$. The spreading function is approximated by a Lorentzian given by:

$$L(E^*) = \frac{1}{2\pi} \frac{\Gamma_s}{(E_{sp} - E^*)^2 + \frac{\Gamma_s^2}{4}} \tag{5.3}$$

The spreading width Γ_s is described by the average transition rate given by first-order perturbation theory ([Lewis 75]):

$$\Gamma_s = 2\pi < C^2 > \Omega(E^*) \tag{5.4}$$

where $\Omega(E^*)$ is the level density of the compound nucleus at E^* and $< C^2 >$ is the average perturbation matrix element between the initial single-particle state and one of the final compound states. The latter equation is known as the Fermi's Golden Rule and says that the transition rate is related to the strength of the coupling between the initial and final states available to the compound nucleus. The differential cross section is given by:

$$\frac{d\sigma_c}{d\Omega dE^*} = \sum_{all\ sp} L(E^*) . \frac{d\sigma_{sp}}{d\Omega dE^*} \tag{5.5}$$

where σ_{sp} is the cross section for the formation of the particular state $J\Pi_{sp}$ fed by the transfer reaction and is usually determined by DWBA calculations in the continuum. Figure 5.8 illustrates the spreading of only one populated single-particle strength (top panel) into the continuum of compound states (middle panel). As a result of the near energy degeneracy between the populated particular state and the complex states, this particular state readily mixes with the continuum of compound levels. The associated differential cross section σ_c (bottom of figure) corresponds to the «thermalization» of the single-particle energy.
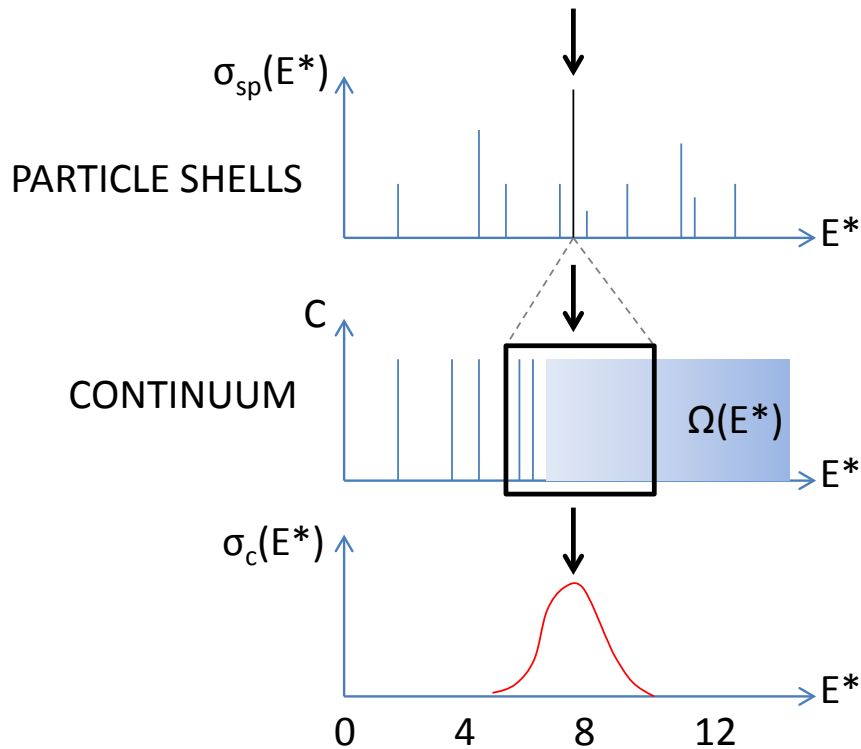
Figure 5.8: Schematic illustration of the spreading of a single-particle strength (upper panel) into the continuum of compound states (middle panel) that leads to the associated cross section σ_c (bottom panel). [Lewis 75]

We make a further approximation where we consider that the spreading function is simply proportional to the level density:

$$L(E^*) \propto \Omega(E^*) \tag{5.6}$$

The main argument behind the above equation is to consider that the matrix element $< C^2 >$ does not depend on the excitation energy E^*, spin J and parity Π of the compound state. This yields to a simplified expression for eq. 5.5 where the spin and parity distributions of the residual nucleus populated at the excitation energy E^* through

the particular state $J\Pi_{sp}$ are given by:

$$F_s^{CN}(E^*, J, \Pi) \propto \Omega(E^*, J).P_{sp}(E^*, J, \Pi) \tag{5.7}$$

where:

- $\Omega(E^*, J)$ is the level density. As shown in section 1.4.2, $\Omega(E^*, J) = R(E^*, J).\Omega_0(E^*)$ and $R(E^*, J) \approx R(J)$.

- $P_{sp}(E^*, J, \Pi)$ is the probability for the formation of the particular state $J\Pi_{sp}$ fed by the transfer reaction.

In this work, we will suppose that the two quantities Ω and P_{sp} are independent of E^*:

$$F_s^{CN}(J, \Pi) = R(J).P_{sp}(J, \Pi) \tag{5.8}$$

We would like to stress that the latter equation has been already used by B. Back et al. ([Back 74b]), M. Mermaz ([Mermaz 80]) and W. Younes et al. ([Younes 03a]). In the following, we explain our derivation of the quantity $F_s^{CN}(J, \Pi)$. According to eq. 5.1, we define the total angular momentum transferred as:

$$\vec{j} = \vec{i} + \vec{l} \tag{5.9}$$

Starting from a final spin J we have two unknown and correlated quantities $\vec{j}$ and $\vec{l}$. We know from the eqs. 5.1 and 5.9 that the modulus of $\vec{j}$ and $\vec{l}$ are restricted to:

$$\mid J - I \mid < j < (J + I) \tag{5.10}$$

$$\mid j - i \mid < l < (j + i) \tag{5.11}$$

The final spin and parity distribution of the compound-nucleus is then given by:

$$F_s^{CN}(J, \Pi) = R(J). \sum_{j=|J-I|}^{J+I} \sum_{l=|j-i|}^{j+i} \frac{P_l.\delta(\Pi_I, \Pi_i, (-1)^l)}{N_l} \tag{5.12}$$

Note that the double summation takes into account all possible ways to compose $\vec{J}$ from $\vec{j} + \vec{I}$ (with eq. 5.10) and all possible ways to compose $\vec{j}$ from $\vec{l} + \vec{i}$ (with eq. 5.11). The number of these couplings is given by:

$$N_l = \sum_{j=|J-I|}^{J+I} \sum_{l=|j-i|}^{j+i} 1 \tag{5.13}$$

The final expression for F_s^{CN} is normalized:

$$\sum_{J,\Pi} F_s^{CN}(J,\Pi) = 1 \tag{5.14}$$

The dimensionless quantity P_l describes the probability for transferring a given orbital angular momentum in the transfer reaction. We recall that, in our case, P_l was not determined by DWBA calculations. We assumed an analytical form and constrained it via a fit to the experimental capture decay probability using TALYS branching ratios $G_\gamma^{TALYS}(E^*, J, \Pi)$. In this work, we tested several shapes of P_l without dependence on the excitation energy. Very often the spin distribution is described by the sharp cutoff description:

$$P_l \propto (2l+1) \quad if \quad l \leq l_{max} \quad ; \quad P_l = 0 \quad if \quad l > l_{max} \tag{5.15}$$

where the unknown parameter is nothing but the term l_{max} described in figure 5.9. A more sophisticated description consists in using a Wood-Saxon function to smooth the drop at l_{max}:

$$P_l \propto (2l+1) \frac{1}{1 + e^{-\frac{(l-l_{max})^2}{\delta_l}}} \tag{5.16}$$

The term δ_l gives the decay slope of the Wood-Saxon function. Nevertheless, as shown schematically in figure 5.9, a Gaussian distribution reproduces nicely the latter distribution at high angular momenta which are known to be preferentially populated in transfer reactions (peripheral collisions):

$$P_l \propto \frac{1}{2\sigma\sqrt{2\pi}} e^{-\frac{(l-\bar{l})^2}{2\sigma^2}} \tag{5.17}$$

with the two free parameters $\bar{l}$ and σ corresponding to the average value and the standard deviation of the angular momentum transferred. We obtained the full spin distribution by combining eq. 5.16 and eq. 5.12, and eq. 5.17 and eq. 5.12. The fit to our experimental data using TALYS branching ratios gave very similar results in both cases. Therefore, for simplicity, we will concentrate on the Gaussian description (eq. 5.17) in the following.

The latter quantities are obtained by fitting our experimental data with the the angular momentum distribution given by the combination of eqs. 2.1 and 5.17 and the branching ratios (see Fig. 5.5). In the case of the transfer reaction $(^3He, p)$, the 1-proton and 1-neutron transferred can be coupled in two ways: $i = \frac{1}{2} - \frac{1}{2} = 0\hbar$ and $i = \frac{1}{2} + \frac{1}{2} = 1\hbar$. Results of the fit for both cases are shown in figure 5.10. The transferred angular momentum in the $^{174}Yb(^3He, p)$ reaction is about 8 $\hbar$ with a RMS deviation equal to 3.4-3.8 $\hbar$ depending on the value of $\vec{i}$ considered. Note that the spin of the transferred particle does not play a significant role in the average angular momentum and σ. However, as shown in figure 5.11, the parity distribution is found to be very sensitive to the spin of the
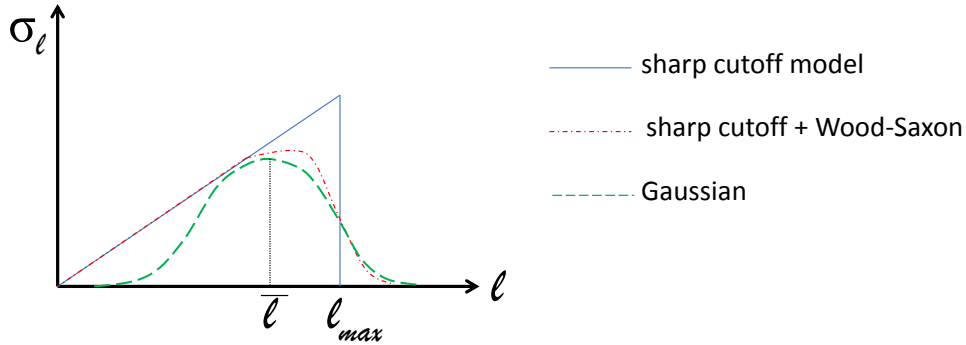
Figure 5.9: Transferred angular-momentum distributions investigated in this work.

transferred particle. For $i = 0\hbar$, only natural parities are populated. On the other hand, the case $i = 1\hbar$ allows for all spin-parity combinations. The spin distribution obtained in section 5.1.4 (assuming that the parities are equally populated) is represented by the dashed line in figure 5.11. The latter is in very good agreement with the distribution that results from adding the distributions for positive and negative parities.

5.1.6 Information on the spin distribution from Ge detectors

Low-lying transition intensities have been used to derive the radiative capture probability in section 4.8.3. We compare in figure 5.12 the γ-ray spectra relative to our surrogate experiment at $E^* = S_n$ with data obtained in the neutron-induced reaction $^{175}Lu(n, \gamma)$ at thermal energies ([Andrejtscheff 74]). In our data, the γ-ray transitions coming from de-excitation of the 8^+ level (located at 424.9 keV) are clearly observed at 424.9 keV and 241 keV. In Andrejtscheff's spectra, these γ-ray transitions are not observed. On the other hand, the 139.3 keV transition coming from the decay from the 4^+ level ($E^* = 372.5$ keV) is well fed in the neutron-induced reaction, whereas it is not observed in our surrogate data. These kind of observations clearly reinforce our previous conclusion, namely the population of higher spins in the $(^3He, p)$ transfer reaction.

$$\vec{i} = 0\ \hbar \qquad\qquad\qquad \vec{i} = 1\ \hbar$$
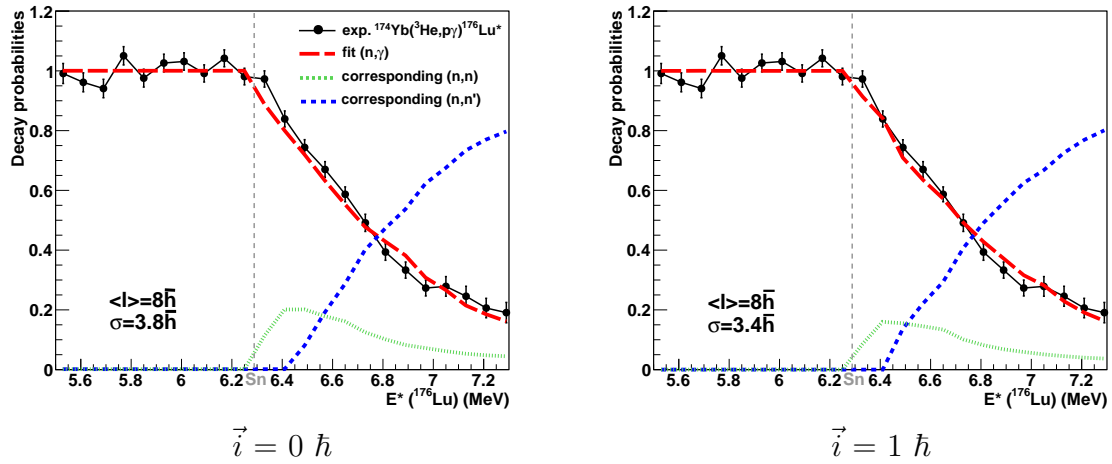
Figure 5.10: Fit of the experimental P_γ. The two fit parameters correspond to the average angular momentum transferred $\bar{l}$ and the σ of the Gaussian distribution, respectively. The corresponding neutron-emission probabilities are also shown. They can be compared to the ones shown in Fig. 5.4.

$$\vec{i} = 0\ \hbar \qquad\qquad\qquad \vec{i} = 1\ \hbar$$
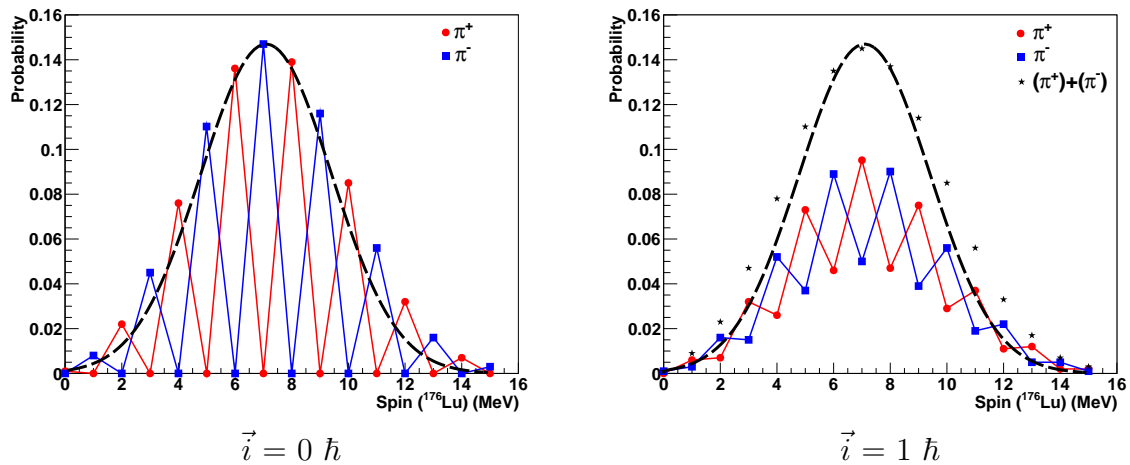
Figure 5.11: Spin distributions obtained from the fit shown in Fig. 5.10. The dashed line corresponds to the spin distribution obtained in section 5.1.4.
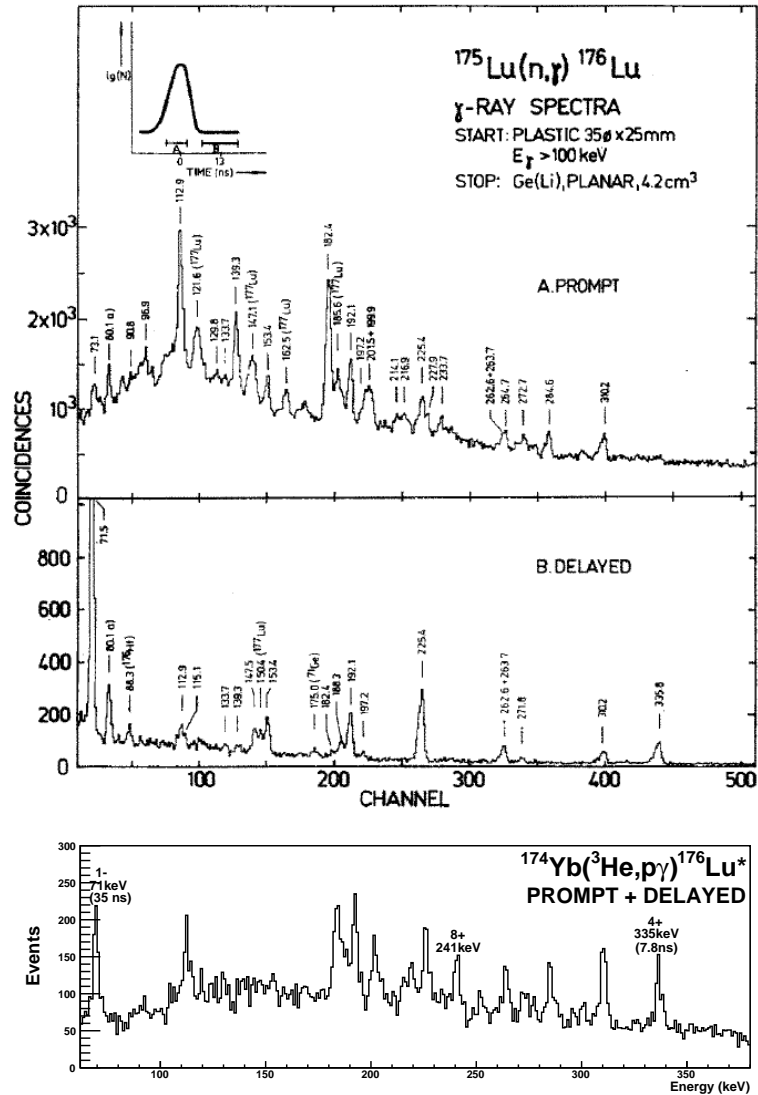
Figure 5.12: Gamma-ray spectra obtained in the thermal $^{175}Lu(n, \gamma)$ reaction ([Andrejtscheff 74], top panel) compared with the spectrum obtained in our $^{174}Yb(^3He, p\gamma)^{176}Lu^*$ experiment at $E^* = S_n$ (bottom panel).

5.2 Study of the $^{174}Yb(^3He, \alpha\gamma)^{173}Yb^*$ reaction as a surrogate for $^{172}Yb(n, \gamma)$

5.2.1 TALYS calculations for the compound-nucleus formation cross section

As in the previous section, different parameters of the TALYS code were tuned by P. Romain to best reproduce the existing neutron-induced data for $^{172}Yb(n, \gamma)$. Figure 5.13 shows the different contributions to the total reaction cross section. Direct and pre-equilibrium reactions are clearly below the compound-nucleus cross section and are neglected in the application of the surrogate method.
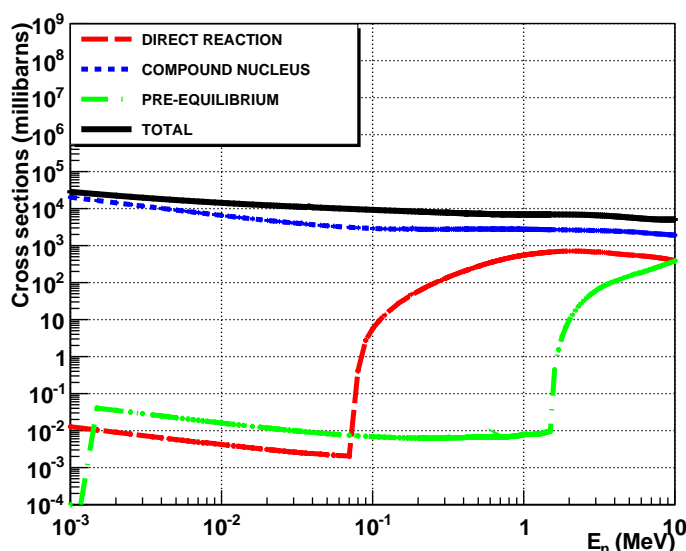
Figure 5.13: Competition between the different reaction mechanisms in $^{172}Yb + n$. The compound-nucleus formation cross section is given (dotted blue line).

5.2.2 Comparison with neutron-induced data and with calculations

The (n, γ) capture cross section of ^{172}Yb, in the neutron energy range from 0 to 1 MeV, has been deduced via the product of the measured γ-decay probability $P_\gamma(E^*)$ of $^{173}Yb^*$ and the calculated compound-nucleus formation cross section in the neutron-induced reaction. Our data are compared with already existing neutron-induced data and various predictions in figure 5.14. Again, the transfer-induced results are much higher (by a factor 10 at the lowest energies!) than the neutron-induced data.
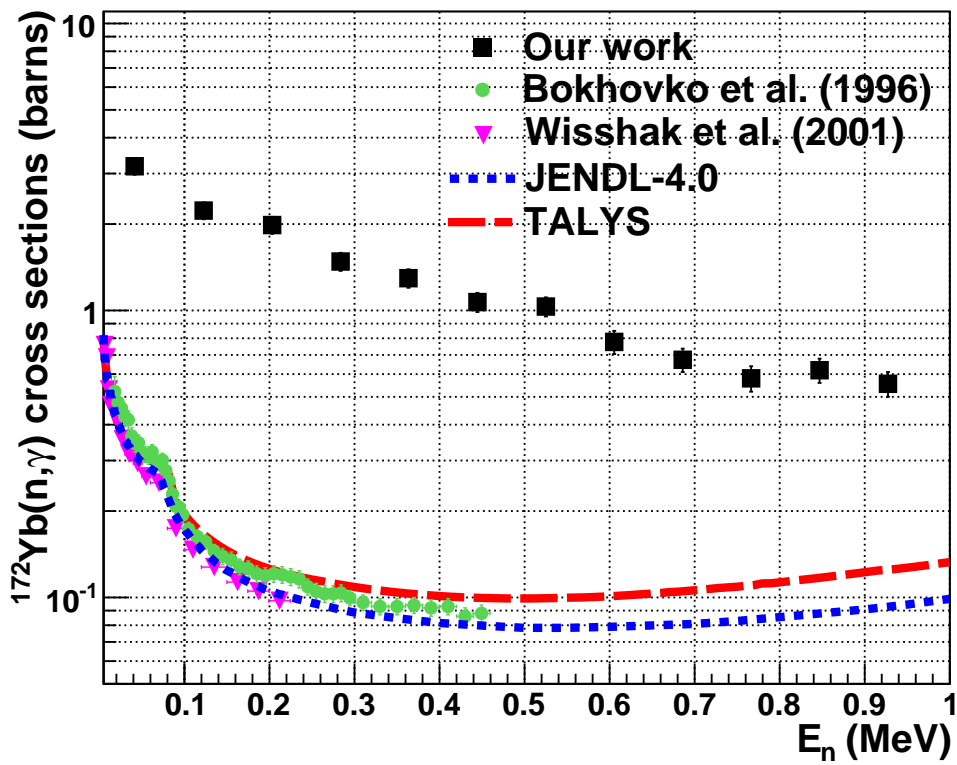
Figure 5.14: Radiative capture cross section of ^{172}Yb compared to existing neutron-induce data and to various predictions. Details on the corresponding neutron-induced measurements can be found in [Bokhovko 96] and [Wisshak 00].

5.2.3 Comparison of the experimental radiative capture probability with TALYS calculations

To understand such discrepancies, the experimental γ-decay probability is compared with TALYS calculations for the neutron-induced capture probability of ^{172}Yb and for the photon-induced capture probability of ^{173}Yb. Results are presented in figure 5.15. Obviously, our surrogate data present big discrepancies with respect to the neutron-induced data. In this case, the photon-induced capture probability is shown to be below the transfer-induced data. The two TALYS calculations show clear changes of slope at S_n and at energies that correspond to the first and second excited states of the even-even ^{172}Yb. They indicate the reduction of the capture decay probability caused by the competition with neutron emission leaving the residual nucleus ^{172}Yb in the ground state, in the first or in the second excited state. These changes in slope can also be observed at similar energies for the $^{174}Yb(^3He,\alpha)^{173}Yb$ reaction although in this case the changes due to higher states are also observed. We recall that the energy resolution of our measurements is 80 keV. Similar observations are very difficult in the case of an odd-odd nucleus like ^{175}Lu because of our excitation-energy resolution and the important number of states already present at low E^*. Whereas the neutron-induced reaction decays preferentially (90%) through the (n,n) channel (see figure 5.16), for the transfer and photon-induced reactions the decay probability remains high until the E^* of the first excited states are reached, indicating that the emission of neutrons to the ground state of ^{172}Yb is strongly suppressed. Also the drops in the experimental capture probability are less intense than for the (n,γ) and (γ,γ) reactions. This suggests that the average angular momentum populated in the transfer reaction is significantly bigger and that the spin distribution is broader than for the neutron and photon-induced reactions. The spin population of $^{173}Yb^*$ is around $0-1\hbar$ in the neutron-induced reaction. The ground state of ^{173}Yb is $\frac{5}{2}^-$, therefore the angular momentum of ^{173}Yb after photon absorption will lie between $\frac{3}{2}$ and $\frac{7}{2}\hbar$. The latter values are smaller than the ones populated for ^{176}Lu whose ground-state spin is 7^+. This explains why in this case the radiative capture probability obtained in the photon-induced reaction is clearly below the one obtained in the transfer reaction.

5.2.4 Determination of the populated angular momentum distribution using TALYS

Figure 5.17 shows TALYS calculations of the γ-decay probability for various spin/parity contributions as a function of the excitation energy of the ^{173}Yb compound-nucleus. Due to the low level density in the residual even-even nucleus ^{172}Yb below the pairing gap, the onset of the neutron-decay to each state corresponds clearly to a discontinuity. The drop at S_n corresponds to the opening of the elastic neutron channel that is only observed for spin values close to 0 $\hbar$ and is particularly strong for positive parity. The Weisskopf-Ewing approximation is also clearly not appropriate here. As a conclusion,
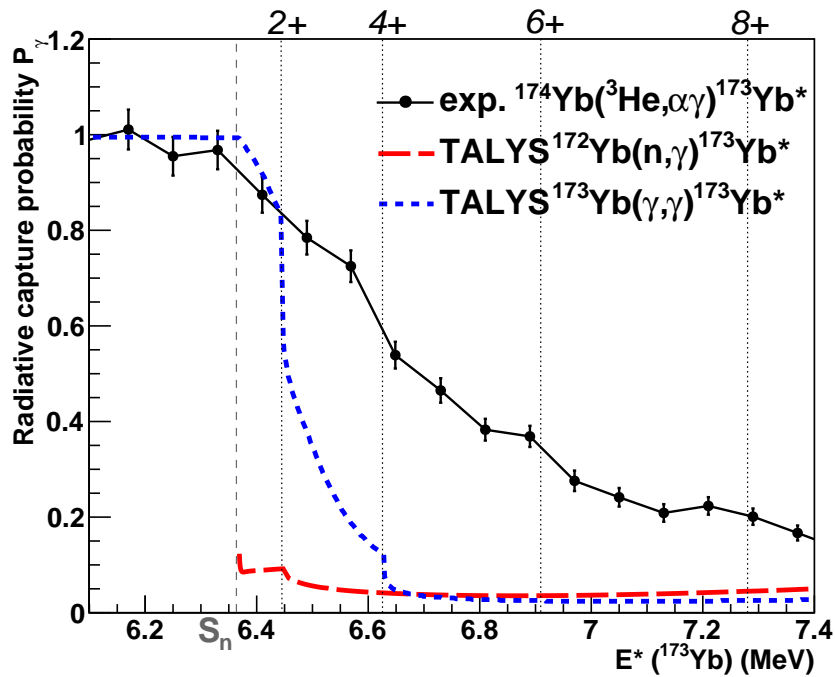
Figure 5.15: Capture probability measured in the $^{174}Yb(^3He, \alpha\gamma)^{173}Yb^*$ reaction (black) compared to predictions performed with TALYS. The red line is the neutron-induced capture probability (n, γ) of ^{172}Yb. The blue line is the photon-induced capture probability (γ, γ) of ^{173}Yb. The S_n and the first excited states energy positions of the residual ^{172}Yb are represented by the vertical lines.
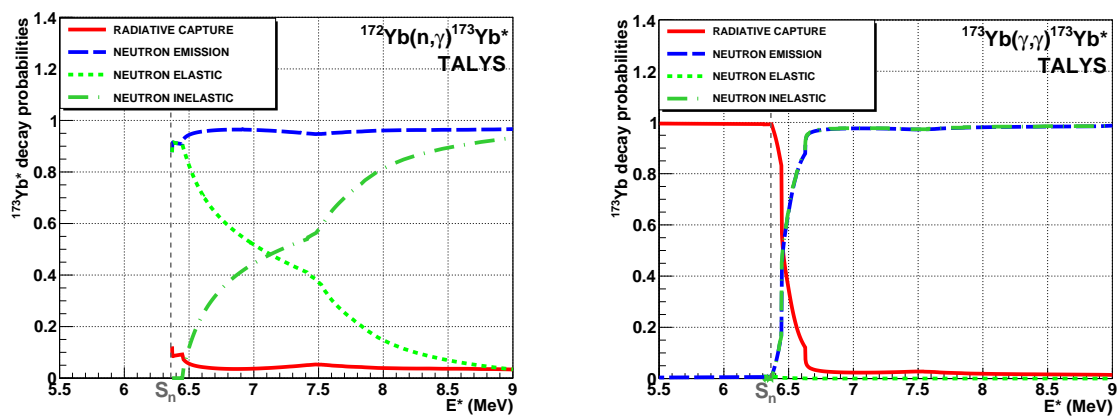
Figure 5.16: TALYS calculations for the decay probabilities obtained in the $^{172}Yb + n$ (right) and the $^{173}Yb + \gamma$ reactions (left).

γ-decay probabilities are extremely sensitive to $J\Pi$ because of the high spin-selectivity of neutron-decay. Gamma-decay is therefore strongly influenced by the structure of the low-lying states of the residual nucleus after neutron emission. As already discussed in section 1.6.2, the situation is hence expected to improve as one moves to heavier nuclei and away from closed shells.

As for the $(^3He, p)$ reaction, we can extract rather direct information on the transferred angular momentum in the $^{174}Yb(^3He, \alpha)$ reaction from a fit to the experimental capture probability using equation 5.2 and the branching ratios from TALYS. We recall that eq. 5.2 assumes equal probability for positive and negative parities. As illustrated in figure 5.18, we obtained a spin distribution centered on $J = 3.9\hbar$ with $\sigma = 3.2\hbar$. The considered energy range extends from 5.5 to 7.5 MeV and the χ^2-value was found to be reasonably good. For comparison, the spin distribution populated in a neutron-induced reaction for $E_n = 1$ MeV has $< \overline{J} >= 0\hbar$ with $\sigma = 1.3\hbar$, see fig. 5.19.

5.2.5 Determination of a more realistic populated angular momentum distribution

As explained in section 5.1.5, we extracted the transferred angular momentum and spin distributions through a more realistic approach that takes into account the explicit parity dependence. In the case of the transfer reaction $(^3He, \alpha)$, the spin of the transferred neutron is $i = \frac{1}{2}\hbar$. Results of the fit are shown in figure 5.20. We deduced the transferred angular momentum in the $^{174}Yb(^3He, \alpha)$ reaction, which is about 3 $\hbar$ with a RMS deviation equal to 3.8 $\hbar$. Applying eq. 5.12, the spin-parity distribution of the CN can be inferred. As shown in figure 5.21, the obtained spin distribution is in good agreement with the one obtained in section 5.2.4 (dashed line). However, there are important discrepancies for lower spins. In this region, the spin distribution seems to have a linear trend and is not well reproduced by the Gaussian.
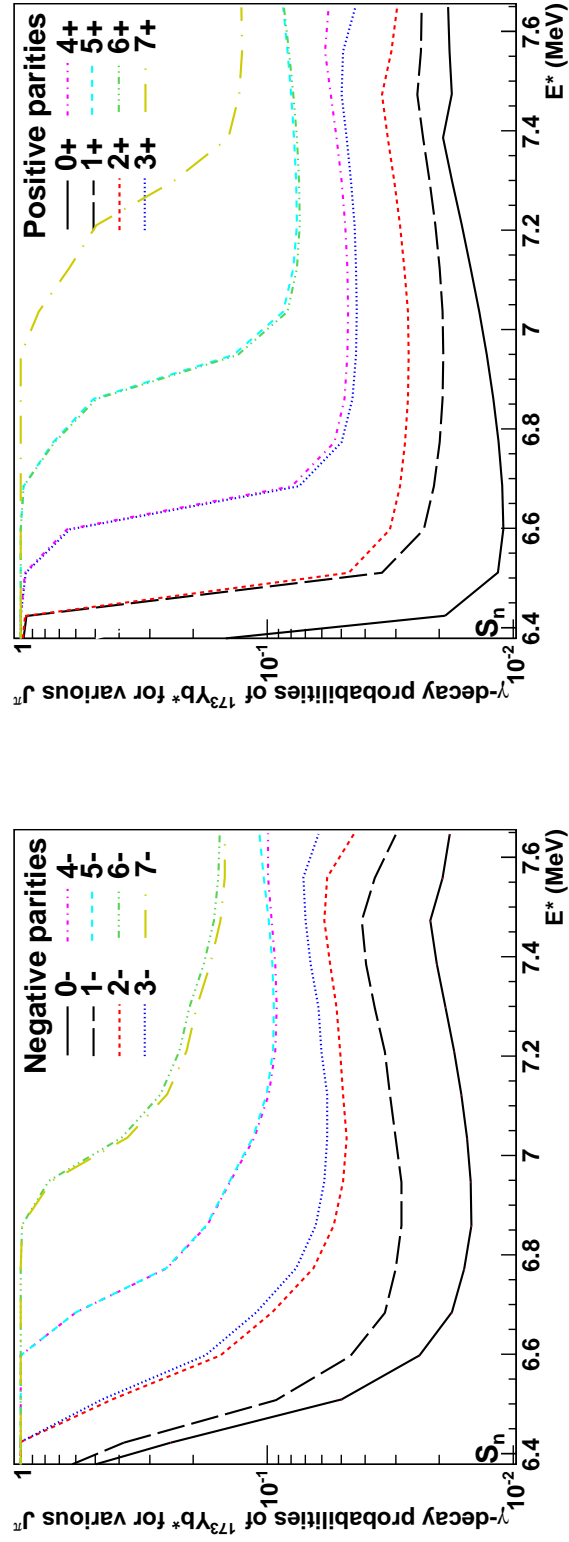
Figure 5.17: Calculated γ-decay probabilities $G_\gamma^{TALYS}(E^*, J, \Pi)$ for ^{173}Yb. Shown is the probability that the compound-nucleus, when produced with a specific $J\Pi$ combination, decays via the γ channel. The excitation energies (above $S_n = 6.368$ MeV) shown correspond to incident neutron energies of 0-1,2 MeV. The left and right parts are dedicated to negative and positive parities, respectively.
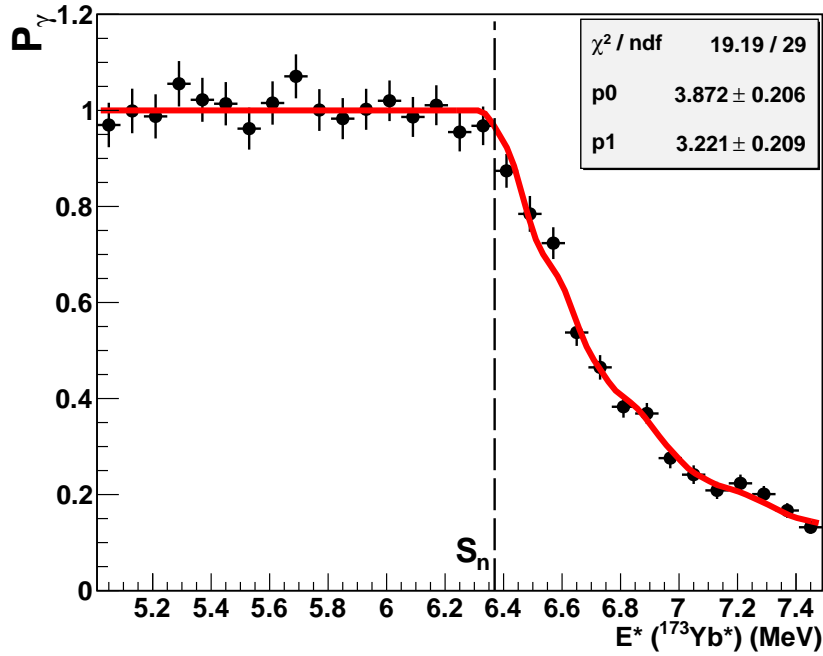
Figure 5.18: Fit of the experimental $P\gamma$ relative to the surrogate reaction $^{174}Yb(^{3}He, \alpha\gamma)^{173}Yb^{*}$. The parameters $p0$ and $p1$ correspond to the average spin-value $\overline{J}$ and the σ of the Gaussian distribution, respectively.
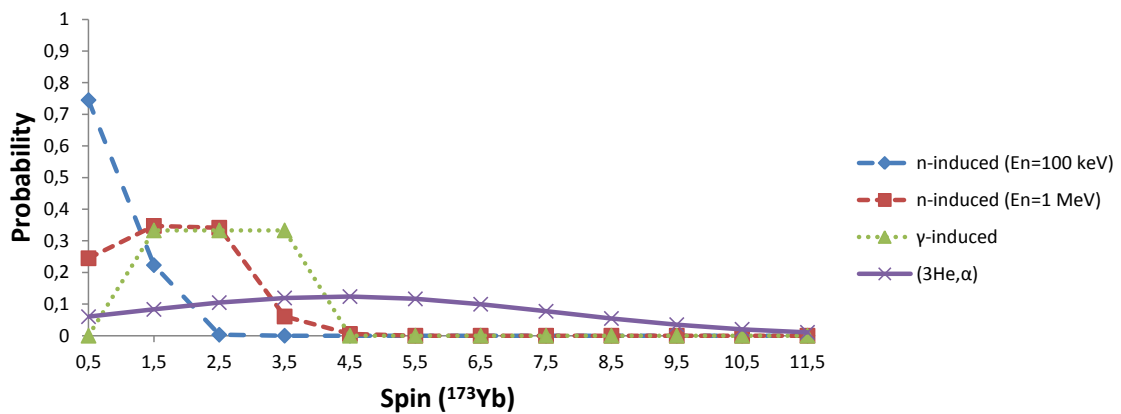
Figure 5.19: Spin distributions of $^{173}Yb^{*}$ populated in different reactions.
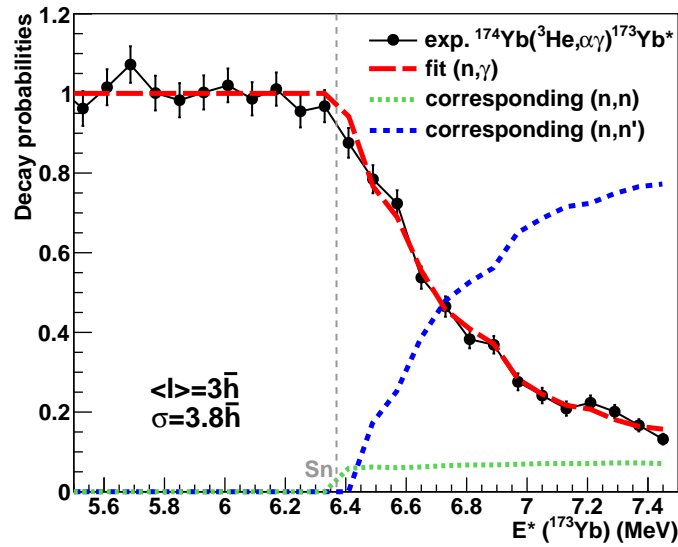
Figure 5.20: Fit of the experimental P_γ. The two fit parameters correspond to the average angular momentum transferred $\bar{l}$ and the σ of the Gaussian distribution, respectively. In addition, the fit gives the corresponding neutron-emission probabilities that can be compared to the ones shown in Fig. 5.16.
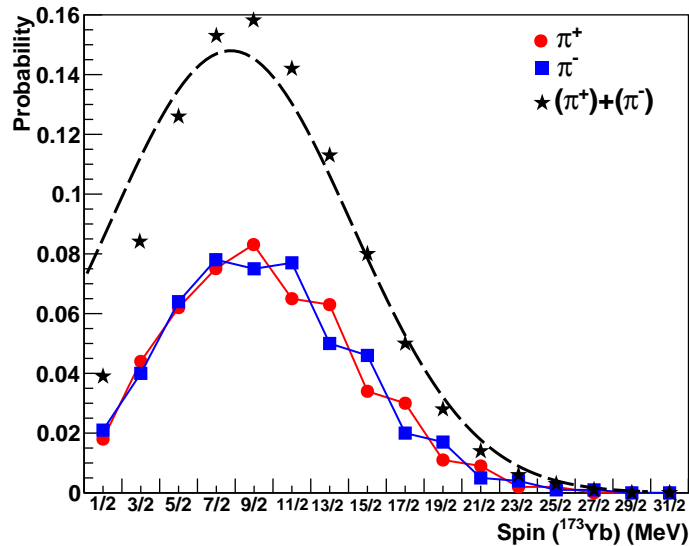
Figure 5.21: Spin distributions obtained from the fit shown in Fig. 5.20. The dashed line corresponds to the spin distribution obtained in section 5.2.4.

5.2.6 Comparison of our results with a theoretical prediction of angular momentum distribution

We saw in sections 1.6.1 and 5.1.5 that it is very difficult to determine theoretically the angular momentum distributions populated in transfer reactions. We believe that the spin distributions obtained in this work are very valuable for this purpose. We recall that in [Thompson 06], DWBA calculations were performed with FRESCO ([Thompson 00]) to infer the angular-momentum distributions generated using a $(^3He, \alpha)$ stripping reaction on ^{238}U. In collaboration with I. Thompson, we plan to perform similar calculations for the $^{174}Yb(^3He, \alpha)$ reaction. This work is in progress. We stress that this study is extremely important to investigate the dependence of the transferred angular-momentum distribution with the target nucleus. In this way we can evaluate to which extent we can use the spin distributions obtained in this work for the same transfer reaction but with a heavier target nucleus.

5.3 Study of the $^{174}Yb(^3He, d\gamma)^{175}Lu^*$ and $^{174}Yb(^3He, t\gamma)^{174}Lu^*$ reactions as surrogates for $^{174}Lu(n, \gamma)$ and $^{173}Lu(n, \gamma)$

In this section we consider the $(^3He, d)$ and $(^3He, t)$ channels that lead to nuclei for which there are no neutron-induced data. Nevertheless, neither the neutron transmission coefficients nor the gamma-strength functions are expected to be very different from those of the neighbouring nuclei studied before. TALYS calculations have been performed by P. Romain. As shown in figures 5.22 and 5.23, our experimental radiative capture probabilities for $^{174}Yb(^3He, d\gamma)^{175}Lu^*$ and $^{174}Yb(^3He, t\gamma)^{174}Lu^*$ over-estimate TALYS predictions for the corresponding neutron-induced reactions. A study of these reactions has been realized in order to infer the angular momentum distributions populated in these transfer channels. A preliminary analysis assuming a Gaussian distribution for σ_l (see eq. 5.17) gives a transferred angular momentum around $4\hbar$ with a σ of 4.9 $\hbar$ in the case of $^{174}Yb(^3He, d)$ reaction. The analysis of the $^{174}Yb(^3He, t)$ seems to predict much more transferred angular momentum. This work is in progress.

Figure 5.22: Radiative capture probability measured in the $^{174}Yb(^3He,d\gamma)^{175}Lu^*$ reaction as a function of the E^* of the ^{175}Lu (black dots) compared to TALYS predictions for $^{174}Lu(n,\gamma)$ reaction (red dashed-line).
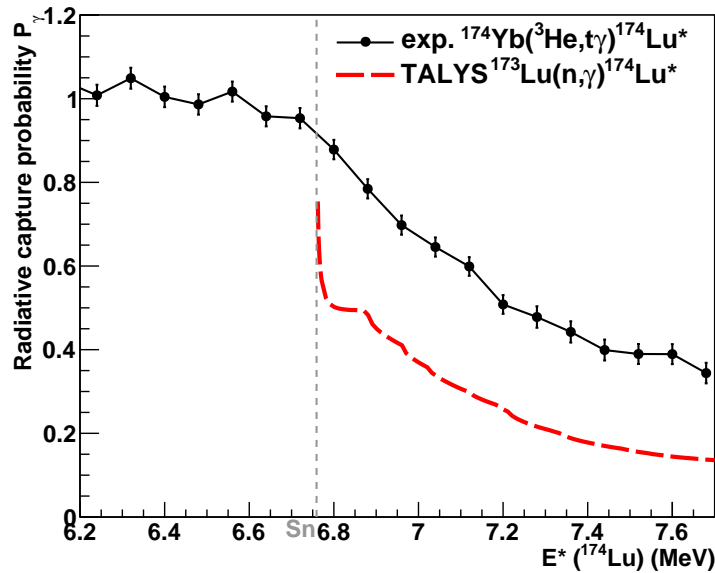
Figure 5.23: Radiative capture probability measured in the $^{174}Yb(^3He,t\gamma)^{174}Lu^*$ reaction as a function of the E^* of the ^{174}Lu (black dots) compared to TALYS predictions for $^{173}Lu(n,\gamma)$ reaction (red dashed-line).

Chapter 6

Discussion

6.1 Consequence of the spin-parity mismatch in the entrance channel

Our experimental results indicate that the angular momentum populated in the transfer reactions used is significantly higher than the one populated in neutron-induced reactions. These differences explain the big discrepancies observed between the surrogate and the neutron-induced capture measurements. Right above S_n, the compound elastic (n,n) decay channel is predominant and has the particularity to be extremely sensitive to the spin and the parity of the decaying nucleus. Our experimental data clearly reflect that this decay channel is not accessible in the transfer reactions we have considered.

At low neutron energy, the transferred angular momentum is $\pm\frac{1}{2}$ $\hbar$ and this is most probably the angular momentum carried away by the neutron in the compound elastic reaction. The consequence is a very good matching of the compound-nucleus spin with the ground state of the target nucleus. This is why neutron emission leading directly to the ground state of the residual nucleus is the natural way of decay for neutron-induced reactions at low energies. However it is highly improbable for any other reaction (photon-induced, transfer-induced, ...) to transfer so little angular momentum. That is, transfer reactions involve a blocking of the elastic neutron emission that leads to the supremacy of γ-decay. Since, for rare-earth and actinide nuclei, the neutron binding energy is around 6 MeV, the excited nucleus is in the continuum and can consequently always decay by the emission of γ-rays that carry both large angular momenta and part of the excitation energy of the compound-nucleus.

When the equivalent neutron energy increases, the first excited states of the residual nucleus after neutron emission become available. The spins of these states are usually relatively small. Consequently, one expects neutron emission to these states to be also highly suppressed for decaying nuclei with high angular momentum (see Fig. 6.1).
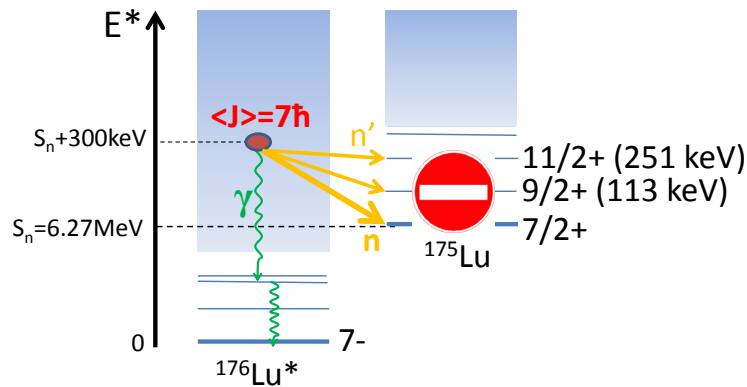
Figure 6.1: Schematical representation of the decay of of $^{176}Lu^*$ assuming an initial spin around 7 $\hbar$. The competition between gamma and neutron decay for $E^* = S_n + 300$ keV is considered. Neutron emission to the first states of ^{175}Lu is very unlikely.

At higher equivalent neutron energies, the spin-parity selectivity of the neutron emission is strongly attenuated by the high level density. The Weisskopf-Ewing hypothesis may be valid in these conditions. Actually, the Weisskopf-Ewing limit strongly depends on the structure of the residual nucleus after neutron emission. This limit becomes lower as one moves to heavier target nuclei. For example, while the well-deformed odd-odd rare-earth ^{175}Lu has over 60 levels below 1 MeV (with the first excited state at 113 keV), the even-odd actinide nucleus ^{235}U has approximately 90 levels (with the first excited state at 76 keV).

To summarize, we have shown that the spin sensitivity of neutron emission at the lowest energies is at the origin of the important discrepancies found between neutron-induced data and the results obtained with the transfer reactions investigated here. This hinders the use of the surrogate method to infer (n, γ) cross sections in the vicinity of S_n.

6.2 Comparison with other surrogate experiments applied to radiative capture

Previous surrogate experiments applied to radiative capture have been reviewed in section 2.1.2. The $^{233}Pa(n, \gamma)$ cross section was determined by S. Boyer et al. via the $^{232}Th(^3He, p)$ surrogate reaction ([Boyer 06]). Our conclusions may indicate that the $^{233}Pa(n, \gamma)$ cross section is likely to be overestimated, perhaps by as much as a factor of 2. As illustrated in figure 2.6, a smaller cross section would be more in line with the recent evaluations. The discrepancies are smaller than for the nuclei studied here which makes sense because the increased number of levels of the residual nucleus ^{233}Pa

compared to rare-earth nuclei. For instance, the first excited state $(\frac{1}{2}^-)$ of ^{233}Pa is just 6.65 keV above the ground state $(\frac{3}{2}^-)$ and higher spin states are available at low energies $(\frac{7}{2}^-$ at 57 keV, $\frac{9}{2}^+$ at 109 keV, $\frac{11}{2}^+$ at 133 keV, $\frac{13}{2}^+$ at 173 keV, etc...).

Our conclusions are reinforced by the recent work of N. Scielzo et al. ([Scielzo 10]) where the $^{156,158}Gd(p, p'\gamma)$ surrogate reactions were used as surrogates for $^{155,157}Gd(n, \gamma)$, respectively. As illustrated in figure 2.9, the obtained $^{155,157}Gd(n, \gamma)$ cross section differs up to a factor of three from the directly-measured cross section. These discrepancies have also been attributed to the $J\Pi$ mismatch. The comparison of the surrogate data with calculations using a statistical model indicates that higher spins (between 5 and 8 $\hbar$) are populated in the (p, p') reactions. Note that a similar observation was also done in the case of the $^{238}U(\alpha, \alpha')$ reaction as a surrogate for $^{237}U(n, \gamma)$ (see fig. 2.8, [Bernstein 06]).

Recently, J. Wilson et al. used the $^{232}Th(d, p\gamma)^{233}Th^*$ reaction as surrogate for the well known $^{232}Th(n, \gamma)$ reaction ([Wilson 11]). As shown in figure 2.11, a good agreement between the surrogate and the neutron-induced data above 600 keV was found. For $E_n < 600$ keV the discrepancies are probably due to the spin-parity mismatch and the spin selectivity of the neutron decay. For higher energies, the populated spin distribution in the (d, p) reaction gets closer to the neutron-induced one and/or the spin selectivity of neutron-emission is attenuated by the higher level density of the residual nucleus.

We also would like to discuss the studies performed by B. Goldblum et al. where the SRM was used to infer the $^{161}Dy(n, \gamma)$ cross section using both $(^3He, ^3He'\gamma)$ and $(^3He, \alpha\gamma)$ surrogate reactions ([Goldblum 10]). The reference cross section was $^{160}Dy(n, \gamma)$. Details on the experiment can be found in section 2.2.1.2. In this work:

- the measured capture cross section was found to be under-estimated when compared with already existing neutron-induced data. However, we have seen in the previous sections that for transfer reactions, angular momentum effects lead to capture probabilities that are considerably higher than the neutron-induced ones. Therefore, the results of [Goldblum 10] illustrate the difficulty for interpreting results obtained with the SRM.

- the surrogate cross section extracted using the $(^3He, ^3He'\gamma)$ reaction overlaps within the systematic error with the cross section extracted using the $(^3He, \alpha\gamma)$ reaction, indicating no significant entrance-channel effects. However, our work provides an estimation of the angular momentum transferred in $(^3He, p)$ and $(^3He, \alpha)$ reactions and proves that the angular momentum transferred strongly depends on the transfer reaction used. Again, we think that it is difficult to interpret in terms of populated angular momentum the agreement found for the two transfer reactions in [Goldblum 10]. The agreement can be the result of the interplay of various effects that cancel by chance when two decay probabilities are divided.

- the authors proposed to put a high threshold in the γ-energy in order to detect only statistical γ-rays and suppress the effect of angular momentum discrepancies in the entrance-channel. Note that this work concerns even-even compound nuclei which are susceptible to decay through resolved states. Our work shows clearly that the problem does not come from the γ-decay of the compound-nucleus itself but from the structure of the residual nucleus after neutron emission. We recall that in our case, a 200-400 keV gamma threshold (depending on E^*) was applied on even-odd and odd-odd compound nuclei where the level density is relatively important. This allowed us to suppress the γ-rays emitted by the residual nucleus after neutron emission. Except for suppressing the $(n'\gamma)$ contribution, a high threshold does not remove the spin-parity mismatch effects since statistical γ-rays will still be sensitive to the competition with neutron decay.

6.3 Perspectives of the surrogate method applied to radiative capture

The strong spin-parity dependence of the neutron-decay channel makes extracting (n, γ) cross sections from surrogate measurements very challenging. This underscores the absolute need to account for the spin-parity mismatch between the surrogate and the neutron-induced reactions. We think, however, that surrogate γ-decay probabilities can provide very valuable information if the angular momentum distribution populated in the transfer reaction is known. The procedure is schematically illustrated in figure 6.2. According to eq. 1.55, one can use the spin-parity distribution to extract the γ-branching ratios from the γ-decay probability measured in a surrogate experiment. These branching-ratios can in turn be used to tune key parameters of the statistical model, which in combination with the optical model can then yield reliable predictions for (n, γ) cross sections.

One should stress that such perspective is applicable if the spectroscopy of the decaying and the residual nucleus after neutron emission is well known, since we have seen that the competition with neutron emission is principally responsible for the form of the γ-decay probability. At present, promising work is underway to model pickup and stripping reactions (see section 1.6.1). Note that surrogate reactions will probably be the only possibility to access short-lived nuclei whose cross sections are highly relevant for reactor physics and nuclear astrophysics. In this context, (d, p) and (p, d) reactions are particularly important for surrogate measurements using radioactive beams in inverse kinematics. Last, but not least, the modelling of $(^3He, p)$, $(^3He, d)$ and $(^3He, t)$ reactions is also of great interest. Since the angular momentum distribution populated by the compound-nucleus depends on the detection angle of the ejectile, such predictions will be very useful to find experimental conditions (target, transfer reaction, detection angle) that reduce the difference of spin distributions in the surrogate and neutron-
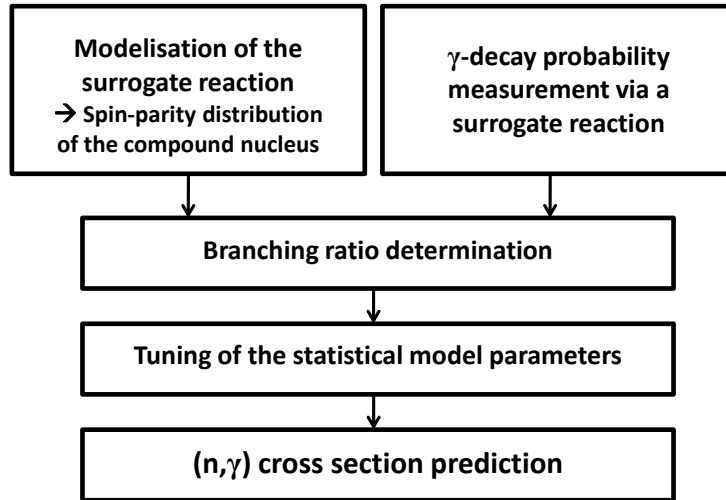
Figure 6.2: Procedure for extracting (n, γ) cross sections using surrogate reactions.

induced reactions. Unfortunately, reaction mechanisms involving the transfer of several nucleons are still poorly known theoretically. An important effort from theoreticians and experimentalists should be done in order to determine these distributions.

6.4 Why does the surrogate method work for fission?

Even though this work concerns rare-earth nuclei, we would like to stress that it has important consequences for the application of the surrogate method in the actinide region. This section focuses on the following question: why the fission probabilities of the actinides measured by G. Kessedjian et al. ([Kessedjian 10]) appear not to be sensitive to the differences in populated spin distributions? We recall that the reactions $^{243}Am(^{3}He, \alpha)^{242}Am^*$, $^{243}Am(^{3}He, t)^{243}Cm^*$ and $^{243}Am(^{3}He, d)^{244}Cm^*$ were used as surrogates for $^{241}Am(n, f)$, $^{242}Cm(n, f)$ and$^{243}Cm(n, f)$, respectively. The obtained cross sections are shown in figure 6.3 for low neutron energies.

6.4.1 Study of the $^{243}Am(^{3}He, \alpha)^{242}Am^*$ reaction as surrogate for $^{241}Am(n, f)$

In the $^{243}Am(^{3}He, \alpha)$ reaction, the fissioning nucleus ^{242}Am is doubly-odd (S_n=5.537 MeV, B_{f_A}=6.32 MeV) and the residual nucleus after neutron emission ^{241}Am is odd-even. Assuming that the transferred angular momentum distribution does not depend so much on the target nucleus, the present work has shown that the angular momentum transferred in the $(^{3}He, \alpha)$ reaction is around 4 $\hbar$ according to what we learnt in the study of $^{174}Yb(^{3}He, \alpha)$. The ground-state spin and parity of ^{243}Am are $\frac{5}{2}^{-}$, hence
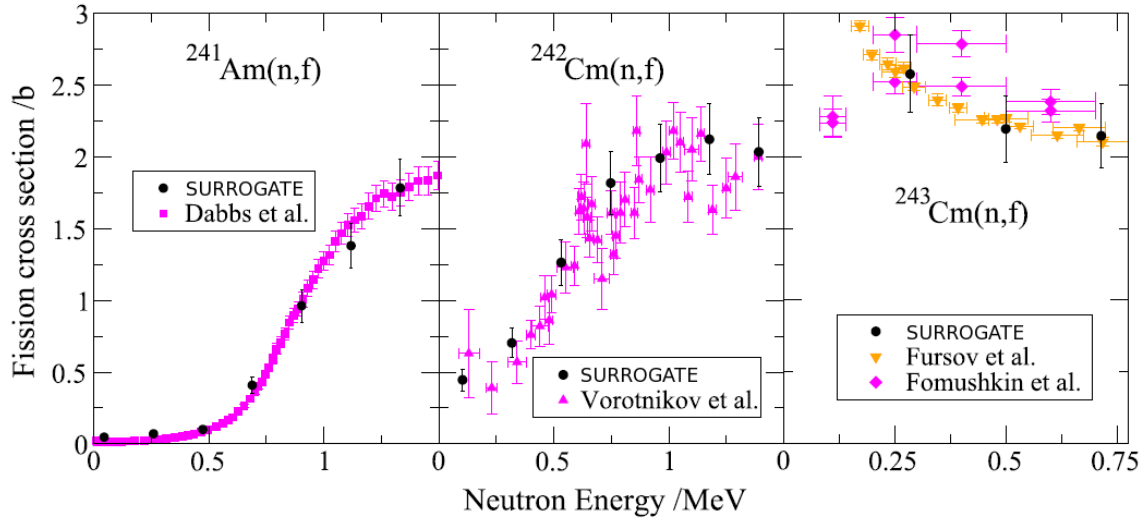
Figure 6.3: Cross sections for $^{241}Am(n,f)$, $^{242}Cm(n,f)$ and $^{243}Cm(n,f)$ obtained via $^{243}Am(^3He,\alpha)^{242}Am^*$, $^{243}Am(^3He,t)^{243}Cm^*$ and $^{243}Am(^3He,d)^{244}Cm^*$, respectively. Neutron-induced measurements are also shown for comparison.

we can predict that for the $^{243}Am(^3He,\alpha)$ reaction the spin of the compound-nucleus $^{242}Am^*$ is centered around $\frac{13}{2}$ $\hbar$. In contrast, the neutron-induced reaction is expected to populate a spin distribution around 3 $\hbar$. However, as shown in figure 6.3, the surrogate data for fission are in very good agreement with the direct measurements. If neutron emission would be blocked, we would have seen a clear increase of fission. Thus, the good agreement with the neutron data at the fission threshold indicates that neutron emission is not sensitive to a difference of a factor 2 between the spins populated in both reactions. This may be due to several aspects. The fissioning nucleus ^{242}Am is odd-even and there are many states available above the fission barrier B_{f_A}. Moreover, the fission threshold is located at about $E^* = S_n + 800$ keV, that is, high enough to give access to many nuclear states of the residual nucleus ^{241}Am after neutron emission. To deeply understand the experimental results, TALYS calculations have been performed using the spin distributions described above. Table 6.1 gives the decay probabilities corresponding to different spin distributions of $^{242}Am^*$ at $E^* = 7$ MeV ($E_n = 1.43$ MeV). The experimental fission probability is in good agreement with the calculated ones. However, the calculations show that the radiative capture probability is particularly sensitive to the spin-parity distribution. Unfortunately, important relative deviations are always observed for capture. Since the radiative capture cross section drops very quickly, it only represents few % of the total decay. Consequently, any variation of few % due to the spin-parity mismatch represents in relative several factors. For example, given $P_\gamma = 6.8\%$ and $P_f = 60.6\%$, an absolute variation of $\Delta P_\gamma = 6.9\%$ and $\Delta P_f = 3.3\%$ leads to a relative variation of $\frac{\Delta P_\gamma}{P_\gamma} = 101\%$ and $\frac{\Delta P_f}{P_f} = 5.4\%$. Note that in this case, the

calculated discrepancies are however found to be considerably lower than the measured deviations observed for rare-earth nuclei (factor 5 to 10).

	$n +^{241} Am$	$^{242}Am^*$	$^{234}Am(^3He, \alpha f)^{242}Am^*$
	J≈3ℏ, σ≈2ℏ	J=6ℏ, σ=3.2ℏ	[Kessedjian 10]
P_f	60.6%	57.3%	59.053% (4.94%)
P_n	32.6%	29%	not measured
P_γ	6.8%	13.7%	not measured

Table 6.1: Calculated decay probabilities of $^{242}Am^*$ at $E^* = 7MeV$ obtained with TALYS for two different $J\Pi$ distribution compared to the experimental fission probability obtained in [Kessedjian 10].

6.4.2 Study of the $^{243}Am(^3He, t)^{243}Cm^*$ and $^{243}Am(^3He, d)^{244}Cm^*$ reactions as surrogates for $^{242}Cm(n, f)$ and $^{243}Cm(n, f)$

For these cases, unfortunately we have not yet reliable information on the angular momentum induced by the $(^3He, t)$ and $(^3He, d)$ reactions. In the $^{243}Am(^3He, t)$ reaction, the fissioning nucleus ^{243}Cm is even-odd (S_n=5.693 MeV, B_{f_A}=6.40 MeV) and the residual nucleus after neutron emission ^{242}Cm is doubly-even. In the $^{243}Am(^3He, d)$ reaction, the fissioning nucleus ^{244}Cm is even-even (S_n=6.801 MeV, B_{f_A}=6.18 MeV). Note that the neutron-induced data for ^{242}Cm show a structure at E_n= 800 keV that could correspond to a resonant fission transition. However, our energy resolution prevents us from concluding about the reproduction or not of the structure. In general, a good agreement of the surrogate data with the neutron-induced measurements was observed. This can be explained by a relative high level density of the residual and the fissioning nuclei and by spin distributions centered at values that are perhaps a factor 2 higher than for neutron-induced reactions but not much more. Indeed, the first excited states for the doubly-even ^{242}Cm are 2^+ (42 keV), 4^+ (138 keV), 6^+ (284KeV). That indicates that high-spin states are already available at low energies and that neutron emission or fission is possible despite the higher angular momentum of the decaying nucleus.

Chapter 7

Perspectives

7.1 $^{174}Yb(p, d\gamma)$ reaction

In January 2012, our colleagues[1] from CEA-DAM-DIF will study the $^{174}Yb(p, d)$ reaction as a surrogate for the $^{172}Yb(n, \gamma)$ reaction. The counting of the number of γ-cascades using Ge detectors will be used to extract the γ-decay probability of the compound-nucleus created in the $^{174}Yb(p, d)^{173}Yb^*$ reaction. The STARS $\triangle E$ silicon detectors will be placed in order to cover 40-70° and 120°-145° degrees in the laboratory frame. The same method as the one used in this work will be applied to extract the populated spin-parity distributions which will be used to constrain the modelization of the (p, d) reaction.

7.2 $^{238}U(d, pf)$ and $(d, p\gamma)$ reactions

In 2012, we plan to infer the $^{238}U(n, f)$ and the $^{238}U(n, \gamma)$ cross sections via the $^{238}U(d, p)^{239}U^*$ surrogate reaction. We will join the collaboration with the University of Oslo initiated by J. Wilson (IPN Orsay). Preliminary TALYS calculations have also been performed for the neutron-induced reaction. The left part of figure 7.1 shows that the compound-nucleus formation is the predominant reaction mechanism up to 10 MeV. On the right part, decay probabilities of the compound-nucleus are presented. Below the fission threshold, the competition between radiative capture and neutron emission is very similar to what we observed in the $^{172}Yb + n$ reaction. Thus, what we have learnt for radiative capture in the rare-earth region can be extrapolated to the actinide region, although an important difference is the higher level density for actinides. It is interesting to see that, when fission sets in all the other decay channels drop and then remain constant.

---

[1]Vincent Méot, Olivier Roig, Aurélien Blanc, Camille Théroine, Adeline Bail et al.
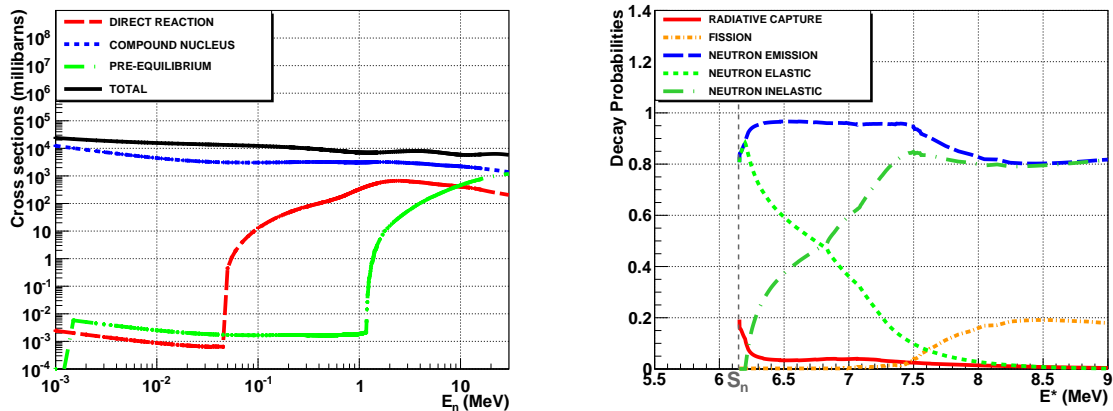
Figure 7.1: TALYS predictions for the reaction $n + {}^{238}U$

This experiment is very important to extract the angular momentum transferred in the (d, p) reaction and also to investigate the deuteron break-up issue (see Refs. [Thompson 10], [Chau 06]).

7.3 Surrogate reactions in inverse kinematics using radioactive beams

(p, d) and (d, p) (neutron pick-up and stripping) are promising reactions in the context of the future radioactive ion-beam facilities. Using inverse kinematics, windowless cryogenic hydrogen targets like the CHYMENE ([Taylor 09]) target, will allow clean measurements of the γ-decay probability or the fission probability for exotic nuclei such as unstable fission fragments or actinides. In the medium term, one could envisage such reactions using fission-fragment beams at HIE-ISOLDE (CERN) and SPIRAL2 (GANIL). Radioactive beams of actinide isotopes (such as Ac, Th and Pa) may be produced by 2015 at HIE-ISOLDE. In this context, fission surrogate experiments are particularly promising and they are not limited to the measurement of cross sections. A big step on the way to more complete surrogate experiments has been done at GANIL where transfer-induced fission of a ${}^{238}U$ beam on a carbon target has been studied ([Derkx 10]). The coupling of inverse kinematics with the large acceptance VAMOS spectrometer has enabled the identification in Z and A of the fission fragments.

7.4 The F-ELISe project

In the long term, outstanding surrogate experiments on fission will be possible at the ELISe (Electron-Ion Scattering experiment) facility of the FAIR project. ELISe is a electron-radioactive ion collider ([Simon 07], [Antonov 11]). A dedicated set-up for studies of fission at ELISe is described in Ref. [Taieb 09]. This project is called Fission-at-ELISe (F-ELISe). The interaction between electrons (125-500 MeV) and a relativistic radioactive actinide beam (200-740 A.MeV, provided by the FAIR facility) occurs by Coulomb excitation. The interaction of virtual photons with the ions leads to an E^* spectrum that corresponds to E_n=0-20 MeV. After the interaction, the electron is inelastically scattered and the excited heavy ion moves further at relativistic energies and may fission. Therefore, as illustrated in figure 7.2, the considered surrogate reaction is electron inelastic scattering.
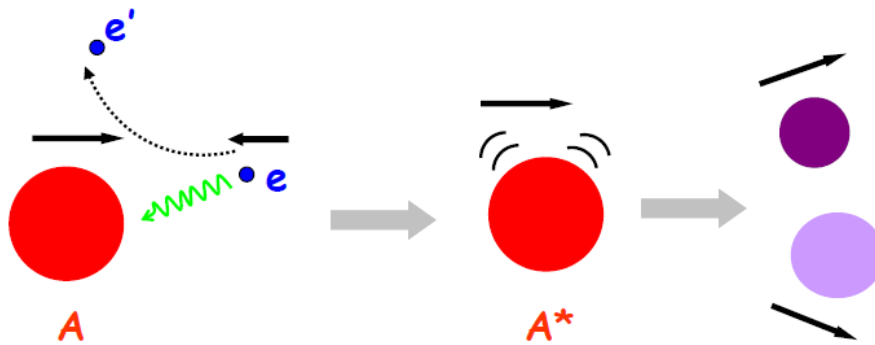
Figure 7.2: Electron inelastic scattering as surrogate reaction for fission studies in inverse kinematics at F-ELISe.

As in any surrogate experiment, the measurement of the energy of the scattered electron and their detection in coincidence of fission fragments leads to the fission probability as a function of E^*. In the ELISe facility the energy,angle and momentum of the electrons is determined with a dedicated spectrometer. Contrary to the surrogate experiments performed up to now, it will be possible to determine experimentally (in a completely model-independent manner) the angular momentum transferred to the fissioning nucleus. In addition, this experiment will provide outstanding data on other fission observables such as highly precise fission-fragment isotopic yields and prompt-neutron yields as a function of E^*.

Conclusion

In this work, we investigated whether the surrogate method can be used to determine neutron-induced capture cross sections in the rare-earth region. We studied the transfer reactions $^{174}Yb(^3He,p\gamma)^{176}Lu$, $^{174}Yb(^3He,d\gamma)^{175}Lu$, $^{174}Yb(^3He,t\gamma)^{174}Lu$, $^{174}Yb(^3He,\alpha\gamma)$ ^{173}Yb as surrogates for the $^{175}Lu(n,\gamma)$, $^{174}Lu(n,\gamma)$, $^{173}Lu(n,\gamma)$ and $^{172}Yb(n,\gamma)$ reactions, respectively. We paid close attention to the $^{175}Lu(n,\gamma)$ and $^{172}Yb(n,\gamma)$ cross sections because they present the advantage to be very well known. The radiative capture probabilities were determined using C_6D_6 scintillators via two independent methods for the determination of the γ-cascade detection efficiency :

- the total-energy principle using the PHWT .

- the constant-efficiency method where the efficiency is given by the ratio $\frac{N_{coinc}}{N_{single}}$ below the neutron separation threshold S_n.

The excellent agreement between the two methods confirms the independence of the γ-cascade-detection efficiency with the excitation energy. This implies that the constant-efficiency method can be used with confidence in the vicinity of S_n also for actinides. The gamma-decay probabilities were corrected for the $(n'\gamma)$ contribution by putting a γ-ray energy threshold. We also investigated another way to infer radiative capture probabilities based on the measurement of the intensities of several low-lying γ-transitions as a function of the excitation energy with an ensemble of Ge detectors. In spite of the lack of statistics, a good agreement was found with the results obtained with the C_6D_6 scintillators. To our knowledge, this is the first experiment where these two methods for determining the capture probabilities have been compared.

Our surrogate data present big discrepancies with respect to the neutron-induced data. Since the gamma-decay probabilities are very sensitive to $J\Pi$, we have extracted the populated angular-momentum distributions from a fit to the experimental decay probability using the branching ratios calculated by TALYS. The average spins populated in these transfer reactions are found to be a factor 2 to 4 higher than the ones populated in the neutron-induced reactions. Right above S_n, neutron emission to the ground state of the residual nucleus is the dominant way of deexcitation for a neutron-induced reaction, whereas in the transfer reactions used, this type of decay is highly improbable

and consequently γ-decay is favoured. One expects that neutron emission to the first excited states is also considerably suppressed for the same reasons. The Weisskopf-Ewing approximation can not be applied at low neutron energies. The sensitivity of the decay probability to $J\Pi$ decreases as the number of states in the residual nucleus after neutron evaporation increases. For this reason, the case of actinides is expected to be better. We would like to stress that what we have learnt on the application of the surrogate method to rare-earth nuclei can be very useful for evaluating whether this technique can be applied to extract capture cross sections in the actinide region.

In particular, the present work has helped us to reinterpret the previous results obtained by the CENBG for the fission cross sections of ^{241}Am and $^{242,243}Cm$. The excellent agreement between the surrogate and the neutron-induced data found for these nuclei at the lowest neutron energies suggests that the surrogate method should give reasonable results for the two other decay modes: neutron emission and radiative capture. As stated by several theoretical work, if neutron emission would have been suppressed in the surrogate measurement, this would have lead to a considerable increase of the fission probability. The agreement found in fission for these actinides can be explained by the fact that the transfer reactions used probably populate spins «only» somewhat higher than the neutron-induced reactions, and that there is a relative big number of states in the residual nuclei after neutron emission and on the top of the fission barrier. Unfortunately, the radiative capture cross section drops very quickly, and very soon it only represents few % of the total decay. Consequently, any variation of few % due to the spin-parity mismatch represents in relative several factors. In the vicinity of S_n, large deviations between surrogate and neutron-induced data are to be expected for capture cross sections. More generally, all the experimental and theoretical studies of the ASM done up to now show that the surrogate γ-decay probabilities represent an upper limit for the corresponding neutron-induced capture probabilities. As the excitation energy increases, the deviations should decrease and at the highest energies, they should reach values that are much smaller for actinides than for lighter nuclei.

We believe that an important effort from theoreticians and experimentalists needs to be done in order to determine the angular momentum distributions populated in surrogate reactions. An important point to be investigated is the dependence of the transferred angular-momentum distribution on the target nucleus. More precisely, one needs to study for example the influence of the single-particle structure of the target nucleus on the angular momentum distribution. If progress is made on this issue, we could use decay probabilities measured with the surrogate method together with experimental or theoretical spin distributions to fix key parameters of the statistical model. The latter can then be used in combination with the optical model to provide reliable predictions of neutron-induced cross sections for unstable nuclei that cannot be measured. In this sense, the surrogate method in combination with radioactive-ion beams (RIB) can help explore regions of the chart of nuclei that cannot be studied with surrogate reactions

using direct kinematics. The (d, p) reaction is particularly interesting for future experiments in inverse kinematics. That is why, in the near future we plan to investigate the $^{238}U(d, p)$ reaction as surrogate for the $^{238}U(n, f)$ and $^{238}U(n, \gamma)$ reactions. Very interesting opportunities for surrogate studies in inverse kinematics open up with new RIB facilities such as HIE-ISOLDE or SPIRAL2. In the very long term, unprecedented surrogate experiments on fission will become possible thanks to the ELISE e^--ion collider. The fissioning nucleus will be fully characterised in (A, Z, E^*, J, Π) and a complete set of fission observables will be precisely measured as a function of E^*.

Conclusion (en français)

Dans ce travail, nous avons étudié si la méthode de substitution pouvait être utilisée pour déterminer des sections efficaces neutroniques de capture radiative dans la région des terres rares. Nous avons étudié les réactions de transfert $^{174}Yb(^{3}He, p\gamma)^{176}Lu^{*}$, $^{174}Yb(^{3}He, d\gamma)^{175}Lu^{*}$, $^{174}Yb(^{3}He, t\gamma)^{174}Lu^{*}$ et $^{174}Yb(^{3}He, \alpha\gamma)^{173}Yb^{*}$ en substitution des réactions neutroniques $^{175}Lu(n, \gamma)$, $^{174}Lu(n, \gamma)$, $^{173}Lu(n, \gamma)$ et $^{172}Yb(n, \gamma)$. En particulier, nous nous sommes intéressés aux sections efficaces de capture radiative de $^{175}Lu(n, \gamma)$ et $^{172}Yb(n, \gamma)$ car elles ont l'avantage d'être bien connues. Les probabilités de désexcitation radiative dans les voies de transfert étudiées ont été mesurées avec des scintillateurs liquides C_6D_6 via deux méthodes indépendantes pour déterminer l'efficacité de détection des cascades-γ :

- le principe de détection totale de l'énergie en combinaison avec la technique des fonctions de poids.

- une méthode originale basée sur une hypothèse d'efficacité constante directement donnée par le rapport $\frac{N_{coinc}}{N_{singles}}$ sous le seuil de séparation neutron S_n.

Le très bon accord entre les deux méthodes confirme l'indépendance de l'efficacité de détection des cascades-γ avec l'énergie d'excitation E^{*}. La densité de niveaux augmentant généralement avec la masse, la méthode d'efficacité constante pourra aussi être utilisée pour des actinides au voisinage de S_n. Les probabilités de désexcitation γ ont été corrigées de la contribution (n'γ) à l'aide d'une coupure sur l'énergie de détection des rayons γ. Nous avons aussi étudié un moyen de déterminer les probabilités de capture radiative avec des détecteurs Germanium. Cette autre méthode est basée sur la mesure d'intensité de plusieurs transitions γ de basse énergie en fonction de E^{*}. Malgré une faible statistique, un bon accord est observé avec les résultats obtenus avec les scintillateurs C_6D_6. A notre connaissance, c'est la première fois que les deux méthodes pour extraire des probabilités de capture radiative sont comparées au sein d'une même expérience.

Nos données « surrogate » présentent d'importants écarts en comparaison avec les données neutroniques. Puisque les probabilités de capture de désexcitation radiative sont particulièrement sensibles au spin J et à la parité π, nous avons extrait des informations sur les distributions des moments angulaires peuplés en fittant nos données expérimentales avec les rapports d'embranchement calculés par le code TALYS. Les spins moyens peuplés dans les réactions étudiées sont 3 à 4 $\hbar$ plus grand que ceux peuplés dans les réactions induites par neutrons. Juste au dessus de S_n, l'émission de neutron vers l'état fondamental du noyau résiduel est la voie dominante de désexcitation dans la réaction induite par neutrons. Dans le cas des réactions de transfert étudiées, ce type de desexcitation devient fortement improbable à cause de la forte sélectivité de l'état fondamental. L'émission de neutrons vers les premiers états excités est aussi considérablement supprimée pour les mêmes raisons. Par conséquent, la compétition favorise la désexcitation radiative. L'approximation Weisskopf-Ewing ne peut pas être appliquée à basse énergie neutrons. La sensibilité au spin et à la parité de la désexcitation radiative diminue donc lorsque le nombre d'états du noyau résiduel après émission de neutrons augmente. C'est pourquoi on s'attend à ce que le cas des actinides soit plus favorable.

En particulier, ce travail a permis de réinterpreter des résultats obtenus en 2008 par le CENBG pour les sections efficaces de fission de ^{241}Am, $^{242,243}Cm$. L'excellent accord entre les données « surrogate » et les données induites par neutrons au seuil de fission implique que la méthode de substitution devrait donner des résultats raisonnables pour les deux autres voies en compétition : l'émission de neutrons et la désexcitation radiative. Comme suggéré par plusieurs travaux théoriques, si l'émission de neutrons est considérablement bloquée dans les réactions de substitution, alors la probabilité de fission doit être fortement influencée. Pour expliquer le bon accord observé pour la fission de ces actinides, nous pensons que les densités de niveaux des noyaux résiduels après émission de neutrons et au dessus des barrières de fission sont assez importantes pour « encaisser » une différence de spins raisonnable de 3-4 $\hbar$. Toutefois, les sections efficaces neutroniques de capture radiative chutent généralement très rapidement pour ne représenter que quelques % de la desexcitation totale. Cela implique qu'une variation absolue de quelques % de la probabilité de désexcitation radiative induite par la différence de spins dans les voies d'entrée peut malheureusement représenter en relatif des écarts de plusieurs facteurs. C'est pourquoi, même si la méthode de substitution appliquée à la fission « marche » bien, des différences non négligeables pour la désexcitation radiative sont aussi attendues pour les actinides. De façon très générale, toutes les expériences et les études théoriques menées à ce jour montrent que les probabilités de désexcitation radiative déterminées via des réactions de substitution sont systématiquement surestimées. Les mesures « surrogate » constituent donc une limite supérieure pour les probabilités de capture radiative induites par neutrons correspondantes. Lorsque l'énergie d'excitation augmente, les différences doivent s'atténuer au fur et à mesure que la densité de niveaux augmente. C'est pourquoi les écarts attendus sont plus petits pour les actinides que pour des noyaux plus légers.

Pour conclure, un effort important des théoriciens et des expérimentateurs est crucial pour déterminer les distributions de moments angulaires peuplés dans les réactions de substitution. En particulier, un point important à investiguer est la dépendance du moment angulaire transféré avec la cible utilisée. Plus précisement, il faut par exemple étudier l'influence de la structure de particules indépendantes du noyau cible sur la distribution des moments angulaires. Si des progrès sont réalisés à ce sujet, les probabilités mesurées avec des réactions de substitution associées aux distributions de spins théoriques (ou nos distributions de spins déduites de l'expérience) permettront de contraindre les paramètres clés du modèle statistique (densités de niveaux, Γ_γ). Les rapports d'embranchement ajustés pourront ensuite être combinés à un calcul de modèle optique pour déterminer de façon fiable des sections efficaces neutroniques pour des noyaux instables qui ne pourraient pas l'être autrement. Dans ce sens, on notera que la méthode de substitution associée à des faisceaux d'ions radioactifs permettra aussi d'explorer des régions de la charte des noyaux qui ne peuvent pas être étudiées en cinématique directe. Les réactions (d, p) et (p, d) sont d'excellentes candidates pour les expériences futures en cinématique inverse. Très prochainement, ces études seront possibles avec les nouvelles installations HIE-ISOLDE ou SPIRAL2. A plus long terme, une nouvelle génération d'expériences de substitution sur la fission sera possible grâce au collisionneur e^--ion ELISE. Le noyau fissionant sera alors caractérisé en (A, Z, E^*, J, π) et un grand nombre d'observables de fission pourront être mesurés très précisement en fonction de E^*.

Appendix

Annexe A

The optical model

A.1 From the Schrodinger equation to the scattering matrix

In the following, we describe the direct interaction of a projectile with a target nucleus made of N nucleons. The relative composite system can be interpreted by taking into account the interactions between all nucleons. The Schrodinger equation can be written in the form of Hamiltonian :

$$H\Psi = \sum_{i=1}^{N} \left(-\frac{1}{2}\nabla_{\vec{r_i}}^2 + V(\vec{r_i}) \right) \Psi = E\Psi \tag{A.1}$$

but it is impossible to resolve numerically the latter equation for N-bodies system. The optical model introduces an average and centered interaction $V(r)$ between the projectile and the whole target instead of the sum of all interactions between nucleons taken separately. The Schrodinger equation becomes :

$$\left(-\nabla^2 + \frac{2\mu}{\hbar^2}V(r) \right)\Psi = \frac{2\mu}{\hbar^2}E\Psi \implies \left(-\frac{\hbar^2}{2\mu}\nabla^2 + V(r) \right)\Psi = E\Psi \tag{A.2}$$

where μ is the reduced mass ($\mu = \frac{1}{\frac{1}{m_1}+\frac{1}{m_2}} = \frac{m_1 m_2}{m_1+m_2}$) of the projectile-target system and E is the system energy in the center of mass. This equation can be resolved in the asymptotic region and the obtained wave function Ψ is described as a sum of an incident (among z) plane wave and a spherical scattered wave :

$$\Psi \underset{r\to\infty}{\sim} e^{ikz} + \frac{e^{ikr}}{r}f(\theta) \tag{A.3}$$

with the wave number $k = \frac{\sqrt{2\mu E}}{\hbar}$ and the scattering amplitude $f(\theta)$. Assuming the optical potential is spherically symmetrical, the wave function Ψ can be expanded into

partial radial waves $u_l(r)$ of orbital angular momentum l :

$$\Psi = \sum_l \frac{u_l(r)}{r} i^l P_l(cos\theta) \tag{A.4}$$

where $P_l(cos\theta)$ are Legendre polynomials. Substituting this in eq. A.2, one obtains the radial wave Schrodinger equation :

$$\frac{d^2 u_l(r)}{dr^2} + \left(\frac{2\mu}{\hbar^2} (E - V(r)) + \frac{l(l+1)}{r^2} \right) u_l(r) = 0 \tag{A.5}$$

The solution of this equation is well known in the asymptotic region. The scattered wave function can be written as :

$$u_l(r) \underset{r \to \infty}{\sim} e^{ikz} sin(kr - \frac{l\pi}{2} + \delta_l) \tag{A.6}$$

In the presence of the optical potential $V(r)$, the radial wave functions $u_l(r)$ are shifted by δ_l, as presented in figure A.1.
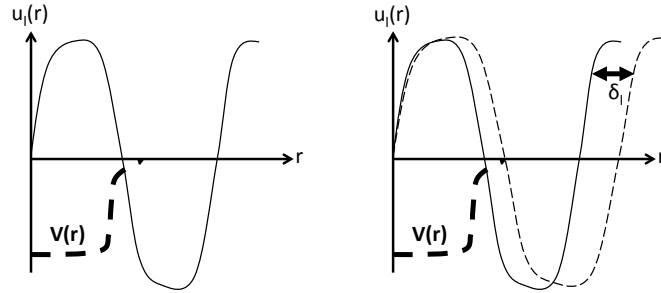
FIGURE A.1: Scattered wave function $u_l(r)$ before and after effect of the potential $V(r)$ [Hodgson 71]

The phase shift contains all the physical information and yields to the S-matrix element that relates the transition probability for the scattering of an incoming particle with a given orbital angular momentum l :

$$S_l = e^{2i\delta_l} \tag{A.7}$$

Finally, a comparison between equations A.3, A.4 and A.6 gives the solution of $f(\theta)$:

$$f(\theta) = \sum_{l=0}^{\infty} (2l + 1) f_l(k) P_l(cos\theta) \tag{A.8}$$

with

$$f_l(k) = \frac{1}{2ik} (S_l - 1) \tag{A.9}$$

A.2 Shape elastic cross section

The optical model elastic cross section $\sigma_{SE}(\theta)$ is also called «potential elastic» or «shape elastic» cross section. This section is dedicated on the relation between this differential elastic cross section and the scattering amplitude $f(\theta)$. This quantity can be defined as :

$$\frac{d\sigma_{SE}}{d\Omega} = \frac{dn}{j_i} \tag{A.10}$$

where dn is the number of projectiles per unit of time within the solid angle Ω detected by a virtual detector place at angle θ, and j is the beam current. In the asymptotic region, as defined in equation A.3, the incident wave is represented by a plane wave e^{ikz} and the associated current is given by :

$$\vec{j} = \frac{\hbar}{2i\mu}(\psi^*\vec{\nabla}\psi - \psi\vec{\nabla}\psi^*) \tag{A.11}$$

where only the radial part $\left(\frac{\partial}{\partial r}\right)$ of the gradient $\vec{\nabla}$ is qualitatively important. The incident current is :

$$j_i = \frac{\hbar k}{\mu} \tag{A.12}$$

By analogy the outgoing wave is represented by a spherical scattered wave $\frac{e^{ikr}}{r}f(\theta)$ and the scattered current is :

$$j_d \approx j_d^{radial} = \frac{\hbar k}{\mu r^2} \mid f(\theta) \mid^2 \tag{A.13}$$

Then the number of scattered particles per time unit, dn, that follow the direction given by θ is $j_d dS$, where $dS = r^2 d\Omega$ corresponds to the opening surface of our virtual detector. Then equation A.12 yields :

$$dn = j_d r^2 d\Omega = \frac{\hbar k}{\mu r^2} \mid f(\theta) \mid^2 r^2 d\Omega = j_i \mid f(\theta) \mid^2 d\Omega \tag{A.14}$$

A comparison with equation A.10 gives the relation between scattering amplitude and elastic scattering cross section :

$$\frac{d\sigma_{SE}}{d\Omega} = \mid f(\theta) \mid^2 \tag{A.15}$$

Then the combination of the latter equation with eq. A.8 gives the shape elastic cross section (see eq. 1.9).

A.3 The Phenomenological and microscopic optical potentials

The choice of a realistic optical potential is of crucial importance in the use of the optical model. Historically, the basis of the optical model was developed by comparing the results of the scattering of neutrons by nuclei to those obtained in optics for the scattering of light by transparent sphere, which verify $d_{sphere} \sim \lambda_{light}$. But the analogy goes further since both models make use of a complex potential :

$$V(r) = U(r) + iW(r) \tag{A.16}$$

where the imaginary part W corresponds to a source term, namely an emission flow for $W > 0$ or an absorption flow if $W < 0$. In term of nuclear reaction, one considers only the main reaction channels. Consequently, a negative imaginary part is introduced to take into account the flow absorption in the other reaction channels.

To be more realistic, the optical potential has the following form :

$$V(r) = Uf(r) + iWg(r) \tag{A.17}$$

U et W are the depths of the real and imaginary parts respectively. The form factors $f(r)$ et $g(r)$ depend on the distance r between the projectile and the target nucleus. $Uf(r)$ represents the nuclear potential, i.e. the nucleon-nucleon interaction, which is uniform inside the core then decreases near the surface. This variation can be described by a Wood-Saxon function :

$$f(r) = \frac{1}{1 + e^{(r-R)/a}} \tag{A.18}$$

with R is nucleus radius. The parameter a gives the decay slope of the Wood-Saxon function that corresponds to the diffusivity of the nuclear surface. $Wg(r)$ represents the absorption potential. For low incident energy (< 10 MeV.A), the absorption can be considered as a surface term and the form factor $g(r)$ can be hence described by a Woods-Saxon derivation peaked at the nucleus surface :

$$g(r) = 4a\frac{\partial f(r)}{\partial r} \tag{A.19}$$

Moreover one includes a spin-orbit potential V_{so} which describes the coupling between the projectile spin and the transferred angular momentum. Last a Coulomb potential V_c is added if the projectile is charged. Finally, the optical potential $V(r)$ can be rewritten with the latter contributions[1] :

---

[1]Actually it is more complicated, see [Koning 03] for example.
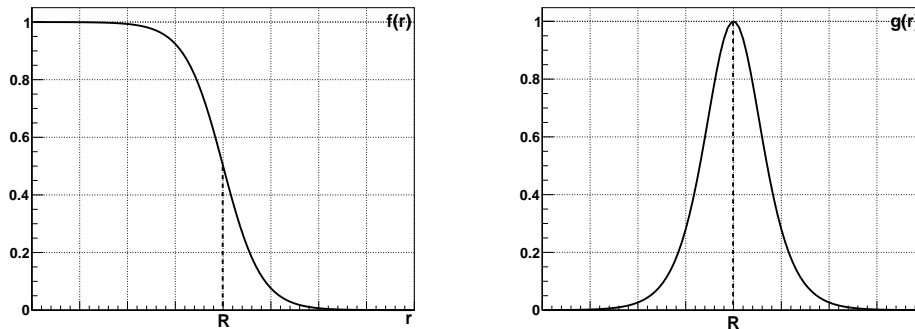
FIGURE A.2: Illustration of the form factors $f(r)$ and $g(r)$

$$V(r) = Uf(r) + iWg(r) + V_{so}(r) + V_c(r) \tag{A.20}$$

Nowadays, several global optical potentials are available to predict the total nucleon cross sections and angular distributions for many nuclei over a wide range of energies[2]. Parametrizations are based on several (~ 20) parameters depending on the mass and atomic number of the given nucleus and the nature and energy of the projectile. This parameters are determined empirically by fitting the experimental total cross section : that is why the obtained optical potential is called **phenomenological**. This approach is very accurate but need the knowledge of the studying reaction. Nevertheless, an other approach consists to determine optical potential without any experimental data. This can be done from a nuclear density information[3] and an effective nucleon-nucleon interaction. This kind of approach is called **microscopic**. The advantage of the microscopic approach is to predict observables for nucleus far from the stability, where no experimental data is available. However the microscopic optical potential is less accurate ($\sim$10-20% on the total cross section in comparison with less than 5% for the phenomenological approach).

---

[2]Note that the standard parametrization for nucleus-nucleus interaction has not yet been achieved. Some works (Broglia, Daehnick) are related to this subject.

[3]This information is based on the accurate description of the target nuclear structure, generally obtained via shell model calculations or mean field calculations (Hartree-Fock, ...).

A.4 Direct inelastic reactions

Direct inelastic excitations may occur with the result that higher-energy states of the nuclei may become populated. Single-particle excitations are another kind of inelastic process, when a particle in one of the nuclei is excited during the reaction from its initial bound state to another state which may be bound or unbound ([Thompson 09]). The direct inelastic contribution σ_{DWBA} can be treated by a «Distorted Wave Born Approximation» approach where the elastic scattering is considered as the predominant process in the reaction. Thus, the inelastic channels is treated via a pertubative quantum theory. But in the case of deformed nuclides, where the coupling with direct inelastic channels is important, the DWBA approach is not correct. A «Coupled Reaction Channels» (CRC) calculation is required. Note that TALYS drives the ECIS-06 code to perform these CRC calculations. The coupled-channels formalism is not described in this work. For a detailed presentation, we refer to Refs. [Tamura 65] or [Hodgson 71].

Annexe B

Kinematic calculations

(MeV)	$\theta_{Y14} = 112,46°$		$\theta_{Y8} = 130,19°$		$\theta_{Y3} = 144,73°$	
E^*	E_{cb}	σ_{E^*}	E_{cb}	σ_{E^*}	E_{cb}	σ_{E^*}
0	23,0875		22,9151		22,8034	
5	18,1721		18,0190		17,9199	
S_n=7,667	15,5518	0,0473	15,4101	0,0489	15,3184	0,0492
10	13,2608		13,1299		13,0452	
15	8,3562		8,2521		8,1848	
20	3,466		3,3986		3,3552	

TABLE B.1: Kinematic calculations for the $^{174}Yb(^3He, d)^{175}Lu^*$ transfer channels.

(MeV)	$\theta_{Y14} = 112,46°$		$\theta_{Y8} = 130,19°$		$\theta_{Y3} = 144,73°$	
E^*	E_{cb}	σ_{E^*}	E_{cb}	σ_{E^*}	E_{cb}	σ_{E^*}
0	21,5191		21,3150		21,1828	
5	16,6394		16,4597		16,3434	
S_n=6,761	14,9219	0,0475	14,7517	0,0492	14,6416	0,0494
10	11,7653		11,6140		11,5162	
15	6,9010		6,7848		6,7099	
20	2,0613		1,9973		1,9562	

TABLE B.2: Kinematic calculations for the $^{174}Yb(^3He, t)^{174}Lu^*$ transfer channels.

(MeV)	$\theta_{Y14} = 112,46°$		$\theta_{Y8} = 130,19°$		$\theta_{Y3} = 144,73°$	
E^*	E_{cb}	σ_{E^*}	E_{cb}	σ_{E^*}	E_{cb}	σ_{E^*}
0	22,8793		22,6689		22,5326	
5	17,9984		17,8116		17,6907	
S_n=7,465	15,5938	0,0475	15,4198	0,0492	15,3073	0,0494
10	13,1225		12,9628		12,8595	
15	8,2548		8,1278		8,0459	
20	3,4047		3,3228		3,2700	

TABLE B.3: Kinematic calculations for the $^{174}Yb(^3He,{}^3He')^{174}Yb^*$ transfer channels.

(MeV)	$\theta_{Y14} = 112,46°$		$\theta_{Y8} = 130,19°$		$\theta_{Y3} = 144,73°$	
E^*	E_{cb}	σ_{E^*}	E_{cb}	σ_{E^*}	E_{cb}	σ_{E^*}
0	35,4266		35,1244		34,9286	
5	30,5706		30,2897		30,1078	
S_n=6,368	29,2424	0,0477	28,9676	0,0494	28,7898	0,0496
10	25,7171		25,4593		25,2925	
15	20,8670		20,6346		20,4843	
20	16,0214		15,8176		15,6858	

TABLE B.4: Kinematic calculations for the $^{174}Yb(^3He,\alpha)^{173}Yb^*$ transfer channels.

Annexe C

Technical data : BICRON C6D6 scintillator

Saint Gobain Crystals (BC-537)	
General Technical Data	
Density (20°C)	0.954 g/cc
Refractive index	1.5
Scintillation Properties	
Wavelength of maximum emission	425 nm
Decay time	2.8 ns
Atomic composition	
No. of D Atoms per cc	4.06×10^{22}
No. of H Atoms per cc	3.55×10^{20}
No. of C Atoms per cc	4.10×10^{22}

TABLE C.1: C_6D_6 detector technical data
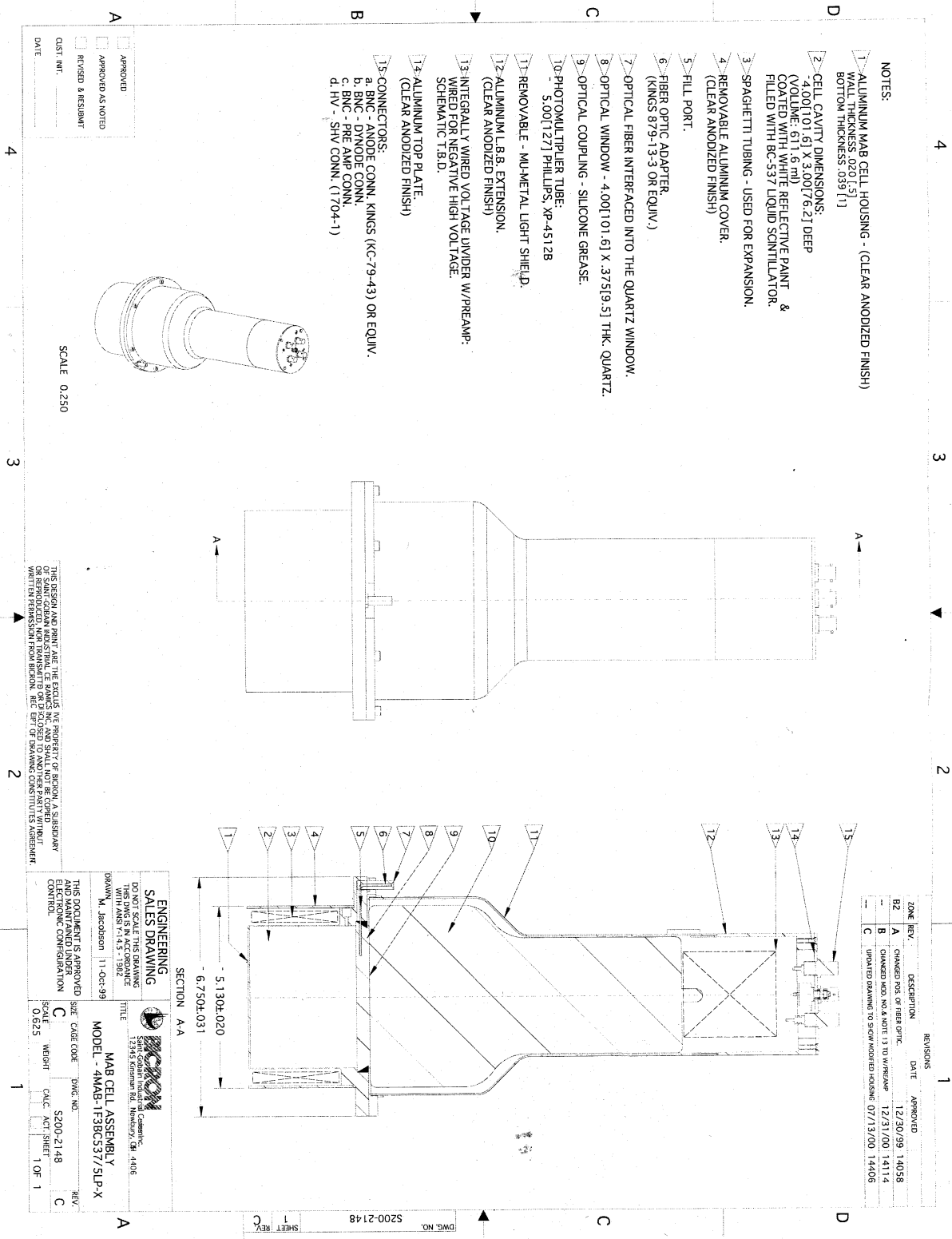
FIGURE C.1: Engineering drawing of a BICRON C_6D_6 detector.

product specification

Ø 130± 2
Ø 110 min

Photocathode

(112) (88)

220±2

Conductive coating

20 max

Ø 1.22
Ø 31.8
Ø 9.5 max
Ø 82.1 max

Typical gain curve

Gain

1E+9
1E+8
1E+7
1E+6
1E+5
1E+4
    1000   1500   2000   2500 3000
                Vht (V)
XP4512

Typical spectral characteristics

Sk (mA/W)

1E+2

1E+1

1E+0
   100 200 300 400 500 600 700 800
                Wavelength (nm)
XP4512

Pin layout:

A D10 D8 D6
G2
D9 D7
ic
D5
D3
D1 G1 sp K, Ct ic
        D2 D4 D1 G2
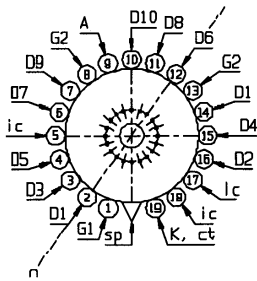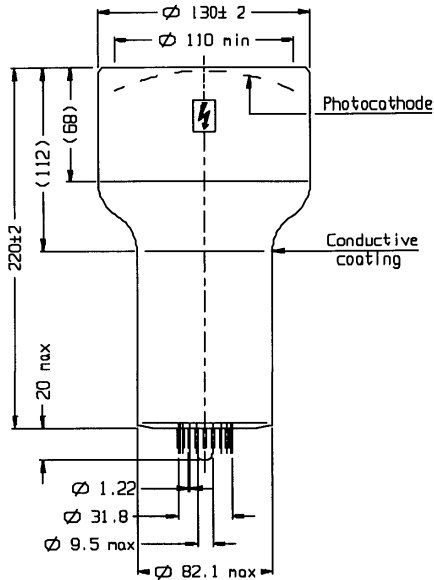
ref.:   99900645
sp: short pin
Ic: internally connected
n: plane of symmetry of the multiplier

K: cathode   Dn: dynode
Gn: focusing electrode
A: anode   Ct : coating
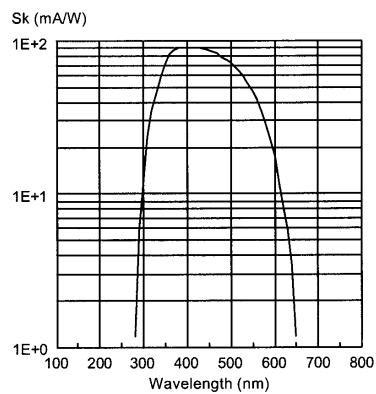
Accessories

Socket :   FE2019
Mu-metal shield: MS175

PAGE 3/3   03/01/2002

PHOTONIS
imaging Sensors

FIGURE C.2: Specification of the XP4512 photomultiplier tube.

233

Annexe D

Technical data : CANBERRA
Germanium detector 70%-efficiency
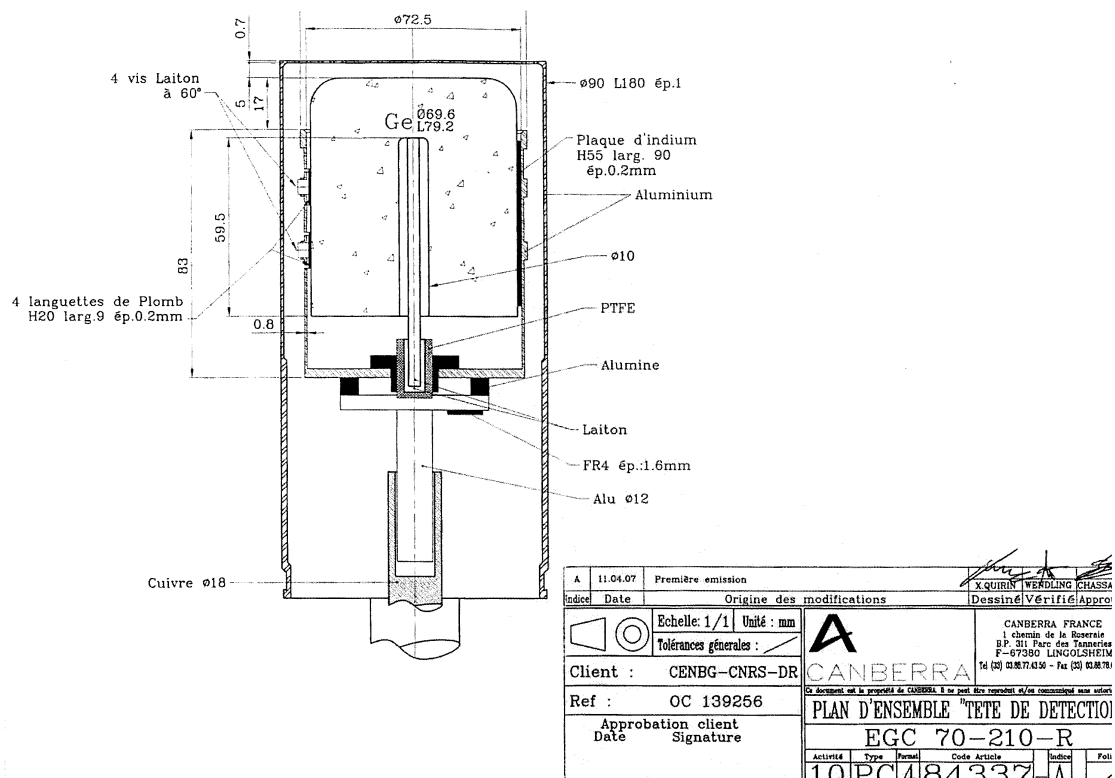
FIGURE D.1: Engineering drawing of a CANBERRA *Ge* detector.

Annexe E

Focus on the electronics used for a Pulse Shape Discrimination

The pulse shape discrimination (PSD) is needed to distinguish between photons and neutrons interacting in the C_6D_6. Practically, the difficulty is to measure the decay time of each pulse and this independently of the amplitude. The usual method is the zero-crossing system shown in figure E.1. The principle is detailed in many references, as [Perkins 79] and [Chalupka 77]. The detector anode output signal is split into two. One branch goes to a CFD which triggers on the fast leading edge of the signal that gives the START of a TAC. The second branch is directly integrated in the PSD module. This «black box» is detailed in the bottom of figure E.1. The signal is preamplified (CR-RC circuit that corresponds to a differentiation combined to an integration and results in an unipolar signal of time constant RC) then doubly differentiated (CR-RC-CR circuit, which gives a bipolar pulse whose zero-crossing time depends on the input rise and decay time). Electronics for pulse signal processing is nicely explained in [Leo 87]. A zero crossover pick-off module triggers on this point and gives a STOP signal for the TAC. Hence the time period measured by the TAC is directly proportional to the decay time. An amplitude selection via a SCA module then permits to perform a discrimination on-line. Nevertheless, one prefers not rejecting any events but selecting the particles of interest using a contour in the analysis. A typical bi-dimensional diagram showing how this selection applies is presented in figure E.2. In parallel, the amplitude signal is obtained by integration of a modified signal taken at the seventh dynode. The reference [Bovet 72] shows how the dynode chain can be modified.

Recently, the company Mesytec has developed a four-channel pulse shape discriminator module, called MPD-4. The interest is that the four-channel unit, namely the equivalent of four zero-crossing PSD systems, fits into a NIM module. Equivalent TAC amplitude, CFD threshold and CFD walk parameters can be tuned with a serial connection for USB device control. Unfortunately, the Mesytec MPD-4 is designed for photons
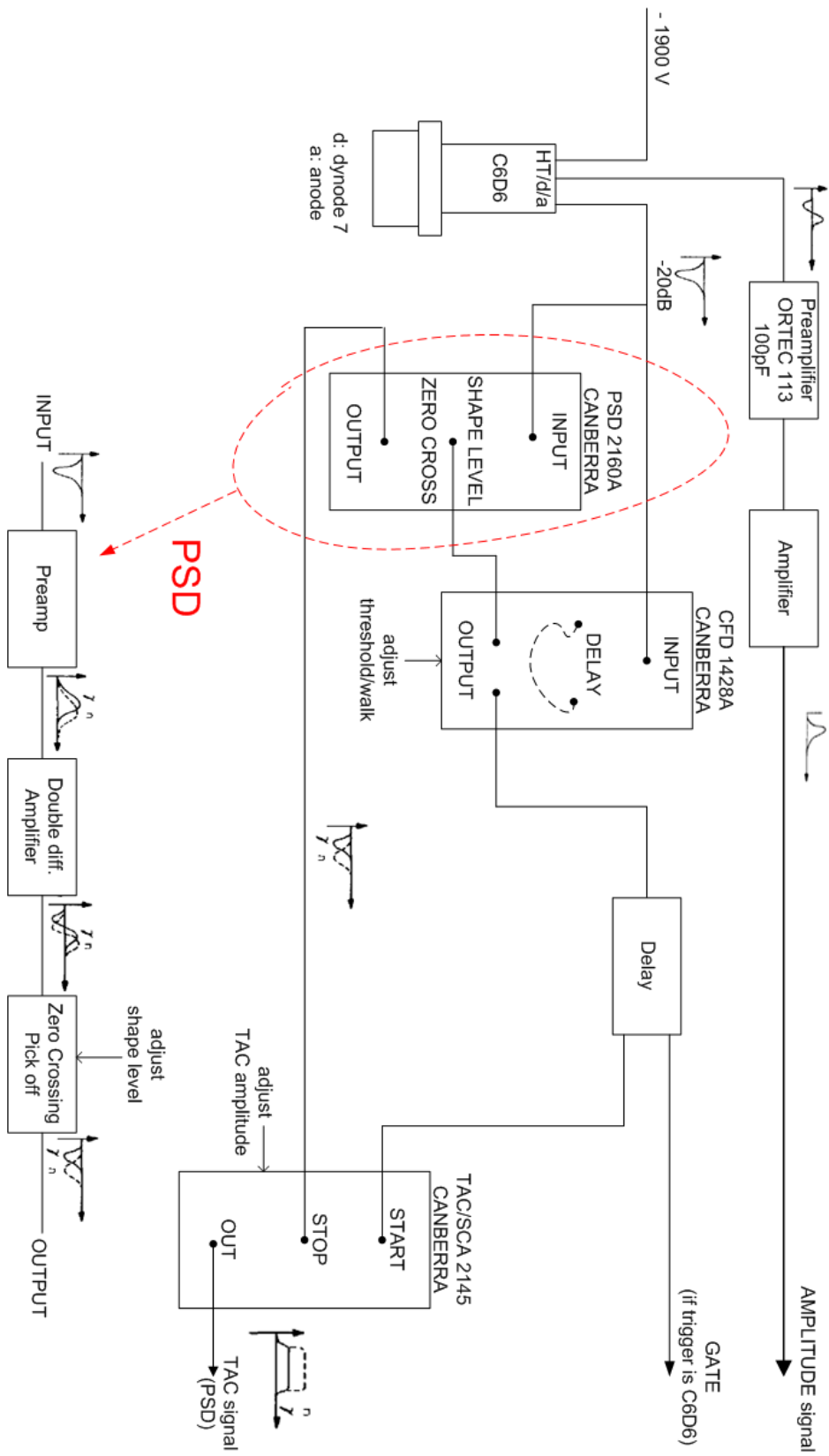
FIGURE E.1: A standard zero-crossing pulse shape discrimination circuit
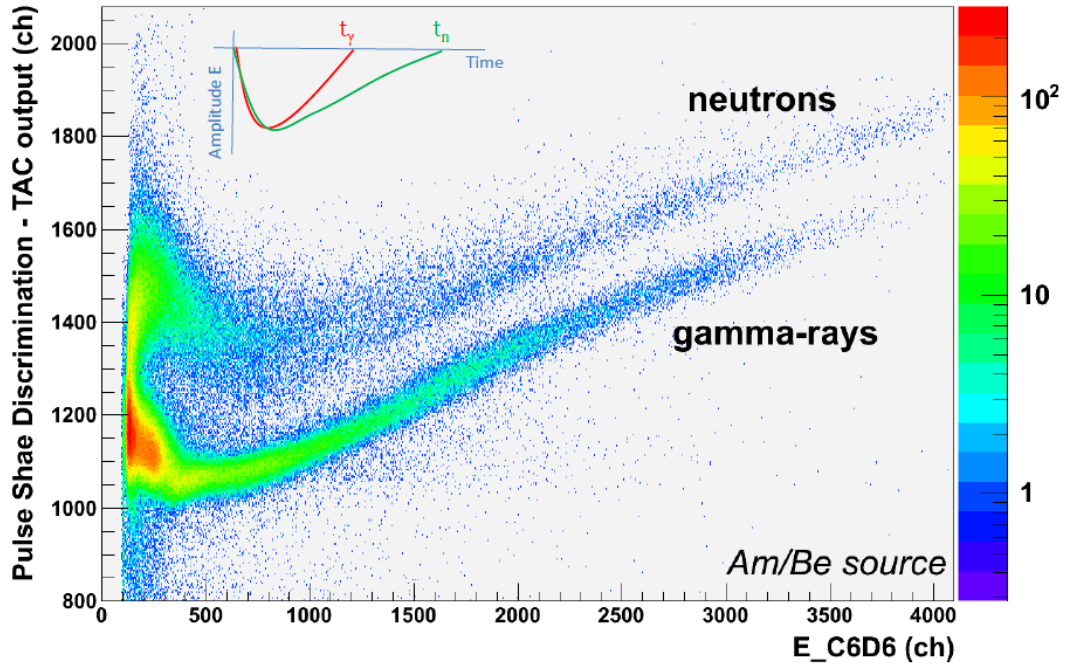
FIGURE E.2: Pulse shape discrimination in a C_6D_6 scintillators using an Am/Be source as a n-γ source.

rejection and the energy dynamic range is consequently adapted to neutron pulses[1]. That leads to a saturation of γ-rays pulses when $E_\gamma \gtrsim 4$ MeV. To overcome this problem, we purposed to use the modified signal taken at the seventh dynode in order to extract the amplitude signal. The PSD was realised by the MPD-4 module, using the detectors anodes outputs signals. The corresponding electronics diagram is presented in figure 3.19.

---

[1] Actually, a neutron is detected into the scintillator due to the recoiling proton or deuteron which participates in the scattering process. In the scintillator, the light produced by a recoiling proton is up to five times less than the light produced by a Compton electron. Consequently, for the same initial particle energy, the neutron pulse amplitude is lower than the γ pulse amplitude.

Annexe F

Calibration parameters of the telescopes

Telescope 1 - $(^3He, d)$ channel calibration parameters		
	$\triangle E_1$	E_1
Strip	$\triangle E_1(MeV) = a.C(ch) + b$	$E_1(MeV) = a.C(ch) + b$
	$- a - \triangle a - b - \triangle b -$	$- a - \triangle a - b - \triangle b -$
1	$\varnothing$	$\varnothing$
2	0.009523 0.000117 -0.662607 0.037449	0.007332 0.000012 -0.537201 0.020668
3	0.008770 0.000090 -0.694594 0.030993	0.007300 0.000010 -0.537201 0.020668
4	0.008719 0.000082 -0.597333 0.027834	0.007364 0.000009 -0.681653 0.019170
5	0.008760 0.000081 -0.567356 0.026972	0.007307 0.000008 -0.536458 0.018438
6	0.009185 0.000080 -1.040584 0.026197	0.007334 0.000008 -0.592870 0.017121
7	0.008308 0.000070 -0.165028 0.023921	0.007332 0.000008 -0.594211 0.016732
8	0.008775 0.000078 -0.795567 0.025863	0.007339 0.000008 -0.596642 0.016443
9	0.008708 0.000068 -0.535366 0.022388	0.007316 0.000007 -0.539828 0.014743
10	0.008793 0.000073 -0.448138 0.023541	0.007338 0.000007 -0.591853 0.015661
11	0.008228 0.000062 -0.132990 0.021123	0.007322 0.000007 -0.542925 0.014814
12	0.009241 0.000098 -0.914969 0.031842	0.007336 0.000008 -0.561906 0.017987
13	0.008429 0.000062 -0.160649 0.021327	0.007316 0.000007 -0.519978 0.014608
14	0.008585 0.000062 -0.961224 0.022362	0.007325 0.000007 -0.531563 0.014656
15	0.008791 0.000093 -0.668026 0.032265	0.007327 0.000010 -0.546417 0.021076
16	$\varnothing$	$\varnothing$

TABLE F.1: Calibration parameters for telescope 1 provided by the $^{208}Pb(^3He, d)^{209}Bi^*$ analysis

	$\triangle E_2$	E_2
	Telescope 2 - $(^3He, d)$ channel calibration parameters	
Strip	$\triangle E_2(MeV) = a.C(ch) + b$	$E_2(MeV) = a.C(ch) + b$
	$- a - \triangle a - b - \triangle b -$	$- a - \triangle a - b - \triangle b -$
1	$\varnothing$	$\varnothing$
2	$\varnothing$	$\varnothing$
3	0.008419 0.000077 -0.768519 0.027989	0.008521 0.000010 -0.617202 0.019203
4	0.008469 0.000076 -1.120507 0.027947	0.008546 0.000011 -0.674800 0.019727
5	0.008549 0.000084 -1.088962 0.030068	0.008584 0.000011 -0.747210 0.020261
6	0.008600 0.000081 -0.704614 0.027444	0.008572 0.000010 -0.717461 0.018449
7	0.008262 0.000077 -0.691277 0.027080	0.008577 0.000010 -0.721633 0.017803
8	0.008153 0.000074 -0.550629 0.026162	0.008554 0.000010 -0.666317 0.018526
9	0.008770 0.000079 -1.430866 0.028329	0.008530 0.000009 -0.625423 0.017631
10	0.008769 0.000076 -1.050735 0.026128	0.008567 0.000009 -0.691649 0.016582
11	0.007993 0.000068 -0.386539 0.024377	0.008523 0.000009 -0.596771 0.016388
12	0.008357 0.000076 -1.250071 0.028533	0.008552 0.000010 -0.653043 0.018561
13	0.007633 0.000063 -0.798269 0.024682	0.008563 0.000009 -0.674252 0.016674
14	0.008372 0.000063 -0.671117 0.022601	0.008538 0.000009 -0.620263 0.017038
15	0.008124 0.000082 -0.911197 0.031195	0.008598 0.000010 -0.744890 0.019255
16	$\varnothing$	$\varnothing$

TABLE F.2: Calibration parameters for telescope 2 provided by the $^{208}Pb(^3He, d)^{209}Bi^*$ analysis

Telescope 1 - ($^3He, \alpha$) channel calibration parameters		
Strip	$\triangle E_1$ $\triangle E_1(MeV) = a.C(ch) + b$ $- a - \triangle a - b - \triangle b -$	E_1 $E_1(MeV) = a.C(ch) + b$ $- a - \triangle a - b - \triangle b -$
1	Ø	Ø
2	0.011091 0.000454 -3.281321 0.608047	0.007936 0.000097 -2.755954 0.243239
3	0.009245 0.000256 -1.397812 0.397121	0.007583 0.000067 -1.668768 0.175626
4	0.008460 0.000202 -0.076418 0.335594	0.007407 0.000060 -1.142929 0.162878
5	0.008548 0.000205 -0.321469 0.331115	0.007485 0.000059 -1.316866 0.161390
6	0.009577 0.000242 -1.614257 0.346434	0.007557 0.000058 -1.519136 0.156193
7	0.008716 0.000201 -0.935763 0.313408	0.007603 0.000055 -1.624451 0.150350
8	0.008748 0.000208 -0.822752 0.320930	0.007444 0.000057 -1.071948 0.158681
9	0.008814 0.000188 -0.647653 0.287927	0.007456 0.000050 -1.143301 0.138917
10	0.008467 0.000169 -0.155552 0.269691	0.007396 0.000046 -0.937571 0.129351
11	0.008417 0.000181 -0.322343 0.290285	0.007460 0.000050 -1.044503 0.140189
12	0.008481 0.000194 -0.376883 0.314031	0.007395 0.000048 -0.875582 0.133073
13	0.008776 0.000189 -0.714773 0.299926	0.007512 0.000051 -1.175262 0.137284
14	0.008308 0.000149 -0.454557 0.251978	0.007310 0.000044 -0.564094 0.122328
15	0.008371 0.000228 -0.375690 0.388923	0.007406 0.000065 -0.872592 0.177839
16	Ø	Ø

TABLE F.3: Calibration parameters for telescope 1 provided by the $^{208}Pb(^3He, \alpha)^{207}Pb^*$ analysis

Telescope 2 - $\left(^3He, \alpha\right)$ channel calibration parameters		
Strip	$\triangle E_2$ $\triangle E_2(MeV) = a.C(ch) + b$ $- a - \triangle a - b - \triangle b -$	E_2 $E_2(MeV) = a.C(ch) + b$ $- a - \triangle a - b - \triangle b -$
1	Ø	Ø
2	Ø	Ø
3	0.008559 0.000227 -1.280468 0.380593	0.008790 0.000077 -1.587409 0.173654
4	0.008693 0.000223 -1.446957 0.360576	0.008744 0.000073 -1.474714 0.168787
5	0.008451 0.000214 -1.489591 0.352329	0.008748 0.000069 -1.414698 0.160636
6	0.008374 0.000191 -0.446870 0.309351	0.008636 0.000064 -1.132518 0.151227
7	0.007891 0.000190 -0.327225 0.326450	0.008593 0.000067 -1.049418 0.159803
8	0.007972 0.000179 -0.426848 0.304109	0.008610 0.000062 -1.057072 0.148254
9	0.008354 0.000190 -0.791833 0.305798	0.008550 0.000063 -0.894638 0.154055
10	0.008583 0.000185 -0.972247 0.292066	0.008631 0.000058 -1.054097 0.140021
11	0.008499 0.000187 -1.264907 0.300663	0.008828 0.000061 -1.516343 0.140833
12	0.008418 0.000178 -1.269042 0.290788	0.008626 0.000059 -1.026298 0.140299
13	0.007710 0.000162 -1.261949 0.292325	0.008706 0.000059 -1.193683 0.139117
14	0.008681 0.000177 -1.047402 0.288207	0.008689 0.000058 -1.137323 0.135786
15	0.008348 0.000199 -1.757687 0.346059	0.008772 0.000072 -1.373300 0.164157
16	Ø	Ø

TABLE F.4: Calibration parameters for telescope 2 provided by the $^{208}Pb(^3He, \alpha)^{207}Pb^*$ analysis

Annexe G

AIFIRA experiment : characterisation of a C6D6 scintillators using proton-induced reactions

In the following, we present a study dedicated to the characterisation of a C_6D_6 scintillators using proton-induced reactions. This experiment was performed in 2010 at AIFIRA[1] to study the response functions of our C_6D_6 liquid scintillators. We used standard sources ^{137}Cs, ^{60}Co, ^{88}Y and the $^{34}S(p,\gamma)^{35}Cl^*$ and $^{27}Al(p,\gamma)^{28}Si^*$ reactions to generate high energy γ-rays which are not accessible with γ-sources. Experimental response functions for the individual γ-rays were obtained and have been compared with simulations performed with GEANT4. For simplicity, this appendix is focused on the $^{34}S(p,\gamma)^{35}Cl^*$reaction.

G.1 Measurements details

We recall that the Corvi technique allows us to measure mono-energetic γ-ray in coincidence technique for a $\gamma - \gamma$ cascades. This technique is described in section 4.3.1.2. It requires identifying a γ-cascade of multiplicity 2. Experimentally, the measurement of $\gamma_1(E_1)$ in one of the C_6D_6 scintillators is made in coincidence with the measurement of $\gamma_2(E_2)$ detected in a Ge detector. The experimental set-up is described in figure G.1. The energy signals of the C_6D_6 scintillators and of the Germanium detector were recorded sequentially. The ADC was gated by a fast signal coming from the splitted Germanium signal. A TDC was used for the time coincidence between the two γ-rays. Signals were

---

[1]AIFIRA stands for "Applications des Faisceaux d'Ions en Région Aquitaine". The ion beam facility is equipped with a single stage electrostatic accelerator designed by the HVEE Europe company (3,5 MV Singletron). It can deliver up to 50 μA beams of light ions (H^+, D^+, He^+). Production of fast mono-energetic neutrons (100 keV - 6.5 MeV and up to 20 MeV using (p,Li), (p,T), (D,D) and (D,T) nuclear reactions).

defined to be coincident if the detector timing pulses arrived within 40 ns of each other. The block diagram of the electronics is shown in G.2. The proton-induced radiative capture $^{34}S(p,\gamma)^{35}Cl^*$ reaction permits to reach γ energies up to 4386 keV. The cascade of interest (multiplicity 2) is identified through the γ-decay scheme for ^{35}Cl (see fig. G.4). The energy of the beam was tuned in order to find a capture resonance. Finally, we used 1.223 MeV protons with an intensity of 3μA ([Aleonard 74]). Note that the resonance is not peaked because of the thickness of the target. The target ^{34}S used (thickness of the Ag_2S layer of about 220 $\mu g/cm^2$) is evaporated on a gold sheet (radius : $\sim$10 mm, thickness : $\sim$0.5 mm) and the whole is deposited on a tantalum support (radius : 15 mm, thickness : 0.5 mm). Note that the proton beam is consequently stopped in the gold/tantalum materials : the target is continuously water-cooled to dissipate heat.
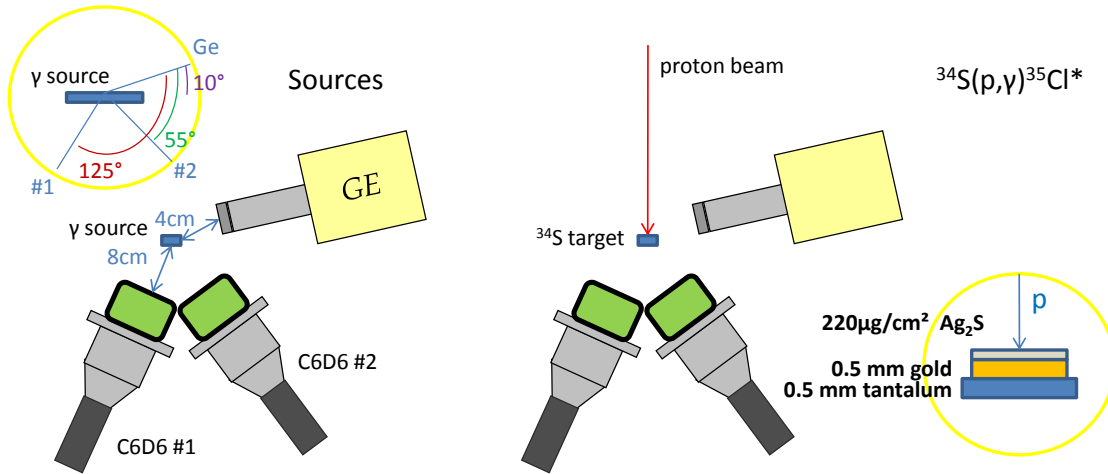
FIGURE G.1: Experimental set-up used for gamma sources measurements (left) and for the $^{34}S(p,\gamma)^{35}Cl^*$ nuclear reaction (right). The both details of the geometry and the ^{34}S target are also shown.

G.2 Experimental function response and efficiency

The statistics correspond to approximately 8 hours. As nicely illustrated in figure G.4, one can extract mono-energetic gamma-ray responses from raw spectra (figure G.3) by applying the Corvi technique for a gamma-cascade of multiplicity 2. The germanium detector is used to tag clean gamma-transitions (see table 4.3). Figure G.5 provides C_6D_6 mono-energetic gamma-ray responses for energies of 3164 keV and 4386 keV. In addition, efficiencies were determined using eq. 4.19.
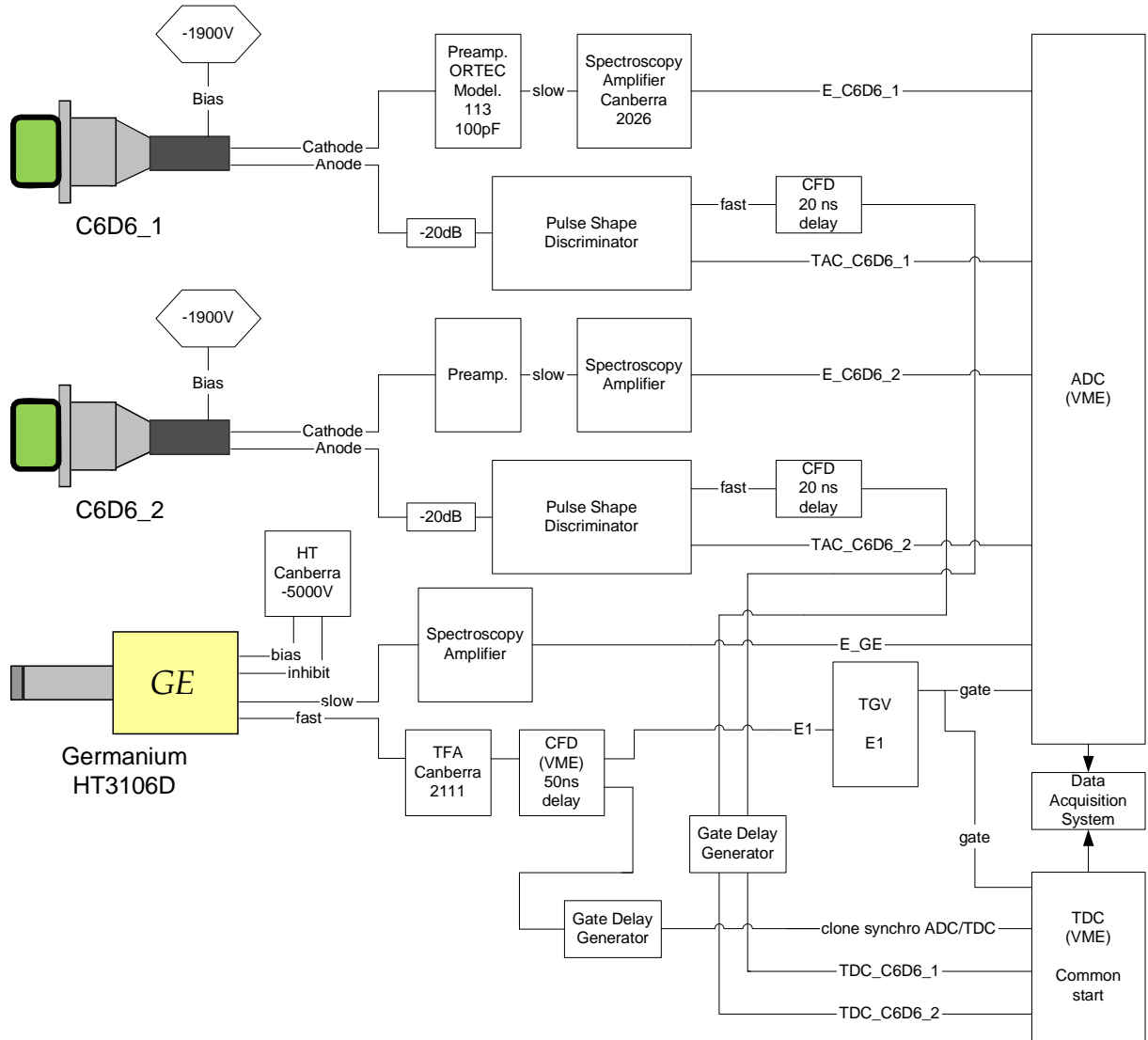
FIGURE G.2: Electronics scheme for the AIFIRA experiment.
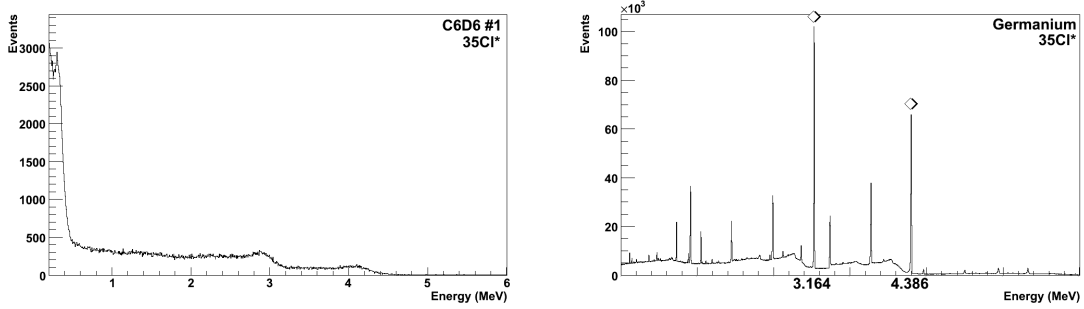
FIGURE G.3: Raw gamma-spectrum obtained with a C_6D_6 scintillator (left) and with a Ge detector (right).
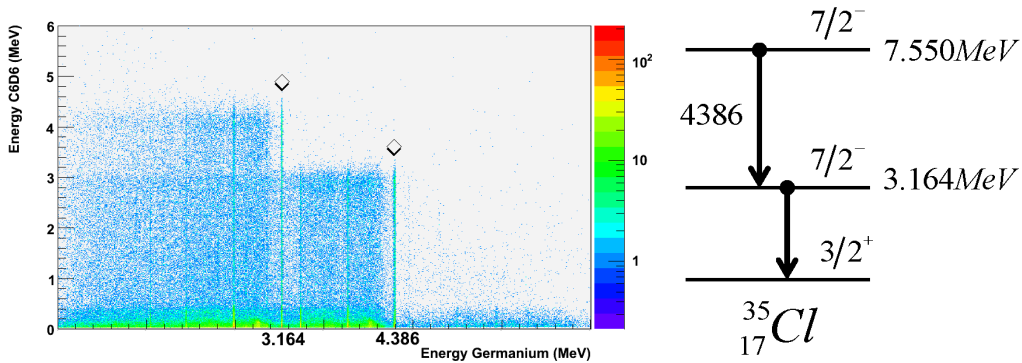
FIGURE G.4: A two-dimensions histogram illustrates the deposit energy in a C_6D_6 as a function of the energy deposit in the Germanium detector. The γ-cascade level scheme of interest is also shown.
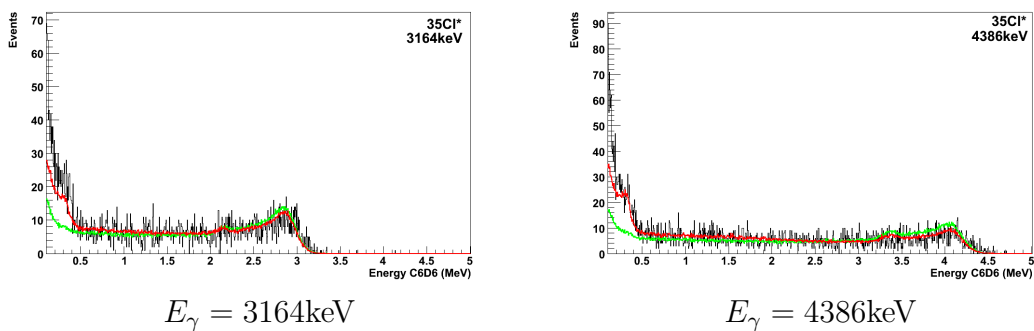
$E_\gamma = 3164\text{keV}$ $E_\gamma = 4386\text{keV}$

FIGURE G.5: Mono-energetic C_6D_6 spectra obtained in coincidence for 3164 keV and 4386 keV γ-rays spectra separately. Experimental results (black) are compared with simulated responses functions (red and green with and without the gold/tantalum backing simulation, respectively).

G.3 Simulations

We performed simulations using GEANT4. The inputted geometry tries to reproduce as far as possible the experimental set-up. The description of the C_6D_6 detectors is taken from the constructor's references and includes the quartz window of the photomultiplier tube. The γ-rays are generated randomly from a point placed in the middle of a very thin layer of target material. For $^{34}S(p,\gamma)^{35}Cl^*$, the geometry of the target and the surrounding materials are accurately reproduced. The *Ge* detector is also included in the simulation. Note that the simulated responses were widened by a Gaussian convolution, as explained in section 4.3.1.3. The analysis of the detector response for high gamma

–(a)–   –(b)–
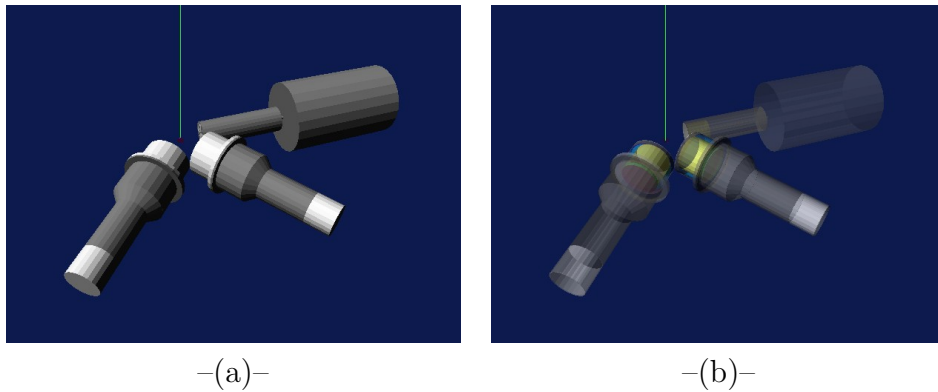
FIGURE G.6: Geometry of the experimental set-up in Geant4. We show a representation without (a) and with (b) transparency.

energies shows the importance of the effect of dead materials, i.e. the materials surroundings the target. Figure G.5 shows the comparison between the $^{35}Cl^*$ experiment results (in black) with a set of simulation calculations. The green histogram corresponds to a simulation by selectively removing the dead materials around the source : the 0,5 mm thick gold layer and the 0,5 mm thick tantalum support. The red histogram is taking into account the exact geometries of the surrounding materials. Note that the simulations are normalized in order to reproduce the Compton edge. The gold/tantalum backing is responsible for the production of an extra low-energy radiation. The origin of this contribution comes from secondary electron/positrons produced by pair-production into materials of high Z close to the source point. Figure G.8(a) illustrates the latter effect for a simulated γ-ray of 4 MeV with and without the gold/tantalum backing. Energy is not only deposited in the detector from pair production electrons generated in the target, but it is also lost from the escape of pair production electrons inside the active volume. That is why the response is lowered at higher energy and boosted at lower energy. The pair-production cross section rises with Z^2, as illustrated in the following equation :

$$\sigma_{pair-production} = 4.Z^2.\alpha.r_e^2.[7/9.(ln(183.Z^{1/3}) - f(Z)) - 1/54]$$

where Z is the atomic number of the material, r_e is the electron radius $(2,817.10^{-15}$ cm$)$ and α is the fine-structure constant $(\alpha = 1/137.036$) compensating for the decreasing Compton scattering cross-section. This contribution clearly plays an important role in the detector efficiency. A comparison between our experimental results and simulations is illustrated in figure G.8(b). Because of a bad setting of the TAC, ^{60}Co data are not available above nearly 450 keV. That is why a 500 keV gamma threshold has been applied in order to obtain our experimental efficiencies and to proceed comparisons.

G.4 Influence of dead materials on the response matrix

The interpolation technique has been used to build the response matrix (see section 4.3.1.5). The gold/tantalum backing is responsible for an important pair-production contribution that leads to a double escape peak in the response matrix, as can be observed in the figure G.7 :
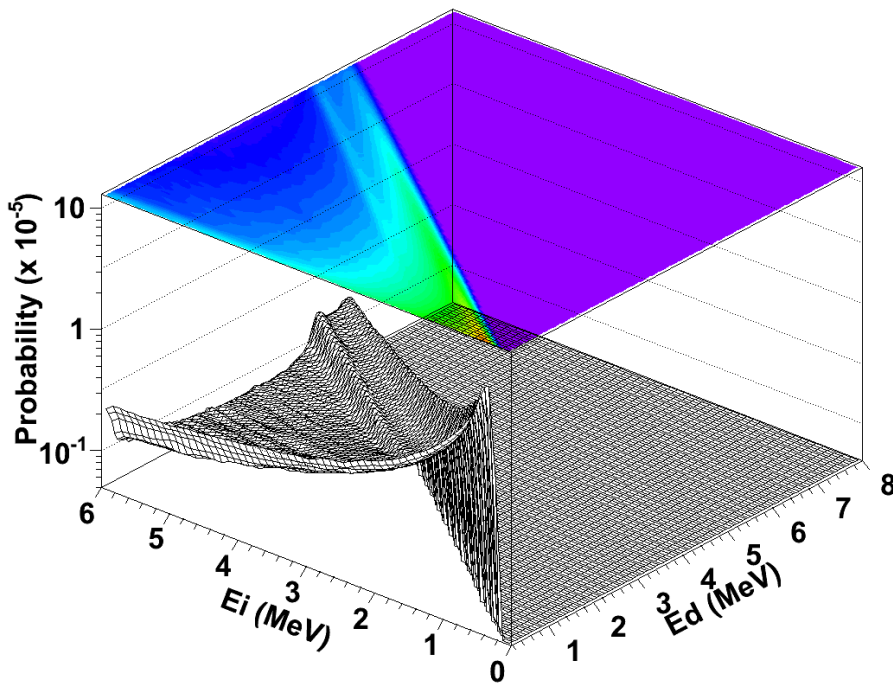
FIGURE G.7: Response matrix of the C_6D_6 scintillator n°1 in the AIFIRA set-up (including the gold/tantalum target).
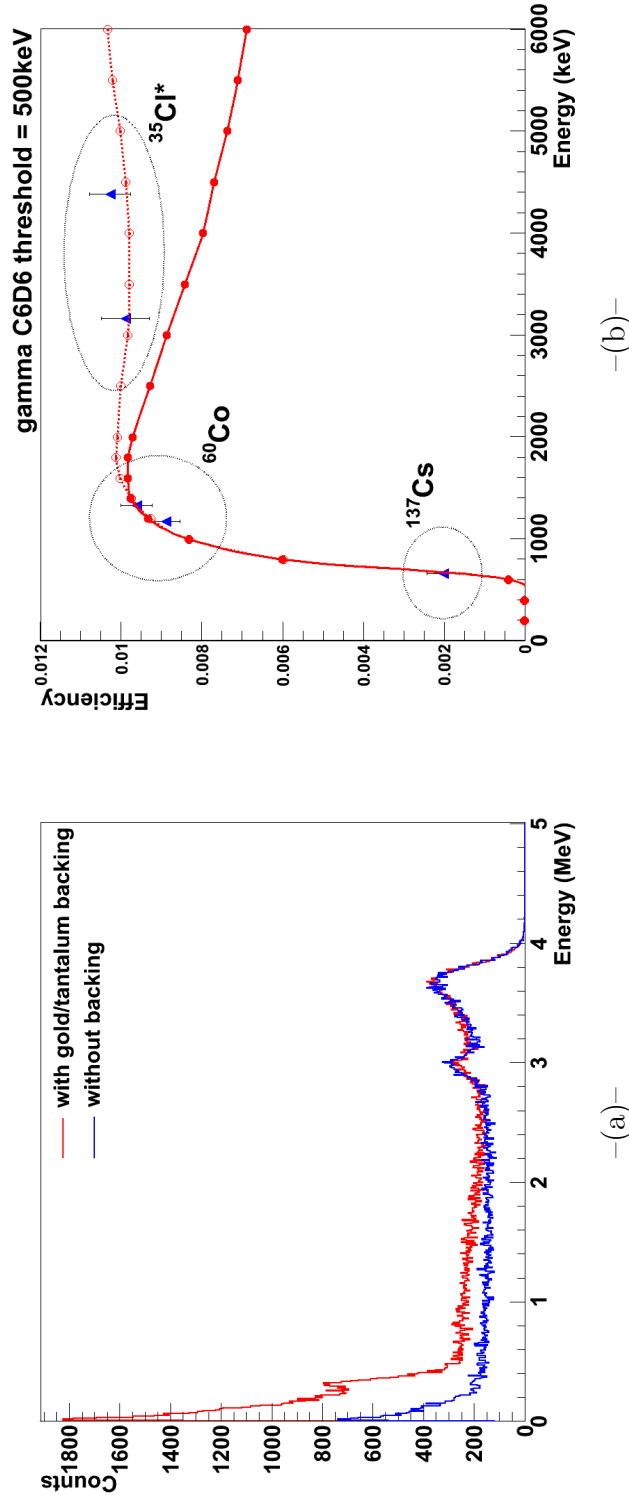
FIGURE G.8: –a– Simulated responses for a 4 MeV γ-ray taking or not into account the gold/tantalum backing. –b– Comparison between the measured and simulated C_6D_6 efficiency. The filled circles are the measured values with corresponding error bars. The red line corresponds to the efficiencies values obtained from simulations of punctual source without surrounding materials while the dotted one takes the gold/tantalum backing into account.

Annexe H

Angular correlations in $\gamma - \gamma$ measurements

H.1 Angular distributions

The theory of angular distributions is well known, we refer to Ref. [Ferguson 65] and [Yamazaki 67]. In nuclear reactions, γ-rays emission is anisotropic with respect to the beam axis. This anisotropy is studied through γ transition angular distributions : in general, when the spin alignment is well known , it is possible to determine the multipolarity L of the transition γ. The transition intensity can be written as a Legendre polynomials P_i sum (see figure H.1) where θ is the emission angle with respect to the beam axis :

$$W(\theta) = 1 + \sum_{k=0}^{L} A_{2k}.P_{2k}(cos\theta) \tag{H.1}$$

where the A_{2k} coefficients depend on the reaction (alignment), the multipolarity of the transition and the spins of the initial and final states of the γ transition. For an oblate alignment[1], a dipolar transition (L=1) has a negative coefficient A_2 and no A_4 whereas a quadrupolar transition (L=2) has a positive coefficient A_2 and a negative A_4, as illustrated in figure H.2.

H.2 Angular correlation

For a non-oriented nucleus, γ-rays emission is isotropic. Nevertheless, when a nucleus decays by two successive radiations (see figure H.3), the second radiation will have an angular distribution about the direction of the first γ-ray. In other words, the spin of

---

[1]The spins of an excited nuclear state produced by a fusion-evaporation reaction are aligned perpendicular to the beam axis (see [Yamazaki 67]) and the population probability of nuclear sub-states can be expressed as a Gaussian distribution around m = 0 for a given spin J.
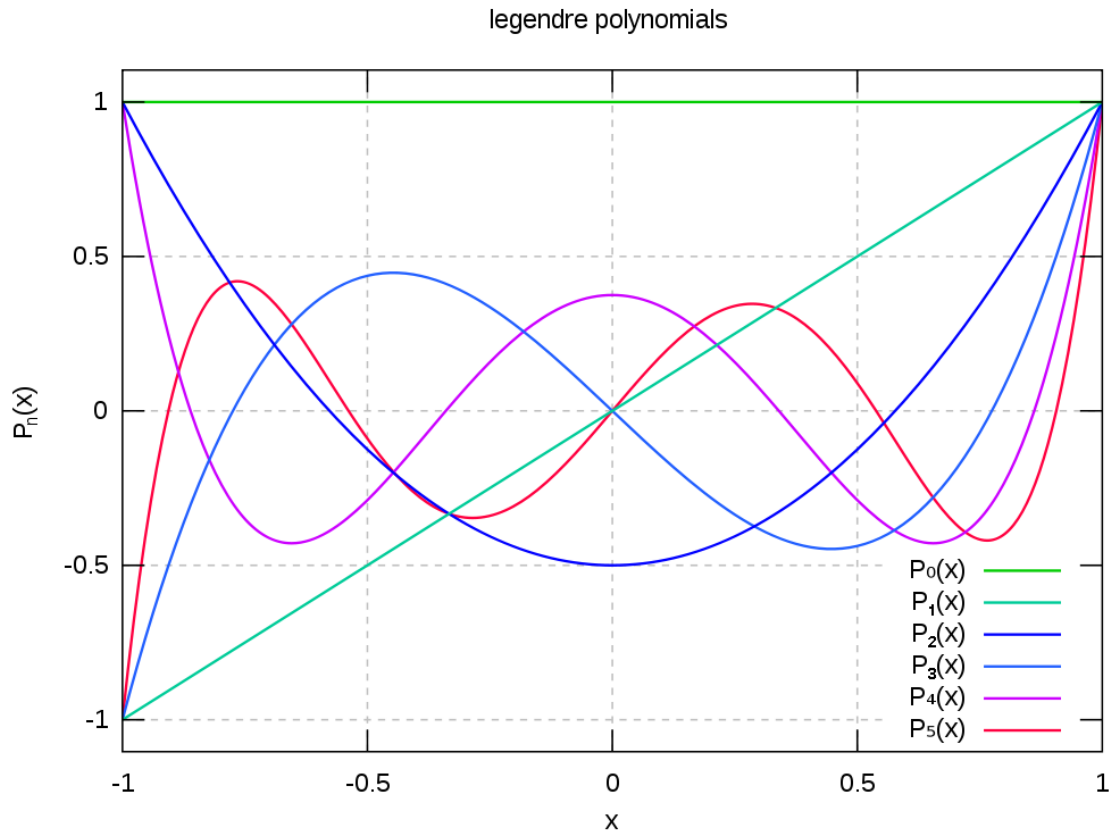
FIGURE H.1: Legendre polynomials P_k for $k = 0...5$
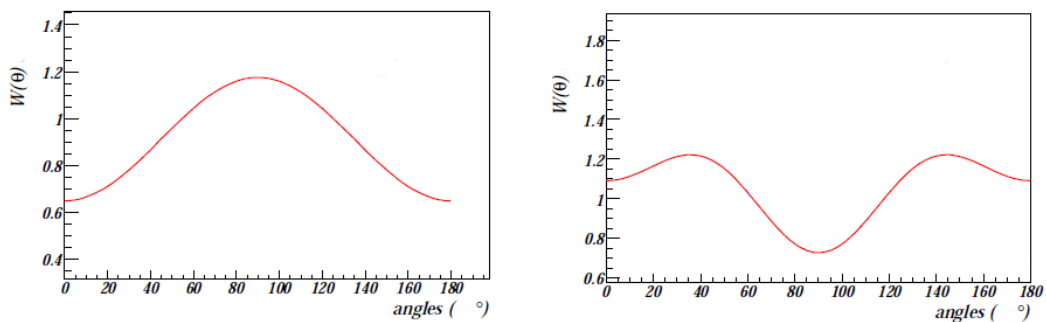
FIGURE H.2: Generic shapes of angular distributions for a transition L=1 (middle) and L=2 (right). ([Gelin 07])
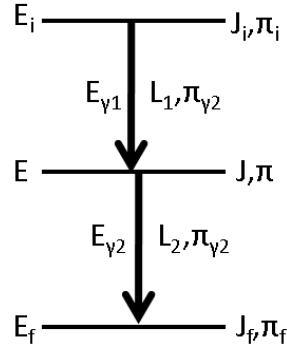
FIGURE H.3: *EM* transitions from an initial quantum state *i* over a final state *f* through a cascade of multiplicity 2.

the nucleus may be oriented after the first γ-ray emission. By analogy, this orientation depends on the character of this transition, namely the multipolarity L of the transition and the spins of the initial and final states of the γ transition, J_i and J_f respectively, and also the spin of the intermediate state J. The angular distribution, $W(\theta)$, of a γ-ray emitted at angle θ is given by :

$$W(\theta) = 1 + \sum_{k=0}^{L} A_{2k}(J_i, J, J_f).P_{2k}(cos\theta) \tag{H.2}$$

One can find coefficients A_2 and A_4 in [Yamazaki 67], where dipolar and quadripolar terms are given as a function of the characteristics of the $\gamma - \gamma$ transition (multipolarity of the two transitions and the multipole mixing ratios). Thus, at the order $k = 2$, one can rewrite the angular distribution probability as :

$$W(\theta) = 1 + A_2.P_2(cos\theta) + A_4.P_4(cos\theta) \tag{H.3}$$

Consequently, angular distribution effects may introduce a systematic bias in the determination of our response functions and in the detection efficiency of the C_6D_6 scintillators, when one proceeds through a $\gamma - \gamma$ coincidence measurement with the *Ge* detectors. Usually, the idea is to set experimentally to zero the $P_2(cos\theta)$ Legendre polynomial component of the angular correlation and consequently avoid performing correction. In the following, we investigate the conditions where the angular correlation could be neglected in our experimental set-up.

H.3 Consequence for our efficiencies determination

To cancel the term $P_2(cos\theta)$, $\gamma_1(E_1)$ and $\gamma_2(E_2)$ should be detected at 55° or 125° of each other. For completeness, we recall that the table 3.15 summarizes the exact geometry

of the detectors with regards to the beam axis. The table H.1 shows the relative angular between our C_6D_6 scintillators ($\gamma_1(E_1)$ detection angle) and Ge detectors ($\gamma_2(E_2)$ detection angle). The corresponding value of $P_2(cos\theta)$ is also given.

C6D61

	Angle (rad)	Angle (deg)	P₂[cos(θ)]
(C6D61,GE1)	1,053771285	60,3766472	-0,133506875
(C6D61,GE2)	2,041096504	116,946215	-0,191977323
(C6D61,GE3)	2,915573284	167,050044	0,924668838
(C6D61,GE4)	2,242671142	128,495591	0,08117425
(C6D61,GE5)	1,357882186	77,8009183	-0,433022677
(C6D61,GE6)	0,56159278	32,1768961	0,574609688

	Angle (rad)	Angle (deg)
(C6D62,GE1)	0,56159278	32,1768961
(C6D62,GE2)	1,357882186	77,8009183
(C6D62,GE3)	2,242671142	128,495591
(C6D62,GE4)	2,915573284	167,050044
(C6D62,GE5)	2,041096504	116,946215
(C6D62,GE6)	1,053771285	60,3766472

C6D62

	Angle (rad)	Angle (deg)
(C6D63,GE1)	2,242671142	128,495591
(C6D63,GE2)	1,357882186	77,8009183
(C6D63,GE3)	0,56159278	32,1768961
(C6D63,GE4)	1,053771285	60,3766472
(C6D63,GE5)	2,041096504	116,946215
(C6D63,GE6)	2,915573284	167,050044

C6D63

	Angle (rad)	Angle (deg)
(C6D64,GE1)	2,915573284	167,050044
(C6D64,GE2)	2,041096504	116,946215
(C6D64,GE3)	1,053771285	60,3766472
(C6D64,GE4)	0,56159278	32,1768961
(C6D64,GE5)	1,357882186	77,8009183
(C6D64,GE6)	2,242671142	128,495591

C6D64

TABLE H.1: Relative angle between C6D6 scintillators and Germanium detectors.

Therefore, to minimize angular correlations in our experiment, the following solution is proposed : $\gamma_1(E_1)$ detection in C_6D_6 1 and 3 could be done in coincidence with $\gamma_2(E_2)$ in Germanium 1 and 4 whereas $\gamma_1(E_1)$ detection in C_6D_6 2 and 4 will be done in coincidence with $\gamma_2(E_2)$ in Germanium 3 and 6.

H.4 Experimental verification of the angular correlation suppression

In the following, we quantify the angular distribution of the γ-rays emitted from the well-know ^{60}Co and ^{88}Y γ-sources and we verify that the latter choice is experimentally justified.

H.4.1 Cobalt 60 : angular distribution for transition L=2

As shown on the γ-decay scheme (see figure 1.13), ^{60}Co is the β-decaying parent of ^{60}Ni, which decays by γ emission. The two transitions of interest ($4^+ \rightarrow 2^+$ and $2^+ \rightarrow 0^+$) are both dominantly $E2$ (electric quadrupole).

In this case, the coefficients A_2 and A_4 are extracted from tables and the angular distribution correlation is :

$$W(\theta) = 1 + 0.102 \times P_2 + 0.09 \times P_4 \tag{H.4}$$
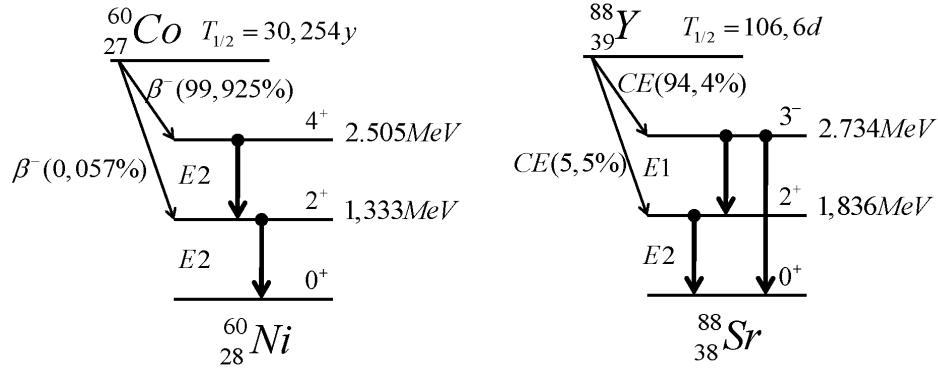
FIGURE H.4: Decay scheme for ^{60}Co and ^{88}Y sources

As a first approximation, we neglect the P_4 component and the equation can be rewritten as :

$$W(\theta) \approx 1 + 0.102 \times P_2 \tag{H.5}$$

Efficiencies for each C_6D_6 scintillator are experimentally determined in coincidence with Germanium detectors separately, namely as a function of the $\gamma - \gamma$ relative angle. Note that Germanium 2 and 5 are not taken into account in this study. In figures H.5 and H.6, we fit our experimental efficiencies for the $4^+ \rightarrow 2^+$ and $2^+ \rightarrow 0^+$ transitions with Legendre polynomials at the second order :

$$W(\theta) \propto \varepsilon(\theta) = \varepsilon_0.(1 + A_2.P_2(cos\theta)) \tag{H.6}$$

where the coefficients A_2 is obtained experimentally and ε_0 is the normalization factor that corresponds to the efficiency for $W(\theta) = 1$. Note that dotted blue line corresponds to the fitted value of ε_0. The general shape of the experimental angular distributions is significant since A_2 is waited to be positive for a γ transition $L = 2$.

H.4.2 Yttrium 88 : angular distribution for transition L=1

The same work has been done for the $3^- \rightarrow 2^+$ transition in ^{88}Sr deexcitation. The γ-decay scheme relative to ^{88}Y source is presented in figure 1.13. The general form of the experimental angular distribution is in good agreement with the fact that A_2 is negative for a γ transition $L = 1$, as shown in figure H.7.

H.5 Conclusion of this study

In the case of C_6D_6 1 and 3, one observe a nice agreement between the fitted ε_0 and the average efficiency obtained in coincidence with Ge 1 and 4. This observation can be

explained by the $\gamma - \gamma$ relative angle close to 55° and 125°, where the $P_2(cos\theta)$ Legendre polynomial component is zero. For the same reason, in the case of C_6D_6 2 and 4, the angular correlation is minimized when the $\gamma - \gamma$ coincidence is made with *Ge* 3 and 6. The table H.2 summarizes our conclusions that will be used in the efficiency determination of the surrogate experiment. On the average, the deviations between the fitted value ε_0 and the average efficiency obtained from chosen $\gamma - \gamma$ coincidence were found to be negligible in comparison with the statistical uncertainties.

$\gamma_1(E_1)$ detected in	in coincidence with$\gamma_2(E_2)$ detected in
C6D6 1	Ge 1 / 4
C6D6 2	Ge 3 / 6
C6D6 3	Ge 1 / 4
C6D6 4	Ge 3 / 6

TABLE H.2: Summary of chosen $\gamma - \gamma$ correlation in order to minimize angular correlation in C_6D_6 efficiencies measurements.
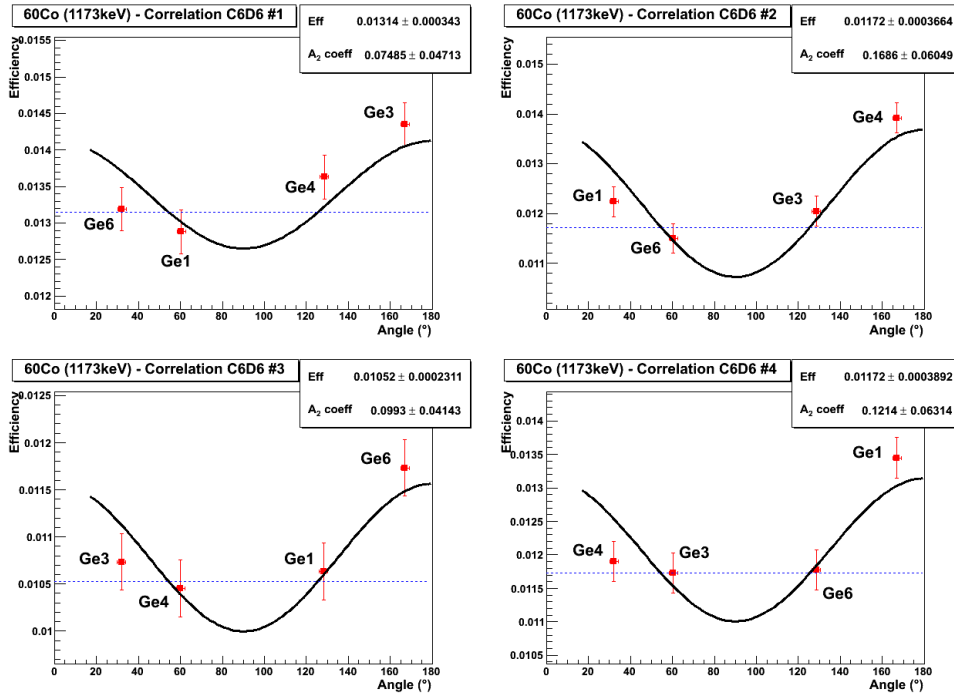
FIGURE H.5: Angular distributions for transition $2^+ \rightarrow 0^+$ in $^{60}Ni^*$
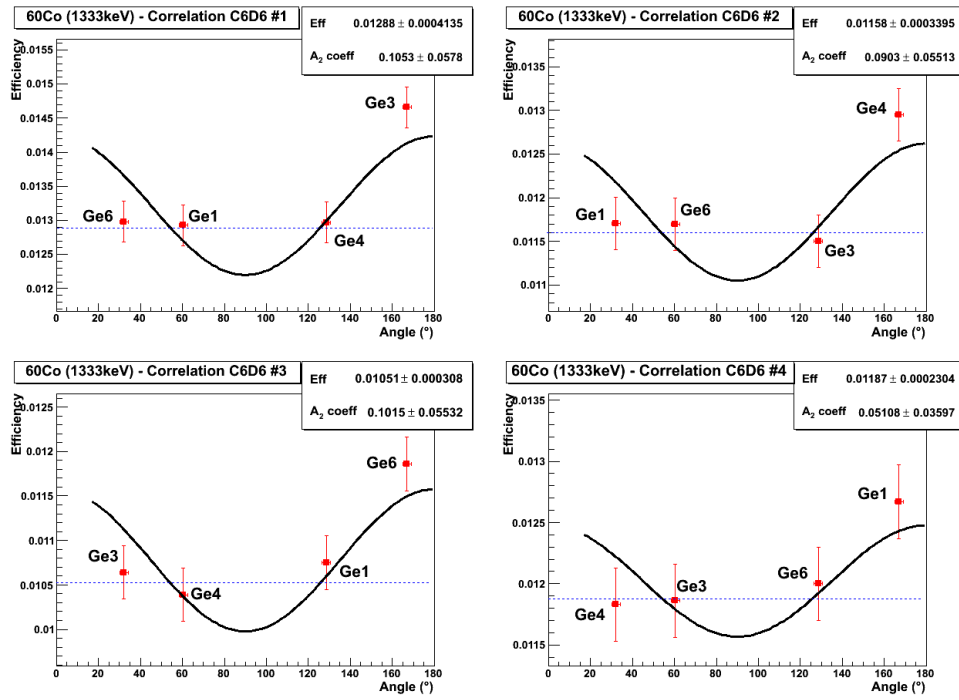
FIGURE H.6: Angular distributions for transition $4^+ \rightarrow 2^+$ in $^{60}Ni^*$
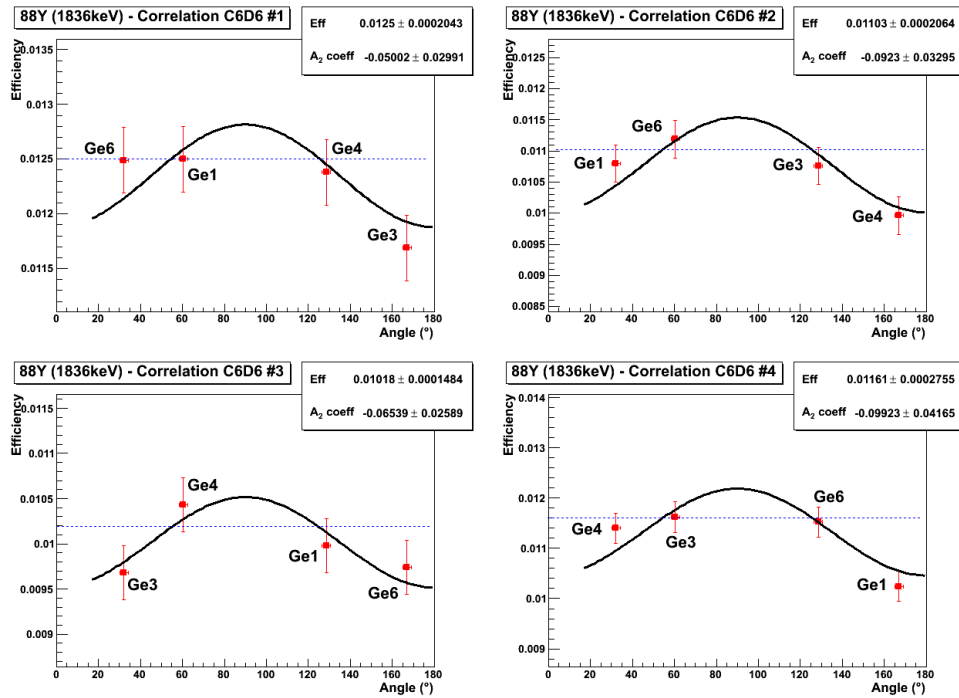
FIGURE H.7: Angular distributions for transition $3^- \rightarrow 2^+$ in $^{88}Sr^*$

Annexe I

Compton edge energies table

Energy of incident gamma E_0(keV)	Equivalent Compton energy $E_{compton}$(keV)
121	38.89
244	119.19
344	197.39
514	343.33
661	476.72
834	638.41
898	699.09
1173	963.20
1333	1118.59
1836	1611.71
2313	2082.92
2614	2381.25
3089	2853.02
3164	2927.59
4386	4144.56
4440	4198.40
5270	5026.31
5922	5677.07
6219	5973.58
6878	6631.65
7000	6753.50

TABLE I.1: Compton energies table

Annexe J

Calibration parameters of C6D6 scintillators

C_6D_6 -1

E=-1,766.10^{-1}+1,974.10^{-3}C+7,657.10^{-8}C^2-1,409.10^{-11}C^3

C_6D_6 -2

E=-1,876.10^{-1}+2,278.10^{-3}C-1,316.10^{-7}C^2-5,285.10^{-11}C^3

C_6D_6 -3

E=-1,272.10^{-1}+1,829.10^{-3}C+1,529.10^{-7}C^2

C_6D_6 -4

E=-1,227.10^{-1}+1,917.10^{-3}C+8,753.10^{-8}C^2
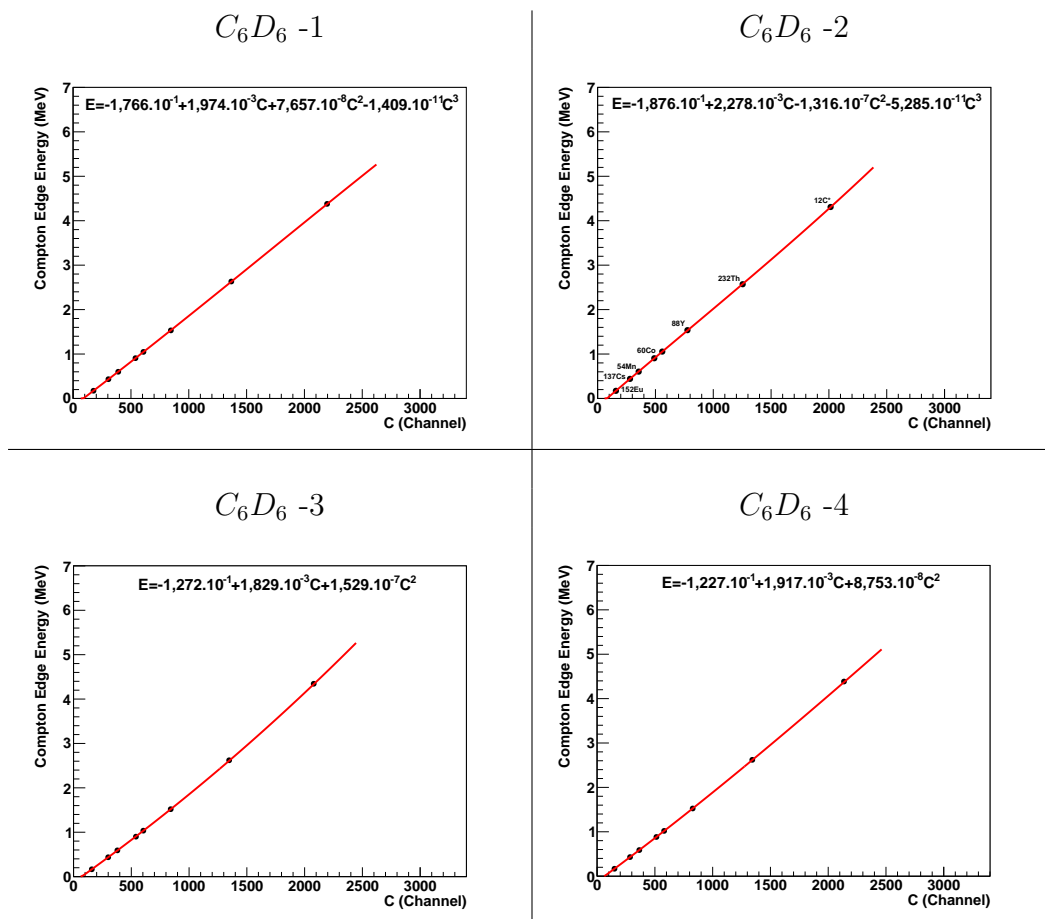
FIGURE J.1: Calibration parameters for our C_6D_6 scintillators.

Annexe K

Weighting functions parameters

E^*(MeV)	$W_{E^*}(a_1, a_2, a_3, a_4, a_5) = a_1 E_d + a_2 E_d^2 + a_3 E_d^3 + a_4 E_d^4 + a_5 E_d^5$
5.53	0.0562941, 1.90336e-05, 1.06495e-06, -3.09729e-09, 3.03785e-12
5.61	0.0552957, 2.59052e-05, 9.80076e-07, -2.80628e-09, 2.70985e-12
5.69	0.0544122, 2.96426e-05, 9.23677e-07, -2.60812e-09, 2.48180e-12
5.77	0.0537275, 2.79765e-05, 9.13873e-07, -2.55673e-09, 2.40616e-12
5.85	0.0530712, 2.57989e-05, 9.09782e-07, -2.52539e-09, 2.35358e-12
5.93	0.0523845, 2.55909e-05, 8.88230e-07, -2.43941e-09, 2.24701e-12
6.01	0.0518072, 2.21408e-05, 8.96362e-07, -2.44754e-09, 2.23661e-12
6.09	0.0512050, 2.00958e-05, 8.92578e-07, -2.41921e-09, 2.19103e-12
6.17	0.0505266, 2.11504e-05, 8.64046e-07, -2.31957e-09, 2.07925e-12
6.25	0.0497957, 2.43973e-05, 8.17653e-07, -2.16762e-09, 1.91870e-12
6.33	0.0490965, 2.66515e-05, 7.82234e-07, -2.05323e-09, 1.79831e-12
6.41	0.0484515, 2.80609e-05, 7.53180e-07, -1.95716e-09, 1.69616e-12
6.49	0.0477985, 2.97945e-05, 7.23335e-07, -1.86169e-09, 1.59701e-12
6.57	0.0471698, 3.14878e-05, 6.93732e-07, -1.76768e-09, 1.50073e-12
6.65	0.0464812, 3.50935e-05, 6.50888e-07, -1.63941e-09, 1.37569e-12
6.73	0.0458050, 3.87458e-05, 6.08339e-07, -1.51381e-09, 1.25522e-12
6.81	0.0451090, 4.32716e-05, 5.60669e-07, -1.37781e-09, 1.12873e-12
6.89	0.0445485, 4.41391e-05, 5.40554e-07, -1.31547e-09, 1.06641e-12
6.97	0.0441713, 4.05325e-05, 5.52727e-07, -1.33760e-09, 1.07639e-12
7.05	0.0437352, 3.89469e-05, 5.50247e-07, -1.32141e-09, 1.05428e-12
7.13	0.0432757, 3.80493e-05, 5.44541e-07, -1.29984e-09, 1.02962e-12
7.21	0.0428377, 3.72802e-05, 5.36044e-07, -1.26762e-09, 9.94336e-13
7.29	0.0422275, 4.10761e-05, 4.97474e-07, -1.16311e-09, 9.02501e-13
7.37	0.0415438, 4.66963e-05, 4.48272e-07, -1.03575e-09, 7.94842e-13
7.45	0.0409473, 5.03989e-05, 4.12410e-07, -9.41832e-10, 7.14629e-13
7.53	0.0405195, 5.00946e-05, 4.03541e-07, -9.13682e-10, 6.86863e-13
7.61	0.0400609, 5.09000e-05, 3.87400e-07, -8.68313e-10, 6.46047e-13
7.69	0.0396220, 5.12372e-05, 3.75106e-07, -8.33080e-10, 6.13780e-13
7.77	0.0392923, 4.92350e-05, 3.78051e-07, -8.33825e-10, 6.09369e-13
7.85	0.0389829, 4.70592e-05, 3.81834e-07, -8.36000e-10, 6.05883e-13
7.93	0.0386264, 4.60228e-05, 3.79077e-07, -8.24004e-10, 5.92387e-13
8.01	0.0383181, 4.44206e-05, 3.78754e-07, -8.15787e-10, 5.80870e-13

TABLE K.1: Weighting-functions parameters as a function of the γ-cascade energy (that corresponds to the excitation energy of $^{176}Lu^*$)

Annexe L

Radiative capture probabilities and associated errors

$E^*(MeV)$	P_γ	$\sigma_{P_\gamma}^{tot}$	$\sigma_{P_\gamma}^{stat}$	$\sigma_{P_\gamma}^{syst}$
5.53	0.991245	0.033529963	0.032390223	0.008667866
5.61	0.961656	0.031851492	0.030721396	0.008409128
5.69	0.940947	0.030943412	0.029829417	0.008228039
5.77	1.050475	0.030678087	0.029270567	0.009185799
5.85	0.975650	0.029984592	0.028745249	0.008531497
5.93	1.026334	0.029640211	0.028248839	0.008974699
6.01	1.031446	0.029024879	0.027587932	0.009019401
6.09	0.991416	0.028819909	0.027485074	0.008669362
6.17	1.042055	0.028400749	0.026899273	0.009112171
6.25	0.981005	0.027918120	0.026567532	0.008578323
6.33	0.971291	0.027386708	0.026036403	0.008493380
6.41	0.839072	0.027000798	0.025984776	0.007337201
6.49	0.743485	0.026001299	0.025175386	0.006501348
6.57	0.670076	0.026133286	0.025467935	0.005859429
6.65	0.586827	0.024906656	0.024372312	0.005131464
6.73	0.491333	0.028884995	0.028460446	0.004934165
6.81	0.393521	0.027606371	0.027322046	0.003951897
6.89	0.333169	0.027192213	0.026985588	0.003345818
6.97	0.273166	0.026656297	0.026514766	0.002743243
7.05	0.278549	0.032859192	0.032739909	0.002797302
7.13	0.245568	0.033474737	0.033383774	0.002466093
7.21	0.206118	0.032598592	0.032532809	0.00206992
7.29	0.190816	0.034137294	0.034083468	0.001916251

TABLE L.1: Results obtained for the radiative capture probability of ^{176}Lu in the $^{174}Yb(^3He,p)$ reaction.

$E^*(MeV)$	P_γ	$\sigma_{P_\gamma}^{tot}$	$\sigma_{P_\gamma}^{stat}$	$\sigma_{P_\gamma}^{syst}$
6.75	0.988892	0.014761372	0.014193333	0.004055538
6.83	1.011127	0.014389772	0.01377934	0.004146726
6.91	1.000007	0.014101688	0.013492161	0.004101122
6.99	0.983956	0.013802238	0.013199173	0.004035295
7.07	0.98716	0.013368313	0.012740564	0.004048435
7.15	0.983275	0.01324828	0.012619662	0.004032502
7.23	0.996605	0.013152859	0.012501709	0.00408717
7.31	0.994373	0.013068301	0.012415727	0.004078016
7.39	1.04784	0.013078065	0.012351887	0.004297289
7.47	1.018478	0.012999133	0.0123098	0.004176873
7.55	0.997292	0.01279726	0.012126082	0.004089987
7.63	0.986331	0.012587873	0.011920245	0.004045035
7.71	0.867199	0.012274708	0.011748192	0.003556464
7.79	0.755429	0.011936866	0.01152782	0.003098085
7.87	0.608519	0.01170959	0.011440564	0.002495593
7.95	0.49528	0.011426012	0.011244022	0.002031189
8.03	0.39768	0.011389793	0.011272421	0.001630923
8.11	0.33516	0.011294911	0.011210963	0.001374522
8.19	0.243723	0.012203809	0.012152119	0.001122031
8.27	0.236924	0.012839629	0.012793216	0.001090731
8.35	0.226641	0.012512747	0.012469169	0.001043391
8.43	0.188304	0.01282331	0.012793974	0.000866898
8.51	0.16682	0.013526453	0.013500477	0.000837889
8.59	0.162127	0.013085508	0.013060146	0.000814318
8.67	0.151912	0.013527773	0.013506238	0.000763011
8.75	0.140294	0.013936414	0.013918588	0.000704657
8.83	0.136698	0.013340049	0.013322368	0.000686595

TABLE L.2: The same as Fig. L.1 but for ^{175}Lu in the $^{174}Yb(^3He, d)$ reaction.

$E^*(MeV)$	P_γ	$\sigma_{P_\gamma}^{tot}$	$\sigma_{P_\gamma}^{stat}$	$\sigma_{P_\gamma}^{syst}$
5.84	0.991014	0.027399196	0.026568817	0.006694316
5.92	1.000895	0.026784087	0.0259167	0.006761062
6	0.969407	0.025799673	0.024954801	0.00654836
6.08	1.039596	0.025912515	0.024942796	0.007022488
6.16	1.042485	0.025547369	0.024557652	0.007042004
6.24	1.008126	0.025301673	0.024368008	0.006809908
6.32	1.048983	0.024975313	0.023949036	0.007085898
6.4	1.004424	0.024540765	0.023584195	0.006784901
6.48	0.986324	0.024325236	0.023395008	0.006662635
6.56	1.017053	0.023908224	0.022899856	0.00687021
6.64	0.957923	0.023932675	0.023041307	0.006470786
6.72	0.952184	0.024259038	0.023390811	0.006432019
6.8	0.87843	0.023166466	0.022393638	0.005933809
6.88	0.784552	0.022965599	0.022345745	0.005299662
6.96	0.697801	0.022869055	0.022378005	0.004713657
7.04	0.645452	0.02286188	0.022442273	0.004360039
7.12	0.59893	0.022305329	0.021935345	0.004045782
7.2	0.508122	0.022379294	0.022114512	0.003432373
7.28	0.478057	0.025650008	0.025379047	0.003718452
7.36	0.442427	0.025385914	0.025151581	0.003441312
7.44	0.399132	0.024949718	0.024755811	0.003104553
7.52	0.389681	0.023815119	0.023621445	0.00303104
7.6	0.389338	0.023850905	0.023657866	0.003028372
7.68	0.34403	0.024502109	0.024355546	0.002675955

TABLE L.3: The same as Fig. L.1but for ^{174}Lu in the $^{174}Yb(^3He,t)$ reaction.

$E^*(MeV)$	P_γ	$\sigma_{P_\gamma}^{tot}$	$\sigma_{P_\gamma}^{stat}$	$\sigma_{P_\gamma}^{syst}$
4.97	0.867644	0.041036552	0.040045762	0.008963013
5.05	0.969669	0.046326297	0.045230369	0.01001696
5.13	0.998884	0.046402635	0.045240775	0.01031876
5.21	0.987579	0.046018695	0.0448736	0.010201976
5.29	1.055506	0.047385256	0.046113688	0.010903681
5.37	1.022098	0.045819984	0.044586855	0.010558567
5.45	1.013934	0.045143983	0.043912068	0.01047423
5.53	0.962093	0.043741513	0.042597445	0.009938698
5.61	1.015466	0.045142467	0.043906731	0.010490056
5.69	1.070976	0.045821197	0.044465507	0.011063491
5.77	1.000818	0.043598731	0.042355163	0.010338738
5.85	0.982877	0.042850238	0.041629933	0.010153403
5.93	1.002354	0.042760335	0.04148769	0.010354606
6.01	1.020093	0.042359696	0.041028008	0.010537855
6.09	0.986419	0.04168723	0.040422632	0.010189992
6.17	1.0108	0.041699778	0.040371267	0.010441855
6.25	0.954926	0.040331069	0.039106056	0.009864661
6.33	0.967923	0.0402711	0.039010037	0.009998923
6.41	0.874169	0.037307109	0.036197678	0.009030418
6.49	0.784526	0.035215859	0.034270625	0.00810438
6.57	0.723615	0.033155683	0.032302035	0.007475151
6.65	0.537504	0.027938023	0.027380689	0.005552571
6.73	0.46492	0.025554657	0.025099283	0.004802758
6.81	0.382854	0.022792684	0.022446926	0.003954992
6.89	0.368835	0.021943753	0.021610435	0.003810172
6.97	0.275903	0.021201812	0.020956786	0.00321402
7.05	0.241452	0.019468943	0.019264695	0.002812697
7.13	0.208681	0.017943023	0.017777586	0.002430945
7.21	0.223422	0.018227721	0.018040952	0.002602664
7.29	0.200941	0.016920567	0.016757873	0.002340781
7.37	0.166798	0.015321343	0.015197635	0.001943046
7.45	0.131907	0.013479834	0.013391968	0.001536597

TABLE L.4: The same as Fig. L.1 but for ^{173}Yb in the $^{174}Yb(^3He,\alpha)$ reaction.

Annexe M

Correlation-matrix
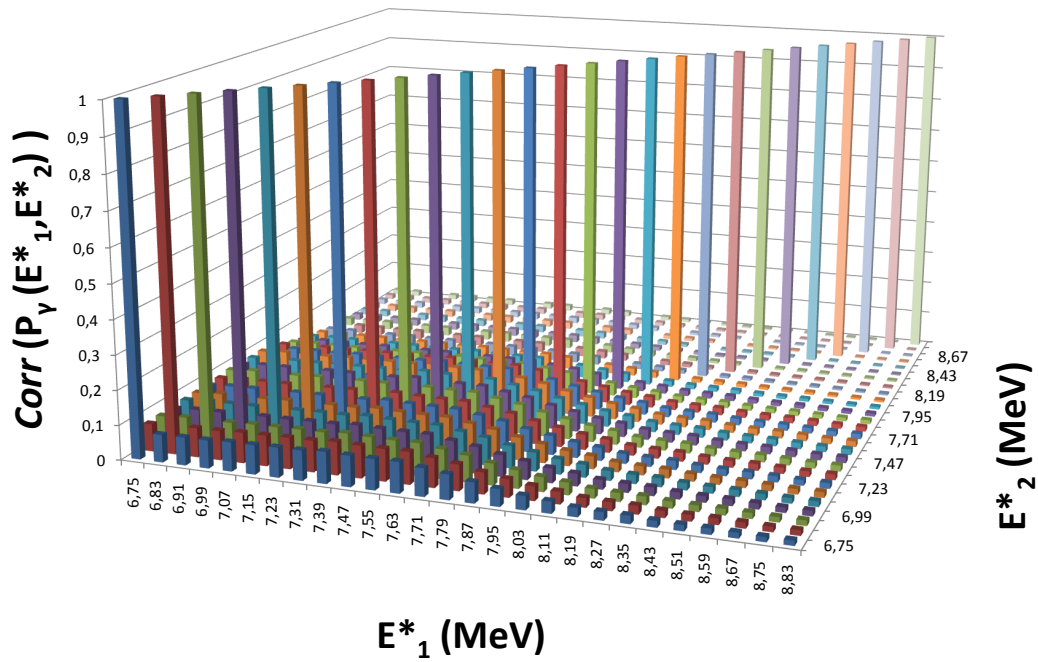
FIGURE M.1: Correlation-matrix for the radiative capture probability obtained in the $(^3He, d)^{175}Lu^*$ reaction.
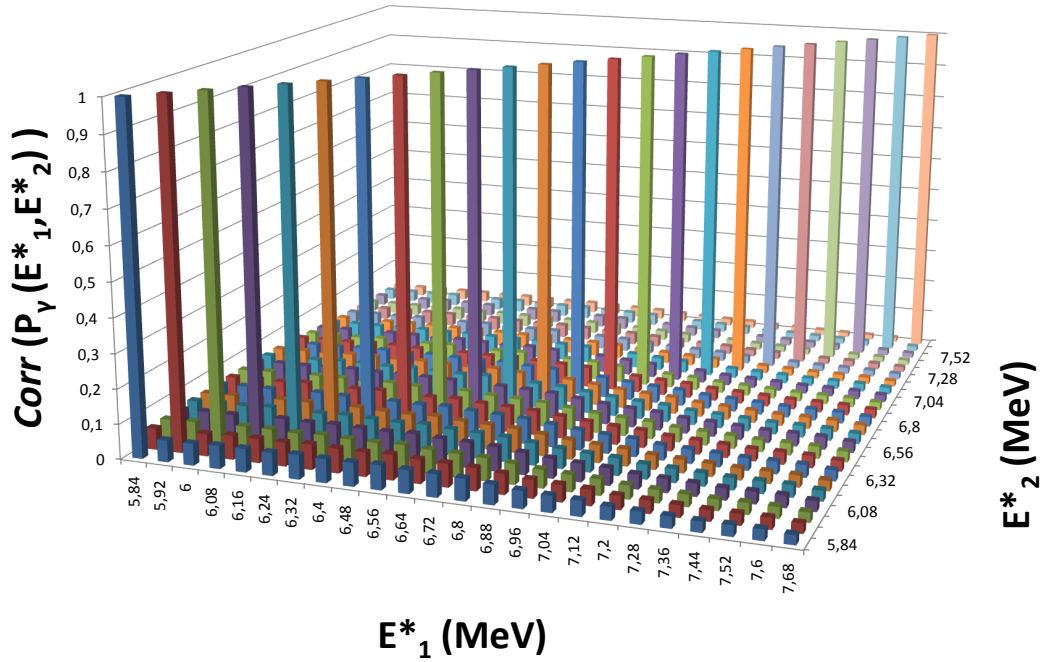
FIGURE M.2: The same as Fig. M.1 but for $(^3He, t)^{174}Lu^*$ reaction.
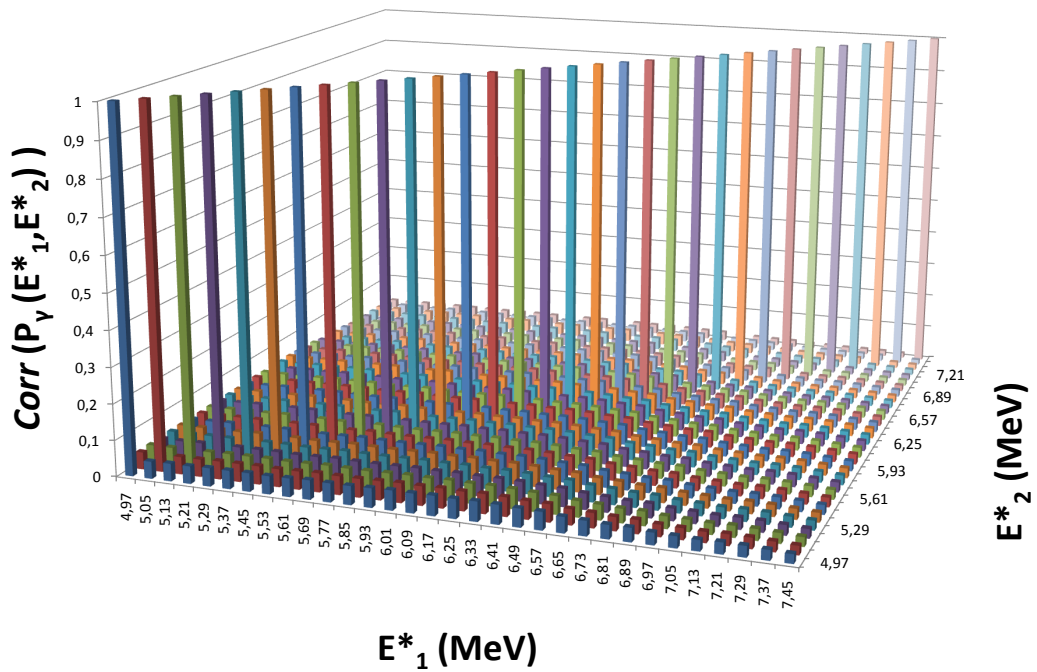
FIGURE M.3: The same as Fig. M.1 but for $(^3He, \alpha)^{173}Yb^*$ reaction.

Annexe N

Identification of the gamma transitions

E_γ(keV)	$J\pi \to J'\pi'$	E_{level}(keV)	$T_{1/2}$	I_γ
71.51	$1^+ \to 1^-$	194.35	35 ns	
112.92	$3^- \to 1^-$	235.76		
182.42	$2^- \to 1^-$	305.26		
184.13	$8^- \to 7^-$	184.1		
186.98	$2^+ \to 1^+$	381.34		
192.21	$1^- \to 1^+$	386.57		100
201.56	$5^- \to 3^-$	437.32		
225.40	$3^- \to 2^-$	658.43	6.3 ns	
240.76	$8^+ \to 8^-$	424.89	2 ns	100
263.73	$1^- \to 1^-$	386.57		49
284.64	$4^+ \to 3^+$	657.13	0.5ns	
310.18	$2^- \to 1^-$	433.03		
335.85	$4^+ \to 3^+$	635.19	7.8 ns	
424.89	$8^+ \to 7^-$	424.89	2 ns	44
563.92	$6^- \to 7^-$	563.92		
838.62	$5^- \to 7^-$	838.62	0.2 ns	

TABLE N.1: Identified gamma transitions in $^{174}Yb(^3He,p\gamma)^{176}Lu^*$ [Basunia 06]

E_γ(keV)	$J\pi \to J'\pi'$	E_{level}(keV)	$T_{1/2}$	I_γ
88.36	$\frac{7}{2}^+ \to \frac{5}{2}^+$	432.74	0.1 ns	100
113.8	$\frac{9}{2}^+ \to \frac{7}{2}^+$	113.8	90 ps	
132.92	$\frac{11}{2}^- \to \frac{9}{2}^-$	529.25		
137.65	$\frac{11}{2}^+ \to \frac{9}{2}^+$	251.46	32.4 ps	100
147.4	$\frac{13}{2}^- \to \frac{9}{2}^-$	562.3		
156.07	$\frac{13}{2}^- \to \frac{11}{2}^-$	685.32		
160.9	$\frac{13}{2}^+ \to \frac{11}{2}^+$	412.39	12.7 ps	
178.8	$\frac{15}{2}^- \to \frac{13}{2}^-$	863.7		
182.9	$\frac{15}{2}^+ \to \frac{13}{2}^+$	595.25		37.4
235.6	$\frac{17}{2}^- \to \frac{13}{2}^-$	798.1		
251.47	$\frac{11}{2}^+ \to \frac{9}{2}^+$	251.46	32.4 ps	77
255.72	$\frac{1}{2}^+ \to \frac{1}{2}^-$	626.53	10.6 ns	
282.52	$\frac{9}{2}^- \to \frac{9}{2}^+$	396.32	3.28 ns	46.6
289.45	$\frac{3}{2}^+ \to \frac{5}{2}^+$	632.76		
298.7	$\frac{13}{2}^+ \to \frac{9}{2}^+$	412.39	12.7 ps	
319.29	$\frac{13}{2}^+ \to \frac{9}{2}^+$	672.83		
324.0	$\frac{7}{2}^- \to \frac{5}{2}^-$	886.3		92
343.38	$\frac{5}{2}^+ \to \frac{7}{2}^+$	343.38	0.281 ns	
343.7	$\frac{15}{2}^+ \to \frac{11}{2}^+$	595.25		100
353.48	$\frac{5}{2}^- \to \frac{7}{2}^+$	353.48	1.49 us	
387.6	$\frac{17}{2}^+ \to \frac{13}{2}^+$	799.95	4.05 ps	
396.32	$\frac{9}{2}^- \to \frac{7}{2}^+$	396.32	3.28 ns	100
432.74	$\frac{7}{2}^+ \to \frac{7}{2}^+$	432.74	0.1 ns	59.8
471.3	$\frac{11}{2}^- \to \frac{9}{2}^-$	886.3		100

TABLE N.2: Identified gamma transitions in $^{174}Yb(^3He, pn\gamma)^{175}Lu^*$ and $^{174}Yb(^3He, d\gamma)^{175}Lu^*$ [Basunia 04]

E_γ(keV)	$J\pi \to J'\pi'$	E_{level}(keV)	$T_{1/2}$	I_γ
88.54	$4^- \to 3^-$	200.29		
105.9	$8^+ \to 7^+$	537.41		
110.906	$5^- \to 4^-$	311.20		
111.12	$7^+ \to 7^-$	431.41	1.5 ns	44.7
129.06	$3^+ \to 3^-$	240.82	395 ns	100
138.16	$6^- \to 5^-$	619.16		
149.45	$7^- \to 6^-$	320.29		
154.83	$3^+ \to 4^+$	414.37		
154.99	$5^+ \to 4^+$	575.66		
166.48	$10^+ \to 9^+$	843.12		
196.11	$3^+ \to 2^-$	240.82	395 ns	33
208.36	$2^+ \to 3^-$	320.11		100
253.43	$4^- \to 3^-$	365.18	145 ns	
260.58	$7^+ \to 6^-$	431.41	1.5 ns	100
281.16	$0^+ \to 1^-$	281.16		
285.8	$5^- \to 6^-$	456.5		
308.9	$4^+ \to 3^-$	420.60		
320.09	$2^+ \to 1^-$	320.11		26
320.51	$8^- \to 6^-$	491.35		
340.69	$8^+ \to 7^+$	771.98		
360.67	$7^+ \to 6^-$	531.3		
475.3	$12^- \to 10^-$	1370.5		
522.42	$1^- \to 1^-$	522.42		

TABLE N.3: Identified gamma transitions in $^{174}Yb(^3He, dn\gamma)^{174}Lu^*$ and $^{174}Yb(^3He, t\gamma)^{174}Lu^*$ [Browne 99]

E_γ(keV)	$J\pi \to J'\pi'$	E_{level}(keV)	$T_{1/2}$	I_γ
117.18	$\frac{9}{2}^+ \to \frac{7}{2}^+$	117.18		
131.10	$\frac{11}{2}^+ \to \frac{9}{2}^-$	580.08		
139.634	$\frac{3}{2}^- \to \frac{5}{2}^-$	263.30	0.16 ns	
141.41	$\frac{11}{2}^+ \to \frac{9}{2}^+$	258.56		
160.23	$\frac{13}{2}^- \to \frac{9}{2}^-$	358.70		
191.18	$\frac{15}{2}^+ \to \frac{13}{2}^+$	1074.71		
229.61	$\frac{3}{2}^+ \to \frac{1}{2}^+$	1359.26		
248.0	$\frac{17}{2}^- \to \frac{13}{2}^-$	606.69		
258.56	$\frac{11}{2}^+ \to \frac{7}{2}^+$	258.56		
296.97	$\frac{1}{2}^+ \to \frac{1}{2}^-$	425.31	0.84 ns	
306.45	$\frac{13}{2}^+ \to \frac{9}{2}^+$	423.62		
311.23	$\frac{3}{2}^+ \to \frac{5}{2}^-$	434.912	0.38 ns	
335.0	$\frac{21}{2}^- \to \frac{17}{2}^+$	941.69		
356.99	$\frac{5}{2}^+ \to \frac{7}{2}^+$	356.99	383 ps	
448.98	$\frac{9}{2}^- \to \frac{7}{2}^+$	448.98	0.58 ns	

TABLE N.4: Identified gamma transitions in $^{174}Yb(^3He, tn\gamma)^{173}Lu^*$ [Shirley 95a]

E_γ(keV)	$J\pi \to J'\pi'$	E_{level}(keV)	$T_{1/2}$	I_γ
78.63	$\frac{7}{2}^- \to \frac{5}{2}^-$	78.64	46 ps	
100.72	$\frac{9}{2}^- \to \frac{7}{2}^-$	179.36	32 ps	100
122.55	$\frac{11}{2}^- \to \frac{9}{2}^-$	301.85	16.7 ps	100
144	$\frac{13}{2}^- \to \frac{11}{2}^-$	445.7		93.4
164.9	$\frac{15}{2}^- \to \frac{13}{2}^-$	610.6	7.3 ps	65.4
171.39	$\frac{7}{2}^+ \to \frac{9}{2}^-$	350.76	0.45 ns	13.7
179.36	$\frac{9}{2}^- \to \frac{5}{2}^-$	179.36	32 ps	26.3
223.16	$\frac{11}{2}^- \to \frac{7}{2}^-$	301.85	16.7 ps	64.3
233.60	$\frac{9}{2}^+ \to \frac{9}{2}^-$	412.96		
266.4	$\frac{13}{2}^- \to \frac{9}{2}^-$	445.7		100
272.1	$\frac{7}{2}^+ \to \frac{7}{2}^-$	350.76	0.45 ns	100
308.9	$\frac{15}{2}^- \to \frac{11}{2}^-$	610.6	7.3 ps	100
398.9	$\frac{1}{2}^- \to \frac{5}{2}^-$	398.9	2.9 us	
461.4	$\frac{3}{2}^- \to \frac{5}{2}^-$	461.5	0.56 ns	

TABLE N.5: Identified gamma transitions in $^{174}Yb(^3He, \alpha\gamma)^{173}Yb^*$ [Shirley 95b]

E_γ(keV)	$J\pi \to J'\pi'$	E_{level}(keV)	$T_{1/2}$	I_γ
78.74	$2^+ \to 0^+$	78.64	1.65 ns	
181.53	$4^+ \to 2^+$	260.26	0.122 ns	
279.71	$6^+ \to 4^+$	539.97	16.6 ps	
372.06	$8^+ \to 6^+$	912.12	3.5 ps	

TABLE N.6: Identified gamma transitions in $^{174}Yb(^3He, \alpha n\gamma)^{172}Yb^*$[Singh 95]

Annexe O

Neutron-induced experiment $^{175}Lu(n, n'\gamma)$ at CEA DAM DIF

O.1 Introduction

In this appendix, the TALYS calculations are confronted to a neutron-induced experiment in order to test the deexcitation parameters inputted in the statistical model. We stress that this work is leaded by our colleagues[1] from CEA-DAM-DIF. The idea is to compare γ-ray intensity ratios measured in the neutron-induced reaction with the surrogate $(^3He, p\gamma)$ experiment. The advantage to measure ratios instead of absolute cross-sections for several low-lying transitions is to reduce systematic errors due to the neutron flux and solid angles uncertainties. Furthermore, no dead-time correction is needed and anisotropy effects are strongly removed in the ratio approach. Three neutron-induced experiments were performed in :

1. <u>July 2008 :</u> $^{175}Lu(n, \gamma)^{176}Lu^*$ using two Germanium detectors. Unfortunately, the TOF technique was unable to discriminate γ-rays coming from the capture reaction (mainly fed by isomeric states) and the $\gamma - n$ background coming from the production target. Probably the n-shielding was not enough efficient. γ-transitions coming from ^{176}Lu were weakly fed (the production cross sections drops very quickly with increasing incident neutron energy) and did not emerge clearly from the background noise. Nevertheless, we observed some γ-transitions coming from the inelastic scattering reaction $^{175}Lu(n, n'\gamma)^{175}Lu^*$.

2. <u>July 2009 :</u> $^{175}Lu(n, \gamma)^{176}Lu^*$ with an array of six $LaBr$ detectors. The idea was to clean considerably our γ-spectra due to the excellent time resolution of the $LaBr$ scintillators. In addition, the γ-rays were detected in coincidence in order to reduce the background noise as the dead time. But again, we were confronted to

---

[1] Vincent Méot, Olivier Roig, Aurélien Blanc, Camille Théroine, Adeline Bail et al.

experimental difficulties. Firstly, $LaBr$ detectors were found to be very sensitive to the ambient temperature and the energy calibration was therefore unstable. Secondly, the $LaBr$ detectors were rather sensitive to neutrons. As a consequence, the bad energy resolution and the activation did not permit us to separate γ transitions coming from ^{176}Lu and the internal radioactivity of the detector. No γ-transitions of interest were identified.

3. <u>November 2010 :</u> A comparison between TALYS calculations and the neutron-induced inelastic experiment is another way to test the deexcitation parameters. In this experiment, we measured some γ-transitions coming from the inelastic scattering reaction $^{175}Lu(n, n'\gamma)^{175}Lu^*$. We used only one Germanium detector. Statistics was sufficient. In this case, the production cross section raises with the incident neutron energy. This is this experiment which is detailed in this appendix. We stress that we show preliminary results.

O.2 Experimental set-up (November 2010)

The experiment was performed using the 4 MV accelerator of CEA-DAM-DIF. This accelerator was used to deliver pulsed proton beam. This beam impinged on titanium-tritium target (TiT) in order to produce mono-energetic neutrons. The neutron production is made in the $T(p, n)^3He$ reaction, as shown in table O.1. To limit the counting rate in the Ge detector below 3000 counts/second, the proton beam intensity on the tritiated titanium target was $\sim 1 \, \mu A$. The neutron flux was measured by a BF_3 detector (proportional counter). Figure O.1 presents a schematic view of the experimental arrangement. The Lu_2O_3 target was a cylinder of 3 cm diameter and 3 cm thickness. It was placed in front of the neutron production target far from about 13 cm. The germanium detector was placed at 40.2 cm from Lu_2O_3 sample and at 130° with respect to the accelerator beam axis. Measurements were also done at 90° in order to compare the obtained ratios for two detection angles.

E_p(MeV)	E_n(MeV)	$\frac{d\sigma}{d\Omega}$ {0°} (mb/sr)
1.2	0.351	56.1
1.4	0.575	51.4
1.8	0.996	58.6
2.2	1.406	77
4.0	3.22	98

TABLE O.1: Details about $T(p, n)^3He$ reaction as neutron production. Note that the neutron energy E_n depends of the emission angle ([Liskien 73]).
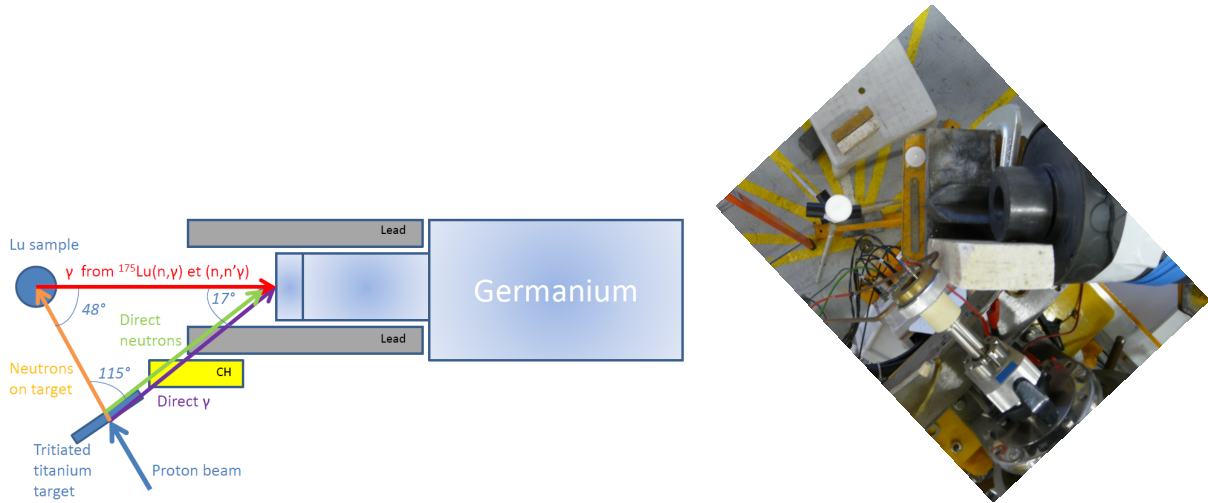
FIGURE O.1: Experimental set-up at CEA-DAM-DIF

O.3 Time-of-Flight technique

The keys of this neutron-induced experiment were to discriminate :

- γ-rays coming directly from the production target,

- γ-rays coming from the Lu sample after a neutron capture,

- neutrons mainly produced in the production target.

Experimentally, fast neutrons were strongly moderated by a screen of CH between the production target and the Germanium detectors. Moreover the detector was also shielded with lead from direct γ-rays. The discrimination is made by the difference of time of flight for a γ-ray and a neutron.

$$TOF_{neutrons}(ns) = \frac{0.72295 \times d_n(cm)}{\sqrt{E_n(MeV)}} \tag{O.1}$$

$$TOF_{\gamma}(ns) = \frac{d}{c} = \frac{d_{\gamma}(cm)}{30} \tag{O.2}$$

where E_n is the neutron energy and d_{χ} is the distance traveled by the particle χ. Obviously these distances need to be high enough to proceed time measurements and observe some differences. The time resolution of the Ge detector ($\approx$10 ns) was not enough precise to separate γ-rays of interest (coming from the $^{175}Lu(n, n'\gamma)$ reaction) from direct γ-rays but the discrimination between γ-rays and neutrons was clean. Figure O.2 gives the time-of-flight scales for a given proton beam energy E_p and shows the schematic form of a time signal. The START signal is done by the pulse of the accelerator and the

STOP signal corresponds to an event in the *Ge* detector. In our case, the acquisition was triggered only when an event is detected in the germanium detector with a chosen γ-ray detection threshold. in order to reduce the background noise and avoid a huge dead time for the acquisition system. The electronics used is shown in figure O.3.
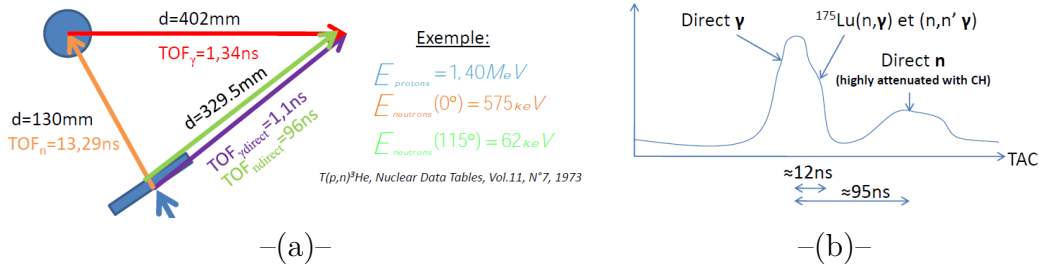

FIGURE O.2: Example of TOF measurements (a) and schematic TAC-spectrum (b)

The γ-rays of interest (coming from $^{175}Lu(n, n'\gamma)^{175}Lu^*$) are identified in a two-dimensions plot. A TAC channel corresponds to about 100 ps. The figure O.4 shows γ-rays zoomed spectra as a function of the TOF, which corresponds to the γ-rays travels. The large horizontal green contribution is due to direct γ-rays of all energies. In comparison, with a delay of almost 10 ns, one observe two γ-transitions at 343 keV and 396 keV. These γ-rays correspond to $5/2^+ \rightarrow 7/2^+ (0.281$ ns) and $9/2+ \rightarrow 7/2^+ (3.28$ ns) respectively and are the main transitions fed in the reaction $^{175}Lu(n, n'\gamma)^{175}Lu^*$. Note that because the $9/2^+$ state is an isomeric state, the γ deexcitation is spreading over the time. Last, one observe many well-defined γ-rays which are not correlated in time : these are γ-rays coming from intrinsic activation of the germanium detectors but also the activation of the lead shield. The experimental TOF spectrum is shown in figure O.5 and three cuts in time which correspond to the background, the γ-rays and the neutrons, respectively, are defined. The corresponding γ-spectra for these three different cuts are also presented. By using the adequate selection (namely CUT 2), γ-rays transition intensities can properly be extracted.

O.4 Efficiency and auto-absorption

Gamma-rays transition intensities need to be corrected for the efficiency in the Germanium detector. The auto-absorption c has to be taken into account :

$$c = \frac{(1 - e^{-\mu.t})}{\mu.t} \tag{O.3}$$

where t is the width of the target (cm) and μ is the absorption coefficients $(cm^2.g^{-1})$. Note that μ depends on the constituents of the target (for Lu_2O_3, the fraction by weight are approximately 12% of $Z = 8$ and 88% of $Z = 71$), the geometry of the target and
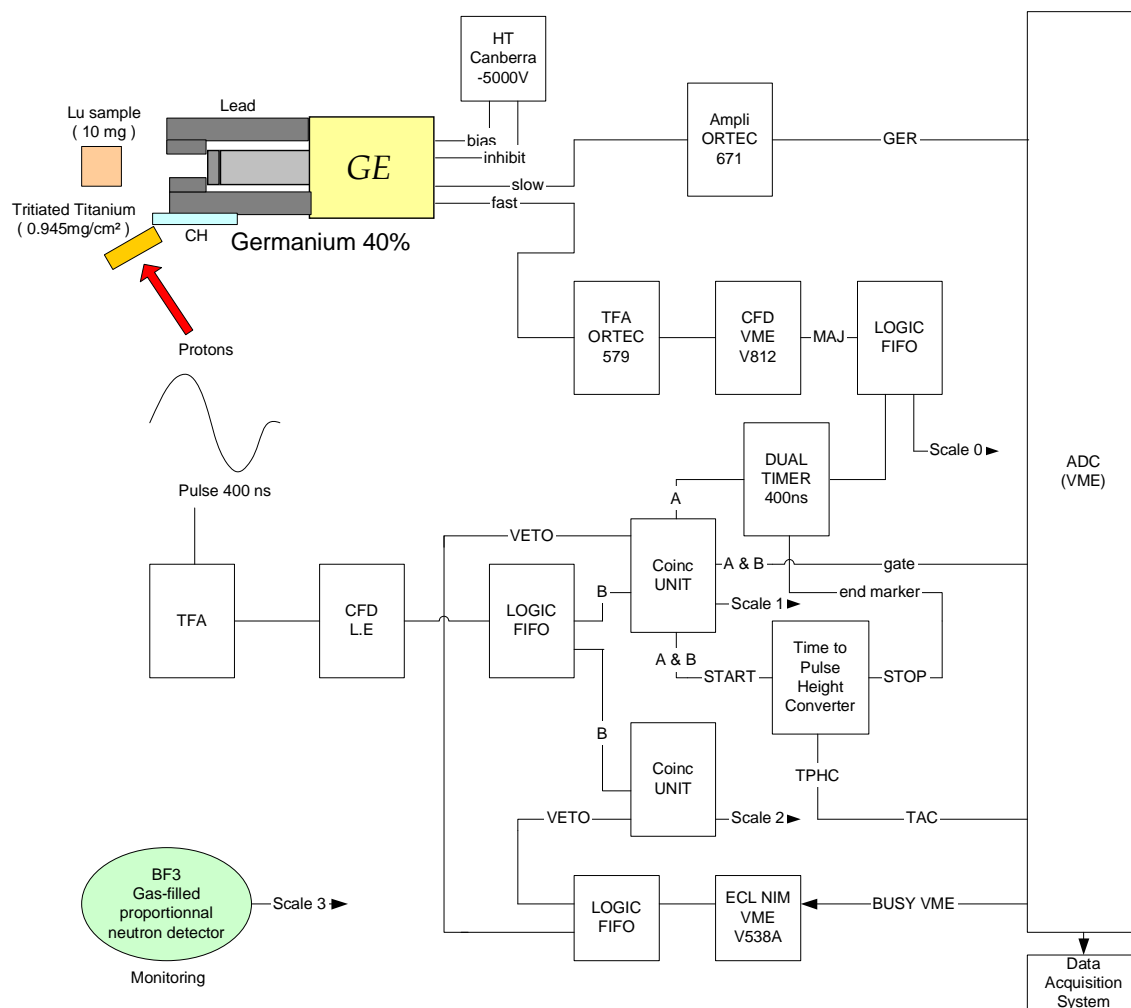
FIGURE O.3: Block diagram of the electronics used for the neutron-induced experiment, using TOF discrimination.
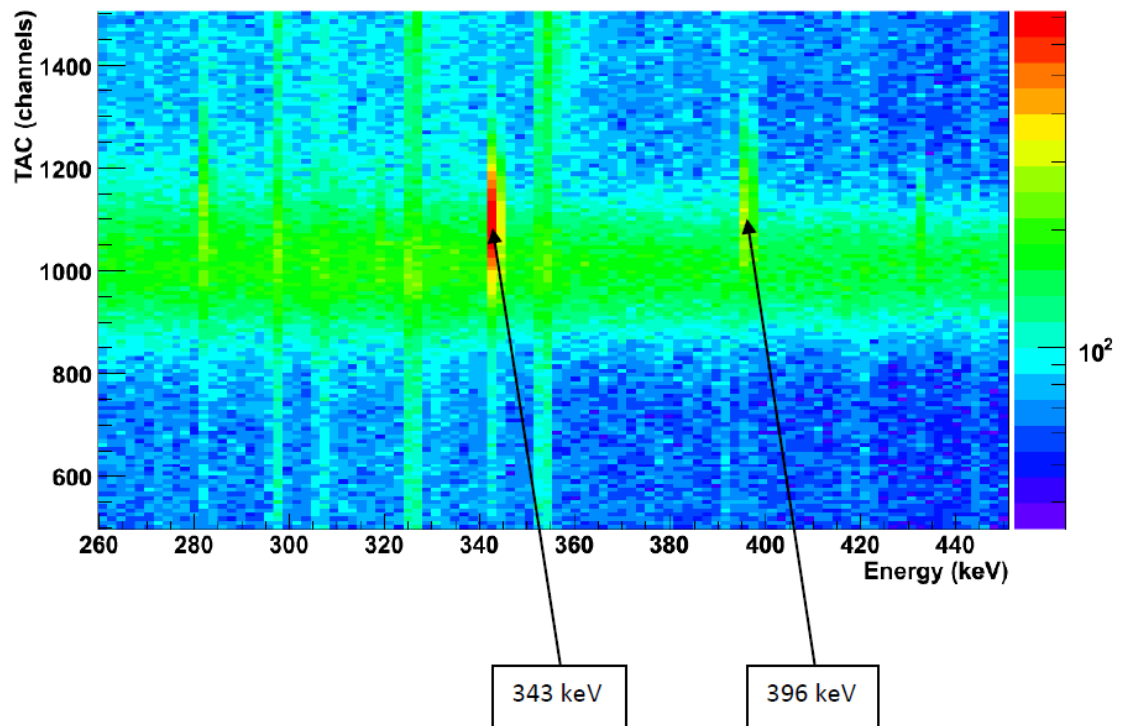
FIGURE O.4: TAC vs energy bi-dimensional plot : identification of the two main γ transitions in ^{175}Lu.
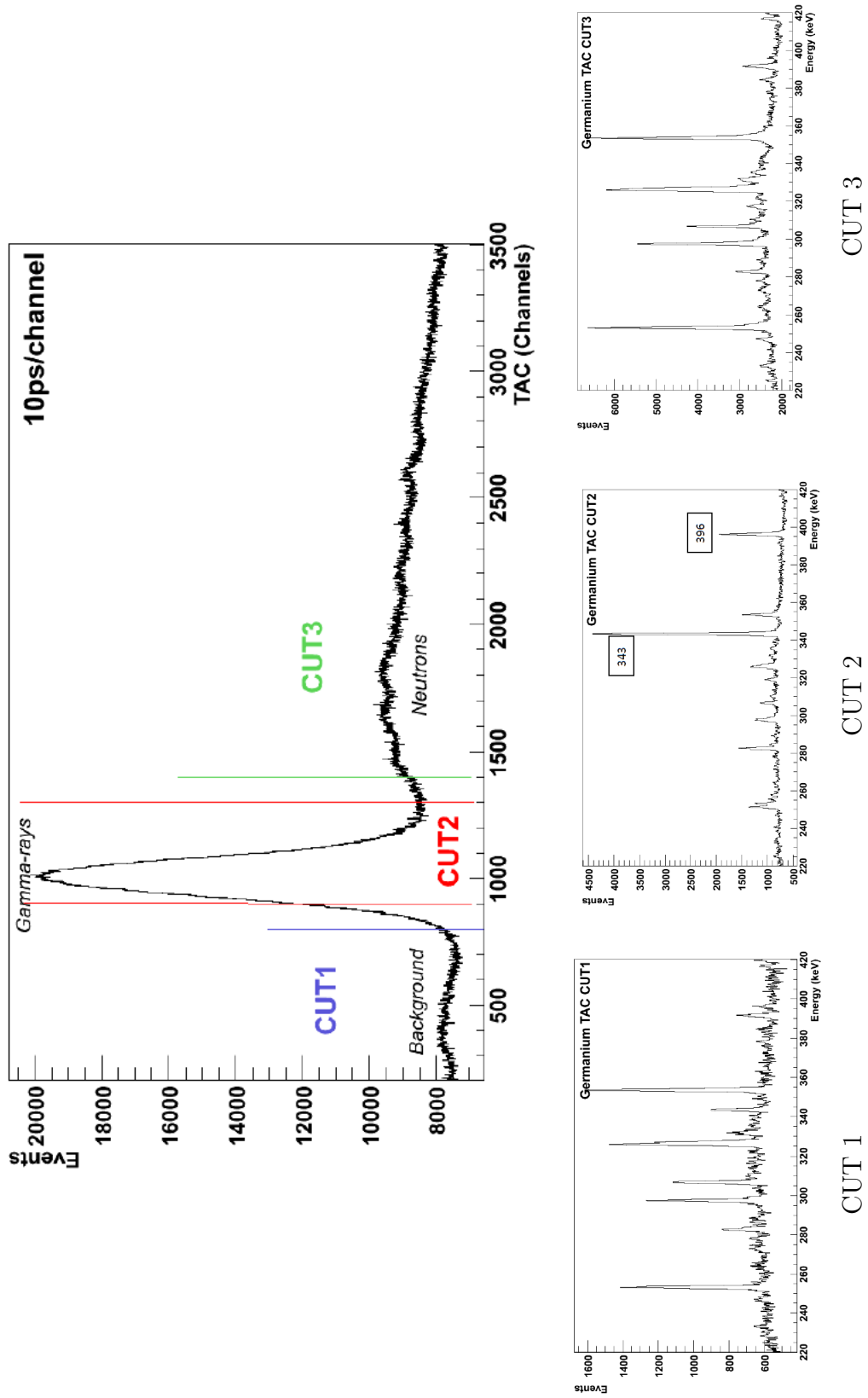
FIGURE O.5: Experimental TOF obtained for E_n=800keV andγ-spectra in coincidence with TAC for the three different cuts.

obviously the energy E_γ of the considered γ-ray. In our case, the experimental efficiency was determined by using ^{152}Eu, ^{133}Ba and ^{241}Am γ-sources. To cover a large range of energy, the efficiency was then simulated with GEANT4. This work was realized by our colleagues from CEA-DAM-DIF (Aurélien Blanc).
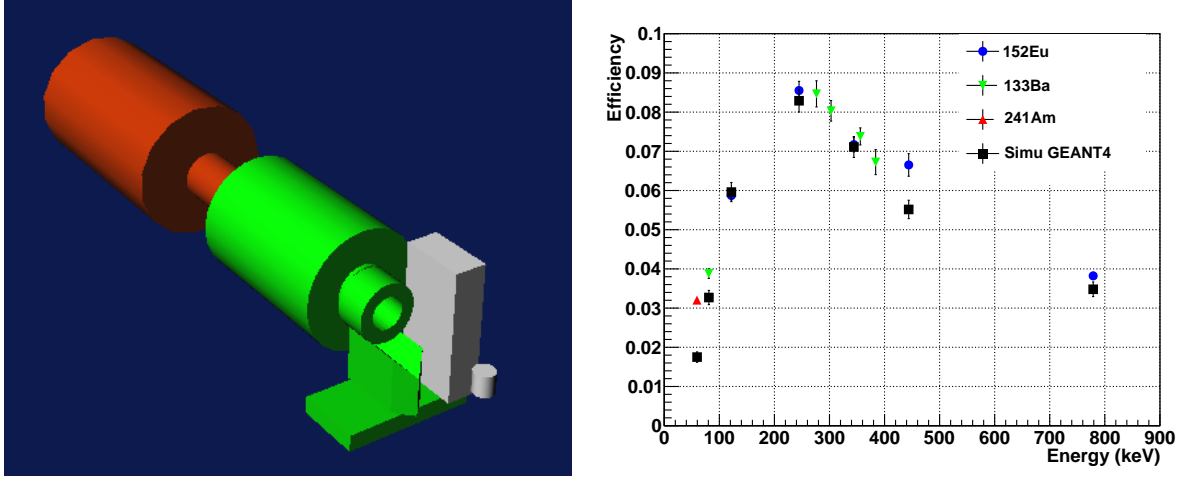
FIGURE O.6: GEANT4 geometry and simulated efficiency compared to experimental efficiency (preliminary results). (Aurélien Blanc, CEA-DAM-DIF)

O.5 Results

We determined the following inelastic (n,n') γ-ray intensity ratios : $\frac{5/2^+\to 7/2^+(343keV)}{9/2^+\to 7/2^+(396keV)}$ and $\frac{5/2^+\to 7/2^+(343keV)}{11/2^+\to 7/2^+(251keV)}$. As shown in figure O.7, the obtained ratios are similar independently on the detection angle. The TALYS calculations are in good agreement with the neutron-induced data. This preliminary study ensures that we have reliable parameters in TALYS. It gives a strong confidence in the TALYS calculations used in Chapter 5.
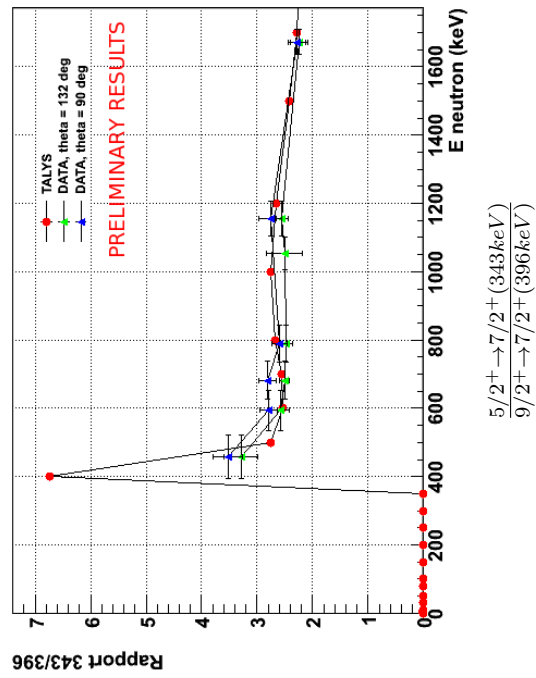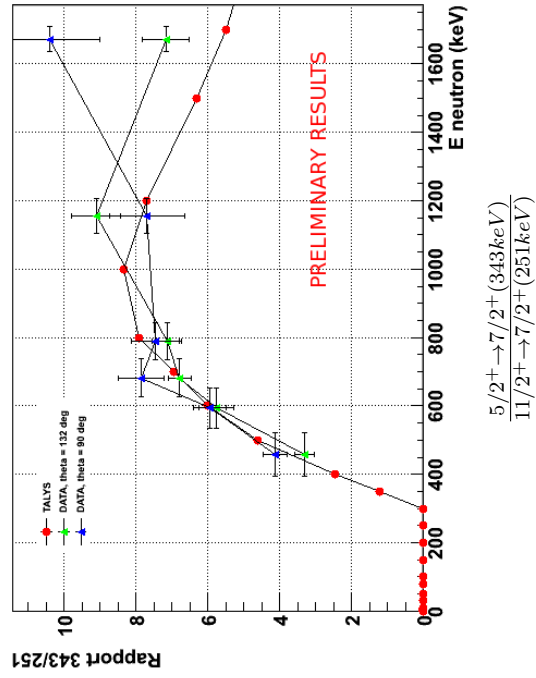
FIGURE O.7: Comparison between experimental γ-transitions ratios and TALYS calculations. (Aurélien Blanc, CEA-DAM-DIF)

Bibliographie

[Adhikari 86]   Sadhan K. Adhikari. *Exit doorways and intermediate structure reso-nances*. Phys. Rev. C, vol. 33, pages 471–480, Feb 1986. [www]

[Aerts 06]   G. Aerts. *Neutron capture cross section of ^{232}Th measured at the nTOF facility at CERN in the unresolved resonance region up to 1 MeV*. Phys. Rev. C, vol. 73, page 054610, 2006. [www]

[Agostinelli 03]   S. Agostinelli. *G4–a simulation toolkit*. Nucl. Instr. Meth. A, vol. 506, no. 3, pages 250 – 303, 2003. [www]

[Aleonard 74]   M.M. Aleonard, C. Boursiquot, P. Hubert & P. Mennrath. *Strengths of (p,γ) resonnances in ^{33}Cl, ^{35}Cl and ^{28}Si*. Phys. Lett. B, vol. 49, no. 1, pages 40 – 42, 1974. [www]

[Allmond 09]   J. M. Allmond, L. A. Bernstein, C. W. Beausang, L. Phair, D. L. Bleuel, J. T. Burke, J. E. Escher, K. E. Evans, B. L. Goldblum, R. Hatarik, H. B. Jeppesen, S. R. Lesher, M. A. McMahan, J. O. Rasmussen, N. D. Scielzo & M. Wiedeking. *Relative $^{235}U(n,\gamma)$ and (n,f) cross sections from $^{235}U(d,p\gamma)$ and (d,pf)*. Phys. Rev. C, vol. 79, page 054610, May 2009. [www]

[Andersen 70]   B.L. Andersen, B.B. Back & J.M. Bang. *One-particle transfer reactions to highly excited states in deformed nuclei*. Nucl. Phys. A, vol. 147, no. 1, pages 33 – 44, 1970. [www]

[Andrejtscheff 74]   W. Andrejtscheff, P. Manfrass & W. Seidel. *Transition probabilities in the doubly odd nuclei ^{176}Lu and ^{182}Ta*. Nucl. Phys. A, vol. 226, no. 1, pages 142 – 156, 1974. [www]

[Antonov 11]   A.N. Antonov. *The electron-ion scattering experiment ELISe at the International Facility for Antiproton and Ion Research (FAIR) : conceptual design study*. Nucl. Instr. Meth. A, vol. 637, no. 1, pages 60 – 76, 2011. [www]

[Aritomo 11]   Y. Aritomo, S. Chiba & K. Nishio. *Dynamical model of surrogate reactions.* Phys. Rev. C, vol. 84, page 024602, Aug 2011. ⎡www⎤

[Austern 70]   N. Austern. *Direct nuclear reaction theories.* ISBN 0471037702, no. XXV, 1970.

[Back 74a]   B. B. Back, H. C. Britt, Ole Hansen, B. Leroux & J. D. Garrett. *Fission of odd-A and doubly odd actinide nuclei induced by direct reactions.* Phys. Rev. C, vol. 10, pages 1948–1965, Nov 1974. ⎡www⎤

[Back 74b]   B. B. Back, Ole Hansen, H. C. Britt & J. D. Garrett. *Fission of doubly even actinide nuclei induced by direct reactions.* Phys. Rev. C, vol. 9, pages 1924–1947, May 1974. ⎡www⎤

[Bass 80]   R. Bass. *"Nuclear reactions with heavy ions".* Springler-Verlag, 1980.

[Basunia 04]   M.S. Basunia. *ADOPTED LEVELS GAMMAS for ^{175}Lu.* Nuclear Data Sheets, no. 102, page 719, 2004.

[Basunia 06]   M.S. Basunia. *ADOPTED LEVELS GAMMAS for ^{176}Lu.* Nuclear Data Sheets, no. 107, page 791, 2006.

[Basunia 09]   M.S. Basunia, R.M. Clark, B.L. Goldblum, L.A. Bernstein, L. Phair, J.T. Burke, C.W. Beausang, D.L. Bleuel, B. Darakchieva, F.S. Dietrich, M. Evtimova, P. Fallon, J. Gibelin, R. Hatarik, C.C. Jewett, S.R. Lesher, M.A. McMahan, E. Rodriguez-Vieitez & M. Wiedeking. *The (^{3}He,tf) as a surrogate reaction to determine (n,f) cross sections in the $10 - 20$ MeV energy range.* Nucl. Instr. Meth. B, vol. 267, no. 11, pages 1899 – 1903, 2009. ⎡www⎤

[Becvar 98]   F. Becvar. *Simulation of gamma cascades in complex nuclei with emphasis on assessment of uncertainties of cascade-related quantities.* Nucl. Instr. Meth. A, vol. 417, no. 2-3, pages 434 – 449, 1998. ⎡www⎤

[Beer 80]   H. Beer & F. Kappeler. *Neutron capture cross sections on ^{138}Ba, ^{142}Ce, $^{175,176}Lu$, and ^{181}Ta at 30 keV : Prerequisite for investigation of the ^{176}Lu cosmic clock.* Phys. Rev. C, vol. 21, no. 2, page 534, 1980. ⎡www⎤

[Beer 81]   H. Beer, F. Kaeppeler, K. Wisshak & R. A. Ward. *^{176}Lu : Cosmic clock or stellar thermometer .* Astrophysical Journal, Supplement, vol. 46, page 295, 1981.

[Beer 84]   H. Beer, G. Walter, R. L. Macklin & P. J. Patchett. *Neutron capture cross sections and solar abundances of ^{160,161}Dy, ^{170,171}Yb, ^{175,176}Lu,*

and ^{176,177}Hf *for the s-process analysis of the radionuclide* ^{176}Lu. Phys. Rev. C, vol. 30, pages 464–478, Aug 1984. www

[Belgya 06]   T. Belgya, O. Bersillon, R. Capote, T. Fukahori, G. Zhigang, S. Goriely, M. Herman, A.V. Ignatyuk, S. Kailas, A. Koning, P. Oblozinsky, V. Plujko & P. Young. *Handbook for calculations of nuclear reaction data RIPL2.* IAEA-TECDOC, no. 1506, 2006. www

[Bernstein 05] L.A. Bernstein & J.T. Burke. *Surrogate Nuclear Reactions using STARS.* AIP Conference Proceedings, vol. 769, no. 1, pages 890–893, 2005. www

[Bernstein 06] L. Bernstein. Deducing the ^{237}u destruction cross-sections using the surrogate ratio method. UCRL-PROC-220800, Proceeding NEDPC 2005, 2006. www

[Bohr 36]   N. Bohr. *Neutron Capture and Nuclear Constitution.* Nature, vol. 137, pages 334–348, 1936. www

[Bohr 39]   Niels Bohr & John Archibald Wheeler. *The Mechanism of Nuclear Fission.* Phys. Rev., vol. 56, pages 426–450, Sep 1939. www

[Bokhovko 96]   M. V. Bokhovko, V. N. Kononov, N. S. Rabotnov, A. A. Voevodskiy, G. N. Manturov & V. M. Timokhov. Neutron radiation cross-section, ,neutron transmission measurements for some fission product nuclei. Private communication, 1996.

[Bonneau 07]   L. Bonneau, T. Kawano, T. Watanabe & S. Chiba. *Direct and semidirect radiative capture of nucleons with Hartree-Fock-BCS bound states.* International Conference on Nuclear Data for Science and Technology 2007, pages 187–190, 2007. www

[Borella 05]   A. Borella. *Determination of the neutron parameters for* $206Pb$ *and of the thermal neutron capture cross section for* $206Pb$ *and* ^{209}Bi. PhD Thesis, vol. IRMM, no. Geel, 2005.

[Borella 07]   A. Borella, G. Aerts, F. Gunsing, M. Moxon, P. Schillebeeckx & R. Wynants. *The use of C6D6 detectors for neutron induced capture cross-section measurements in the resonance region.* Nucl. Instr. Meth. A, vol. 577, no. 3, pages 626 – 640, 2007. www

[Bovet 72]   E. Bovet, P. Boschung & J. Rossel. *Light response and pulse shape discrimination properties for NE 232.* Nucl. Instr. Meth. A, vol. 101, no. 2, pages 315 – 319, 1972. www

[Boyer 06]   S. Boyer, D. Dassie, J.N. Wilson, M. Aiche, G. Barreau, S. Czaj-kowski, C. Grosjean, A. Guiral, B. Haas, B. Osmanov, G. Aerts, E.Berthoumieux, F. Gunsing, Ch. Theisen, N. Thiolliere & L. Perrot. *Determination of the $^{233}Pa(n,\gamma)$ capture cross section up to neutron energies of 1 MeV using the transfer reaction $^{232}Th(^{3}He,p)^{234}Pa$.* Nucl. Phys. A, vol. 775, no. 3-4, pages 175 – 187, 2006. $\boxed{\text{www}}$

[Brink 57]   D.M. Brink. Nucl. Phys., no. 4, page 215, 1957.

[Britt 70]   H. C. Britt & J. D. Cramer. *Fission of Odd-A Uranium and Plutonium Isotopes Excited by (d, p), (t, d), and (t, p) Reactions.* Phys. Rev. C, vol. 2, pages 1758–1768, Nov 1970. $\boxed{\text{www}}$

[Britt 79]   H.C. Britt & J.B. Wilhelmy. *Simulated (n,f) cross sections for exotic actinide nuclei.* Nucl. Sci. and Eng., vol. 347, no. 2, page 222, 1979.

[Britt 80]   H. C. Britt, E. Cheifetz, D. C. Hoffman, J. B. Wilhelmy, R. J. Dupzyk & R. W. Lougheed. *Fission barriers for ^{255}Es, ^{256}Es, and ^{255}Fm.* Phys. Rev. C, vol. 21, pages 761–763, Feb 1980. $\boxed{\text{www}}$

[Browne 99]   E. Browne. *ADOPTED LEVELS GAMMAS for ^{174}Lu.* Nuclear Data Sheets, no. 87, page 15, 1999.

[Browne 07]   D. Browne, W. Younes, I. Thompson & N. Summers. *Proposed ^{237}U Evaluation for the next ENDL Release.* Rapport technique, 2007. LLNL Ext. Reports. $\boxed{\text{www}}$

[Burbidge 57]   E. Margaret Burbidge, G. R. Burbidge, William A. Fowler & F. Hoyle. *Synthesis of the Elements in Stars.* Rev. Mod. Phys., vol. 29, no. 4, pages 547–650, Oct 1957. $\boxed{\text{www}}$

[Burke 06]   J. T. Burke, L. A. Bernstein, J. Escher, L. Ahle, J. A. Church, F. S. Dietrich, K. J. Moody, E. B. Norman, L. Phair, P. Fallon, R. M. Clark, M. A. Deleplanque, M. Descovich, M. Cromaz, I. Y. Lee, A. O. Macchiavelli, M. A. McMahan, L. G. Moretto, E. Rodriguez-Vieitez, F. S. Stephens, H. Ai, C. Plettner, C. Beausang & B. Crider. *Deducing the $^{237}U(n, f)$ cross section using the surrogate ratio method.* Phys. Rev. C, vol. 73, page 054604, May 2006. $\boxed{\text{www}}$

[Chalupka 77]   A. Chalupka, G. Stengl & H. Vonach. *Temperature dependence of the pulse shape discrimination properties of NE 213.* Nucl. Instr. Meth. A, vol. 144, no. 2, pages 167 – 169, 1977. $\boxed{\text{www}}$

[Chau 06]   P. Chau. *Systematic study of elastic and reaction cross sections of deuteron induced reactions within the CDCC approach.* Nucl. Phys. A, vol. 773, no. 1-2, pages 56 – 77, 2006. $\boxed{\text{www}}$

[Chiba 10]   Satoshi Chiba & Osamu Iwamoto. *Verification of the surrogate ratio method.* Phys. Rev. C, vol. 81, page 044604, Apr 2010. www

[Chomaz 97]   Ph. Chomaz. *Collective excitations in nuclei.* Ecole Joliot Curie, 1997. www

[Corvi 88]   F. Corvi, A. Prevignano, H. Liskien & P. B. Smith. *An experimental method for determining the total efficiency and the response function of a gamma-ray detector in the range 0.5-10 MeV.* Nucl. Instr. Meth. A, vol. 265, no. 3, pages 475 – 484, 1988. www

[Cramer 70a]   J. D. Cramer & H. C. Britt. *Fission Studies of Thorium, Uranium, and Plutonium Isotopes with (t, pf) Reactions.* Phys. Rev. C, vol. 2, pages 2350–2358, Dec 1970. www

[Cramer 70b]   J.D. Cramer & H.C. Britt. Nucl. Sci. Eng. 41, no. 177, 1970. www

[Derkx 10]   X. Derkx & F. Rejmund. *Minor actinide fission induced by multinucleon transfer reaction in inverse kinematics.* EPJ Web of Conferences, vol. 2, page 07001, 2010. www

[Escher 06]   Jutta E. Escher & Frank S. Dietrich. *Determining (n, f) cross sections for actinide nuclei indirectly : Examination of the surrogate ratio method.* Phys. Rev. C, vol. 74, page 054601, Nov 2006. www

[Escher 10a]   J.E. Escher, F.S. Dietrich & N.D. Scielzo. *Neutron capture cross sections from Surrogate measurements.* CNR*09 - Second International Workshop on Compound Nuclear Reactions and Related Topics, EPJ Web of Conferences, vol. 2, page 6001, March 2010. www

[Escher 10b]   Jutta E. Escher & Frank S. Dietrich. *Cross sections for neutron capture from surrogate measurements : An examination of Weisskopf-Ewing and ratio approximations.* Phys. Rev. C, vol. 81, page 024612, Feb 2010. www

[Ferguson 65]   A.J. Ferguson. *Nuclear Correlation Methods in Gamma-Ray Spectroscopy.* North-Holland Publishing Company-Amesterdam, 1965.

[Feshbach 74]   H. Feshbach. *Doorway states and pre-equilibrium reactions.* Rev. Mod. Phys., vol. 46, no. 1, pages 1–5, Jan 1974. www

[Feshbach 80]   H. Feshbach, A. Kerman & S. Koonin. *The statistical theory of multistep compound and direct reactions.* Annals of Physics, vol. 125, no. 2, pages 429 – 476, 1980. www

295

[Gelin 07]   M. Gelin. *Spectroscopie gamma des noyaux riches en neutrons autour de N=20.* PhD. Thesis, 2007. ⬚www⬚

[Gilbert 65]   A. Gilbert & A.G.W. Cameron. *"A composite nuclear-level density formula with shell corrections".* Can. J. Phys., no. 43, pages 1446–1496, 1965.

[Goldblum 08]   B. L. Goldblum, S. G. Prussin, U. Agvaanluvsan, L. A. Bernstein, D. L. Bleuel, W. Younes & M. Guttormsen. *Determination of (n, γ) cross sections in the rare-earth region using the surrogate ratio method.* Phys. Rev. C, vol. 78, page 064606, Dec 2008. ⬚www⬚

[Goldblum 09]   B. L. Goldblum, S. R. Stroberg, J. M. Allmond, C. Angell, L. A. Bernstein, D. L. Bleuel, J. T. Burke, J. Gibelin, L. Phair, N. D. Scielzo, E. Swanberg, M. Wiedeking & E. B. Norman. *Indirect determination of the $^{230}Th(n, f)$ and $^{231}Th(n, f)$ cross sections for thorium-based nuclear energy systems.* Phys. Rev. C, vol. 80, page 044610, Oct 2009. ⬚www⬚

[Goldblum 10]   B. L. Goldblum, S. G. Prussin, L. A. Bernstein, W. Younes, M. Guttormsen & H. T. Nyhus. *Surrogate ratio methodology for the indirect determination of neutron capture cross sections.* Phys. Rev. C, vol. 81, page 054606, May 2010. ⬚www⬚

[Griffin 66]   J. J. Griffin. *Statistical Model of Intermediate Structure.* Phys. Rev. Lett., vol. 17, pages 478–481, Aug 1966. ⬚www⬚

[Guttormsen 90] M Guttormsen, A Atac, G Lovhoiden, S Messelt, T Ramsoy, J Rekstad, T F Thorsteinsen, T S Tveter & Z Zelazny. *Statistical Gamma-Decay at Low Angular Momentum.* Physica Scripta, vol. 1990, no. T32, page 54, 1990. ⬚www⬚

[Hatarik 10]   R. Hatarik, L. A. Bernstein, J. A. Cizewski, D. L. Bleuel, J. T. Burke, J. E. Escher, J. Gibelin, B. L. Goldblum, A. M. Hatarik, S. R. Lesher, P. D. O'Malley, L. Phair, E. Rodriguez-Vieitez, T. Swan & M. Wiedeking. *Benchmarking a surrogate reaction for neutron capture.* Phys. Rev. C, vol. 81, page 011602, Jan 2010. ⬚www⬚

[Hauser 52]   Walter Hauser & Herman Feshbach. *The Inelastic Scattering of Neutrons.* Phys. Rev., vol. 87, pages 366–373, Jul 1952. ⬚www⬚

[Hilaire 03]   S. Hilaire, Ch. Lagrange & A. J. Koning. *Comparisons between various width fluctuation correction factors for compound nucleus reactions.* Annals of Physics, vol. 306, no. 2, pages 209 – 231, 2003. ⬚www⬚

[Hill 53]   D.L Hill & J.A. Wheeler. Phys. Rev. C, no. 89, page 1102, 1953.

[Hodgson 71]   P.E. Hodgson. *Nuclear reactions and nuclear strucure*. Oxford, 1971.

[Ignatyuk 75]   A.V. Ignatyuk, G.N. Smirenkin & A.S. Tishin. Sov. J. Nucl. Phys, vol. 21, page 255, 1975.

[Kappeler 06]   F. Kappeler & A. Mengoni. *Nuclear input for the s-process : progress with experiments and theory*. Nuclear Physics A, vol. 777, pages 291 – 310, 2006. ⬚www

[Kessedjian 08] G. Kessedjian. *Mesures de sections efficaces d'actinides mineurs d'interet pour la transmutation*. PhD Thesis - Universite Bordeaux I, 2008. ⬚www

[Kessedjian 10] G. Kessedjian, B. Jurado, M. Aiche & G. Barreau et al. *Neutron-induced fission cross sections of short-lived actinides with the surrogate reaction method*. Phys. Lett. B, vol. 692, no. 5, pages 297 – 301, 2010. ⬚www

[Koning 00]   A. Koning & S. Hilaire. *TALYS-1.2*. 2000. ⬚www

[Koning 03]   A.J. Koning & J.P. Delaroche. *Local and global nucleon optical models from 1 keV to 200 MeV*. Nucl. Phys. A, vol. 713, no. 3-4, pages 231 – 310, 2003. ⬚www

[Kopecky 90]   J. Kopecky & M. Uhl. Phys. Rev. C, no. 42, page 1941, 1990.

[Leo 87]   W.R. Leo. *Techniques for Nucl. and Part. Phys. Experiments*. Springler-Verlag, 1987.

[Lesher 09]   S. R. Lesher, J. T. Burke, L. A. Bernstein, H. Ai, C. W. Beausang, D. L. Bleuel, R. M. Clark, F. S. Dietrich, J. E. Escher, P. Fallon, J. Gibelin, B. L. Goldblum, I. Y. Lee, A. O. Macchiavelli, M. A. McMahan, K. J. Moody, E. B. Norman, L. Phair, E. Rodriguez-Vieitez, N. D. Scielzo & M. Wiedeking. *Surrogate ratio method in the actinide region using the (α,α'f) reaction*. Phys. Rev. C, vol. 79, page 044609, Apr 2009. ⬚www

[Lewis 75]   M. B. Lewis. *Effects of spreading widths upon the direct nuclear reaction continuum*. Phys. Rev. C, vol. 11, pages 145–153, Jan 1975. ⬚www

[Lindholm 80]   A. Lindholm, L. Nilsson, M. Ahmad, M. Anwar, I. Bergqvist & S. Joly. *Direct-semidirect and compound contributions to radiative neutron capture cross sections*. Nucl. Phys. A, vol. 339, no. 2, pages 205 – 218, 1980. ⬚www

[Liskien 73]   H. Liskien & A. Paulsen. *"Neutron Production Cross-sections and Energies for the Reactions T(p,n)³He, D(d,n)³He and T(d,n)⁴He"*. Atomic Data and Nuclear Data Tables, vol. 11, no. 7, pages 569–615, 1973.

[Lyles 07]   B. F. Lyles, L. A. Bernstein, J. T. Burke, F. S. Dietrich, J. Escher, I. Thompson, D. L. Bleuel, R. M. Clark, P. Fallon, J. Gibelin, A. O. Macchiavelli, M. A. McMahan, L. Phair, E. Rodriguez-Vieitez, M. Wiedeking, C. W. Beausang, S. R. Lesher, B. Darakchieva & M. Evtimova. *Absolute and relative surrogate measurements of the $U236(n, f)$ cross section as a probe of angular momentum effects.* Phys. Rev. C, vol. 76, page 014606, Jul 2007. www

[Macklin 63]   R.L. Macklin, J.H. Gibbons & T. Inada. *Neutron capture cross sections near 30 keV using a Moxon-Rae detector.* Nuclear Physics, vol. 43, pages 353 – 362, 1963. www

[Macklin 67]   R. L. Macklin & J. H. Gibbons. *Capture Cross Section Studies for 30-220 keV Neutrons Using a New Technique.* Phys. Rev., vol. 159, no. 4, pages 1007–1012, Jul 1967.

[Macklin 78]   R. L. Macklin, D. M. Drake & J. J. Malanify. *Fast Neutron Capture Cross Sections of ^{169}Tm, ^{191}Ir, ^{193}Ir, and ^{175}Lu for En= 2000 keV.* Rapport technique 7479, 1978. Los Alamos Scientific Lab. Reports.

[Maslov 98]   V.M. Maslov. *IAEA.* RIPL-1 Handbook. TEXDOC-000, vol. 5, 1998.

[Mermaz 80]   M.C. Mermaz. *Direct transfer reaction to discrete and continuum states.* Phys. Rev. C, vol. 21, pages 2356–2365, Jun 1980. www

[Moxon 63]   M.C. Moxon & E.R. Rae. *A γ-ray detector for neutron capture cross-section measurements.* Nucl. Instr. Meth. A, vol. 24, pages 445 – 455, 1963. www

[Naqvi 96]   A.A. Naqvi, M.M. Nagadi, S. Shaheen & Abdul Bari. *Energy resolution measurements of benzene, toluene and cyclohexane scintillators for monoenergetic γ-rays.* Appl. Rad. and Isotopes, vol. 47, no. 2, pages 241 – 246, 1996. www

[Nayak 08]   B. K. Nayak, A. Saxena, D. C. Biswas, E. T. Mirgule, B. V. John, S. Santra, R. P. Vind, R. K. Choudhury & S. Ganesan. *Determination of the $^{233}Pa(n, f)$ reaction cross section from 11.5 to 16.5 MeV neutron energy by the hybrid surrogate ratio approach.* Phys. Rev. C, vol. 78, page 061602, Dec 2008. www

[Nelder 65]   J. Nelder & R. Mead. *A simplex method for function minimization.* Computer journal, vol. 7, no. 4, pages 308–313, 1965.

[Noguere 09]   G. Noguere, E. Rich, C. De Saint Jean, O. Litaize, P. Siegler & V. Avrigeanu. *Average neutron parameters for hafnium.* Nucl. Phys. A, vol. 831, no. 1-2, pages 106 – 136, 2009. ⬚www⬚

[Obloinsky 87] P. Obloinsky. *Preequilibrium γ rays with angular momentum coupling.* Phys. Rev. C, vol. 35, no. 2, pages 407–414, Feb 1987.

[Perkins 79]   L.J. Perkins & Malcolm C. Scott. *The application of pulse shape discrimination in NE 213 to neutron spectrometry.* Nucl. Instr. Meth. A, vol. 166, no. 3, pages 451 – 464, 1979. ⬚www⬚

[Petit 04]   M. Petit, M. Aiche, G. Barreau, S. Boyer, N. Carjan, S. Czajkowski, D. Dassie, C. Grosjean, A. Guiral, B. Haas, D. Karamanis, S. Misicu, C. Rizea, F. Saintamon, S. Andriamonje, E. Bouchez, F. Gunsing, A. Hurstel, Y. Lecoz, R. Lucas, Ch. Theisen, A. Billebaud, L. Perrot & E. Bauge. *Determination of the $^{233}Pa(n,f)$ reaction cross section from 0,5 to $10MeV$ neutron energy using the transfer reaction $^{232}Th(^3He,p)^{234}Pa$.* Nucl. Phys. A, vol. 735, no. 3-4, pages 345 – 371, 2004. ⬚www⬚

[Plag 03]   R. Plag, M. Heil, F. Kappeler, P. Pavlopoulos, R. Reifarth & K. Wisshak. *An optimized C6D6 detector for studies of resonance-dominated (n,γ) cross-sections.* Nucl. Instr. Meth. A, vol. 496, no. 2-3, pages 425 – 436, 2003. ⬚www⬚

[Plettner 05]   C. Plettner, H. Ai, C. W. Beausang, L. A. Bernstein, L. Ahle, H. Amro, M. Babilon, J. T. Burke, J. A. Caggiano, R. F. Casten, J. A. Church, J. R. Cooper, B. Crider, G. Guurdal, A. Heinz, E. A. McCutchan, K. Moody, J. A. Punyon, J. Qian, J. J. Ressler, A. Schiller, E. Williams & W. Younes. *Estimation of (n, f) cross sections by measuring reaction probability ratios.* Phys. Rev. C, vol. 71, page 051602, May 2005. ⬚www⬚

[Raman 88]   S. Raman, S. Kahane & J.E. Lynn. *Direct thermal neutron capture.* Jour. of Phys. G, vol. 14, no. S, page S223, 1988. ⬚www⬚

[Ressler 11]   J. J. Ressler, J. T. Burke, J. E. Escher, C. T. Angell, M. S. Basunia, C. W. Beausang, L. A. Bernstein, D. L. Bleuel, R. J. Casperson, B. L. Goldblum, J. Gostic, R. Hatarik, R. Henderson, R. O. Hughes, J. Munson, L. W. Phair, T. J. Ross, N. D. Scielzo, E. Swanberg, I. J. Thompson & M. Wiedeking. *Surrogate measurement of the*

$^{238}Pu(n,f)$ *cross section.* Phys. Rev. C, vol. 83, page 054610, May 2011. ⬚www⬚

[Salvatores 06]   M. Salvatores. *Fuel cycle strategies for the sustainable development of nuclear energy : The role of accelerator driven systems.* Nucl. Instr. Meth. A, vol. 562, no. 2, pages 578 – 584, 2006. Proceedings of the 7th International Conference on Accelerator Applications - AccApp05. ⬚www⬚

[Santonocito 06]   D. Santonocito & Y. Blumenfeld. *Evolution of the giant dipole resonance properties with excitation energy.* EPJ A, vol. 30, pages 183–202, 2006. ⬚www⬚

[Schmidt 09]   K.H. Schmidt. Deexcitation mechanisms in cn reactions. Curso de Reacciones Nucleares Programa Inter-universitario de Fisica Nuclear, 2009. ⬚www⬚

[Scielzo 10]   N. D. Scielzo, J. E. Escher, J. M. Allmond, M. S. Basunia, C. W. Beausang, L. A. Bernstein, D. L. Bleuel, J. T. Burke, R. M. Clark, F. S. Dietrich, P. Fallon, J. Gibelin, B. L. Goldblum, S. R. Lesher, M. A. McMahan, E. B. Norman, L. Phair, E. Rodriquez-Vieitez, S. A. Sheets, I. J. Thompson & M. Wiedeking. *Measurement of γ-emission branching ratios for $^{154,156,158}Gd$ compound nuclei : Tests of surrogate nuclear reaction approximations for (n,γ) cross sections.* Phys. Rev. C, vol. 81, page 034608, Mar 2010. ⬚www⬚

[Shirley 95a]   V. S. Shirley. *ADOPTED LEVELS GAMMAS for ^{173}Lu.* Nuclear Data Sheets, no. 75, page 377, 1995.

[Shirley 95b]   V. S. Shirley. *ADOPTED LEVELS GAMMAS for ^{173}Yb.* Nuclear Data Sheets, no. 75, page 377, 1995.

[Simon 07]   H. Simon. *The ELISe experiment at FAIR.* Nuclear Physics A, vol. 787, no. 1-4, pages 102 – 109, 2007. ⬚www⬚

[Singh 95]   B. Singh. *ADOPTED LEVELS GAMMAS for ^{172}Yb.* Nuclear Data Sheets, no. 75, page 199, 1995.

[Soisson 10]   S.N. Soisson, B.C. Stein, L.W. May, R.Q. Dienhoffer, M. Jandel, G.A. Souliotis, D.V. Shetty, S. Galanopoulos, A.L. Keksis, S. Wuenschel, Z. Kohley, S.J. Yennello, M.A. Bullough, N.M. Greenwood, S.M. Walsh & C.D. Wilburn. *A dual-axis dual-lateral position-sensitive detector for charged particle detection.* Nucl. Instr. Meth. A, vol. 613, no. 2, pages 240 – 244, 2010. ⬚www⬚

[Stupegia 68]   D. C. Stupegia, Marcia Schmidt, C. R. Keedy & A. A. Madson. *Neutron Capture between 5 keV and 3 MeV*. Journal of Nuclear Energy, vol. 22, page 267, 1968.

[Taieb 09]   J. Taieb. *ELISe : a new facility for unprecedented experimental nuclear fission studies*. Int. Jour. of Mod. Phys. E, vol. 18, page 767, 2009. www

[Tain 04]   J.L. Tain. *New experimental validation of the pulse height weighting technique for capture cross-section measurements*. Nucl. Instr. Meth. A, vol. 521, no. 2-3, pages 454 – 467, 2004. www

[Tamura 65]   T. Tamura. *Analyses of the Scattering of Nuclear Particles by Collective Nuclei in Terms of the Coupled-Channel Calculation*. Rev. Mod. Phys., vol. 37, pages 679–708, Oct 1965. www

[Taylor 09]   W.A. Taylor. J.radio. Nucl.Chem 282, vol. 282, page 391, 2009.

[Thompson 00]   I. Thompson. *FRESCO*. Website, 2000. www

[Thompson 06]   I. Thompson & J. Escher. *Theory of (^{3}He,α) surrogate reactions for deformed uranium nuclei*. Internal report LLNL, 2006. www

[Thompson 09]   I. Thompson. *"Nuclear Reactions for Astrophysics"*. ISBN 9780521856355, 2009.

[Thompson 10]   I. Thompson. *"The Theory of Partial Fusion"*. The 24th International Nuclear Physics Conference (INPC) Vancouver, Canada, vol. LLNL-PROC-444034, 2010.

[Towle 69]   J.H. Towle. *The inelastic scattering of neutrons from ^{89}Y*. Nucl. Phys. A, vol. 131, no. 3, pages 561 – 573, 1969. www

[Tucker 65]   A. B. Tucker, J. T. Wells & W. E. Meyerhof. *Inelastic Neutron Scattering Near Threshold*. Phys. Rev., vol. 137, pages B1181–B1187, Mar 1965. www

[Varaine 06]   F. Varaine. *Processus et faisabilite de la transmutation des dechets a vie longue*. Ecole Joliot Curie, 2006. www

[Weisskopf 37]   V. Weisskopf. *Statistics and Nuclear Reactions*. Phys. Rev., vol. 52, no. 4, pages 295–303, Aug 1937. www

[Weisskopf 57]   Victor F. Weisskopf. *Nuclear Physics*. Rev. Mod. Phys., vol. 29, pages 174–181, Apr 1957. www

[Wilenzick 65]   R.M. Wilenzick, K.K. Seth, P.R. Bevington & H.W. Lewis. *Elastic and inelastic scattering of 6 MeV neutrons*. Nuclear Physics, vol. 62, no. 3, pages 511 – 525, 1965. www

[Wilson 03]   J.N Wilson, B Haas, S Boyer, D Dassie, G Barreau, M Aiche, S Czaj-kowski, C Grosjean & A Guiral. *Measurements of (n,γ) neutron capture cross-sections with liquid scintillator detectors*. Nucl. Instr. Meth. A, vol. 511, no. 3, pages 388 – 399, 2003. www

[Wilson 11]   J. Wilson. Submitted to Phys. Rev. C, 2011.

[Wisshak 00]   K. Wisshak, F. Voss, C. Arlandini, F. Kappeler & L. Kazakov. *Stellar Neutron Capture Cross Sections of the Yb Isotopes*. Physical Review, Part C, Nuclear Physics, vol. 61, no. 6, page 065801, 2000. www

[Wisshak 06]   K. Wisshak, F. Voss, F. Kappeler & L. Kazakov. *Stellar neutron capture cross sections of the Lu isotopes*. Phys. Rev. C, vol. 73, page 015807, 2006. www

[Yamazaki 67]   T. Yamazaki. *Tables of Coefficients for Angular Distribution of Gamma-Rays from Aligned Nuclei*. Nucl. Data 3, vol. 1, 1967.

[Younes 03a]   W. Younes & H. C. Britt. *Neutron-induced fission cross sections simulated from (t, pf) results*. Phys. Rev. C, vol. 67, page 024610, Feb 2003. www

[Younes 03b]   W. Younes & H. C. Britt. *Simulated neutron-induced fission cross sections for various Pu, U, and Th isotopes*. Phys. Rev. C, vol. 68, page 034610, Sep 2003. www

[Younes 03c]   W. Younes, H. C. Britt, J. A. Beckerand & J. B.Wilhelmy. Initial estimate of the $^{237}u(n, f)$ cross section. UCRLID-154194, 2003. www

[Younes 05]   W. Younes & H. C. Britt. Estimates of the $^{237,239}u(n, f)$ cross sections. UCRL-TR-212600, 2005.

Sections efficaces neutroniques via la méthode de substitution

Résumé : _Les sections efficaces neutroniques des noyaux de courte durée de vie sont des données cruciales pour la physique fondamentale et appliquée dans des domaines tels que la physique des réacteurs ou l'astrophysique nucléaire. En général, l'extrême radioactivité de ces noyaux ne nous permet pas de procéder à des mesures induites par neutrons. Cependant, il existe une méthode de substitution (« surrogate » dans la littérature) qui permet de déterminer ces sections efficaces neutroniques par l'intermédiaire de réactions de transfert ou de réactions de diffusion inélastique. Son intérêt principal est de pouvoir utiliser des cibles moins radioactives et ainsi d'accéder à des sections efficaces neutroniques qui ne pourraient pas être mesurées directement. La méthode est basée sur l'hypothèse de formation d'un noyau composé et sur le fait que la désexcitation ne dépend essentiellement que de l'énergie d'excitation et du spin et parité de l'état composé peuplé. Toutefois, les distributions de moments angulaires et parités peuplés dans des réactions de transfert et celles induites par neutrons sont susceptibles d'être différentes. Ce travail fait l'état de l'art sur la méthode substitution et sa validité. En général, la méthode de substitution fonctionne très bien pour extraire des sections efficaces de fission. Par contre, la méthode de substitution dédiée à la capture radiative est mise à mal par la comparaison aux réactions induites par neutrons. Nous avons réalisé une expérience afin de déterminer les probabilités de désexcitation gamma du ^{176}Lu et du ^{173}Yb à partir des réactions de substitution $^{174}Yb(^{3}He, p\gamma)^{176}Lu^{*}$ et $^{174}Yb(^{3}He, \alpha\gamma)^{173}Yb^{*}$, respectivement, et nous les avons comparées avec les probabilités de capture radiative correspondantes aux réactions $^{175}Lu(n, \gamma)$ et $^{172}Yb(n, \gamma)$ qui sont bien connues. Cette expérience a permis de comprendre pourquoi, dans le cas de la désexcitation gamma, la méthode de substitution donne des écarts importants par rapport à la réaction neutronique correspondante. Ce travail dans la région de terres rares a permis d'évaluer dans quelle mesure la méthode de substitution peut s'appliquer pour extraire des probabilités de capture dans la région des actinides. Des expériences précédentes sur la fission ont aussi pu être réinterprétées. Ce travail apporte donc un éclairage nouveau sur la méthode de substitution._

Mots-clès : _méthode de substitution, réactions de transfert induites par ^{3}He, surrogate, noyau composé, théorie Hauser-Feshbach, approximation Weisskopf-Ewing, sections efficaces neutroniques, capture radiative, émission de neutrons, distributions de moments angulaires, spins, efficacité de détection d'une cascade-gamma, fonctions de poids, $C_{6}D_{6}$, germanium, TALYS._

Neutron-induced cross sections via the surrogate method

Abstract : _Neutron-induced cross sections of short-lived nuclei are needed for fundamental and applied physics as nuclear energy or astrophysics. However, very often the high radioactivity of the samples makes the direct measurement of these cross sections extremely difficult. The surrogate reaction method is an indirect way of determining neutron-induced cross sections through transfer or inelastic scattering reactions. This method presents the advantage that in some cases the target material is stable or less radioactive than the material required for a neutron-induced measurement. The method is based on the hypothesis that the excited nucleus is a compound nucleus whose decay depends essentially on its excitation energy and on the spin and parity state of the populated compound state. Nevertheless, the spin and parity population differences between the compound-nuclei produced in the neutron and transfer-induced reactions may be different. This work reviews the surrogate method and its validity. Neutron-induced fission cross sections obtained with the surrogate method are in general good agreement. However, it is not yet clear to what extent the surrogate method can be applied to infer radiative capture cross sections. We performed an experiment to determine the gamma-decay probabilities for ^{176}Lu and ^{173}Yb by using the surrogate reactions $^{174}Yb(^{3}He, p\gamma)^{176}Lu^{*}$ and $^{174}Yb(^{3}He, \alpha\gamma)^{173}Yb^{*}$, respectively, and compare them with the well-known corresponding probabilities obtained in the $^{175}Lu(n, \gamma)$ and $^{172}Yb(n, \gamma)$ reactions. This experiment provides answers to understand why, in the case of gamma-decay, the surrogate method gives significant deviations compared to the corresponding neutron-induced reaction. In this work, we have also assessed whether the surrogate method can be applied to extract capture probabilities in the actinide region. Previous experiments on fission have also been reinterpreted. Thus, this work provides new insights into the surrogate method._

Keywords : _surrogate reaction method, ^{3}He-induced transfer reactions, compound nucleus, Hauser-Feshbach theory, Weisskopf-Ewing approximation, neutron-induced cross sections, radiative capture, neutron emission, angular momentum distributions, spins, detection efficiency for a gamma-cascade, weighting functions, $C_{6}D_{6}$ scintillators, Ge detectors, TALYS code._